FINAL REPORT

FIELD MONITORING OF JOINT-LESS CURVED INTEGRAL ABUTMENT BRIDGE IN NEBRASKA

Ramin Ziaei
Graduate Research Assistant

Yusuf Alhowaidi
Graduate Research Assistant

Chungwook Sim, Ph.D.
Principal Investigator

Jongwan Eun, Ph.D., P.E.
Co-Principal Investigator

Seunghee Kim, Ph.D., P.E.
Co-Principal Investigator

Chung Rak Song, Ph.D.
Co-Principal Investigator

in

Department of Civil and Environmental Engineering

University of Nebraska-Lincoln

Sponsored By

Nebraska Department of Transportation and U.S. Department of Transportation Federal Highway Administration

December 31, 2022

TECHNICAL REPORT DOCUMENTATION PAGE

1. Report No. M087	**2. Government Accession No.**	**3. Recipient's Catalog No.**
4. Title and Subtitle Field Monitoring of Joint-less Curved Integral Abutment Bridge in Nebraska		**5. Report Date** December 31, 2022
		6. Performing Organization Code
7. Author(s) Ramin Ziaei, Yusuf Alhowaidi, Chungwook Sim, Jongwan Eun, Seunghee Kim, and Chung Rak Song		**8. Performing Organization Report No.**
9. Performing Organization Name and Address University of Nebraska-Lincoln Department of Civil and Environmental Engineering 1110 South 67th St., Omaha, NE 68182-0178		**10. Work Unit No.**
		11. Contract Project ID: SPR-P1(19) M087
12. Sponsoring Agency Name and Address Nebraska Department of Transportation Research Section 1,400 Hwy 2 Lincoln, NE 68502		**13. Type of Report and Period Covered** Final Report 7/1/2017 to 12/31/2022
		14. Sponsoring Agency Code
15. Supplementary Notes		

16. Abstract

The research objective of this project is to study the behavior of the curved full integral abutment bridge designed in Nebraska through field monitoring and numerical simulation to 1) understand and model the complex short-term and long-term behavior of curved integral abutment bridges, 2) evaluate if the details provided in Nebraska (pile embedment over 4 ft into the abutment) can be expanded for wider design and construction practices (longer spans and larger curvature for curved bridges), and 3) better maintain existing full curved integral bridges in Nebraska based on the findings of this study (revise and optimize design, if needed). The research team carefully instrumented a curved full-integral abutment bridge following the construction schedules of the bridge starting from Jan. 2020 to Aug. 2021, and measured the abutment backfill pressure, abutment tilts, and pile movement profiles. This study documents the measurements completed between April 2021 to July 2022, including a full annual cycle since the bridge has been fully integral. A three-dimensional finite element model was developed for numerical simulation, and the backfill pressure, tilt, and pile top displacement calculated through the model and measured at the field were compared. The results demonstrate that the backfill pressure and the pile top displacement are within 5% difference, and comparable while the tilt has 20% difference between the model and field measurements. However, the change in tilt due to the annual temperature change (ambient) and the shape of the change (trend) is similar between the simulation and monitoring results. A parametric study was conducted additional to these annual cyclic measurements to study the limits of the curved full integral abutment bridge and recommendations are provided based on the findings. Continuous measurements of the backfill pressure, tilt, and pile movement is recommended until the entire bridge movements level out in several years.

17. Key Words Integral abutment bridge; horizontally curved integral abutment bridge; numerical simulation, field monitoring; soil-structure interaction		**18. Distribution Statement** No restrictions. This document is available through the National Technical Information Service. 5285 Port Royal Road Springfield, VA 22161	
19. Security Classification (of this report) Unclassified	**20. Security Classification (of this page)** Unclassified	**21. No. of Pages** 300	**22. Price**

Form DOT F 1700.7 (8-72) Reproduction of completed page authorized

DISCLAIMER

The contents of this report reflect the views of the authors, who are responsible for the facts and the accuracy of the information presented herein. The contents do not necessarily reflect the official views or policies neither of the Nebraska Department of Transportations nor the University of Nebraska-Lincoln. This report does not constitute a standard, specification, or regulation. Trade or manufacturers' names, which may appear in this report, are cited only because they are considered essential to the objectives of the report.

The United States (U.S.) government and the State of Nebraska do not endorse products or manufacturers. This material is based upon work supported by the Federal Highway Administration under SPR-P1(19) M087. Any opinions, findings and conclusions or recommendations expressed in this publication are those of the author(s) and do not necessarily reflect the views of the Federal Highway Administration.

ACKNOWLEDGMENTS

This study was financially supported by the Nebraska Department of Transportation (NDOT). Their support is gratefully acknowledged. The technical support and valuable discussions provided by the Technical Advisory Committee (TAC) of this project is appreciated.

TABLE OF CONTENTS

Page

TECHNICAL REPORT DOCUMENTATION PAGE i
DISCLAIMER ii
ACKNOWLEDGMENTS iii
TABLE OF CONTENTS iv
LIST OF TABLES vii
LIST OF FIGURES ix

1. INTRODUCTION 19
  1.1 Background 19
  1.2 Research Objective 23
  1.3 Research Scope 24

2. LITERATURE REVIEW 28
  2.1 Introduction 28
  2.1 Long-term Studies Sponsored by State Department of Transportations (DoTs) 28
    2.1.1 Indiana 28
    2.1.2 Iowa 31
    2.1.3 Pennsylvania 35
    2.1.4 Tennessee 36
  2.2 Other Previous Research on Straight and Curved Integral Abutment Bridges 36
    2.2.1 Straight Integral Abutment Bridges 37
    2.2.2 Curved Integral Abutment Bridges 45
  2.3 Review of Bridge Design Manuals for Integral Abutment Bridges 50
  2.4 Statistics of the Full and Semi-Integral Abutment Bridges in Nebraska 52
  2.5 Summary 59

3. FIELD INSTRUMENTATION 60
  3.1 Introduction 60
  3.2 Bridge Layout 61
  3.3 Instrumentation Plan and Installation 64
    3.3.1 Pressure Cell 64
    3.3.2 Tilt Meter 68
    3.3.3 Moisture Sensor 70
    3.3.4 Inclinometer 71
    3.3.5 Inclinometer Reading Process 78
    3.3.6 Concrete Cut–Open 81
    3.3.7 Fiber Optic Cable Based Distributed Strain Sensing (DSS) 85

3.3.7.1 Fiber Optic DSS Cable Installation on Piles 86
3.3.7.2 Fiber Optic DSS Cable Installation on Girders 92
3.3.7.3 Fiber Optic DSS Cable Installation at Approach Slab 95
3.3.8 Remote Data Logger Installation 98
3.4 Summary of Sensor Installation following the Construction Schedules 103

4. FIELD MONITORING RESULTS 104
4.1 Introduction 104
4.2 Pressure Cell Measurements 105
4.3 Tiltmeter Measurements 114
4.4 Inclinometer Measurements 117
4.5 Moisture Sensor 141
4.6 Summary 142

5. NUMERICAL MODEL 144
5.1 Introduction 144
5.2 Structural Elements 145
5.2.1 Piles 145
5.2.2 Girders 148
5.2.3 Deck 149
5.2.4 Abutments 150
5.2.5 Bent 150
5.3 Soil Elements 152
5.3.1 P–y Curves 153
5.3.2 Soil Properties 155
5.4 Soil–Pile Interaction 156
5.5. Soil – Abutment Interaction 165
5.5.1 Rankine’s Theory and Computation of the Spring Constant 166
5.6 Loading 171
5.6.1 Temperature 172
5.6.2 Shrinkage 175
5.7 Model Verification 176
5.7.1 Backfill Soil Pressure 176
5.7.2 Pile Deflection 180
5.7.3 Tiltmeter 187
5.8 Summary 191

6. PARAMETRIC STUDY 192
6.1 Introduction 192
6.2 Bridge Properties 194
6.3 Shrinkage Load 195

6.4 Temperature Load ... 196
6.5 Soil-Pile Springs ... 197
6.6 Bearings ... 202
6.7 Parametric Study Results ... 204
    6.7.1 Length and Curvature ... 205
    6.7.2 Shrinkage Model ... 224
    6.7.3 Soil Type ... 245
    6.7.4 Bearing ... 253
    6.7.5 Pile ... 267
6.8 Summary ... 274

7. SUMMARY AND CONCLUSION ... 277
7.1 Summary ... 277
7.2 Conclusions ... 277
    7.2.1 Length and Curvature ... 278
    7.2.2 Shrinkage Model ... 279
    7.2.3 Soil Type ... 280
    7.2.4 Bearing Type ... 281
    7.2.5 Pile Type and Orientation ... 282
7.2 Recommendations ... 282
    7.2.1 Deck Longitudinal Displacement ... 283
    7.2.2 Pile Head Longitudinal Displacement ... 283
    7.2.3 Pile Head Stress and Moment ... 283
7.3 Further Research ... 284

REFERENCES ... 285

APPENDICES ... 291
Appendix A Properties of Foundation Soil and Backfill Soil ... 291
Appendix B Numerical Simulation Model of the Backfill ... 293

LIST OF TABLES

Table Page

Table 2.1: Summary of the U.S. DOTs Design Manuals regarding Curved IABs 50

Table 3.1: Final Lengths of Inclinometer Casings 78

Table 4.1: Pressure Cell Readings before Installing the Remote Data Acquisition System....... 105

Table 4.2: Inclinometer Measurement Dates 120

Table 5.1: CFT Transformed Section Properties 148

Table 5.2: Dry Unit Weight for Typical Soils in Natural State. 156

Table 5.3: Typical Dry Densities for Different Soil Groups 157

Table 5.4: Approximate Correlation among SPT number, Consistency, and Unconfined Compression Strength in Cohesive soil 157

Table 5.5: Qualitative Description of Granular Soil Deposits 159

Table 5.6: South Abutment Soil Properties 159

Table 5.7: North Abutment Soil Properties 160

Table 5.8: Recommended Values of k for Fine Sand below the Water Table 162

Table 5.9: Recommended Values of k for Fine Sand above the Water Table 162

Table 5.10: Recommended Values of Strain Factor for Clays 163

Table 5.11: Weekly Max., Min. and Average Temperature at Big Springs Weather Station 172

Table 6.1: Geometric Parameters of the Numerical Models 193

Table 6.2: Shrinkage Strains and Temperature Fluctuations used in the Parametric Study 196

Table 6.3: Soil Properties for the Parametric Study 199

Table 6.4: Soil Stiffness for Loose and Dense Sand 200

Table 6.5: Soil Stiffness for Very Soft and Very Stiff Clay 201

Table 6.6: Primary and Secondary Parameters 205

Table 6.7: Interior and Exterior Pile Head and Deck Movements (CEB–FIP 90) 207

Table 6.8: Interior and Exterior Pile Head and Deck Movements (ACI 209R) 223

Table 6.9: Bridge Displacements for Shrinkage Models (L = 400 ft and R = 600 ft) 242

Table 6.10: Bridge Displacements for Shrinkage Models (L = 400 ft and R = 1,000 ft) 242

Table 6.11: Bridge Displacements for Shrinkage Models (L = 400 ft and R = 1,400 ft) 243

Table 6.12: Bridge Displacements for Shrinkage Models (L = 400 ft and R = 1,800 ft) 243
Table 6.13: Bridge Displacements for Shrinkage Models (L = 400 ft and Straight Bridges) 244
Table 6.14: Pipe Pile and H pile Section Properties 267
Table A.1: Properties of Foundation Soil obtained from Borehole Logs of Abutments 292
Table A.2: Properties of Backfill Soil obtained from Laboratory Tests (Kim et al., 2021) 292
Table A.3: Plastic Hardening Input Parameters used to Represent Backfill Soil 295
Table A.4: Properties of the Embankment and the Foundation Soil behind the IAB 296
Table A.5: Input Parameters for the Normal and Shear Spring Constant used in the North Abutment 297

LIST OF FIGURES

Figure Page

Figure 1.1: Expansion and Contraction of Joint-less Bridges and Damage Observed in Approach Spans (retrieved from Arsoy et al., 1999) 20
Figure 1.2: Grade Beam Supporting the Approach Span Attached to the Integral Abutment Bridge (drawings retrieved from Big Springs, Nebraska West I-80 Loop Bridge) 21
Figure 1.3: Details of the Superstructure/Abutment and Pile/Abutment Connection of the Integral Abutment Bridge in Nebraska (drawings retrieved from Big Springs West I-80 Loop Bridge) .. 22
Figure 2.1: IAB Pile Types in Nebraska 53
Figure 2.2:H-pile Orientation in Nebraska IABs 54
Figure 2.3: Possible H-pile Orientations (retrieved from Lovell, 2010) 54
Figure 2.4 H-piles Alignment for IABs in Nebraska 55
Figure 2.5: Use of Predrilled Holes Filled with Sand in IABs in Nebraska 55
Figure 2.6: IABs with MSE Walls in Nebraska 56
Figure 2.7: IABs with CMP Sleeves in Nebraska 56
Figure 2.8: Semi–IAB Pile Types in Nebraska 57
Figure 2.9: H-pile Orientation in Nebraska Semi–IABs 57
Figure 2.10: Use of Predrilled Holes Filled with Sand in Semi–IABs in Nebraska 58
Figure 2.11: Semi–IABs with MSE Walls in Nebraska 58
Figure 2.12: Semi–IABs with CMP Sleeves in Nebraska 59
Figure 3.1: Big Springs Bridge (S080-10302) over I-80 60
Figure 3.2: Pavement Replacement as Part of the Big Springs West Project 61
Figure 3.3: Plan and Elevation Views of the Big Springs Bridge (drawings retrieved from Big Springs West I-80 Loop Bridge) 62
Figure 3.4: Elevation View of the Abutments (drawings retrieved from Big Springs West I-80 Loop Bridge) 63
Figure 3.5: Cross Section of the Integral Abutment (drawings retrieved from Big Springs West I-80 Loop Bridge) 63
Figure 3.6: Cross Section of the Abutment with its Installed Instruments 65

Figure 3.7: Pressure Cell Locations on Each Abutment 65
Figure 3.8: Preparation for Pressure Cell Installation 66
Figure 3.9: Adding Epoxy to the Contact Area to Secure the Installation 67
Figure 3.10: Pressure Cell Cable Arrangement 67
Figure 3.11: Top View of the Biaxial Tiltmeter 68
Figure 3.12: Drilling the Abutment's Wall to Install the Mounting Bracket 69
Figure 3.13: Tiltmeter Installation 69
Figure 3.14: Moisture Sensor Installation 70
Figure 3.15: Geokon Model GK-604D containing the Inclinometer probe, the reel-mounted cable and the Field PC (retrieved from Geokon Model GK-604D instruction manual) 71
Figure 3.16: Inclinometer Casing 72
Figure 3.17: Locations of Inclinometer Installation 73
Figure 3.18: Location and Length of the Inclinometer Casing 74
Figure 3.19: Creating Bore Holes in the Foundation Soil using a Drilling Rig Machine 75
Figure 3.20: Installation of Inclinometer Casings 76
Figure 3.21: Inclinometer Casing Extension at Different Stages, and their Exit Locations 77
Figure 3.22: Orthogonal Grooves in each Casing 78
Figure 3.23: Inclinometer Probe (retrieved from Inclinometer Manual) 79
Figure 3.24: Taking Inclinometer Readings 80
Figure 3.25: GSSI SIR-4000 GPR System 81
Figure 3.26: Cut Open Section near Approximate Location of the Inclinometer Casing 82
Figure 3.27: Reflected EM Wave Patterns 83
Figure 3.28 Inclinometer Casings after Cutting Open the Approach Slab 84
Figure 3.29: Structure of a Fiber Optic Cable 85
Figure 3.30: Strain causing Brillouin Frequency Shift 86
Figure 3.31: Location of Fiber Optic Cables Instrumented on Piles 87
Figure 3.32: Composite Beam with Grooves, Fiber cables and the Protective Epoxy 88
Figure 3.33: Composite Beams for Each Pile 89
Figure 3.34: Fiber Optic Cables on Composite Beams 90
Figure 3.35 Lowering the composite beams into the pile 90
Figure 3.36: Rubber Tube Installation for Cable Protection 91

Figure 3.37: Casting Mortar inside Piles with Fiber Optic Cables 91
Figure 3.38 Three instrumented girders 92
Figure 3.39: Locations of Fiber Optic Cable Installation and Splice Locations 92
Figure 3.40: Fiber Optic Cable Installation on the Girder with Epoxy and Waterproof Coat, and the Lead Cable Protected in Plastic Bags for Future Splicing Task 93
Figure 3.41: Performing Fiber Optic Cable Fusion Splice at the Girder Splice Point and Connecting Pigtails at the End of Each Cable 94
Figure 3.42: Plan View of the Location of Fiber Optic Cable in the Approach Slab 95
Figure 3.43: L-channels with Fiber Optic Cables attached to the Top Reinforcement Mat 96
Figure 3.44 Rubber Tube Protection over L-channels 97
Figure 3.45: Photo of Solar Panel, the Node and the Supervisor on both Abutments 99
Figure 3.46: Interior view of the south abutment and its wiring scheme 100
Figure 3.47: Settings for the Agent Software 101
Figure 3.48: Measurements on Sensors from the South Abutment 101
Figure 3.49: Entry for Calibration Factors 102
Figure 4.1: Daily Temperature Change of the North Platte Weather Station 104
Figure 4.2: Location of Pressure Cells on Each Abutment 105
Figure 4.3: Pressure Cell and Tiltmeter Readings 106
Figure 4.4: Pressure Cell Measurements 108
Figure 4.5: Cyclic Behavior of the Pressure Cell Measurements 110
Figure 4.6: East Bottom Pressure Cells on North and South Abutments 112
Figure 4.7: East Top Pressure Cells on North and South Abutments 113
Figure 4.8: West Bottom Pressure Cells on North and South Abutments 113
Figure 4.9: Longitudinal Tilts for North and South Abutments 115
Figure 4.10: Lateral Tilts for North and South Abutments 115
Figure 4.11: Cyclic Behavior of the Tiltmeter Measurements 118
Figure 4.12: Indication of A and B Directions for Each Inclinometer 119
Figure 4.13: Longitudinal Profile of the North-East Inclinometer 122
Figure 4.14: Lateral Profile of the North-East Inclinometer 123
Figure 4.15: Longitudinal Profile of the North-West Inclinometer 124
Figure 4.16: Lateral Profile of the North-West Inclinometer 125

Figure 4.17: Longitudinal Profile of the South-East Inclinometer 126
Figure 4.18: Lateral Profile of the South-East Inclinometer.. 127
Figure 4.19: Longitudinal Profile of the South-West Inclinometer 128
Figure 4.20: Lateral Profile of the South-West Inclinometer 129
Figure 4.21: Longitudinal Deflection of the North-East inclinometer 131
Figure 4.22: Lateral Deflection of the North-East Inclinometer.. 132
Figure 4.23: Longitudinal Deflection of the North-West Inclinometer.................................... 133
Figure 4.24: Lateral Deflection of the North-West Inclinometer 134
Figure 4.25: Longitudinal Deflection of the South-East Inclinometer 135
Figure 4.26: Lateral Deflection of the South-East Inclinometer.. 136
Figure 4.27: Longitudinal Deflection of the South-West Inclinometer.................................... 137
Figure 4.28: Lateral Deflection of the South-West Inclinometer 138
Figure 4.29: Longitudinal Deflection of the Top Inclinometer Readings (4 ft from top) 139
Figure 4.30: Lateral Deflection of the Top Inclinometer Readings (4 ft from top).................. 140
Figure 4.31: Moisture Content 141
Figure 5.1: CMP Sleeves around Pipe Piles and the Loose Sand in between 146
Figure 5.2: CFT Cross Section Transformation.. 147
Figure 5.3: Cross Section of Girders at Different Locations 149
Figure 5.4: Concrete Slab Cross Section 149
Figure 5.5: Drawings of Abutments.. 151
Figure 5.6: Bent, Bent Cap and its Supporting Piles 152
Figure 5.7: Three-Dimensional Soil-Pile Interaction... 153
Figure 5.8: Distribution of Stresses around a Pile, (a) Before Lateral Deflection, (b) After Lateral Deflection (retrieved from LPILE 2019 Technical Manual) 154
Figure 5.9: Soil–Pile Model used by LPILE and P–Y curves 155
Figure 5.10: Soil Properties at the North and South Abutments.. 155
Figure 5.11: Characteristic Shape of P-y Curves in Sand... 160
Figure 5.12: Matlock P–y curve in soft clay for cyclic loading... 161
Figure 5.13: *k* values versus Angle of Friction for Fine Sand in LPILE 163
Figure 5.14: Typical Load–Displacement Curve for Nonlinear Springs around a Pile............. 164
Figure 5.15: Rankine's Solution to Passive Pressure (retrieved from Lovell, 2010) 166

Figure 5.16: Lateral Pressure Distribution on the Abutment's Wall 167
Figure 5.17: Typical Load–Displacement Curve for the Abutment's Backfill Soil.................. 169
Figure 5.18: Location of the Nonlinear Links on Each Abutment 171
Figure 5.19: Weekly Ambient Temperature at the Big Springs Site 175
Figure 5.20: Pressure and Average Temperature Variation of the Nonlinear Links on the South Abutment.. 177
Figure 5.21: Comparisons between the South Abutment Backfill Pressures 178
Figure 5.22: Pressure and Average Temperature Variation of the Nonlinear Links on the North Abutment.. 180
Figure 5.23: Comparisons between the North Abutment Backfill Pressures 181
Figure 5.24: Comparisons between Simulated Longitudinal Pile Deflection and Inclinometer Measurements for June 17, 2021 (Southeast Sensor) 183
Figure 5.25: Comparisons between Simulated Longitudinal Pile Deflection and Inclinometer Measurements for June 17, 2021 (Southwest Sensor) 183
Figure 5.26: Comparisons between Simulated Longitudinal Pile Deflection and Inclinometer Measurements for June 17, 2021 (Northeast Sensor) 184
Figure 5.27: Comparisons between Simulated Longitudinal Pile Deflection and Inclinometer Measurements for June 17, 2021 (Northwest Sensor) 184
Figure 5.28: Comparisons between Simulated Longitudinal Pile Deflection and Inclinometer Measurements for November 17, 2021 (Southeast Sensor)... 185
Figure 5.29: Comparisons between Simulated Longitudinal Pile Deflection and Inclinometer Measurements for November 17, 2021 (Southwest Sensor) 185
Figure 5.30: Comparisons between Simulated Longitudinal Pile Deflection and Inclinometer Measurements for November 17, 2021 (Northeast Sensor)... 186
Figure 5.31: Comparisons between Simulated Longitudinal Pile Deflection and Inclinometer Measurements for November 17, 2021 (Northwest Sensor) 186
Figure 5.32: Model Simulation Results of North and South Abutments Tilts and Corresponding Weekly Average Temperature 188
Figure 5.33: Longitudinal Tilt of the South Abutment... 189
Figure 5.34: Longitudinal Tilt of the North Abutment... 190
Figure 6.1: Shrinkage Models in CSiBridge... 195

Figure 6.2: Bilinear Force Displacement Relationship of Soil–Pile Springs............................. 202
Figure 6.3: Default Bearing Configuration over All Piers.. 203
Figure 6.4: Roller Bearing Configuration over All Piers.. 203
Figure 6.5: Longitudinal Roller Bearing Configuration over All Piers 204
Figure 6.6: Fixed Bearing Configuration over All Piers... 204
Figure 6.7: Location of Interior and Exterior Pile and Deck Readings 206
Figure 6.8: Interior Pile Head Longitudinal Movement (CEB–FIP 90) 208
Figure 6.9: Interior Pile Head Lateral Movement (CEB–FIP 90) 208
Figure 6.10: Interior Deck Longitudinal Movement (CEB–FIP 90) 209
Figure 6.11:Interior Deck Lateral Movement (CEB–FIP 90)... 209
Figure 6.12: Exterior Pile Head Longitudinal Movement (CEB–FIP 90) 210
Figure 6.13: Exterior Pile Head Lateral Movement (CEB–FIP 90) 210
Figure 6.14: Exterior Deck Longitudinal Movement (CEB–FIP 90) 211
Figure 6.15: Exterior Deck Lateral Movement (CEB–FIP 90).. 211
Figure 6.16: Pile Max. von Mises Stress at the Pile–Abutment Connection (CEB–FIP 90)...... 215
Figure 6.17: Pile Max. Bending Moment at the Pile–Abutment Connection (CEB–FIP 90)..... 215
Figure 6.18: Girder Bottom Flange Max. von Mises Stress at the Girder–Abutment Connection (CEB–FIP 90) 216
Figure 6.19: Girder Top Flange Max. von Mises Stress at the Girder–Abutment Connection (CEB–FIP 90) 216
Figure 6.20: Interior Pile Head Longitudinal Movement (ACI 209R) 217
Figure 6.21: Interior Pile Head Lateral Movement (ACI 209R) 217
Figure 6.22: Interior Deck Longitudinal Movement (ACI 209R) 218
Figure 6.23: Interior Deck Lateral Movement (ACI 209R)... 218
Figure 6.24: Exterior Pile Head Longitudinal Movement (ACI 209R)..................................... 219
Figure 6.25: Exterior Pile Head Lateral Movement (ACI 209R) 219
Figure 6.26: Exterior Deck Longitudinal Movement (ACI 209R) 220
Figure 6.27: Exterior Deck Lateral Movement (ACI 209R).. 220
Figure 6.28: Pile Max. von Mises Stress at the Pile–Abutment Connection (ACI 209R).......... 221
Figure 6.29: Pile Max. Bending Moment at the Pile–Abutment Connection (ACI 209R)......... 221

Figure 6.30: Girder Bottom Flange Max. von Mises Stress at the Girder–Abutment Connection (ACI 209R) 222
Figure 6.31: Girder Top Flange Max. von Mises Stress at the Girder–Abutment Connection (ACI 209R) 222
Figure 6.32: Interior Pile Head Longitudinal Movement for the Two Shrinkage Models 225
Figure 6.33: Exterior Pile Head Longitudinal Movement for the Two Shrinkage Models 225
Figure 6.34: Interior Deck Longitudinal Movement for the Two Shrinkage Models 226
Figure 6.35: Exterior Deck Longitudinal Movement for the Two Shrinkage Models 226
Figure 6.36: Interior Pile Head Lateral Movement for the Two Shrinkage Models 227
Figure 6.37: Exterior Pile Head Lateral Movement for the Two Shrinkage Models 227
Figure 6.38: Interior Deck Lateral Movement for the Two Shrinkage Models 228
Figure 6.39: Exterior Deck Lateral Movement for the Two Shrinkage Models 228
Figure 6.40: Interior Pile Head Longitudinal Movement for the Two Shrinkage Models 229
Figure 6.41: Exterior Pile Head Longitudinal Movement for the Two Shrinkage Models 229
Figure 6.42: Interior Deck Longitudinal Movement for the Two Shrinkage Model 230
Figure 6.43: Exterior Deck Longitudinal Movement for the Two Shrinkage Models 230
Figure 6.44: Interior Pile Head Lateral Movement for the Two Shrinkage Models 231
Figure 6.45: Exterior Pile Head Lateral Movement for the Two Shrinkage Models 231
Figure 6.46: Interior Deck Lateral Movement for the Two Shrinkage Models 232
Figure 6.47: Exterior Deck Lateral Movement for the Two Shrinkage Models 232
Figure 6.48: Interior Pile Head Longitudinal Movement for the Two Shrinkage Models 233
Figure 6.49: Exterior Pile Head Longitudinal Movement for the Two Shrinkage Models 233
Figure 6.50: Interior Deck Longitudinal Movement for the Two Shrinkage Models 234
Figure 6.51: Exterior Deck Longitudinal Movement for the Two Shrinkage Models 234
Figure 6.52: Interior Pile Head Lateral Movement for the Two Shrinkage Models 235
Figure 6.53: Exterior Pile Head Lateral Movement for the Two Shrinkage Models 235
Figure 6.54: Interior Deck Lateral Movement for the Two Shrinkage Models 236
Figure 6.55: Exterior Deck Lateral Movement for the Two Shrinkage Models 236
Figure 6.56: Interior Pile Head Longitudinal Movement for the Two Shrinkage Models 237
Figure 6.57: Exterior Pile Head Longitudinal Movement for the Two Shrinkage Models 237
Figure 6.58: Interior Deck Longitudinal Movement for the Two Shrinkage Models 238

Figure 6.59: Exterior Deck Longitudinal Movement for the Two Shrinkage Models 238
Figure 6.60: Interior Pile Head Lateral Movement for the Two Shrinkage Models.................. 239
Figure 6.61: Exterior Pile Head Lateral Movement for the Two Shrinkage Models 239
Figure 6.62: Interior Deck Lateral Movement for the Two Shrinkage Models......................... 240
Figure 6.63: Exterior Deck Lateral Movement for the Two Shrinkage Models........................ 240
Figure 6.64: Pile Head Longitudinal Movement for the Two Shrinkage Models 241
Figure 6.65: Deck Longitudinal Movement for the Two Shrinkage Models 241
Figure 6.66: Interior Pile Head Longitudinal Displacement for Different Soil Types 247
Figure 6.67: Interior Pile Head Lateral Displacement for Different Soil Types (L = 400 ft)..... 247
Figure 6.68: Interior Deck Longitudinal Displacement for Different Soil Types (L = 400 ft) .. 248
Figure 6.69: Interior Deck Lateral Displacement for Different Soil Types (L = 400 ft)............ 248
Figure 6.70: Exterior Pile Head Longitudinal Displacement for Different Soil Types 249
Figure 6.71: Exterior Pile Head Lateral Displacement for Different Soil Types (L = 400 ft) ... 249
Figure 6.72: Exterior Deck Longitudinal Displacement for Different Soil Types (L = 400 ft) . 250
Figure 6.73: Exterior Deck Lateral Displacement for Different Soil Types (L = 400 ft)........... 250
Figure 6.74: Pile Max. von Mises Stress at the Pile–Abutment Connection for Different Soil Types (L = 400 ft)... 251
Figure 6.75: Pile Max. Bending Moment at the Pile–Abutment Connection for Different Soil Types (L = 400 ft)... 251
Figure 6.76: Girder Bottom Flange Maximum von Mises Stress at the Girder–Abutment Connection for Different Soil Types (L = 400 ft)... 252
Figure 6.77: Girder Top Flange Maximum von Mises Stress at the Girder–Abutment Connection for Different Soil Types (L = 400 ft) 252
Figure 6.78: Interior Pile Head Longitudinal Displacement for Different Bearing Configurations (L = 400 ft)... 254
Figure 6.79: Interior Pile Head Lateral Displacement for Different Bearing Configurations (L = 400 ft)... 254
Figure 6.80: Interior Deck Longitudinal Displacement for Different Bearing Configurations (L = 400 ft)... 255
Figure 6.81: Interior Deck Lateral Displacement for Different Bearing Configurations (L = 400 ft) 255

Figure 6.82: Exterior Pile Head Longitudinal Displacement for Different Bearing Configurations (L = 400 ft) 256
Figure 6.83: Exterior Pile Head Lateral Displacement for Different Bearing Configurations (L = 400 ft) 256
Figure 6.84: Exterior Deck Longitudinal Displacement for Different Bearing Configurations (L = 400 ft) 257
Figure 6.85: Exterior Deck Lateral Displacement for Different Bearing Configurations (L = 400 ft) 257
Figure 6.86: Pile Max. von Mises Stress at the Pile–Abutment Connection for Different Bearing Configurations (L = 400 ft) 258
Figure 6.87: Pile Max. Moment at the Pile–Abutment Connection for Different Bearing Configurations (L = 400 ft) 258
Figure 6.88 Girder Bottom Flange Max. von Mises Stress at the Girder–Abutment Connection for Different Bearing Configurations (L = 400 ft) 259
Figure 6.89 Girder Top Flange Max. von Mises Stress at the Girder–Abutment Connection for Different Bearing Configurations (L = 400 ft) 259
Figure 6.90: Interior Pile Head Longitudinal Displacement for Different Bearing Configurations (L = 200 ft) 261
Figure 6.91: Interior Pile Head Lateral Displacement for Different Bearing Configurations (L = 200 ft) 261
Figure 6.92: Interior Deck Longitudinal Displacement for Different Bearing Configurations (L = 200 ft) 262
Figure 6.93: Interior Deck Lateral Displacement for Different Bearing Configurations 262
Figure 6.94: Exterior Pile Head Longitudinal Displacement for Different Bearing Configurations (L = 200 ft) 263
Figure 6.95: Exterior Pile Head Lateral Displacement for Different Bearing Configurations (L = 200 ft) 263
Figure 6.96: Exterior Deck Longitudinal Displacement for Different Bearing Configurations (L = 200 ft) 264
Figure 6.97: Exterior Deck Lateral Displacement for Different Bearing Configurations 264

Figure 6.98: Pile Max. von Mises Stress at the Pile–Abutment Connection for Different Bearing Configurations (L = 200 ft) 265
Figure 6.99: Pile Max. Moment at the Pile–Abutment Connection for Different Bearing Configurations (L = 200 ft) 265
Figure 6.100: Girder Bottom Flange Max. von Mises Stress at the Girder–Abutment Connection for Different Bearing Configurations (L = 200 ft) 266
Figure 6.101: Girder Top Flange Max. von Mises Stress at the Girder–Abutment Connection for Different Bearing Configurations (L = 200 ft) 266
Figure 6.102: Interior Pile Head Longitudinal Displacement for Different Pile Sections 268
Figure 6.103: Interior Pile Head Lateral Displacement for Different Pile Sections 268
Figure 6.104: Interior Deck Longitudinal Displacement for Different Pile Sections 269
Figure 6.105: Interior Deck Lateral Displacement for Different Pile Sections (L = 400 ft) 269
Figure 6.106: Exterior Pile Head Longitudinal Displacement for Different Pile Sections (L = 400 ft) 270
Figure 6.107: Exterior Pile Head Lateral Displacement for Different Pile Sections 270
Figure 6.108: Exterior Deck Longitudinal Displacement for Different Pile Sections 271
Figure 6.109: Exterior Deck Lateral Displacement for Different Pile Sections (L = 400 ft) 271
Figure 6.110: Pile Max. von Mises Stress at the Pile–Abutment Connection for Different Pile Sections (L = 400 ft) 272
Figure 6.111: Pile Max. Moment at the Pile–Abutment Connection for Different Pile Sections (L = 400 ft) 272
Figure 6.112: Girder Bottom Flange Max. von Mises Stress at the Girder–Abutment Connection for Different Pile Sections (L = 400 ft) 273
Figure 6.113: Girder Top Flange Max. von Mises Stress at the Girder–Abutment Connection for Different Pile Sections (L = 400 ft) 273
Figure A.1: Numerical Simulation Model to Investigate Thermal Loading Effect on backfill of the North Abutment 296

1. INTRODUCTION

1.1 Background

There are more than 9,000 integral abutment bridges (IAB) and 4,000 semi-integral abutment bridges (semi-IAB) in U.S., which increased dramatically in the past two decades (White 2^{nd}, 2007). Nebraska is no exception – there are hundreds of integral and semi-integral abutment bridges in the state of Nebraska, and thus guidelines and specifications for these structures are included in the Bridge Office Policies and Procedures (BOPP, 2016). The obvious advantage of using integral abutment bridges is their reduced construction cost and maintenance costs by eliminating bearings and expansion joints that make the bridge “joint-less” and simple. This fits well with Nebraska's "well-timed" bridge preservation practice of eliminating problems before they occur. Despite the wide acceptance in usage (more than 40 states are using integral abutment bridges) and the advantage listed above, integral and semi-integral abutment bridges are often built with specific limitations under each state’s bridge design manuals, and the design primarily relies on local practice based on limited empirical data. Each state design integral and semi-integral abutment bridges with different limitations (or no limitations) regarding the skew angle, pile type, pile orientation, superstructure to abutment embedment length, pile to abutment embedment length, span length, curvature, or construction practices. AASHTO LRFD Bridge Design Specifications no longer have any design limits for integral abutment bridges. This inconsistency provides room for improvement and need for increase in understanding the complex soil-structure interaction behavior based on further studies.

For the past few decades, state agencies in Illinois, Indiana, Iowa, Kentucky, Maine, Massachusetts, Minnesota, Nebraska, New Jersey, Pennsylvania, Tennessee, Utah, Virginia, West Virginia, and the FHWA made efforts to investigate integral abutment or semi-integral abutment bridges. Four states (Indiana, Iowa, Pennsylvania, and Tennessee) conducted an extensive research program and long-term field monitoring effort for these types of bridges. These studies have confirmed that the seasonal and daily temperature fluctuation, thermal cycles of loads, and the time-dependent behavior of concrete are the main driving forces that expand and contract these joint-less bridges and their behavior will level out to a steady state 5 to 7 years after the construction. The temperature loads and/or the time dependent behavior of concrete (creep and shrinkage) will cause contraction resulting in soil settlements below the approach span. Several states including Iowa and South Dakota near Nebraska have reported this problem where they observed voids forming with a size ranging between 0.5 to 14 in. Annual thermal fluctuations and the time dependent behavior of the concrete deck and girder induce relative movements between the abutment, the foundation, and the soil behind the abutment which cause such problems as shown in Figure 1.1. Settlement behind the abutments is not an issue in Nebraska with such systems because the approach span attached to the integral abutment bridges have grade beams as shown in Figure 1.2.

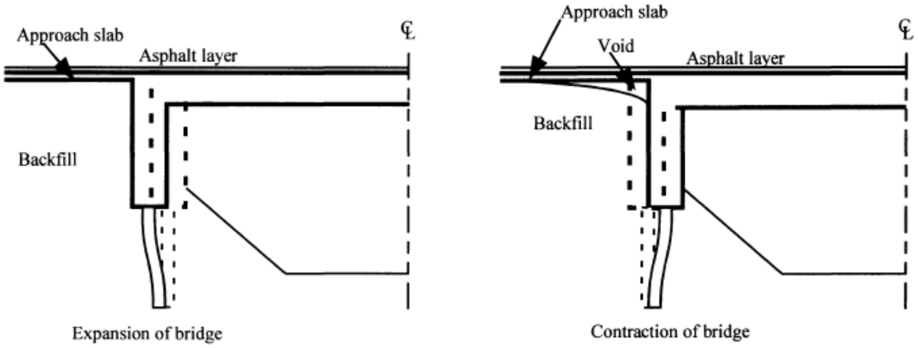

Figure 1.1: Expansion and Contraction of Joint-less Bridges and Damage Observed in Approach Spans (retrieved from Arsoy et al., 1999)

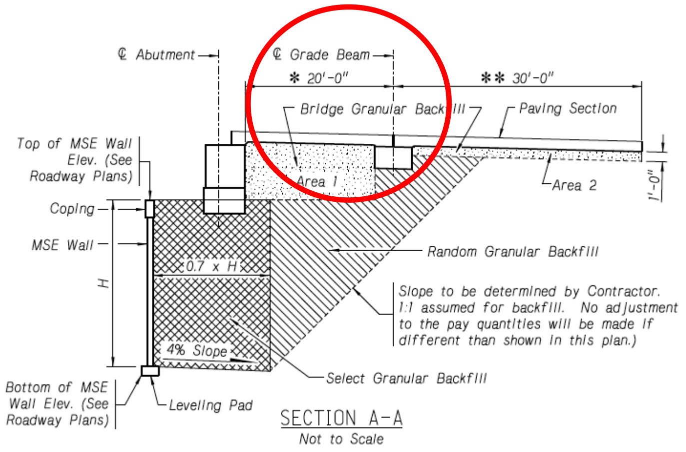

Figure 1.2: Grade Beam Supporting the Approach Span Attached to the Integral Abutment Bridge (drawings retrieved from Big Springs, Nebraska West I-80 Loop Bridge)

Details of the approach slabs in Nebraska were extensively studied by Morcous and Abo-Elkhier (2021) and drawings of the Nebraska approach slabs are specified in the Bridge Office Policies and Procedures (BOPP, 2016). Yet, there are still remaining questions on the bounding limits regarding the span length, skew angle, proper details at the superstructure/abutment interface and pile/abutment interface, and/or the curvature of the bridge if a curved joint-less bridge is designed. The IAB design vary by state which is controlled by the details of the connection where the girders, abutment, and piles are joining. An example of the details of integral abutment bridge designed and constructed in Nebraska is shown in Figure 1.3. This Figure was retrieved from the drawings of the Big Springs West I-80 Loop Bridge constructed above the I-80 interstate near Big Springs, Nebraska. This bridge is a curved full-integral abutment bridge where the movements are expected to occur in three-dimensional stage which makes the full integral abutment behavior more complex requiring further studies. Since, predicting the 3-D thermal movements of complex bridge geometry (highly skewed or curved) is nearly impossible as stated by the Tennessee Bridge Engineer, Edward Wasserman (Olson et al., 2013), this could be a good reason to eliminate bearings and construct bridges with complex geometry as an integral abutment bridge. Moorty and Roeder (1992) who analyzed the temperature-dependent bridge movements also stated that although thermal movements can be controlled by integral construction, the movements are controlled by the restrains provided by the strength and stiffness of the substructure, foundation, and backfill which increases the internal forces in this type of bridges and requires careful caution and design when used for skew or curved bridges.

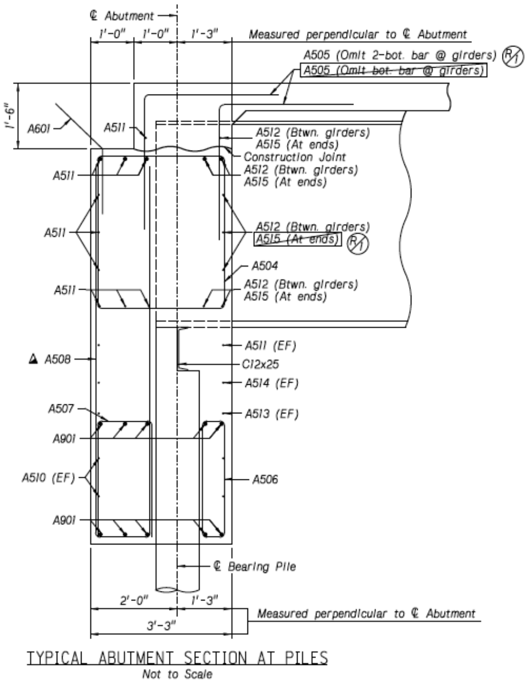

Figure 1.3: Details of the Superstructure/Abutment and Pile/Abutment Connection of the Integral Abutment Bridge in Nebraska (drawings retrieved from Big Springs West I-80 Loop Bridge)

The example shown in Figure 1.3 is an indication where a complex curved steel girder bridge is designed and constructed as a full curved integral abutment bridge following this statement. As shown in Figure 1.3, the pile penetrates deeply into the abutment making the pile-abutment interface closer to a fixed condition. With the increased fixity and stiff connection, the moment created by the thermal expansion of the superstructure is more likely to be higher than joint-less bridges with less embedment provided. Details of other states are provided in the literature review section in the next chapter of this report. This study is interested in measuring and analyzing the movements of a curved full integral abutment bridge in Nebraska with such details as shown in Figure 1.3 and interested in evaluating the moments that are created by such connections with deep embedment. As shown in Figure 1.3, the steel girder is embedded inside the concrete abutment approximately 20 in. while the pile is embedded inside the concrete abutment approximately 54 in. The piles in Nebraska are connected together with the steel channels to create a girder sear and the entire abutment is continuously poured. The approach slab is tied together to the abutment with a diagonal reinforcement allowing the approach to move together with the joint-less bridge. The expansion joint is located at the end of the approach slab away from the bridge. But the approach and the bridge deck are cast separately having a construction joint and allows the approach to behave more like a hinge connection with the IAB structure through the diagonal reinforcement connecting them together.

1.2 Research Objective

The research objective of this project is to study the behavior of the curved full integral abutment bridge designed in Nebraska through field monitoring and numerical simulation to 1) understand and model the complex short-term and long-term behavior of curved integral abutment bridges (behavior of superstructure/abutment connection, pile/abutment connection, backfill/abutment, the soil-structure interaction, and time-dependent behavior), 2) evaluate if the details provided in Nebraska (pile embedment over 4 ft into the abutment) can be expanded for wider design and construction practices (longer spans, and larger curvature for curved bridges), and 3) better maintain existing full integral and semi-integral abutment bridges in Nebraska based on the findings of this study (revise and optimize design). The research team will investigate the loads produced in abutments over the Nebraska integral abutment bridges, measure the load-displacement of piles, and examine the ratcheting effects (passive pressure increases and inward residual displacement) of these structures through field measurements and numerical simulations.

1.3 Research Scope

The research will be divided into four tasks in order to successfully conduct monitoring and numerical analysis of a curved joint-less integral abutment bridge in Nebraska. The proposed study will provide background knowledge for new design and construction practices as well as providing solutions for any necessary repair/strengthening solutions, if needed.

Task 1: Literature Review

This task will focus on comparing current integral abutment bridge practices and design guidelines adopted in Nebraska including those utilized in other states. Following are the specific activities to be included in this task regarding practices in Nebraska:

- Compile information of all joint-less integral or semi-integral abutment bridges in Nebraska focusing on the followings:
    a) Predrilling practices, backfill material, unconnected wing walls in integral abutment bridges and connected wing walls in semi-integral abutment bridges
    b) Details of connection between superstructure and abutment or abutment and pile.

Task 2: Field Instrumentation / Monitoring

This task will be the critical component of this project to better understand and provide background information for the complex soil-structure interaction of integral abutment bridges in Nebraska. A curved full integral abutment bridge was provided by the NDOT Technical Advisory Committee (TAC) members for field instrumentation since there are limited research that involves field monitoring of this bridge type. The bridge site was provided in December 2019 and instrumentation took place starting January of 2020 as the construction started. The instrumentation took place following the construction schedules between 2020 and 2021 for a full year. And the full monitoring process started in August of 2021. Followings are the list of items the research team monitored to better understand the in-service behavior of a typical curved integral abutment bridge. Field monitoring requires at least 12 months of data collection to reflect a full cycle of annual temperature fluctuation that is reported to impose the maximum influence. This report contains the full 12 months of data collection between August 2021 to August 2022 with the following information.

- Seasonal temperature variations
- Thermal expansion/contraction displacement of curved integral abutment bridge
- Pile displacement
- Abutment displacement and tilting
- Abutment backfill pressure

Task 3: Numerical Simulation

This task will allow the research team to extend the knowledge gathered beyond the monitoring efforts and literature review. The objective of this task is to thoroughly understand and thus be able to predict the complex behavior of curved joint-less bridges. To achieve this goal, an adequate soil-structure interaction model with constitutive equations will be used to simulate the soil behavior under repeated cycles of loading and to better reflect the interaction between soil and the joint-less structure. Monitoring efforts made in Task 2 will help provide and calibrate input parameters for these simulations.

Once the numerical model is verified with the monitoring results, it will be used as in a parametric study and/or predictive tool. The followings can be investigated in depth: (1) the effect of connection types between the abutment and piles (e.g. pinned or fixed moment connection), (2) maximum stresses induced by ratcheting, bridge geometry, and temperature fluctuations, with the application to Nebraska practice, (3) stresses and deformations induced by bridge skew, (4) stresses and deformations as a function of bridge length, (5) stresses and deformations as a function of curvature for curved bridges, and (6) effect of time-dependent changes in concrete deck. This evaluation will be conducted using parametric analysis where design parameters and soil conditions are varied to ascertain the influence of each parameter. The range of parameters will be within those that are typical in integral abutment bridge design and construction practices of Nebraska. The benefit of this analysis is that the primary variables that influence the behavior of integral abutment bridges will be identified. Finally, the numerical analyses will provide recommendations for standardized design of integral abutment bridges including the maximum bridge length, skew, and curvature through the extended study beyond the completion of this project.

Task 4: Design Recommendations and Continuing Monitoring Efforts

The outcomes from the first three tasks of proposed study will be integrated into developing optimized design and construction recommendations for Nebraska joint-less integral and semi-integral abutment bridges to possibly extend the use of joint-less bridges with less limitations, which are mostly provided through the engineers' judgment or experience. Recommendations will be provided regarding:

- Maximum bridge length of the curved integral abutment bridge
- Maximum curvature of the integral abutment bridge
- Recommendations for continuous monitoring efforts with installed/embedded sensors

As part of this project, the recommendations will be provided as a package for integration into the NDOT BOPP manual and NDOT Standard Specifications for Highway Construction that can be applied statewide and countywide.

2. LITERATURE REVIEW

2.1 Introduction

This chapter provides a literature review focusing on 1) long-term studies conducted in Indiana and Iowa related to integral abutment bridges including the long-term monitoring efforts and numerical simulation, 2) other previous research on straight and curved integral abutment bridges, 3) review on bridge design manuals of different states, and 4) data and information of full and semi-integral abutment bridges designed and constructed in Nebraska.

2.1 Long-term Studies Sponsored by State Department of Transportations (DoTs)

2.1.1 Indiana

Four reports (Frosch et al. 2006, Frosch et al. 2009, Frosch and Lovell 2011, and Frosch et al. 2014) were generated for the research conducted at Purdue University for approximately 14 years sponsored through Indiana Department of Transportation (INDOT). The first report (Frosch et al. 2006) summarizes the four years (field data collected between 2000-2004) of effort in field measurements and the test results of an experimental program of nine piles (six steel H piles and three concrete-filled steel tube piles). The study evaluated the influence of pile size, pile orientation, axial loads permitted on piles, minimum embedment length of piles in abutment, and minimum pile length below the ground level on the behavior of integral abutment bridges. A minimum of 24 in. pile embedment in abutment was recommended based on experimental studies. Regarding the minimum pile length below ground to prevent the displacement at the pile base, 30-50 ft range was recommended as the minimum pile length for piles in clay while 25-35 ft below ground was recommended for piles in sand. The maximum length for integral abutment bridge (IAB) was recommended as 500 ft for both steel and concrete structures with skew angles less than 30 degrees, if sufficient pile embedment length in abutment and pile embedment below ground is provided as recommended. The study stated that if the decks are casted in the range of 40-50°F, the maximum length limit can be extended to 770 ft.

The second report (Frosch et al. 2009) evaluated the earthquake resistance of integral abutment bridges. One of the bridges that was instrumented in the previous research effort for studying the behavior and design of piles was continuously monitored for another four years between 2003 and 2007. Other bridges had some issues with the instrumentation where some of the sensors were malfunctioning. Within the four-year long-term monitoring, the ambient temperature ranged between 0 to 90°F and the abutment movements had an annual variation of 0.6 in. The abutment displacements steadily moved away (contraction and active pressure) from the backfill for the four-year period. However, the measured earth pressures increased when the abutment was moving towards (expansion and passive pressure) the backfill and came back to near zero (at-rest pressure) values during each winter repeatedly over the four-year monitoring period. Based on the earth pressure measured and the displacements measured during this research, annual load-displacement curves were generated for each year between 2003-2007. And an approximate linear relationship (stiffness) between displacement and earth pressure was summarized to be 11,000 psf/in. In addition, seven specimens were tested with the abutment-pile connection details of Indiana to estimate the displacement capacity and analytical models were developed to estimate the seismic displacements of the abutment. One of the purposes of this study was to investigate whether the 500 ft maximum length limit recommended in the first project had adequate seismic resistance for the Maximum Considered Earthquake (MCE) for Indiana. The study concluded that if the details provided in Indiana is improved with confining reinforcement provided around the pile head with a No. 4 spiral reinforcement with 2.5 in. pitch, the integral abutment bridge maximum length can be extended to 1,000 ft for seismic applications.

The third report (Frosch and Lovell, 2011) summarized the long-term behavior of integral abutment bridges. With two previous projects, this project continued the long-term field monitoring program of the three integral abutment bridges in service. In addition, a single-span quarter-scale integral abutment bridge was constructed and tested to evaluate the behavior of highly skewed bridges. This report summarizes the findings of the 7-year continuous long-term field monitoring results, the quarter-scale outdoor laboratory testing results, and analytical models developed based on the field and laboratory investigations. The findings of this study indicate that the lateral earth pressure is not the cause of ratcheting because it returns back to approximately zero during winter and the net inward movement of the integral abutment bridges is rather caused by the concrete deck shrinkage and temperature differentials. The study also stated that a steady-state displacement takes place approximately seven years after the construction is completed. In addition, the study stated that the influence of skew angle towards the overall behavior of IAB is minimal when skew is less than 30 degrees. It affects the IAB movement when the skew is larger than 30 degrees. Two expressions were developed from this study to compute the IAB displacements. These equations were developed based on the 7-year long-term monitoring effort, outdoor quarter-scale laboratory testing results, and analytical studies that considers concrete deck shrinkage, temperature differentials, and different skew angles. As a result, a design chart that allows 2 in. of pile lateral displacement and zero lateral displacement was provided for various skew angles and span lengths for integral abutment bridges.

The last report (Frosch et al. 2014) summarizes the total research period of 14 years of study at Purdue University, including long-term field monitoring results, indoor and outdoor laboratory structural testing, and analytical studies. The findings include the efforts to develop and calibrate a constitutive model that captures the field and lab test results and to conduct three-dimensional numerical simulations for the coupled geotechnical and structural behavior of IABs. This study stated that active state earth pressure is reached only after the first contraction cycle. The study re-stated that concrete shrinkage and temperature differentials govern the displacement demand of the supporting piles and displacement is lower during the expansion cycle and larger during the contraction cycles. Based on the calibration and verification of the constitutive model developed, a parametric study was conducted, and the analysis demonstrated that a 500 ft integral abutment bridge with a 60° skew will provide acceptable long-term performance. Acceptable performance indicates a pile displacement of less than 2.0 in. The study recommended that soil-structure interaction analysis should be conducted if bridges over 1,000 ft are considered on a soft to very soft foundation soil.

2.1.2 Iowa

There have been various research projects (approximately 12) for the past 40 years since 1980 that were published by the Iowa State Department of Transportation. A nationwide survey was conducted by Wolde-Tinsae (1981) regarding the state-of-the-art methods for design of integral abutment bridges up to the 1980s and the report indicated that the bridge length limit was around 200-300 ft around 1973 but there were several states building concrete IABs that were over 400 ft in the late 70s. At the time of survey, stresses generated at the piles due to thermal movements were in most cases ignored or calculated based on simplified fixity conditions and assumed effective lengths. And the studies did indicate that the analytical results are only approximations of the actual conditions and therefore there is a need for full-scale testing of piles. Iowa State University conducted several tests in the mid-80s and an in-house finite element computer program (Integral Abutment Bridge Two-Dimensional; IAB2D) was developed under the various research contracts in the early and mid-80s sponsored by the Iowa Department of Transportation.

Greimann et al. (1987) summarized the effort of several model tests that were conducted in sand with a scale factor of approximately 1:10 to simulate pile and bridge girder loading cases with vertical load only, horizontal displacement only, and the combined cases of both loads. This study concluded, although the lateral displacements of the combined load tests caused a reduction in the friction resistance along the upper portion of the pile, that the vertical frictional resistance of the lower portion of the test piles was significantly larger than the upper portion and for that reason, the horizontal displacement at the top did not affect the vertical load capacity of piles significantly.

Abendroth et al. (1998) instrumented two integral abutment bridges with prestressed concrete girders and multiple spans with a skew for two years. The report shows the instrumentation of each bridge while preliminary test results are provided for one of the bridges monitored. The report indicates that for an average temperature range of 73°F for the superstructure concrete, the change in bridge length was approximately 1 and 1/8 in. The maximum strain shown on the abutment piles was approximately 400 micro-strains.

Abendroth and Greimann (2005) summarized in this report the monitoring efforts of the field instrumentation that started in 1997 (initial monitoring results reported in the 1998 preliminary report listed above) and finalized in 2005 after 8 years of monitoring and numerical analysis efforts. Two integral abutment bridges with prestressed girders that are skewed were monitored. Displacement transducers, strain gages, thermocouples were installed on Guthrie County and Story County bridge where the pile and girder strain were recorded over a two-year span. The longitudinal displacements measured from the sensors did not match on each abutment of these two skewed bridges and the Iowa research team concluded that it could be caused from the difference in horizontal stiffnesses with the soils surrounding the abutments. The measurements on the piles also indicated that the pile strain was beyond yield strain on one of the piles. This study recommended that further efforts should be made in monitoring more integral abutment bridges regarding measuring displacements, rotations, member strains, and temperatures since the report concluded that the results found from this study may not be entirely representative of these types of bridges. The study also recommended for measuring the soil-pressures on the abutment and additional precautions should be made with long-term monitoring with moisture infiltration into equipment.

Dunker and Abu-Hawash (2005), bridge engineers at Iowa DOT have summarized the efforts of both design and construction practice and research efforts of Iowa State University up to 2005 in this journal proceedings. This paper summarizes that with the effort of Iowa beginning to use IABs from mid 1960s, earlier research efforts in the 1980s focused on conducting testing on piles (Greimann et al. 1987) in integral abutments and developing analysis methods. After simple analysis models were developed from the studies conducted in the 1980s, Iowa DOT issued a guideline for integral abutment bridges that were affective until the year of 2002. The earlier limits only allowed integral abutment bridges up to a length of 150 ft with 45-degree skew angle and up to 300 ft with skews up to 30 degrees, while allowing 500 ft, if special investigation is conducted. With the development of a fixed-head equivalent cantilever pile model that was suggested by the researchers at Iowa State University, Iowa DOT conducted parametric studies (Abendroth and Greimann, 2005) and revised their limits on integral abutment bridge length limits up to 575 ft for concrete bridges and 400 ft for steel bridges without skews. The end span length limits also increased to 150 ft by using compact pile sections with deeper pre-bored holes and higher Grade-50 H piles compared to the lower yield strength Grade-36 H-piles that were used in the earlier days.

Greimann et al. (2014) summarized the recent efforts made by Iowa DOT. Two curved full integral abutment bridges, two curved semi-integral abutment bridges, and two straight integral abutment bridges were instrumented through a research project pool funded through states, Iowa (lead), Ohio, Pennsylvania, and Wisconsin. Long-range displacement meters were installed at each abutment and pier, and the strain was measured at the top of the abutment piles, and exterior girders. Soil pressure behind the abutment was also measured. The main conclusion from this study is that there are not much significant measurable differences between curved bridges and straight bridges if the length of the bridge is comparable and the thermal strains in integral abutment bridge and semi-integral abutment bridges were not noticeably different. A finite element model was developed to validate measured strains and was used to conduct parametric studies. Based on the parametric studies, the research team concluded that the stresses in the girders did change based on skew and curvature but suggested that with a ten degree skew and 0.06 radians arc span to radius ratio, the curved and skew integral abutment bridges can be designed as a straight integral abutment bridge if differences in stress of 10% is acceptable between the two bridges.

2.1.3 Pennsylvania

Long-term behavior of Integral Abutment Bridges was studied through several monitoring projects at Pennsylvania. Four PennDOT bridges on I-99 near Port Matilda, PA were monitored between 2002 to 2008 for seven years and thesis (Paul, M.D. 2003), dissertation, (Kim, W.S. 2008), reports (Laman and Kim, 2009), and journal articles (Fennema et al. 2005, Paul et al. 2005, Kim and Laman 2010) were published to report the long-term study results. Stress was measured on girders and piles. In addition, displacements and rotations at the abutment were measured on four integral abutment bridges with lengths varying between 19 ft to 420 ft. Numerical models were also developed, and approximate analysis was conducted to evaluate girder stresses, girder moments, pile forces, pile moments, and pile head displacements. The Pennsylvania studies highlighted that the superstructure expansion and contraction can influence the concrete integral abutment if there are horizontal construction joints at the abutment-backwall. This is not a practice in Nebraska but a standard integral abutment joint detail which requires much less reinforcement in the abutment than regular abutments permitting significant rotation between the superstructure and abutment similar to a hinge behavior. Therefore, the abutment height is a parameter that is associated with the girder stresses, moments, and pile moments that was measured and numerically measured in the Pennsylvania long-term studies. The Pennsylvania studies also indicated that creep and shrinkage play a significant role in axial response of the girders. And therefore, the typical movements measured in IABs level out when long-term creep and shrinkage strain is leveled out.

2.1.4 Tennessee

The longest integral abutment bridge (1,175 ft) is in Tennessee and Professor Burdette at the University of Tennessee Knoxville has been studying IABs for several decades. Lateral load tests on prestressed concrete piles that support integral abutment bridges were heavily studied by Professor Burdette's research team. In addition, Tennessee Department of Transportation (TDOT) has designed and constructed over more than 50 years for challenging to push the limits for a longer jointless bridge. E. Wasserman (Olson et al. 2013) who was the director of Structures Division at TDOT have pushed the limits where currently there is no explicit limits on either the length of the Tennessee IABs or limitations for skew angles which was possible because 95% of the bridge design in completed in-house at TDOT. Most of the studies by Prof. Burdette (Burdette et al. 1999, 2002, 2004, 2007) reported the adequate pile embedment length and movements (2-2.5 in. for H-piles and 1-in. for concrete piles). One foot pile embedment would be sufficient while 2 ft embedment would enhance the capacity significantly. Field tests indicated that a pile embedment of 2 ft would experience up to 4.3 in. pile head displacement with very stiff clay surrounding the pile.

2.2 Other Previous Research on Straight and Curved Integral Abutment Bridges

According to the AASHTO Bridge Design Specifications (2017), straight I–girder bridges are those that satisfy all the following four criteria:

- Girders are concentric,
- Bearing lines are not skewed more than 10° from radial,
- Girders have similar stiffness,
- The arc span divided by the girder radius in feet is less than 0.06 radians for all spans.

Therefore, in order to calculate the major axis bending moments and bending shears for bridges that meet all these conditions, curvature effects may be disregarded. Otherwise, a detailed analysis (e.g., FEM) of the curved bridge is needed. Neither the AASHTO Guide Specifications for Horizontally Curved Highway Bridges (2003) nor the NCHRP report 563 "Development of LRFD specifications for horizontally curved steel girder bridges (2006)" address the effects of integral abutments on curved bridge behavior. Several states, including New Jersey, Ohio, and Rhode Island, prohibit the construction of curved bridges with integral abutments because their performance is not fully understood. While some other states permit their use but with severe limitations. For instance, Maine, New Hampshire, North Carolina and Pennsylvania allow IABs with curved alignments but require the girders to be straight. Even though jointless straight IABs and jointed curved bridges have been constructed in the U.S. for several decades now, their combination is a fairly new concept, and not many of these bridges can be found.

2.2.1 Straight Integral Abutment Bridges

A two–phase study by Frosch and Chvichien (2004) examined the soil–pile interaction for IABs to better understand their performance and limitations. During these two phases, four in-service IABs were studied in the field, and common piles used to construct IAB systems were evaluated experimentally. According to their findings from the field investigation, IABs respond primarily in translation during contraction and expansion, and rotational movements can be ignored. There is a tendency for piles to bend in double curvature in IABs, which can be avoided with pin connections at the pile's head. In addition, neither the deflected shape nor the distribution of moments along the pile is significantly affected by pile axial load. Finally, field results showed that as the soil stiffness increases, the deflected shape of the pile changes (e.g., the inflection point and zero moment depth decrease). Their experiments showed that concrete–filled steel tubes (CFT) and steel H piles are capable of exceeding their yield displacement without losing their axial strength. Moreover, with increasing the axial load, a decrease in the displacement capacity was observed. Lastly, the change in axis of the pile orientation from weak to strong lowered the displacement capacity and caused severe deterioration at the abutment-pile connection.

Frosch, et al. (2006) published a report on behavior of IAB piles and several recommendations about their design for incorporation into Indiana Department of Transportation (INDOT) bridge design manuals. In their recommendations, IAB pile sizes should be selected so that they can withstand vertical loads while being flexible enough to accommodate longitudinal deformations. It is also recommended to position piles about their weak axis to maximize ductility and reduce stresses at the abutment–pile connection. Furthermore, they recommended that the pile–abutment connection embedment length should be increased from 15 to 24 inches in order to decrease the connection from deteriorating. Last but not least, they provided a table indicating the minimum pile lengths below ground in order to prevent its base from shifting. Depending on the pile and soil type, this length will vary. The authors concluded that if these recommendations are followed, integral abutment steel and concrete bridges up to 500 feet can be built with skew angles less than 30 degrees.

Lovell (2010) conducted a three–phase study including a field monitoring program, an analytical parametric study and an experimental investigation to capture long–term behavior of IABs. They monitored three already instrumented IABs in the state of Indiana that had been in service for several years. The instrumentation plans included convergence meters, tilt meters, pile and girder strain gages, and earth pressure cells. The author concluded that thermal load and concrete deck shrinkage primarily govern the behavior of IABs. A phenomenon commonly occurring in IABs called "ratcheting" is also believed to be caused by shrinkage deformations. In addition, they showed that a two-dimensional analysis can be sufficient if there is no skew. Skewed IABs, however, experience larger displacements at acute corners indicating that a three–dimensional analysis is necessary. The performance of IABs can be affected minimally by skews up to 30 degrees, but more than 30 degrees of skew can impact the system significantly. Whether an IAB is skewed or not, the longitudinal pile deformation demand is determined only by thermal loads, shrinkage, and soil–pile interaction, not by the backfill–abutment interaction.

Cook (2011) investigated the behavior of an IAB supported on steel H piles embedded in concrete drilled shafts. The bridge was monitored for two years using a monitoring system developed and installed by the team. In addition to displacement meters to measure longitudinal and lateral movements, strain gages were installed in steel piles and concrete drilled shafts as part of the instrumentation plan. This bridge's steel pile–drilled shaft system proved to be problem–free.

Sherafati (2011) investigated the possibility of expanding IABs' length. Considering that the IAB's thermal movement is proportional to its length, its length cannot be significantly increased using the pile–abutment connection design currently in use. In order to increase the pile head displacement capacity, they proposed a new connection with rotational capacity (reducing the moment–rotation stiffness) for the pile–abutment connection. They conducted an experiment to test their proposed connection of a CFT pile and a concrete cap. Two specimens were used in their experiments, one representing the current pile–abutment connection and the other representing the proposed design. A nonlinear pushover parametric study was also performed. As a result of providing rotational capacity through the proposed connection, the longitudinal displacement capacity of the piles supporting IABs can be increased by up to 500%. They also recommend that piles be bent about their strong axis since this will increase displacement capacity by 250% to 300%. DOTs generally align IAB piles around their weak axis, contrary to the proposed method in this work. Finally, results showed that the proposed connection had smaller stiffness with much higher displacement capacity.

Based on laboratory tests on skewed abutments, Jessee (2012) investigated the effect of different skew angles on the mobilized passive earth pressure in the backfill. Compacted dense sand was used for the backfill, and they considered four skew angles of 0°, 15°, 30°, and 45°. The results show that the mobilized passive pressure behind the abutment decreases significantly with increasing skew angles up to 50% with 30° skew angles. Based on the skew angle of the bridge, a factor was proposed to adjust the passive pressure calculation. They also found that to mobilize the full passive pressure, the abutment must move horizontally about 2 to 3.5% of its wall height. Passive pressure will drop to its residual value, approximately 55 to 65% of the maximum pressure, if it moves further after reaching the full passive pressure.

Kirupakaran (2013) sought to gain a deeper understanding of the complex behavior of soil–structure interaction (SSI) in IABs. A skewed integral abutment bridge in Comanche County, Oklahoma was selected for this purpose which was instrumented with strain gages, earth pressure cells, tilt meters and crack meters. In addition to the field data that was collected for three years, a numerical model of this bridge was also developed using FE and validated with the field data. A daily temperature gradient was detected along the depth of the superstructure, which was more noticeable for positive thermal gradients than for negative thermal gradients. Additionally, earth pressure changes are greater at obtuse corners of the bridge than at acute corners. Locations closer to the approach slab also experience more pressure changes than those further down. During the course of three years, the earth pressure cells recorded a steadily increasing pressure. The study shows that piles in the bridge undergo bending moments well beyond their yield limits. Following the verification of the FE models with the field data, they proposed a general design guideline for all IABs. For the upper portion of steel H piles oriented about their weak axes, pre–drilled holes filled with loose materials are recommended. Moreover, thermal gradients in the superstructure should be considered when designing IABs. To reduce backfill pressure and settlement, a compressible material behind the abutment and a soil reinforcing system like geosynthetic can be used, respectively.

For the development of design guidelines for IABs, Barr et al. (2013) studied an IA bridge in Utah for over a year. The bridge was equipped with 32 Sokkia RS30N reflective targets at the approach slab expansion joint, abutment–girders connection and the pier diaphragm. A survey of these targets was conducted every month for a year in order to measure how the bridges moved. It appears that the bridge deck undergoes an in–plane twist as the movement of the expansion joints at opposite corners of the approach slabs moved in similar patterns. A 12° skew angle on only one of the abutments is believed to have caused this behavior. A detailed FE model of the bridge was also developed to verify the field data. According to the parametric study, an increase of 5° in skew angle can significantly increase abutment bending moments. The span length is also a crucial factor affecting IAB performance. They showed when the span length is doubled, the abutment bending moment increases by 60%. The authors concluded by pointing out that when designing the abutment, thermal gradients of the superstructure must be taken into account.

Khasawneh (2014) conducted a comprehensive study to develop guidelines for IAB design processes. As part of this research, field and lab tests were performed, data were collected from already instrumented IABs in Indiana, a soil constitutive model was developed, and finally a parametric study was conducted to provide design limitations for IABs. Results show that backfill passive pressure and pile displacement demand are mainly controlled by thermal and shrinkage loadings. According to the large–scale test results, the bridge deck will rotate in-plane, depending on the skew angle and the stiffness of the backfill. During both expansion and contraction phases, acute corners experience largest displacement, indicating a slight increase in the bridge’s skew angle during expansion and a decrease during contraction. As the backfill is cyclically loaded, passive pressure will be mobilized until it reaches its maximum, after which it will stabilize. The highest pressures were measured at acute corners, while the bridge centerline underwent the lowest pressures. Additionally, among all piles, those at acute corners exhibit the greatest displacement demand. An IAB's long term performance is not significantly influenced by lateral passive earth pressure behind the abutment, according to their parametric study. Consequently, the maximum allowable abutment movement should be considered in the design process while the pile local buckling at the pile–abutment connection remains the primary concern. It is recommended that the abutment movement be limited to 2 inches in order to prevent this buckling. It was determined in their parametric study that an acceptable long–term performance is probable as long as the bridge total length and skew angle are less than 500 feet and 60 degrees, respectively.

A study by Guo (2015) investigated how skew angles affected passive forces acting on bridge abutments. Their objective was to validate a 3–D FE model with field test results. The team performed a large–scale test setup with skew angles ranging from 0° to 15°, 30°, and 45°.

Results from the FE models were verified against the field test results including, but not limited to, passive pressure–deflection outputs, displacement contours and ground heave, and failure plane geometry. There were several variables affecting the results, including soil and wall friction angles, soil stiffness and the dilatancy angle. The maximum passive pressure will increase by 7%, 1%, and 1.8%, respectively, with every degree increase in soil friction angle, wall friction angle, and dilatancy angle. As the skew angle increases, the passive pressure decreases significantly, according to the findings from the FE analyses. Based on the analytical results, abutments will slide significantly if the skew angle exceeds the wall friction angle, resulting in a substantial reduction in passive pressure.

Russel (2016) investigated the influence of pile shape and Corrugated Metal Pipes (CMP) on pile lateral load resistance. In this research, various types of piles were tested to find their P–Y curves, including pipe, pipe wrapped with High Density Polyethylene Sheeting (HDPE), pipe embedded in a CMP sleeve, square and H. Test results show that square piles mobilize the soil resistance 14% more than pipe piles with similar characteristics. Moreover, HDPE did not appear to reduce lateral pile resistance noticeably. Additionally, CMP sleeves increased the effective width of a pipe pile, resulting in a larger failure wedge. Moreover, contrary to what is generally believed, CMP sleeves increased the lateral resistance of pipe piles. Furthermore, they observed that pile rotation is determined by pile head deflection rather than pile shape. To more accurately predict the lateral resistance of non–circular piles, they recommended using different multipliers for square and H piles.

Paraschos (2016) conducted a parametric study to examine the effects of different types of wingwalls on the performance of straight IABs with zero skew angles. Three-dimensional FE analyses were performed considering three different cantilever wingwall types (inline, flared and

U–shaped), three backfill soil consistencies (dense, medium and loose sand), lengths ranging from 100 to 1,200 ft and with/without predrilled holes for the top portion of the piles. Based on their findings, pile stresses are most affected by bridge contraction, and predrilled holes play a critical role in their performance. For the axial loads in girders, however, the most critical load is bridge expansion where its length is the crucial factor. For shorter bridges, cantilever wingwalls can increase the axial loads on steel girders during the expansion phase, resulting in a plastic hinge at the top of the pile. Bridges without cantilever wingwalls do not experience this phenomenon. There is a greater importance to the orientation of cantilever wingwalls than to their length. Among three types of wingwall studied in this work, inline cantilever wingwalls have the greatest impact on the performance of IABs.

As a continuation of Smith's (2014) research at Brigham Young University (BYU), Snow (2019) explored passive force on skewed abutments with cantilever wingwalls. He numerically modeled the large–scale tests on the reduction of passive force for skewed IABs with Reinforced Concrete (RC) wingwalls that were performed in the previous research. There is good agreement between the results in this study and those in prior studies (e.g., Shamsabadi et al. (2006), Jessee (2012) and Smith (2014)), which have shown that the maximum passive force declines with increase in skew angle. A wider abutment also results in a lower passive force reduction factor, indicating that smaller abutments sustain higher passive pressures under the same conditions. Their numerical analysis also revealed that the soil lateral pressure acting on the wingwall on the obtuse corner of a 45°–skewed bridge was 10–14 times greater than that on the acute side. The researchers concluded that increasing the length of the wingwall at the obtuse corner could increase soil passive force resistance and bridge stability by changing the effective skew angle.

2.2.2 Curved Integral Abutment Bridges

Thanasattayawibul (2006) conducted an extensive FE parametric study on horizontally curved steel I–girder IABs. A number of parameters were considered, including, but not limited to, the bridge and span length, ambient temperature, soil profile, girder radius and pile type. They showed that a curved IAB differs from a straight IAB in that pile stress intensity increases as the bridge length increases, until reaching its maximum, and then drops as the curved bridge gets longer. Pile stress intensity, however, always increases with increasing bridge lengths for straight bridges. In addition, as the length of curved IABs increases, the lateral displacement will increase until it reaches its maximum, and then it will gradually decrease. Furthermore, their findings show that a curved bridge with a span of 50 feet shows higher lateral displacement than a bridge with a span of 100 feet. Finally, the outermost piles are subjected to higher stresses as well as larger lateral and longitudinal displacements.

Research was conducted by Eghtedardoost (2011) to investigate how integral abutment bridges could be integrated with curved bridges. Two types of jointless bridges were considered in this study. First, there is the IA steel I–girder bridge with bearings at the piers. In contrast, the second bridge type is an IA concrete bridge with flexible piers in which the pier is cast integrally with the deck with no bearings in between. They studied the effects of the bridge's geometry such as horizontal curvature and length as well as different loads including but not limited to temperature, shrinkage and backfill earth pressure. According to their findings, abutments in curved bridges always experience a smaller amount of internal force than a straight bridge when the bridge contracts. Furthermore, the internal forces of a curved bridge decrease as its radius of curvature decreases. In addition, the internal forces and moments in piles of straight or large–radius curved bridges increase as the bridge length increases. A curved bridge's internal forces increase as it expands, until it reaches a specific length. However, for curved bridges that exceed this length, internal forces start to decrease, even below those in straight bridges. The curve of the bridge directly determines this length.

In 2011, Kaufmann and Alvarez wrote an overview of the revised Swiss Federal Roads Office (FEDRO) guidelines (Edition published in 2010) for IABs. According to this study, 40% of the bridges on the FEDRO network have either integral or semi–integral abutments. According to the revised FEDRO guidelines, an integral bridge abutment must be as flexible as possible (flexible integral bridge ends) to accommodate longitudinal displacement for straight and slightly curved integral bridges. The reason this is in contrast to North America, is because their integral abutments rest on a single row of concrete piles. In contrast to straight and slightly curved integral bridges where the primary deflection is longitudinal, curved bridges experience transverse bending moments and deformations as well. Therefore, there will be a slight change in the radius of curvature of the bridge. As a result, these curved bridges can avoid some of the longitudinal restraint caused by the backfill soil. Because of this behavior, the FEDRO, edition published in 2010, recommends building curved bridges with as rigid abutments as possible. Compared to a straight bridge with flexible abutments, this will reduce deformations at the bridge ends. If these steps are followed, much longer curved IABs are feasible in comparison to straight bridges. Lastly, a length limit for IABs is spelled out in the new edition of FEDRO guidelines. It instead sets a maximum permissible horizontal displacement of the bridge end that depends on many factors, including geometry, deck type, soil conditions, and horizontal–vertical loads which can vary between 2 and 3 cm (0.8 to 1.2 in.).

Kalayci et al. (2012) investigated the thermal behavior of curved integral abutment bridges through a parametric study. Three–dimensional FE models were created to explore the effects of IAB curvature, backfill soil, wingwalls and lateral restraint at piers bearings. Results show that longitudinal displacements, backfill pressures, and pile moments around the weak axis of curved IABs decrease with increasing curvature. Curvatures between 0 and 20 degrees do not show significant decreases, however. As the curvature increases, the lateral movement will increase, leading to an increase in the pile's strong axis moment. Moreover, for all curvatures they considered, rotational mode dominates the behavior of the abutments. Lastly, higher curvatures reduce the bending stress on the superstructure more.

From 2012 to 2015, students and faculty members at Iowa State University published several theses, journal papers, and reports on curved bridges with IAs. Shryack (2012) studied a few curved steel girder bridges with integral abutments located in Des Moines. Their first step was to conduct a survey of all Departments of Transportation (DOT) in the U.S. to understand their experiences with IABs that have curved girders. According to the survey, most of the agencies that responded (27 agencies) do not place any limits on the length or curvature of curved IABs beyond the existing limits for straight IABs. Different states use different analysis and design methods, however. Among the agencies that responded, 46% claimed to use the grillage method for design and analysis, 31% the FE method, 27% the V–load method, and finally, 8% said they would use the M/R method to design and analyze curved IABs. Since several states use more than one design method, the sum does not add up to 100%. Thereafter, they instrumented six steel–girder bridges (two of which are curved with integral abutments, two are curved with semi–integral abutments, and the last two are straight IABs) and started monitoring them for 15 months, so they could gain a deeper insight into their behaviors. Curved bridges have degrees of curvature between 14 and 19 and skew angles equal to either 15 or 35. Among the instruments used were strain gauges on girders, temperature sensors, extensometers for girder–substructure displacement differentials, and earth pressure cells.

Hoffman (2013), another scholar at the Iowa State University (ISU), investigated horizontally curved integral abutment bridges, further developing the work of Shryack (2012). This research also considered the same six bridges reported in the previous study (Shyrack, 2012), one of which was analytically modeled in a FE software package. This is a curved steel–girder bridge with integral abutments and fixed bearings at its piers. The results of field tests indicate that bridges with a smaller curvature have more uniform distributions of strong axis moments among girders. Additionally, lateral bottom flange bending is much more significant for curved bridges than straight bridges. Finally, fixed bearings at piers (translational restrained locations) should be carefully planned when designing curved bridges as this type of bridge is prone to more lateral movements.

In 2014, a report was submitted by scholars at ISU on “Field monitoring of curved girder bridges with integral abutments”. This is the final report combining some of the works done by graduate students at ISU (two of which were mentioned previously). This study investigated the behavior of horizontally curved bridges with integral abutments and semi-integral abutments with a particular focus on their response to temperature changes. They concluded that there were no noticeable differences between the behavior of curved and straight IABs under thermal loads, so they suggested using stresses and displacements of a straight bridge with the same length to initiate the design of a curved IAB. It appears that expansion bearings (located at piers) reduce the thermal stresses in straight bridge girders, but not in curved bridges. In conclusion, they stated that curved IABs may be designed as straight bridges with up to 10% error in stresses when they have a skew angle of 10 degrees and an arc length to radius ratio of 0.06 radians.

In 2021, Civjan et al. evaluated four curved steel girder integral abutment bridges that could be found in Vermont. According to the AASHTO guidelines, these bridges do not meet the criteria for straight bridges, so they could not be designed as straight bridges. Despite this, all of these bridges were designed using assumptions derived from straight IABs. In order to accommodate the curvature, biaxial bending and displacements were taken into account in the pile design process, as well as additional reinforcement in the wingwalls. These curved IABs are estimated to have saved up to 30% in costs compared with traditional joined bridges. These bridges have been operating for between one and twelve years, and with the exception of minor cracks in the abutment backwalls, are in good condition and performing as expected, according to Civjan et al.'s site visit. After assessing the performance of these bridges, they recommended short to medium span bridges can be constructed with curved IABs, when needed.

Based on the literature review, curved IABs are not well studied, and there is need for more research to be conducted to better understand their long–term performance. As discussed previously, in contrast to curved IABs, research on straight IABs has been considerably more extensive. This type of bridge has been studied both analytically and experimentally by researchers throughout the world. As a result of these studies, DOTs have incorporated IABs into their design manuals, allowing 85% of the U.S. states to build them (IABs are the preferred method of construction in some states).

2.3 Review of Bridge Design Manuals for Integral Abutment Bridges

Our research included examining the bridge design manuals of every state in the US regarding their common practice and limitations when it comes to IABs, particularly those with horizontally curved alignments. The summary of this in-depth review can be found in Table 2.1.

The design manuals for 12 states could not be found online though. In 2014, researchers at the University of Maryland, College Park, conducted a survey and sent out a questionnaire to the department of transportation of all the states with 17 questions related to design limitations and performance of IABs, including but not limited to length, skew, alignment, piles and wingwalls (Paraschos, 2014). In this survey, however, no information is given on curvature limits. Data from this research was used instead for states whose information was not readily available online. Alaska, Alabama, Arizona, Florida, Louisiana, Mississippi, Texas, and Washington are the only 8 states that do not currently use IABs, which means they either have never utilized one or used to use it in the past but discontinued it due to their performance. According to this table, IABs with steel girders are allowed a maximum length that is less than or equal to the length of a prestressed concrete superstructure, with the exception of New Mexico.

Table 2.1: Summary of the U.S. DOTs Design Manuals regarding Curved IABs

State	Use of IABs?	Superstructure Length limit (ft)		Skew Limit (°)	Curved?		
		Steel	Concrete		Alignment	Limit (°)	Girder
Alaska	No	—	—	—	—	—	—
Alabama	No	—	—	—	—	—	—
Arkansas	Yes	250		25	NA	NA	NA
Arizona	No	—	—	—	—	—	—
California	Yes	400		NA	NA	NA	NA
Colorado	Yes	460		30	Allowed	5	Curved
Connecticut	Yes	NA	NA	NA	NA	NA	NA
Delaware	Yes	NA	NA	NA	NA	NA	NA
Florida	No	—	—	—	—	—	—
Georgia	Yes	300	500	NA	NA	NA	NA
Hawaii	Yes	No limits		NA	NA	NA	NA
Idaho	Yes	350	650	No limits	NA	NA	NA

Illinois	Yes	610		45	NA	NA	NA
Indiana	Yes	500		60	Allowed	30	Curved
Iowa	Yes	400	575	45	Allowed	NA	Straight
Kansas	Yes	380	410	NA	Allowed	NA	NA
Kentucky	Yes	500		NA	NA	NA	NA
Louisiana	No	—	—	—	—	—	—
Maine	Yes	300	500	20	Allowed	NA	Straight
Maryland	Yes	150	110	30	NA	NA	NA
Massachusetts	Yes	350	600	30	Allowed	NA	NA
Michigan	Yes	300	400	30	NA	NA	NA
Minnesota	Yes	300		45	Allowed	Slight	NA
Mississippi	No	—	—	—	—	—	—
Missouri	Yes	500	600	NA	NA	NA	NA
Montana	Yes	NA	NA	20	NA	NA	NA
Nebraska	Yes	NA	NA	45	Allowed	NA	Curved
Nevada	Yes	150	250	20	Allowed	10	Curved
New Hampshire	Yes	300	600	20	Allowed	NA	Straight
New Jersey	Yes	450		30	Not Allowed	NA	NA
New Mexico	Yes	200	135	30	NA	NA	NA
New York	Yes	330		45	Allowed	NA	Curved
North Carolina	Yes	300	400	20	Allowed	NA	Straight
North Dakota	Yes	350		30	NA	NA	NA
Ohio	Yes	400	500	30	Not Allowed	NA	NA
Oklahoma	Yes	400		10	NA	NA	NA
Oregon	Yes	NA	NA	30	Allowed	5	NA
Pennsylvania	Yes	390	590	45	Allowed	NA	Straight
Rhode Island	Yes	350	600	30	Not Allowed	NA	NA
South Carolina	Yes	240	300	30	NA	NA	NA
South Dakota	Yes	350	700	35	NA	NA	NA
Tennessee	Yes	No limits		NA	NA	NA	NA
Texas	No	—	—	—	—	—	—
Utah	Yes	300	NA	30	Allowed	NA	NA
Vermont	Yes	145	145	20	NA	NA	NA
Virginia	Yes	300	500	30	NA	NA	NA
Washington	No	NA	NA	NA	NA	NA	NA
West Virginia	Yes	NA	NA	30	NA	NA	NA
Wisconsin	Yes	150	300	15	NA	NA	NA
Wyoming	Yes	350	350	NA	NA	NA	NA

Across all states, the longest steel IAB permitted for construction is 500 ft (Missouri), while a prestressed concrete IAB can be built up to a length of 700 ft (South Dakota). The only states with no limits on IAB lengths were Hawaii and Tennessee. The maximum skew angle for Indiana IABs is 60°, whereas in Oklahoma, IABs can only have skew angles up to 10°. It is worth mentioning that in some states like Indiana, there is a reverse relationship between the skew angle and the maximum lengths permitted when the skew angle passes a limit. For instance, Indiana Department of Transportation manual shows that for every 10° increase in skew angle beyond 30°, the maximum length of an IAB drops by 67 ft. According to the survey, 63% of the states with IABs allow them to be built on curved alignments but fails to specify whether this is a curved alignment with straight or curved girders. The following states are among those in which IABs are allowed on curved alignment, according to the available bridge manuals: Colorado, Indiana, Iowa, Kansas, Maine, Massachusetts, Minnesota, Nebraska, Nevada, New Hampshire, New York, North Carolina, Oregon, Pennsylvania and Utah. However, three states explicitly prohibit the construction of IABs on curved alignments, including New Jersey, Ohio, and Rhode Island. Unfortunately, very little information is available about maximum curvature limits on curved IABs. Oregon and Colorado report a maximum curvature of 5°, Nevada goes up to 10° and Indiana limits its curvature to 30°. In Minnesota, however, "slight" curves are allowed, but no further details are given. Among all the states with curved aligned IABs, only five allow the use of curved girders including Colorado, Indiana, Nebraska, Nevada, and New York. Furthermore, there are five states that allow only straight girders with curved alignments. These states include Iowa, Maine, New Hampshire, North Carolina and Pennsylvania. As a final note, the fact that Nebraska allows curved IABs with curved girders is not found in the Nebraska bridge design manual. We learned about it from the Nebraska Department of Transportation (NDOT) engineers and from what we observed in Nebraska. It is clear from the table that far more information is available about the length and skew limits of IABs than their alignment (curvature), which implies that there has not been much research on this subject.

2.4 Statistics of the Full and Semi-Integral Abutment Bridges in Nebraska

As a part of the literature review to understand the parameters of integral and semi–integral bridges in Nebraska, we received the Nebraska IAB and semi–IAB database from NDOT Bridge Division for this study. This database contains 566 bridges in Nebraska from what 188 are IABs and 329 are semi–IABs. Figure 2.1 shows that 77% of IABs were built on H piles followed by 21% on pipe piles. The remaining 2% had other pile types.

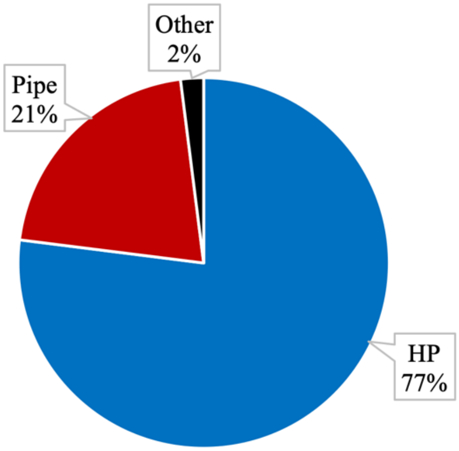

Figure 2.1: IAB Pile Types in Nebraska

Displacements in IABs are accommodated through pile deformations. As Figure 2.2 displays, 96% of IABs with H piles in Nebraska, have their piles oriented about their weak axis to maximize their flexibility. Figure 2.3 displays the four possible orientation of H piles including weak–axis oriented with superstructure, weak–axis oriented with abutment, strong–axis oriented with superstructure and strong–axis oriented with abutment.

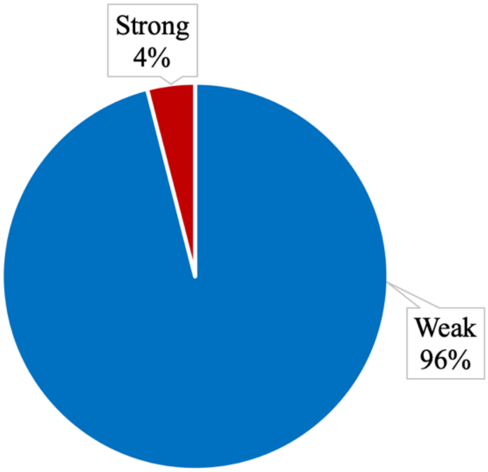

Figure 2.2:H-pile Orientation in Nebraska IABs

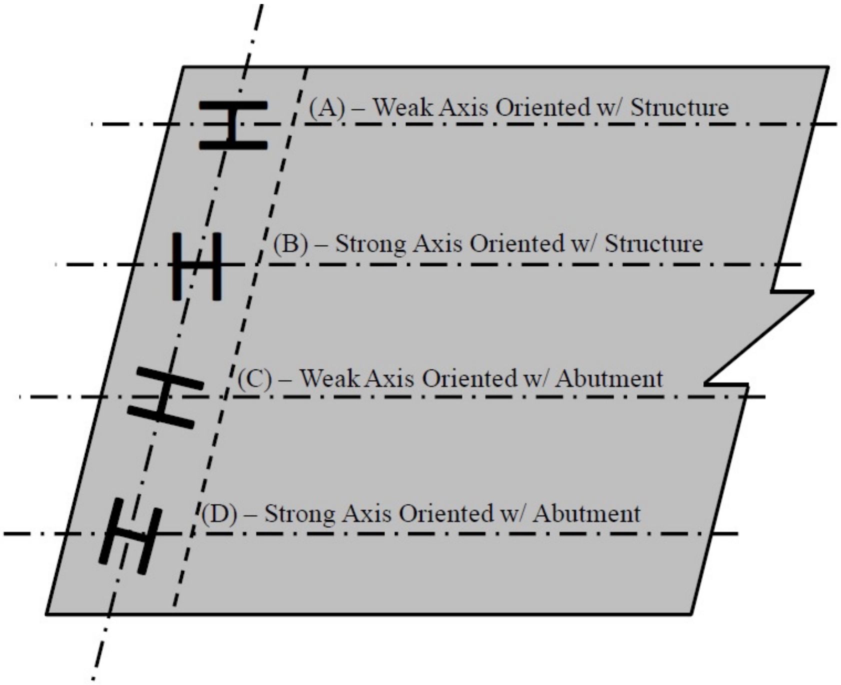

Figure 2.3: Possible H-pile Orientations (retrieved from Lovell, 2010)

Weak–strong axis orientation of H piles is shown in Figure 2.4. Similar to the current practice in many states on IABs, most of the IA bridges in Nebraska are built on H Piles oriented around their weak axis.

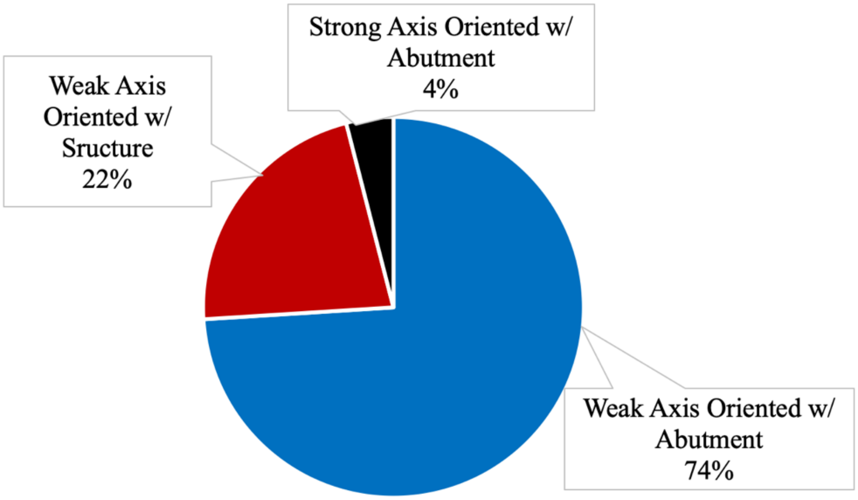

Figure 2.4 H-piles Alignment for IABs in Nebraska

Figure 2.5 shows that almost 40% of the IABs in Nebraska have their piles placed inside predrilled holes which will be filled with sand later.

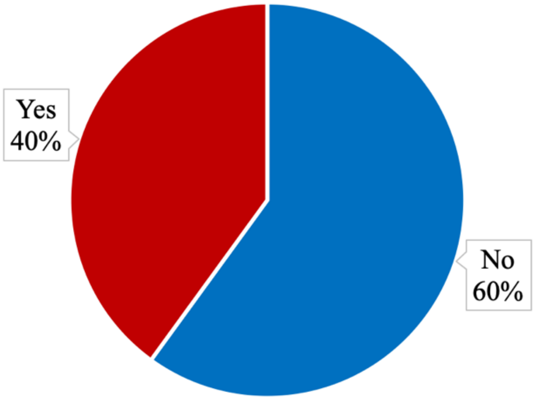

Figure 2.5: Use of Predrilled Holes Filled with Sand in IABs in Nebraska

Approximately 35% of IABs in Nebraska are constructed with Mechanically Stabilized Earth (MSE) walls (Figure 2.6). Finally, Figure 2.7 displays that 34% of the IABs in Nebraska have their piles placed inside Corrugated Metal Pipe (CMP) sleeves.

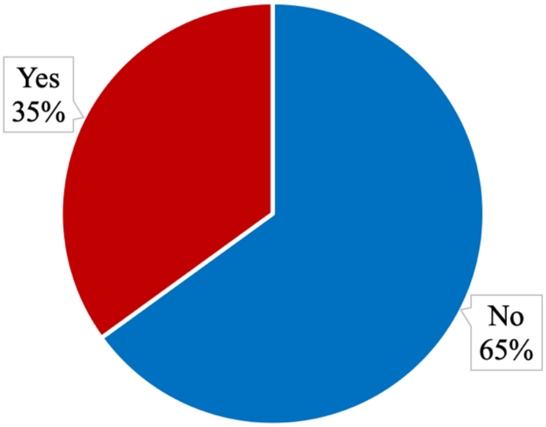

Figure 2.6: IABs with MSE Walls in Nebraska

CMP sleeves are used to reduce the down drag forces acting on the pile from the backfill. It needs to be noted that almost all IABs with MSE walls (97%) have CMP sleeves around their abutment piles.

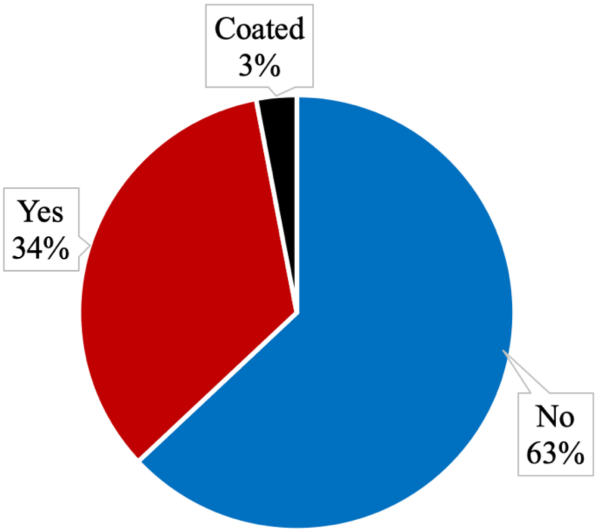

Figure 2.7: IABs with CMP Sleeves in Nebraska

For semi–IABs, on the other hand, pile types consist of H piles (65%), Concrete Box (18%) and Pipe (14%), as shown in Figure 2.8.

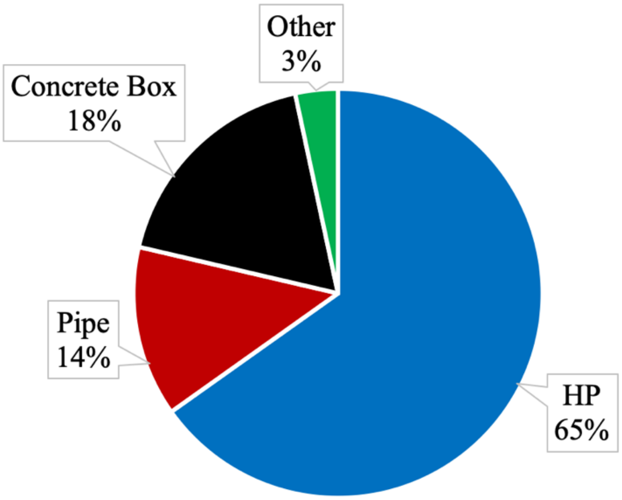

Figure 2.8: Semi–IAB Pile Types in Nebraska

Unlike IABs, H piles in semi–IABs are mostly oriented about their strong axis since pile deflection is not needed for displacement accommodation in this type of bridge (Figure 2.9).

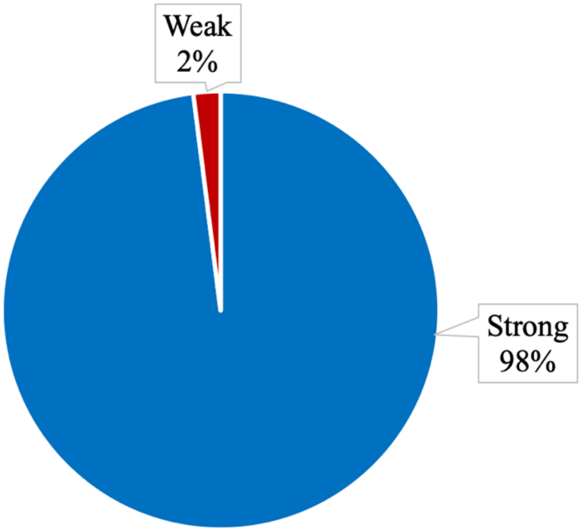

Figure 2.9: H-pile Orientation in Nebraska Semi–IABs

Figure 2.10 shows that fewer semi–IABs are built with pre–drilled holes for abutment piles compared to full IABs. This again demonstrates that pile displacement is not needed for superstructure displacement accommodation in semi-IABs.

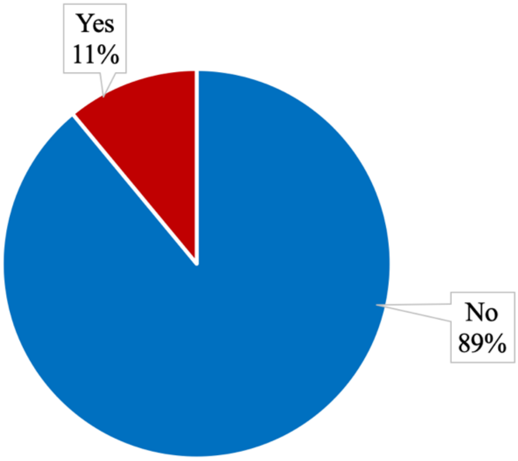

Figure 2.10: Use of Predrilled Holes Filled with Sand in Semi–IABs in Nebraska

As Figures 2.11 and 2.12 display, the percentages of semi-IABs with MSE walls and CMP sleeves are nearly identical. It should be noted that using these two is less frequent among semi-IABs compared to IABs.

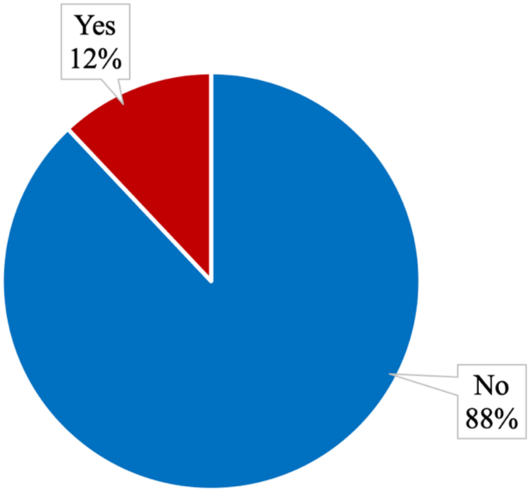

Figure 2.11: Semi–IABs with MSE Walls in Nebraska

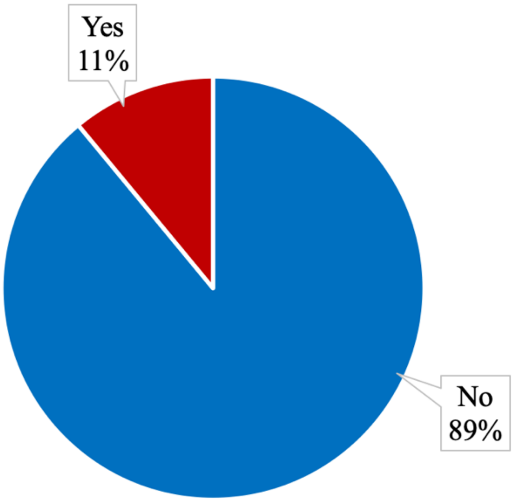

Figure 2.12: Semi–IABs with CMP Sleeves in Nebraska

2.5 Summary

Literature review has demonstrated that there is not much research conducted regarding the limitations of curved full integral abutment bridges. In addition, even including the straight integral abutment bridges, although there have been many studies throughout several decades, there have been continuous efforts in long-term monitoring of these types of bridges to understand the complex behavior. It is also demonstrated through several state studies that the long-term monitoring efforts and development of numerical models have been continued through several different research projects. Each state department of transportation still has different limits or no limits which indicates that there is not a consensus regarding how these types of bridges are designed and constructed. The database that Nebraska DOT has provided lacks the information of curved integral abutment bridges, or it is simply not including the curvature information, which should be updated.

3. FIELD INSTRUMENTATION

3.1 Introduction

The Bridge Division engineers of Nebraska Department of Transportation provided the research team, a recently constructed curved–skewed–steel girder bridge with cast in place concrete deck in Nebraska to monitor and provide insights into the behavior of curved IABs. In addition to the bridge (S108–10302), pavement replacement and a detour route for I–80 traffic were included in the Big Springs West project (Figures 3.1 and 3.2). The bridge was planned as a bypass over the I–80 highway, and is in Big Springs, Nebraska, only three miles away from the Nebraska–Colorado borderline. The lower right corner of Figure 3.1 is the south side of the bridge. The lower right corner of Figure 3.2 is the east side of the project.

Figure 3.1: Big Springs Bridge (S080-10302) over I-80

Figure 3.2: Pavement Replacement as Part of the Big Springs West Project

An instrumentation plan was implemented to collect information on the deformation of the girders, the translational movement and rotation of the abutments, the settlement of the approach slabs, the lateral earth pressure behind the abutments, the deflection of the piles and the surrounding soils. This chapter contains the description of this bridge and the instrumentation plan.

3.2 Bridge Layout

The Big Springs West I-80 Bridge is a two–span curved, skewed, fully integral abutment bridge with welded plate girders and a cast in place concrete deck. The 125.25 ft and 101.25 ft spans make up the bridge's total length to 226.5 ft (abutment to abutment). A single row of nine steel pipe piles supports each abutment. The expansion joint is installed away from the superstructure at the end of a 20 ft long approach slab attached to each abutment. North and south abutments have different skew angles, with 11.8° and 14.6°, respectively. It is also worth mentioning that wingwalls were not cast with the abutments (a common practice for fully integral abutments in Nebraska), and they are supported by two pipe piles on each side. Figure 3.3 shows the plan and elevation views of the bridge, while Figures 3.4 and 3.5 depicts the elevation view and cross section of each abutment. It should also be noted that the approach spans are supported by additional girders to minimize the potential damage of approach spans due to backfill settlement. This is a common practice in Nebraska but not in other states.

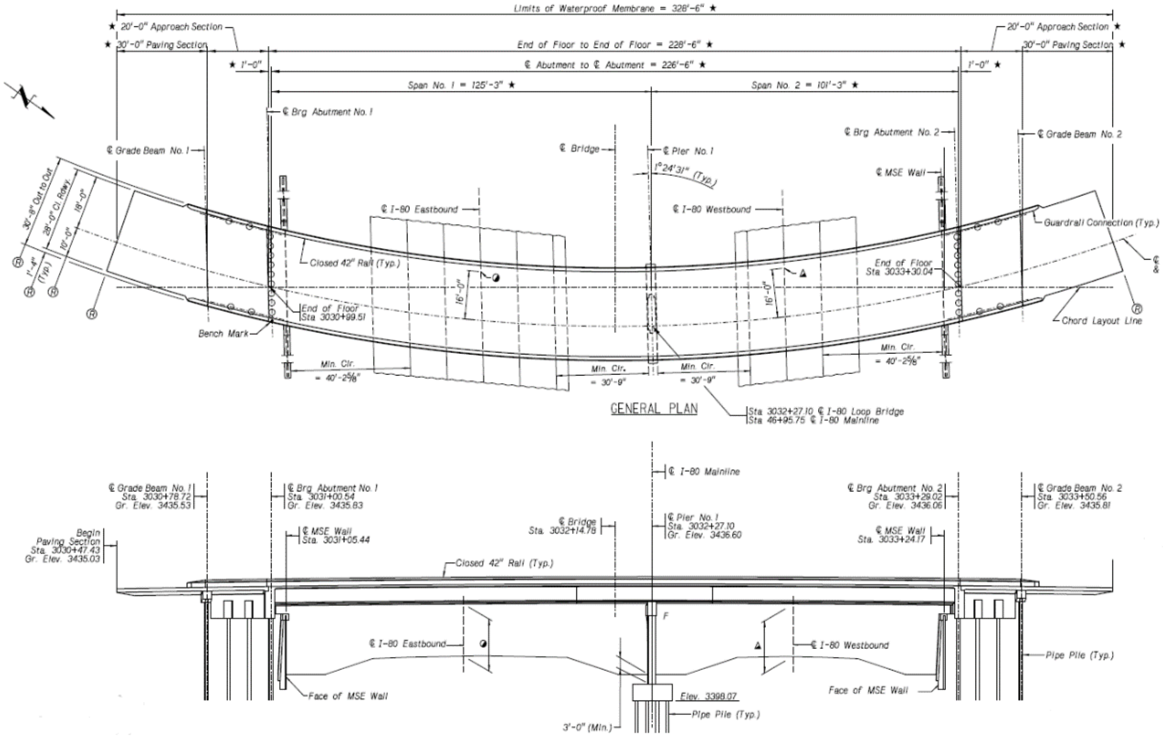

Figure 3.3: Plan and Elevation Views of the Big Springs Bridge (drawings retrieved from Big Springs West I-80 Loop Bridge)

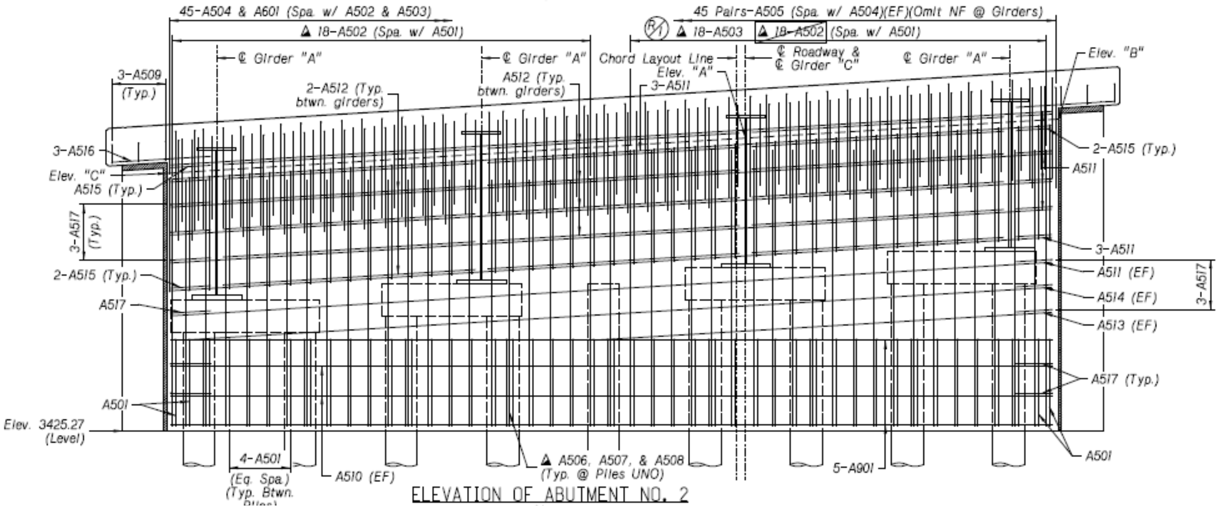

Figure 3.4: Elevation View of the Abutments (drawings retrieved from Big Springs West I-80 Loop Bridge)

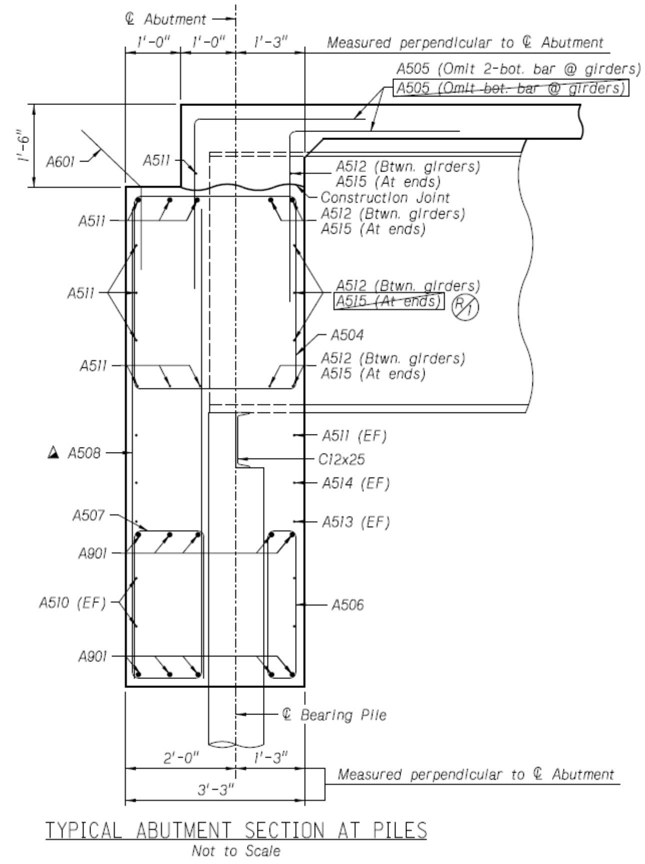

Figure 3.5: Cross Section of the Integral Abutment (drawings retrieved from Big Springs West I-80 Loop Bridge)

3.3 Instrumentation Plan and Installation

The research team decided to monitor the following parameters based on a careful review of the literature, the bridge construction timeline, and the research budget.

- Passive pressure in backfill (6 pressure cells)
- Rotation of the abutment (2 tilt meters)
- Moisture in backfill (4 moisture sensors)
- Soil movement in backfill (Inclinometer)
- Strain on girders and piles (fiber optic cable)
- Settlement in approach slab (fiber optic cable)

3.3.1 Pressure Cell

Six Geokon's Model 4800 Vibrating Wire Earth Pressure Cells with a measurement range of 700 kPa were purchased for measuring total backfill pressure. Each abutment was equipped with three pressure cells, two on the east side and one on the west side.

The abutment with its installed instrumentation is shown in Figure 3.6. Figure 3.7 shows the location of the pressure cells. Each pressure cell is located at a distance of 2 ft from the side of the abutment (or the front face of the wingwall). There are two pressure cells on the east side of each abutment, 1 and 5 feet from the bottom of the abutment, but only one on the west side, 1 ft above the bottom. After cleaning, leveling, and marking the centers of the pressure cells on each abutment, the abutments were prepared for pressure cell installation (Figure 3.8).

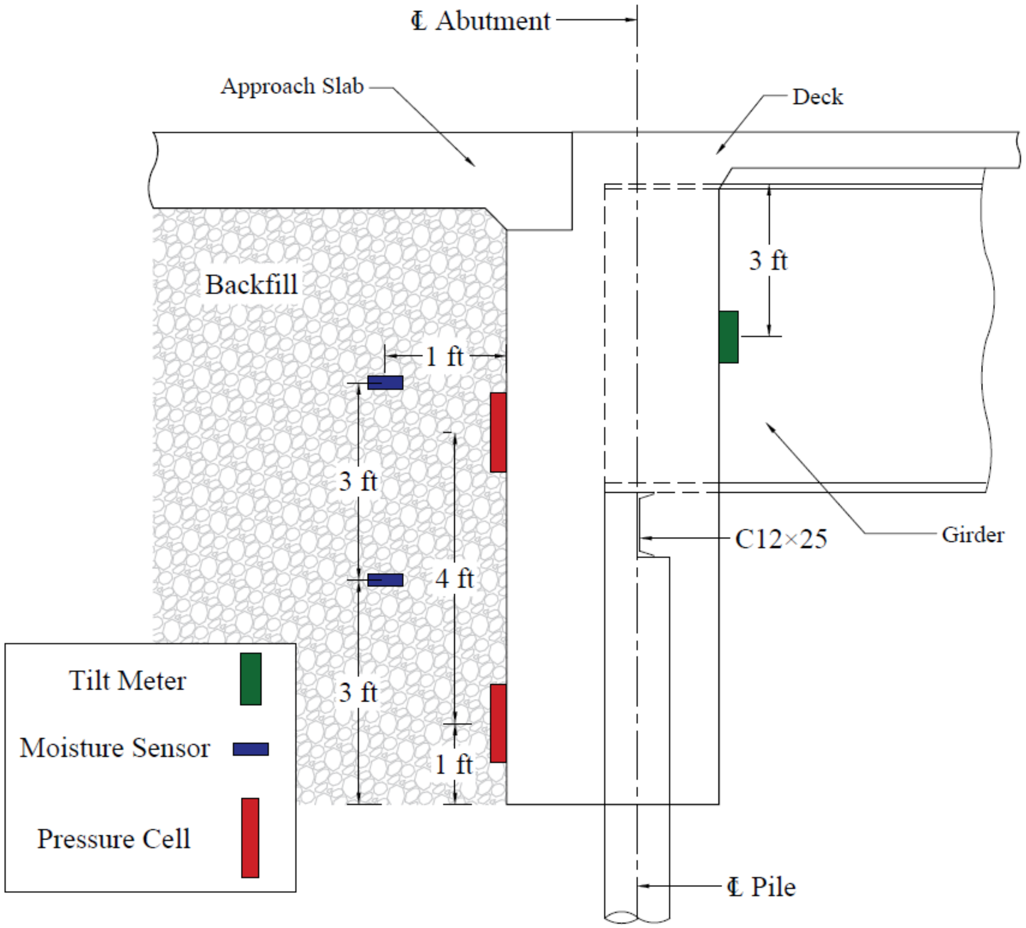

Figure 3.6: Cross Section of the Abutment with its Installed Instruments

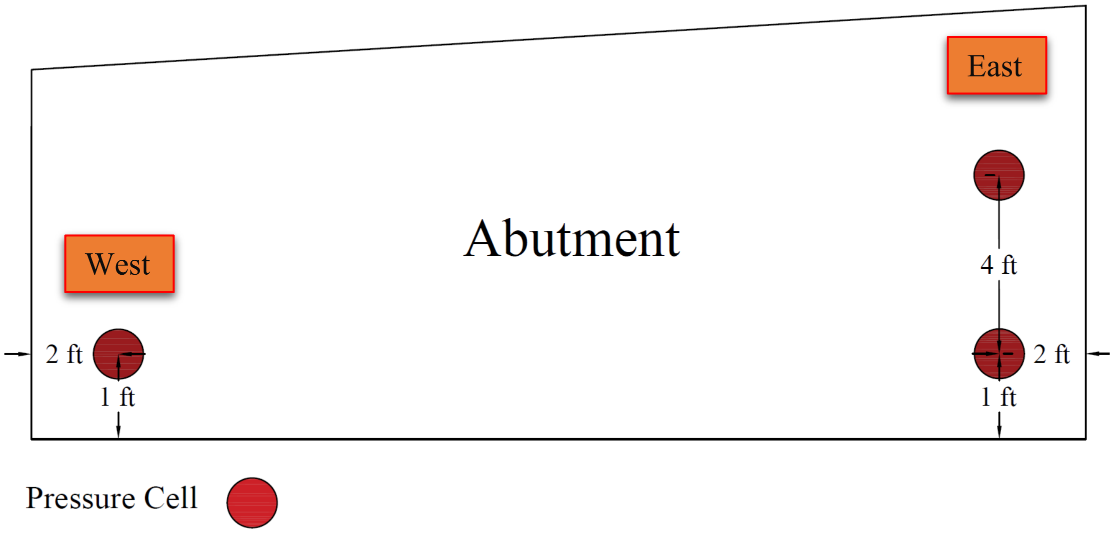

Figure 3.7: Pressure Cell Locations on Each Abutment

(a) cleaning and leveling the installation location (b) marking the center of each pressure cell on the abutment walls

Figure 3.8: Preparation for Pressure Cell Installation

Despite having four mounting lugs on each pressure cell, epoxy was added to the contact area on the abutment to secure the connection. In order to ensure proper contact between the pressure cell's disc and the abutment's wall as well as eliminating any possible gap between the two, epoxy was added to the contact area when installing the pressure cell as shown in Figure 3.9. As a final step, concrete nails were driven through the lugs to fully attach the pressure cells to the face of each abutment. Afterwards, their cables were routed out of the backfill area and secured behind the wingwalls to provide a connection to the data logger (Figure 3.10). Following the epoxy setting, initial zero readings were recorded as the reference data for future measurements.

Figure 3.9: Adding Epoxy to the Contact Area to Secure the Installation

(a) channeling out the pressure cell cables (b) securing them behind the wingwalls

Figure 3.10: Pressure Cell Cable Arrangement

3.3.2 Tilt Meter

On each abutment wall, 3 ft below the bottom face of the concrete deck, one Geokon's Model 6350 biaxial vibrating wire tiltmeter as shown in Figure 3.6 was installed in order to measure the tilt of the abutment. The standard measurement range of this tiltmeter is ±10°, beyond the potential angle (tilt) of the abutment. In a biaxial tiltmeter, consisting of two uniaxial tiltmeters, the tilt is measured in two directions simultaneously, parallel to the abutment's wall (lateral tilt) and perpendicular to it (longitudinal tilt) (Figure 3.11).

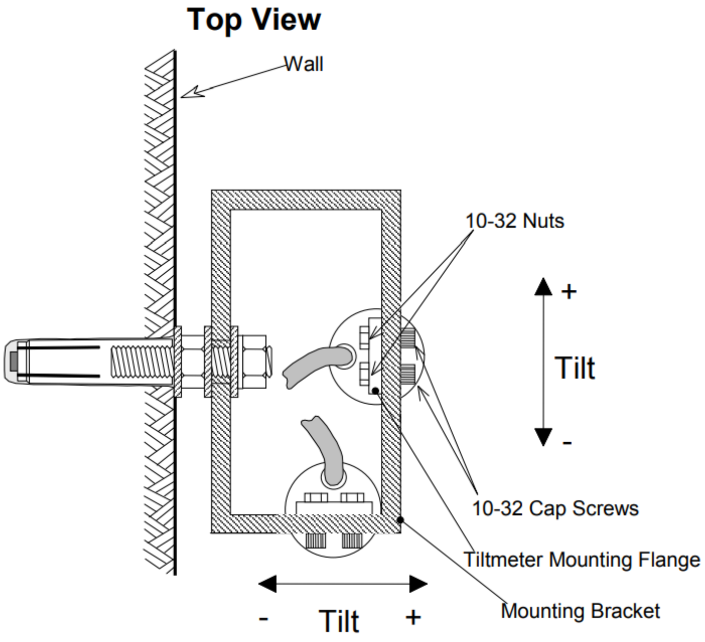

Figure 3.11: Top View of the Biaxial Tiltmeter (retrieved from the Geokon's installation manual for Model 6350)

The location where the tiltmeter was mounted from the top of the abutment was recorded so that the measurements can be used later on to back calculate the abutment top displacement. Therefore, the tiltmeter was placed 3 ft below the bottom of the concrete bridge deck, at the center of the abutment's wall. The installation process started by drilling a hole in the wall to fix the mounting bracket to the abutment as shown in Figure 3.12. Longitudinal and lateral tiltmeters were then attached to the mounting bracket.

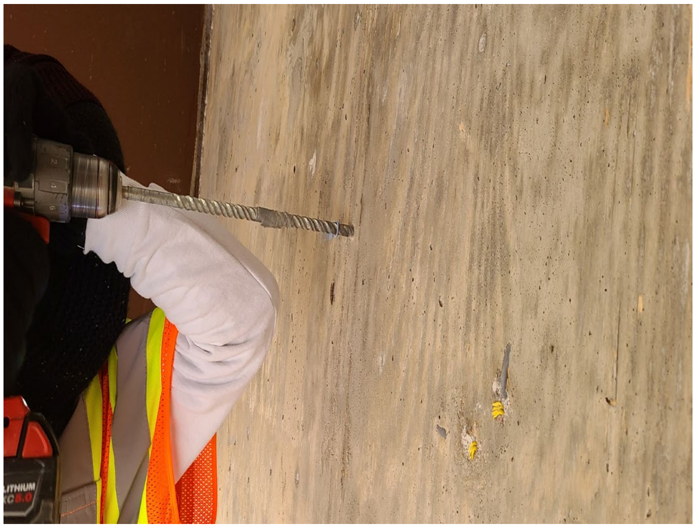

Figure 3.12: Drilling the Abutment's Wall to Install the Mounting Bracket

(a) longitudinal and lateral tiltmeters (b) protection box with extended cables

Figure 3.13: Tiltmeter Installation

Afterwards and for calibration and initial zero reading purposes, the tiltmeter cables were extended to the data logger where the reference point was recorded. Finally, a protection box was installed over the tiltmeters to protect them from severe weather (Figure 3.13).

3.3.3 Moisture Sensor

Four Teros 10 volumetric soil moisture sensors from Meter group were selected for this project to measure the water content in the backfills of each abutment. They are located approximately 1 ft away from the wall of the abutment and 3 and 6 ft away from the bottom of the wall, respectively, as shown in Figure 3.6. Using a wireless data logger, the data were recorded and retrieved remotely from these sensors.

(a) moisture sensor embedded in the backfill

(b) wireless data logger

Figure 3.14: Moisture Sensor Installation

3.3.4 Inclinometer

The Model GK–604D Digital Inclinometer System was purchased for this project. The system contains a Model 6100D digital inclinometer probe, a reel–mounted cable, and a handheld field PC as shown in Figure 3.15. This inclinometer probe has two MEMS accelerometers, with axes oriented 90 degrees apart, enabling it to measure soil deformation in both longitudinal and lateral directions simultaneously. Along with the inclinometer system, a 160 ft of Model 6400 Glue–Snap ABS inclinometer casing (10–ft long sections) was also used in this project (Figure 3.16).

Figure 3.15: Geokon Model GK-604D containing the Inclinometer probe, the reel-mounted cable and the Field PC (retrieved from Geokon Model GK-604D instruction manual)

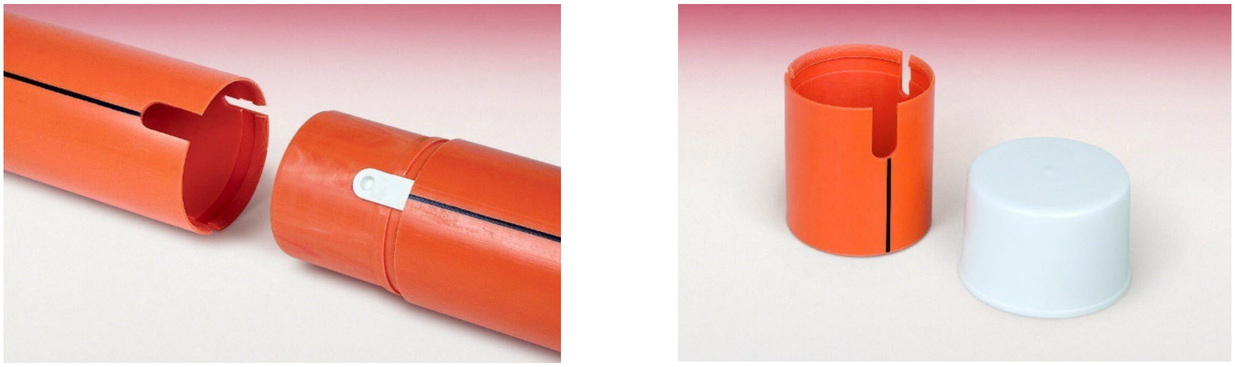

(a) glue snap connection (b) protective top cap

Figure 3.16: Inclinometer Casing

In order to monitor the horizontal movement of the backfill, four locations were selected at each corner of the bridge, approximately 1-2 ft away from the abutment and wingwall creating the casings to be located under the approach slab as shown in Figure 3.17.

We decided to monitor only the top 40 ft of soil behind each abutment since soil movement below that level is negligible. According to the bridge's geometry and soil profile, which requires drilling 10 ft into the foundation soil (Figure 3.18). Once the pile driving and CMP sleeves installation were complete, we took our drill rig to the site and drilled 10 feet long holes in the foundation soil as shown in Figure 3.19.

After this step, the first section of inclinometer casing of 10 ft was inserted into the hole. Then, the casing was adjusted so that two of the groves in the casing are parallel to the wall (capturing lateral soil deformation), and the other two are perpendicular to the abutment (indicating longitudinal soil deformation).

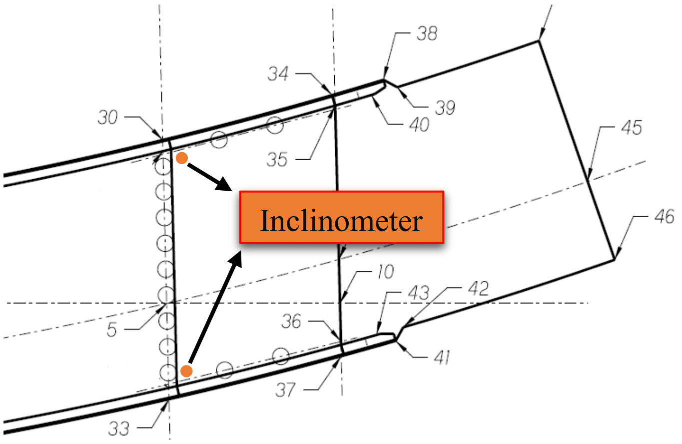

(a) north abutment

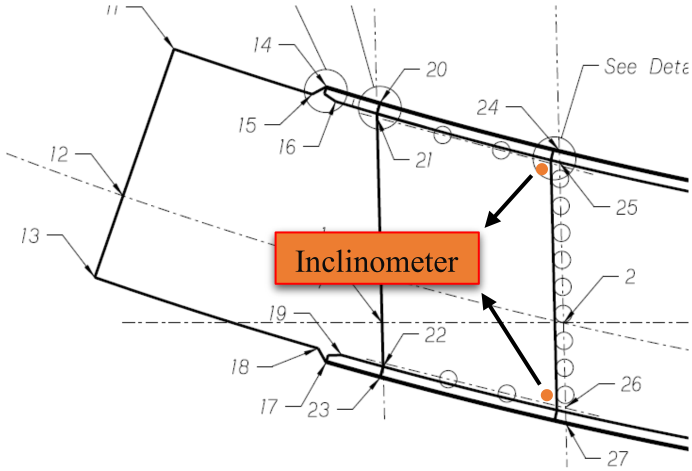

(b) south abutment

Figure 3.17: Locations of Inclinometer Installation

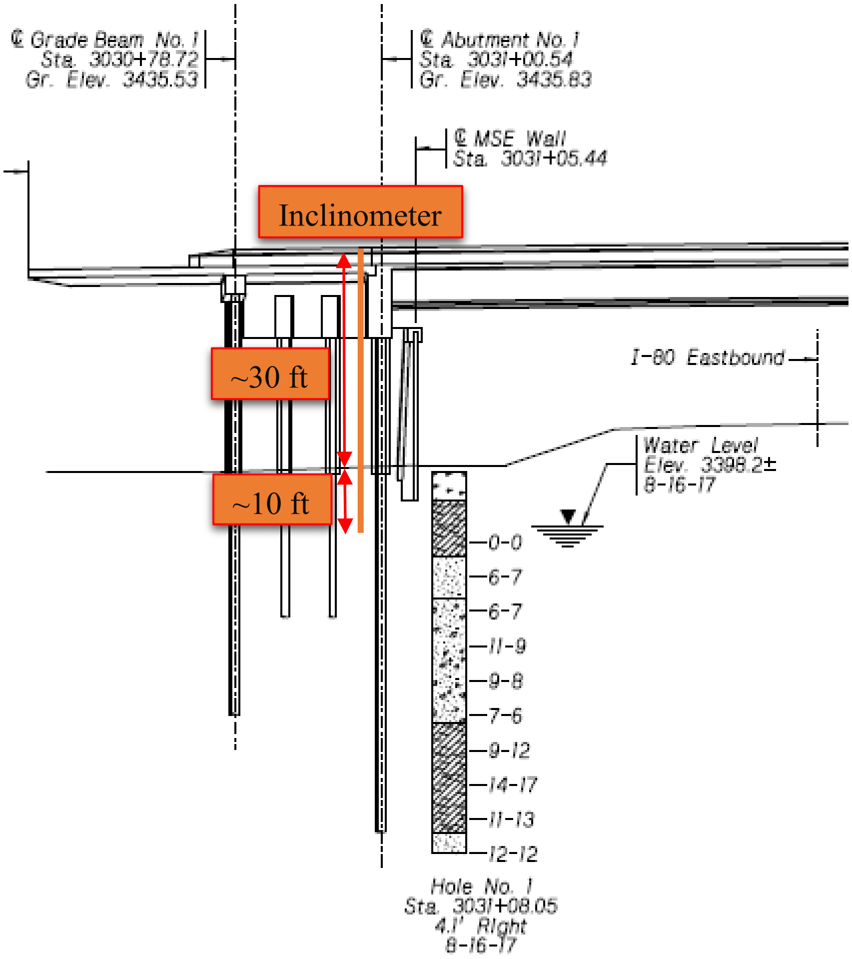

Figure 3.18: Location and Length of the Inclinometer Casing

Figure 3.19: Creating Bore Holes in the Foundation Soil using a Drilling Rig Machine

Following approval of the casing direction, the gap between the casing and the hole was filled with bentonite to prevent the casing from shifting (Figure 3.20). Compaction of the backfill soil was completed in stages. Therefore, the research team would make a trip to the site once the soil was close to the top of each inclinometer casing to connect the next casing segment until reaching the final elevation at which the casing would eventually exit the pavement (Figure 3.21). Since the bottom of the casings were not exactly at the same level once we inserted them into their holes, the final cut–off elevation was different for each casing. In order to align the exit location with the top of the concrete deck, a final cut–off elevation was calculated for each casing. As soon as the pavement was finished, protection caps were placed over the top of inclinometer casings exit locations to prevent dust and water from entering them. Table 3.1 shows the final length of each casing after it was cut.

(a) grovves inside each casing

(b) filling the gap with bentonite

(c) distance between CMP sleeves and casing

(d) final view of the installed casing

Figure 3.20: Installation of Inclinometer Casings

Figure 3.21: Inclinometer Casing Extension at Different Stages, and their Exit Locations

Table 3.1: Final Lengths of Inclinometer Casings

Inclinometer Installation	Location			
	SW	SE	NW	NE
Length (ft)	34’15”	40’8”	36’	36’17”

Note: SW, SE, NW and NE stand for Southwest, Southeast, Northwest and Northeast with respect to the center of the bridge, respectively.

It is worth noting that, to begin taking measurements, we did not wait until the process of casing extension had ended. If the casing top was accessible during any of our site visits, a measurement was taken regardless of the overall length of the casings. This unavoidable process brought the inclinometer based deformation plots that have different top elevation.

3.3.5 Inclinometer Reading Process

As shown in Figure 3.22, each casing has four grooves, positioned perpendicular to each other, which fit the inclinometer probe’s wheels.

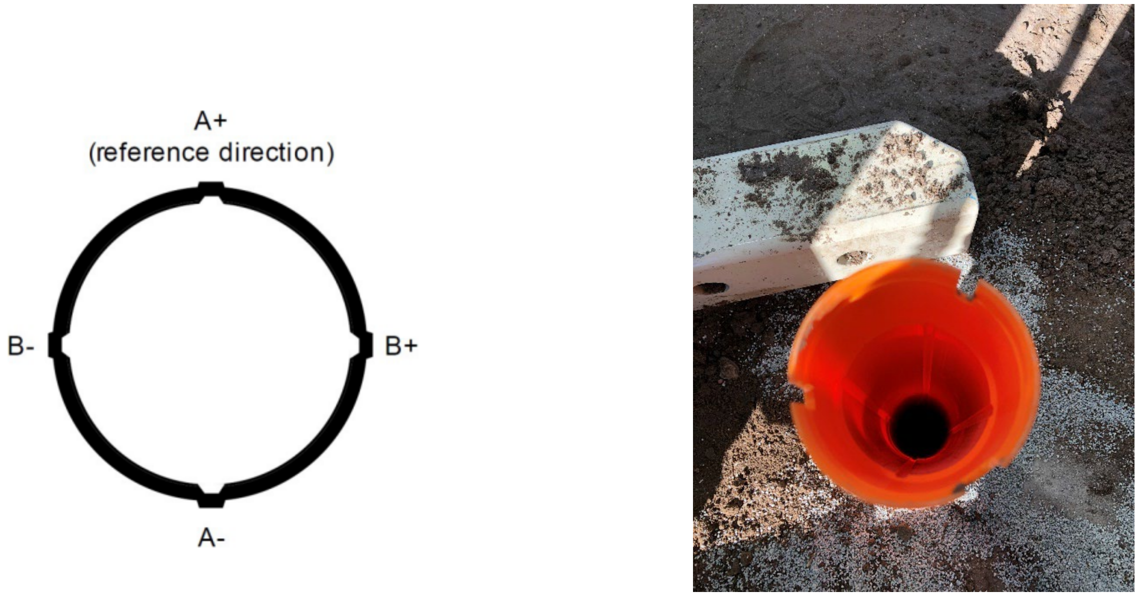

Figure 3.22: Orthogonal Grooves in each Casing (left figure retrieved from Inclinometer Manual)

There are four directions on each casing A^+, A^-, B^+ and B^- (one for each groove). As explained previously, we adjusted the inclinometer casings in a way that one set of grooves was parallel to the abutment wall (B^+, B^-), and another set was perpendicular to it (A^+, A^-). A common practice is to place the A direction where the major movements are expected to occur, in our case, perpendicular to the abutment wall or parallel to the bridge longitudinal axis. There are two sets of wheels on the probe, spaced two feet apart, connected to the readout device via its cable as shown in Figure 3.23.

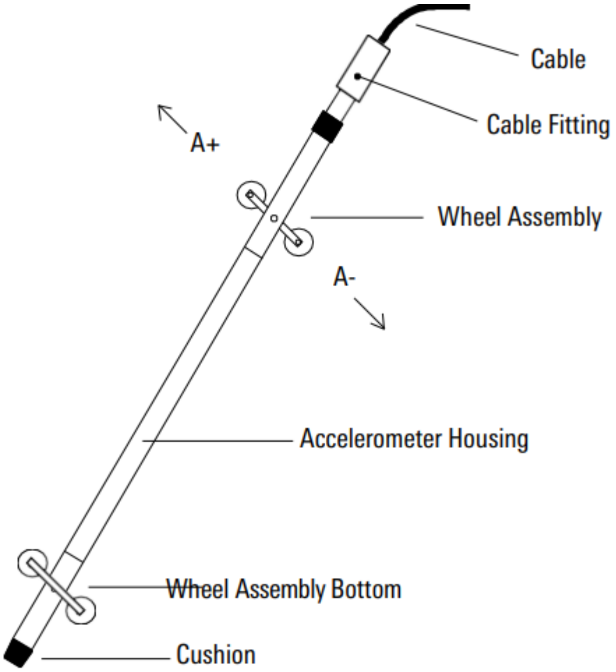

Figure 3.23: Inclinometer Probe (retrieved from Inclinometer Manual)

The survey starts by lowering the probe through the A direction grooves until reaching the bottom of each casing where the first reading is made. Once this very bottom measurement is complete, readings are taken every 2 feet by raising the probe until reaching the top of the casing. The probe is then removed from the casing, rotated 180°, and lowered to the bottom of the casing through the A direction grooves, and the same process is repeated. Once the probe reaches the top of the casing for the second time, the survey is complete. Every two feet, the casing's inclination (as a result of soil movement) is recorded in relation to a vertical line. When the research team performed the survey for the A direction, B direction was simultaneously recorded since the inclinometer contains two accelerometers. For consistency, the research team started every survey by pointing the probe in the A^+ direction towards the abutment wall. Figure 3.24 shows how a measurement was made for each inclinometer location.

Figure 3.24: Taking Inclinometer Readings

3.3.6 Concrete Cut–Open

A lack of communication between the research team and the contractor led to all four inclinometer casings being embedded inside the concrete approach slab after the casings were cut to their final height. Concrete was poured over all casings, with no metal protection provided (duct tapes were covering the casing though). Inclinometer openings could be located by guessing their locations and then cutting open the approach slab's concrete since the research team knew the approximate locations. The only downside was that it could damage a considerable portion of the pavement, which was not desirable. It was decided to use a method called GPR (Ground Penetrating Radar) after consulting with other researchers who specialize in Non-Destructive Testing (NDT) of concrete members. In this technique, electromagnetic waves (EM) are used to assess the concrete and indicates what is inside the concrete (for instance reinforcement and strands). This method works based on the EM waves travelling through the concrete and being reflected from cracks, holes, and rebars. Typically, this method is used to find cracks or deterioration inside concrete panels such as rebar corrosion. The researchers used a GSSI SIR-4000 system for this work (Figure 3.25).

(a) GPR device on concrete (b) portable PC

Figure 3.25: GSSI SIR-4000 GPR System

Figure 3.25 (a) shows the GPR device that is positioned on top of the concrete surface and scanning is over the desired area to evaluate the location of inclinometer casing (void) under the surface. Figure 3.25 (b) is the portable PC that is connected to the GPR device to show the output of the scanning part. Because the approximate location of each inclinometer casing was known, a mesh of five inches by five inches was drawn around the probable locations for all four casings (Figure 3.26).

Figure 3.26: Cut Open Section near Approximate Location of the Inclinometer Casing

After the mesh were drawn on the surface, the GPR device was run over each mesh line in both directions. The exact location of each casing was subsequently found by observing the reflected pattern. In Figure 3.27, the white–black–white pattern of the reflected wave indicates a potential void inside the concrete panel. These patterns are shown with red ovals. In contrast, if the pattern of reflection is black–white–black, it might indicate a metallic material such as rebar (marked with blue ovals).

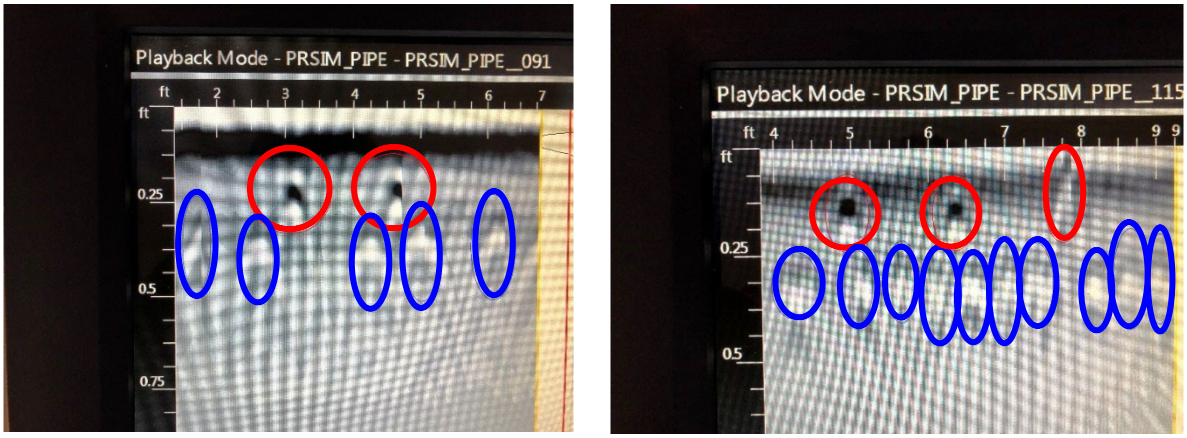

Figure 3.27: Reflected EM Wave Patterns

Note that the vertical axis represents the depth of the object from which the waves were reflected. According to the bridge drawings, rebars were placed at a depth of 3 inches from the surface, which is consistent with what is shown in Figure 3.27. Moreover, the research team knew that the top of each casing was very close to the concrete surface and above the rebar mesh depth. As a result of the GPR images, the research team were able to successfully pinpoint the exact location of all four casings. Following the marking of each casing's center, the concrete was cut open with a 6–in. core drill to reach the top of the casings as shown in Figure 3.28.

Figure 3.28 Inclinometer Casings after Cutting Open the Approach Slab

3.3.7 Fiber Optic Cable Based Distributed Strain Sensing (DSS)

Fiber optic cable based DSS method have been used for strain measurements in many civil engineering projects and have shown reliable results. The technique detects any changes in light transmission caused by deformations due to loads applied to the attached object. As shown in Figure 3.29, each fiber optic cable consists of three main parts: 1) Core, a wire of glass fiber that transmit a signal by laser waves, 2) Cladding, a reflective glass responsible for bouncing the light back into the core to ensure long distance light transmission, and 3) Insulation or buffer which is a protective coating layer usually made from plastic or rubber.

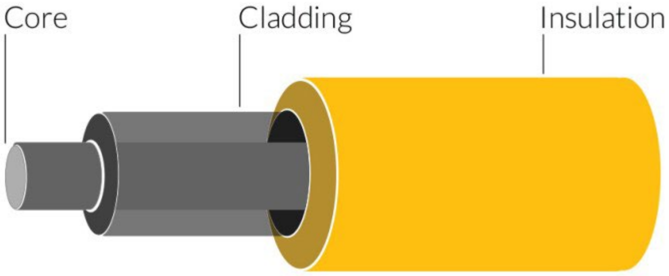

Figure 3.29: Structure of a Fiber Optic Cable (information retrieved from https://www.thorlabs.com/)

The research team chose fiber optic DSS over standard strain gauges because of their cost–effectiveness and ability to measure continuous strain along the length of the target structure over a very long distance. For this research, the BOTDR Single Mode Fiber (SMF–28 cable) was purchased from THORLABS Inc. The Brillouin Optical Time–Domain Reflectometer (BOTDR) DSS works on the basis of the Brillouin light scattering phenomenon, and can measure strains continuously for several kilometers (information retrieved from https://www.thorlabs.com/). In this type of sensor, light pulses are launched into one end of the fiber optic cable, and Brillouin backscattered light from them is received in the same end. By measuring the difference in time between the launched pulse and the received backscattered light, one can compute the strain. The Brillouin frequency shift caused by strain in the fiber can be used to measure the amount of strain in that position, as illustrated in Figure 3.30.

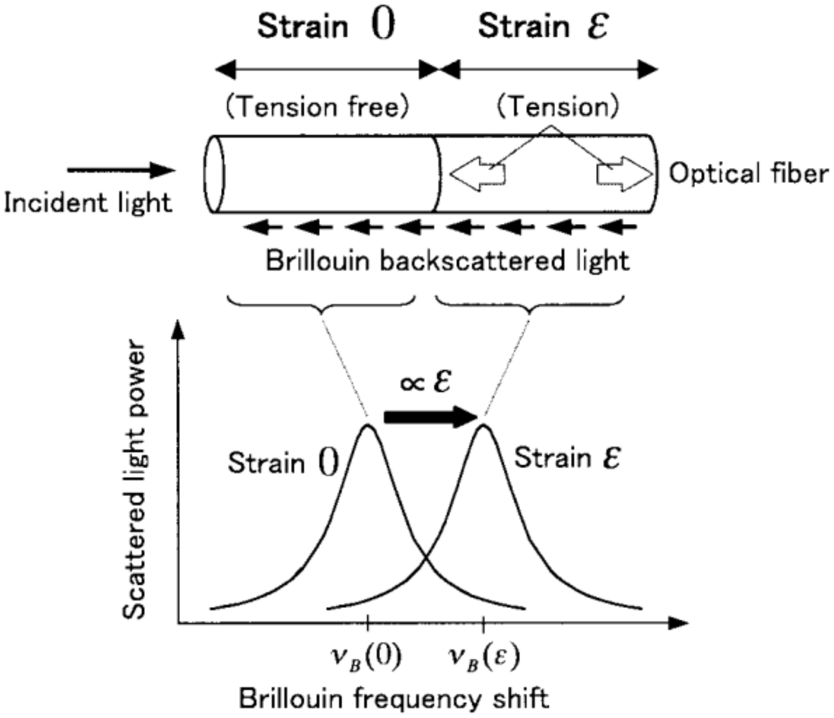

Figure 3.30: Strain causing Brillouin Frequency Shift (information retrieved from https://www.thorlabs.com/)

3.3.7.1 Fiber Optic DSS Cable Installation on Piles

Two corner pipe piles under each abutment were selected for installing DSS as shown in Figure 3.31. Since the research team were dealing with pipe piles, it was not possible to attach the cable inside the pile. In addition, the research team did not want to attach the cable to its outside since the pile would be driven into the ground, which could damage the cable. A number of options were considered and discussed with the contractor, and it was finally decided to attach fiber cables to flexible composite beams, and then lower them into the piles after the piles are driven.

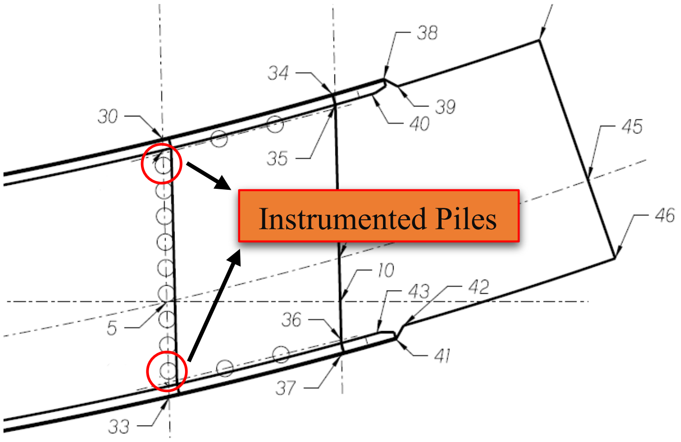

(a) north abutment

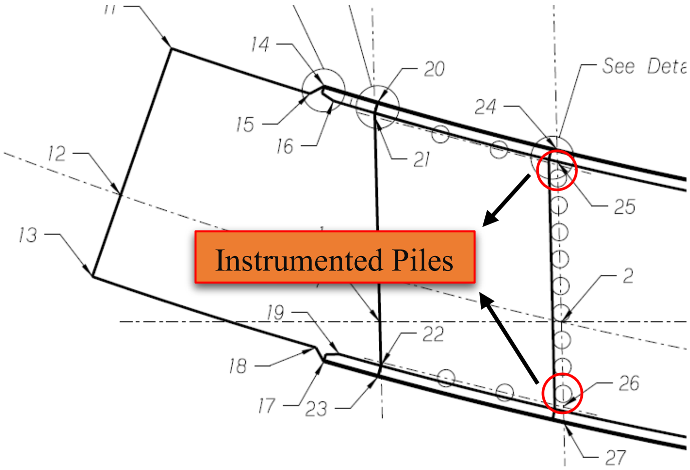

(b) south abutment

Figure 3.31: Location of Fiber Optic Cables Instrumented on Piles

To accommodate this installation process, DSS cables were inserted into the precut grooves of the composite beams which were filled with epoxy later to fix and protect the cables (Figure 3.32). Two lines of grooves and cables were utilized to have a backup system and ensure that if one cable was damaged during installation or transportation, the other cable line can be used for readings. To reach the 75 ft pile length, 15 composite beams for each pile were then chained together as shown in Figure 3.33. This was due to the limitation of the size (length) of transportation. Therefore, composite beams that were less than 8 ft was used. This part of the preparation was completed at the lab at the university, and all beams were transferred to the bridge site. The research team checked all fiber optic cables attached to the composite beams to see if there were any damages before transferring them to the bridge site. No damage was observed prior to placing them inside the piles.

Figure 3.32: Composite Beam with Grooves, Fiber cables and the Protective Epoxy

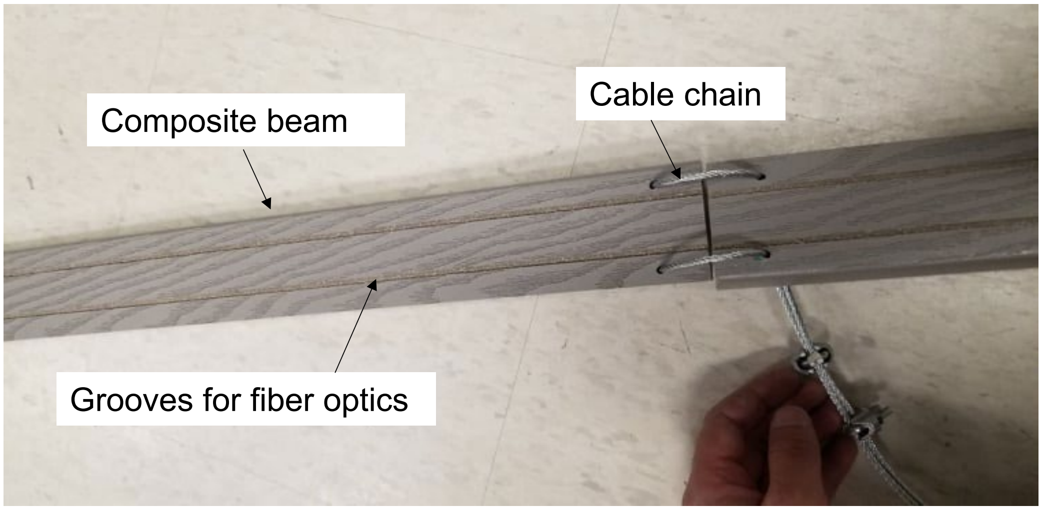

(a) Composite beam details and cable chain splices

(b) Composite beam laid on floor (c) Folded for transportation

Figure 3.33: Composite Beams for Each Pile

At the site, the research team positioned the composite beams on the ground, and a steel anchor was inserted into the center of each beam as a means to keep the composite beams as close as possible to the pile's wall (Figure 3.34 (b)). Then, the research team carefully lowered the composite beams until they reached the bottom of each pile (Figure 3.35).

(a) extended composite beams for one pile (b) anchors on the center of each beam

Figure 3.34: Fiber Optic Cables on Composite Beams

Figure 3.35 Lowering the composite beams into the pile

Figure 3.36 show two pictures of the drilled hole at the top portion of each pile as the exit location for both fiber optic cables inside. After this preparation, the cables were inserted into a rubber hose as shown in Figure 3.36. The final step involved filling all four piles with mortar to fix their position so that the piles - mortar - composite beams would act as one solid body with identical deformations during pile movements.

Figure 3.36: Rubber Tube Installation for Cable Protection

Figure 3.37: Casting Mortar inside Piles with Fiber Optic Cables

3.3.7.2 Fiber Optic DSS Cable Installation on Girders

The bridge superstructure is consisted of four curved girders. A total of three girders were selected to be monitored, including two exterior girders and one interior girder as shown in Figure 3.38 (looking down the North End).

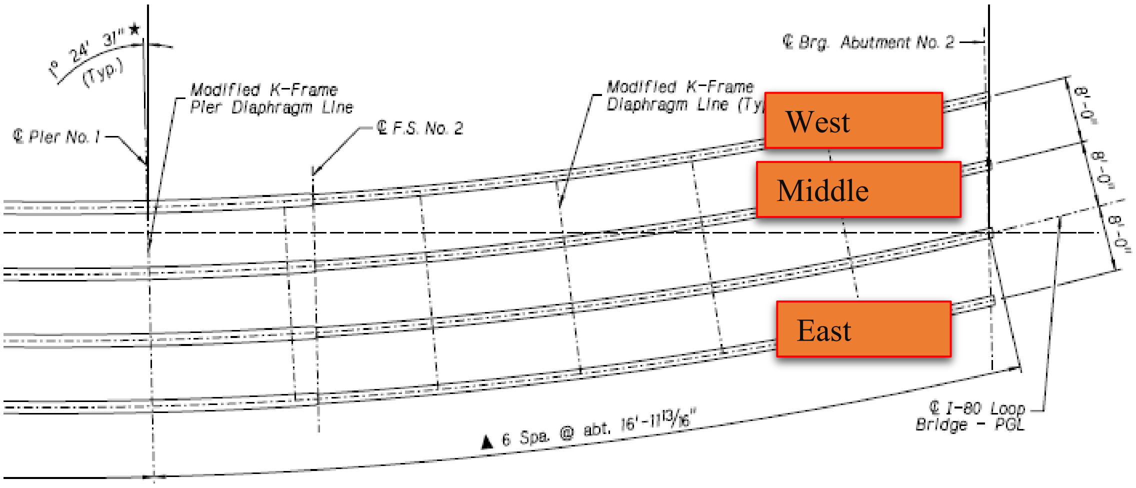

Figure 3.38 Three instrumented girders

The research team were able to attach fiber optic cables directly to the selected locations on the web of the each girder. To ensure redundancy, two sets of fiber optic DSS cables were attached to the top and bottom of each girder web, adjacent to the top and bottom flanges. It should be noted that each girder line consists of three curved segments, as shown in Figure 3.39. Before all girders were placed on the substructure, segments 2 and 3 were bolted together on the ground.

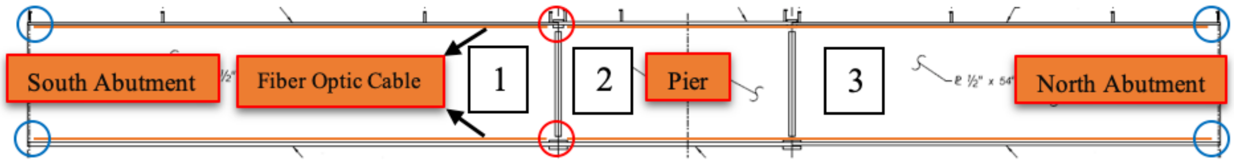

Figure 3.39: Locations of Fiber Optic Cable Installation and Splice Locations

Following the connection of segments 2 and 3, the research team went to the site to install the fiber optic cables on segments 2–3 (as a single piece) and 1, separately.

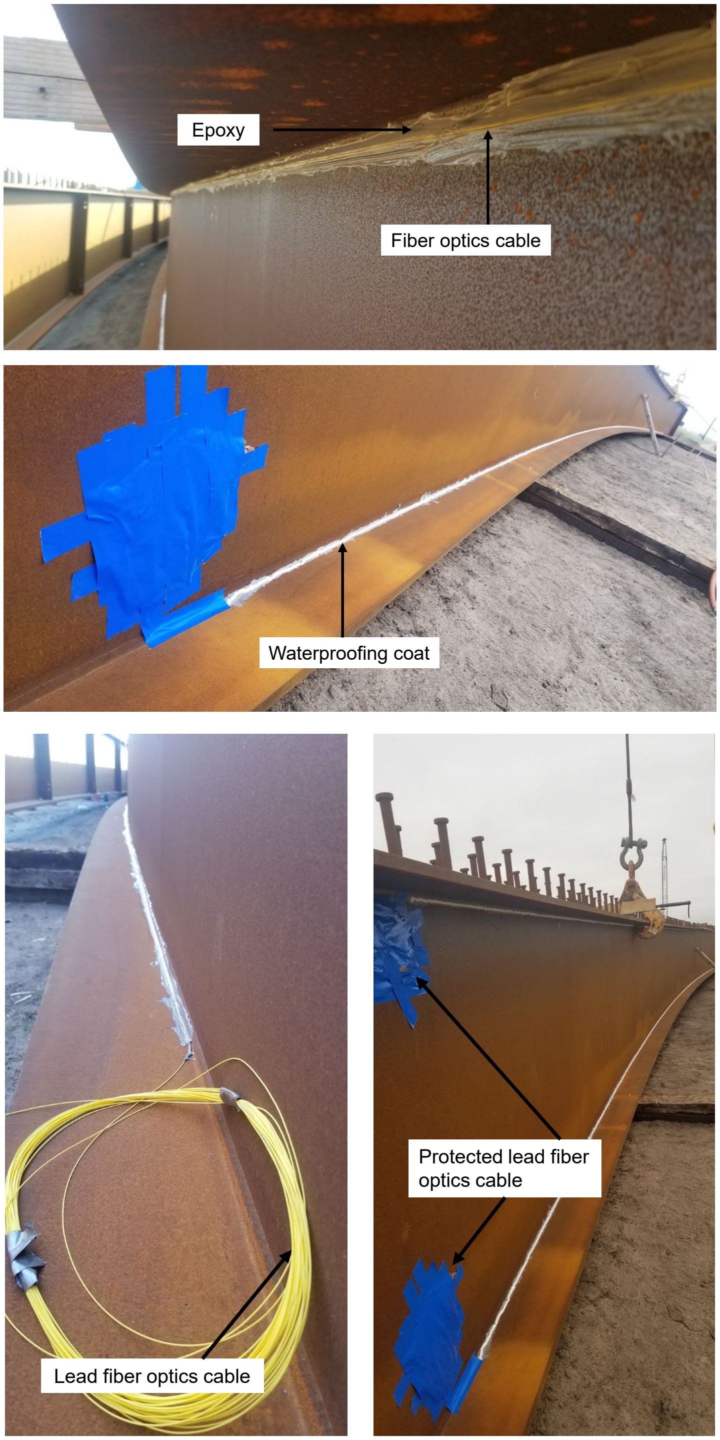

Figure 3.40: Fiber Optic Cable Installation on the Girder with Epoxy and Waterproof Coat, and the Lead Cable Protected in Plastic Bags for Future Splicing Task

In order to facilitate splicing later, additional lead fiber cables were secured in plastic bags at both ends of each cable line. Attaching the cables to the girders was conducted using epoxy, and sufficient time was given for it to cure. On top of the epoxy coat, a waterproof silicon coat was applied to further protect the cables against severe weather (Figure 3.40).

Figure 3.41: Performing Fiber Optic Cable Fusion Splice at the Girder Splice Point and Connecting Pigtails at the End of Each Cable

The two girder segments (1 and 2–3) were spliced together (this location is shown with red circles in Figure 3.39) after they were placed on the substructure (abutments and piers). In order to connect fiber optic cables at the splice point, the research team returned to the site after all girders were installed, and the concrete deck had been poured. The contractor helped temporarily close one lane of I–80 eastbound so that the research team could complete the splicing task using a manlift (Figure 3.41). DSS Cable Splicing was completed using a Greenlee 910FS fusion splicer unit, and heat shrinkage tubes were used to protect the Connections. Finally, in order to connect the fiber optic cables to the LIOS unit, the research team attached pigtails to the ends of each cable.

3.3.7.3 Fiber Optic DSS Cable Installation at Approach Slab

Lastly, fiber optic DSS cables were installed in the approach slab. The idea arose from the fact that approach slab settlement is a common problem in IABs shared by many states. DSS Cable installation was conducted in order to monitor both longitudinal or lateral deformation under the slab, as well as measure settlement, if any. The following plan (Figure 3.42) was developed to capture deformations in both directions and was later approved by NDOT.

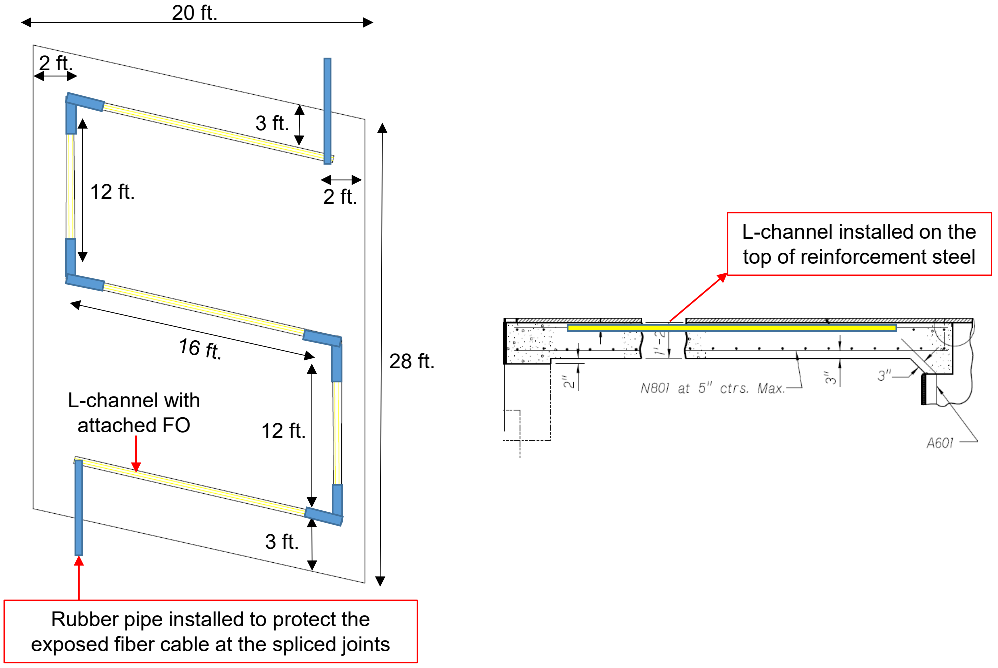

Figure 3.42: Plan View of the Location of Fiber Optic Cable in the Approach Slab

In Figure 3.42, cables are shown in both directions, parallel and perpendicular to the flow of traffic. The cables were prepared to exit the approach slab at the corner, to be connected to the strain data reader. The research team planned to attach the cables to the top reinforcement mat of the approach slab. It was not possible to directly attach cables to the rebars, due to the possibility of future concrete casting damaging them. Thus, it was decided to install the cable and secure it using epoxy within steel L-channels. Afterwards, these channels were transported to the job site and affixed to the top reinforcement mat according to the plan in Figure 3.42.

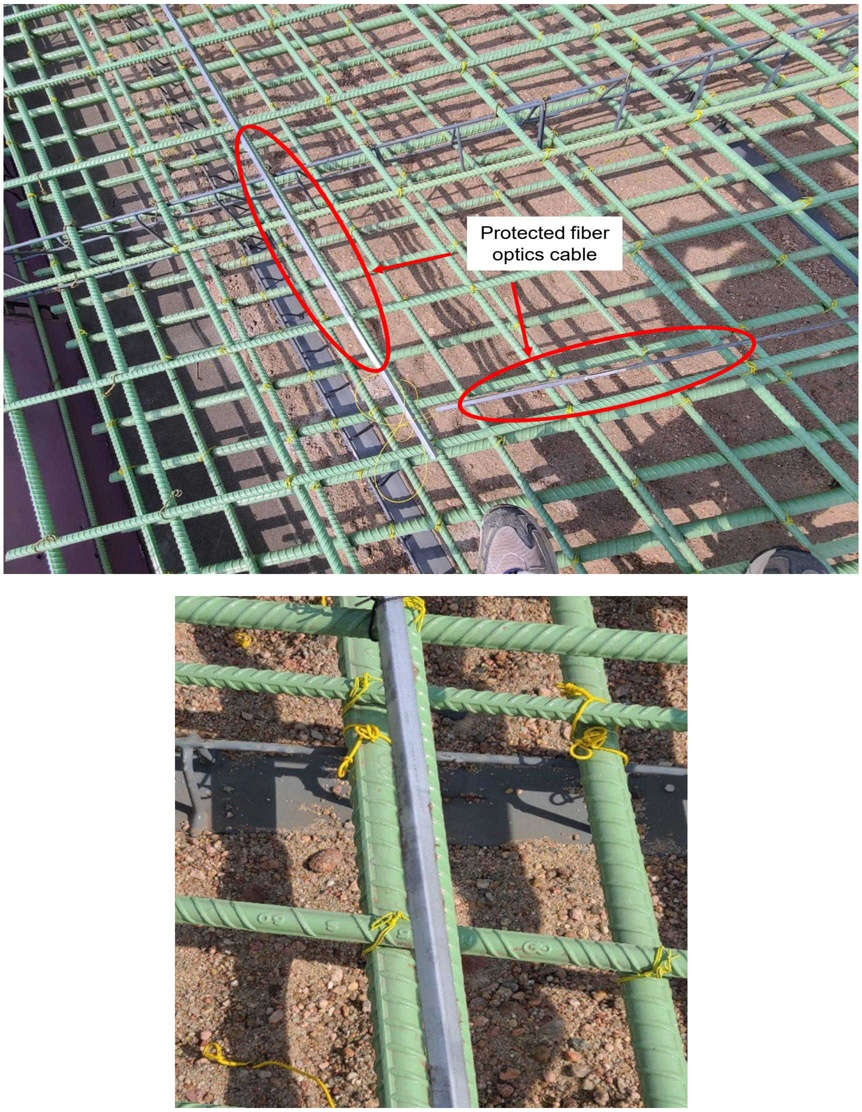

Figure 3.43: L-channels with Fiber Optic Cables attached to the Top Reinforcement Mat

Finally, on top of the exposed portion of the cable, where two L-channels meet at a 90-degree angle, rubber tubes were placed to protect it from being damaged by concrete. Rubber tubes were placed on top of the exposed part of the cable where two L-channels meet at a 90-degree angle. Likewise, rubber tubes were inserted into the exit locations to protect the cables (Figure 3.44).

Figure 3.44 Rubber Tube Protection over L-channels

3.3.8 Remote Data Logger Installation

During the first few months of monitoring the bridge behavior, earth pressure cell and tilt meter readings were taken at the bridge every time the team visited. Since the site was far from the UNL campus, it was not an efficient method of collecting data. In addition, even if measurements could be made once a day, the data collection would not be continuous throughout the entire day, so it would not be sufficient to observe the daily expansion and contraction cycles. Continuous measurements, on the other hand, will reveal the differences in behavior of pressure cells and tilt meters during day and night, which will correlate directly to changes in temperature. It is also not convenient to take readings manually at the site especially when the weather is extremely hot or cold. The research team, therefore, purchased and installed a remote data acquisition system to continuously monitor all pressure cells and tilt meters.

For this work, GeoNet 8900, a wireless data acquisition system was selected. The system consists of a Cellular Gateway + Mesh Supervisor, two 8–channel Vibrating Wire Mesh Nodes, and a solar panel for charging the supervisor. The Cellular Gateway + Mesh Supervisor lets us manage and integrate the nodes in our network using a mesh supervisor, as well as sending and receiving data using a cellular module. Therefore, three pressure cells and two tilt meters from each abutment were connected to their corresponding node where their data would be sent to the supervisor for data collection. Because the supervisor possesses a cellular module as well, it will also send the collected data to the cloud, allowing it to be downloaded from anywhere. In order to prevent any signal blockage from causing loss of data, both nodes and the supervisor were situated on the west side of the bridge so they could receive and transmit data freely. The supervisor and its solar panel were installed on the west wingwall of the north abutment for maximum sunlight exposure due to the bridge's location. The solar panel, sensor nodes, and the supervisor for both abutments are displayed in Figure 3.45. In both of these photos, there are five blue cables connected to each node, three of which come from three pressure cells attached to each abutment, and the last two come from tilt-meters.

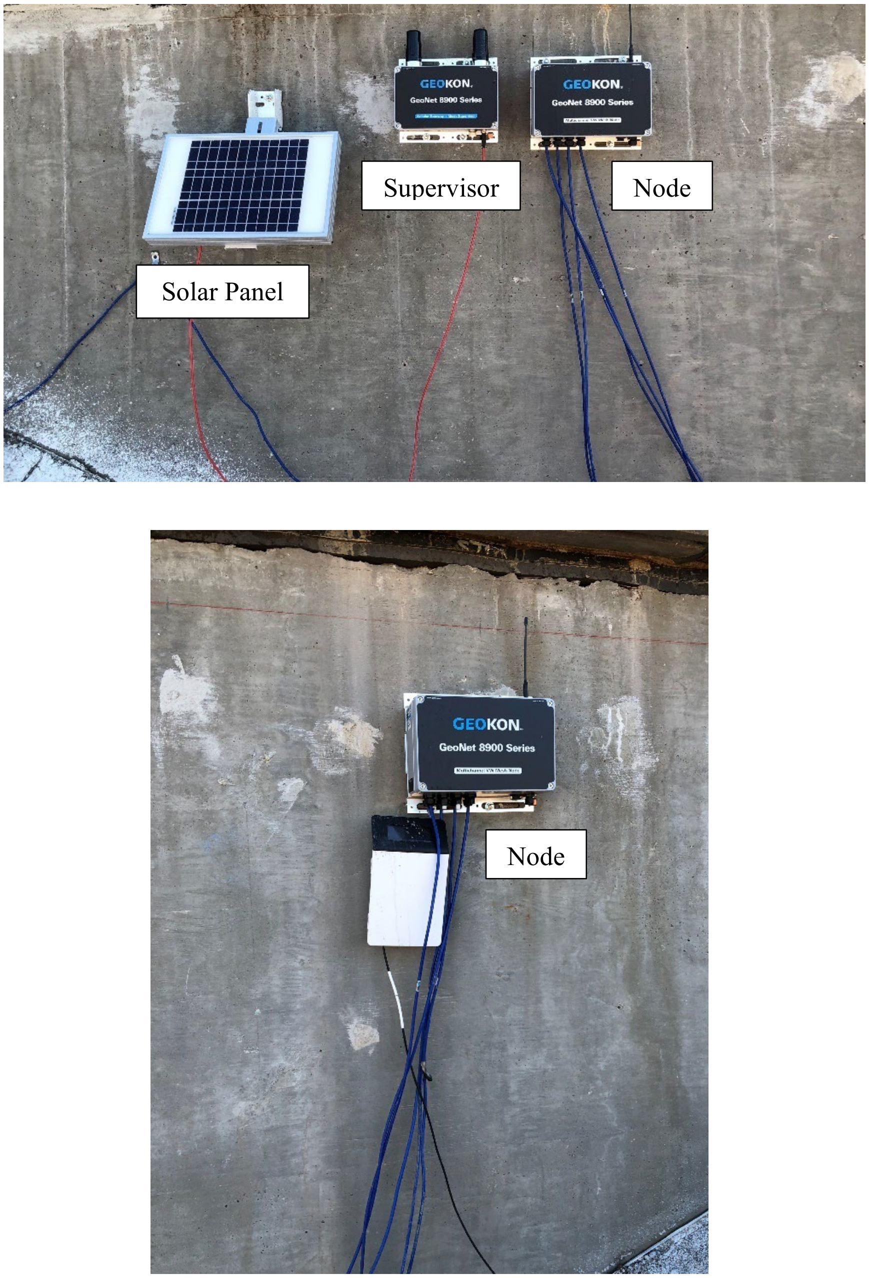

Figure 3.45: Photo of Solar Panel, the Node and the Supervisor on both Abutments

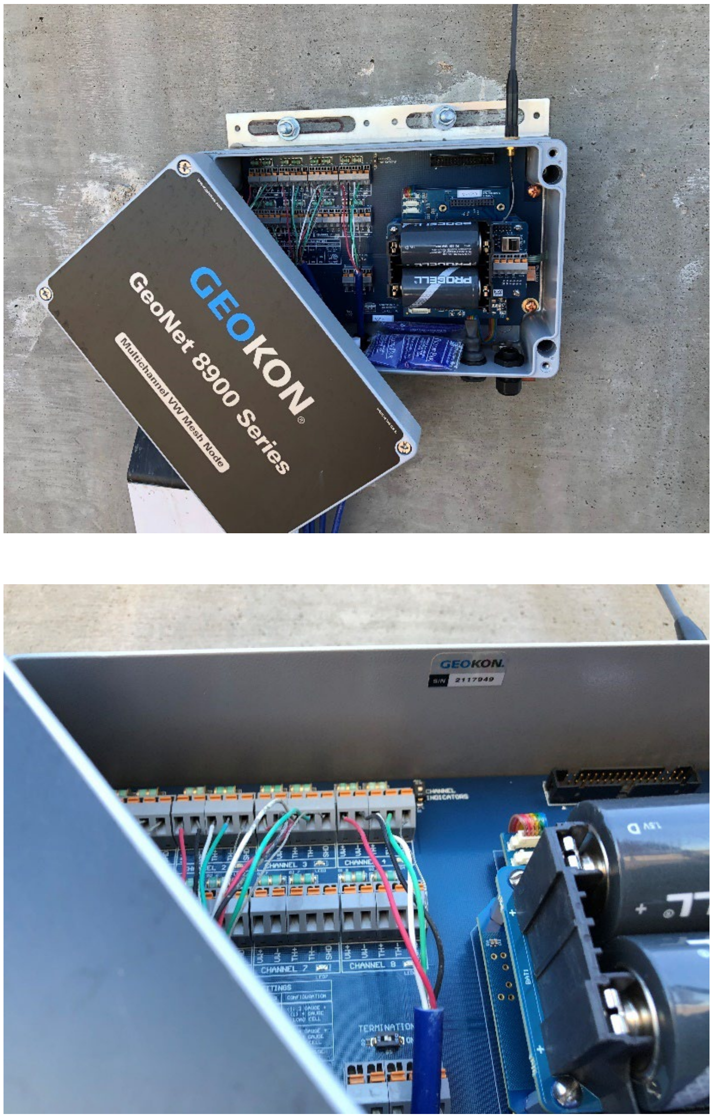

Figure 3.46: Interior view of the south abutment and its wiring scheme

An example of how a node's interior appears is shown in Figures 3.46. Nodes and the supervisor were turned on, and data was recorded and collected after all wires from pressure cells and tiltmeters were connected. In the beginning, the default scan rate was every 10 minutes. In addition, a software package called Agent is included with this system, which allows users to configure the scanning rate of the nodes and plots the output of the connected instruments. The research team adjusted the scan rate to every hour using the software to capture hourly temperature changes. The supervisor setup page is shown in Figure 3.47. Afterwards, two nodes (each with five sensors, three pressure cells and two tilt meters) were created in the software, on for each abutment as shown in Figure 3.48.

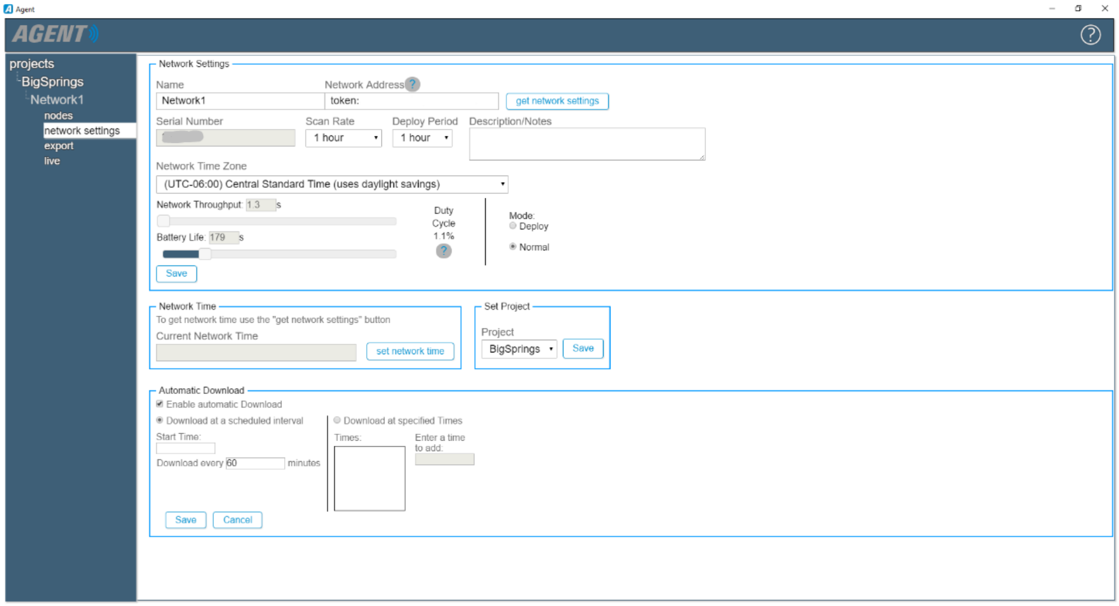

Network Settings

Name: Network1

Network Address: token:

Serial Number: [redacted]

Scan Rate: 1 hour

Deploy Period: 1 hour

Description/Notes:

Network Time Zone: (UTC-06:00) Central Standard Time (uses daylight savings)

Network Throughput: 1.3 s

Battery Life: 179 s

Duty Cycle 1.1%

Mode:
○ Deploy
● Normal

Network Time

To get network time use the "get network settings" button

Current Network Time:

Set Project

Project: BigSprings

Automatic Download

☑ Enable automatic Download

● Download at a scheduled interval

Start Time:

Download every 60 minutes

○ Download at specified Times

Times:

Enter a time to add:

Figure 3.47: Settings for the Agent Software

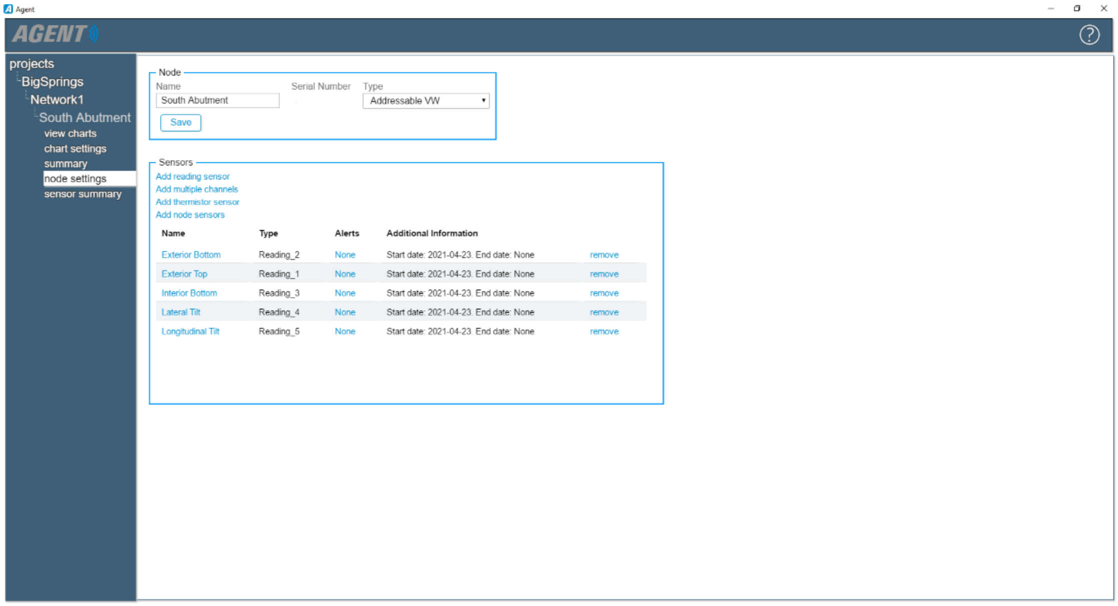

Node

Name: South Abutment

Serial Number:

Type: Addressable VW

Sensors

Name	Type	Alerts	Additional Information	
Exterior Bottom	Reading_2	None	Start date: 2021-04-23. End date: None	remove
Exterior Top	Reading_1	None	Start date: 2021-04-23. End date: None	remove
Interior Bottom	Reading_3	None	Start date: 2021-04-23. End date: None	remove
Lateral Tilt	Reading_4	None	Start date: 2021-04-23. End date: None	remove
Longitudinal Tilt	Reading_5	None	Start date: 2021-04-23. End date: None	remove

Figure 3.48: Measurements on Sensors from the South Abutment

As a next step, each of the five sensors created needs to be adjusted and represent different pressure cells and tiltmeters installed on the bridge. There are six different categories of sensors available including pressure, load, distance, strain, tilt and temperature, where we set the sensor type to either pressure or tilt for this project. The last step is to set the calibration factors and zero readings. A calibration factor for each sensor was provided by the manufacturer company, Geokon. Each sensor was calibrated to zero immediately after installation, and every subsequent reading was compared to this benchmark.

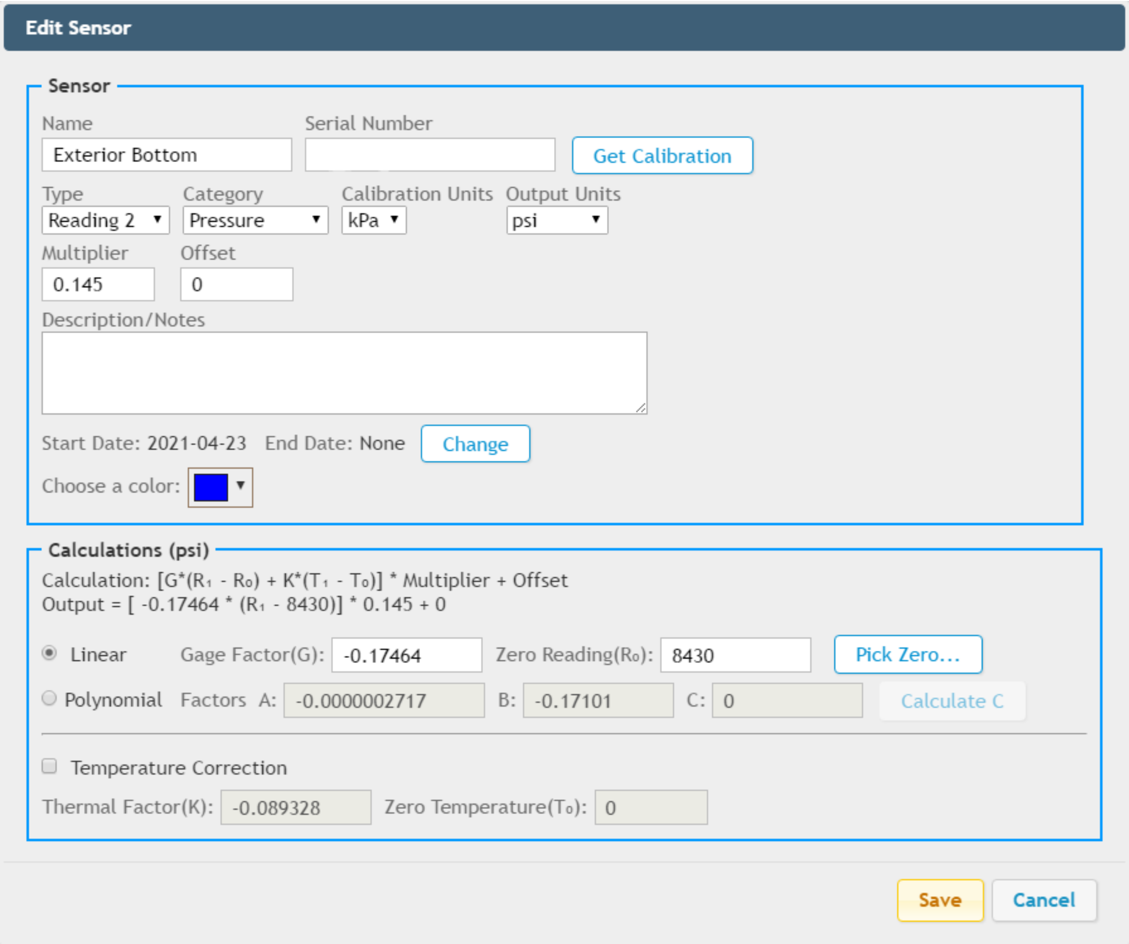

Edit Sensor

Sensor

Name: Exterior Bottom
Serial Number:

Type: Reading 2
Category: Pressure
Calibration Units: kPa
Output Units: psi

Multiplier: 0.145
Offset: 0

Description/Notes:

Start Date: 2021-04-23 End Date: None

Choose a color: 🟦

Calculations (psi)

Calculation: $[G*(R_1 - R_0) + K*(T_1 - T_0)]$ * Multiplier + Offset
Output = $[-0.17464 * (R_1 - 8430)] * 0.145 + 0$

● Linear Gage Factor(G): -0.17464 Zero Reading(R_0): 8430
○ Polynomial Factors A: -0.0000002717 B: -0.17101 C: 0

☐ Temperature Correction
Thermal Factor(K): -0.089328 Zero Temperature(T_0): 0

Figure 3.49: Entry for Calibration Factors

3.4 Summary of Sensor Installation following the Construction Schedules

The research team has visited the Big Springs West I-80 Bridge which is 350 miles apart from the university campus and completed 20 trips during 2020 and 2021 to follow up the construction schedules of the bridge. This was not an easy task due to travel restrictions during the COVID-19 pandemic. Each research team personnel had to drive in separate cars and was not able to stay in accommodation which required the team to make daily travel plans for this remote site. Table 3.2 shows an overview of every trip the research team made to install the sensors described in Chapter 3. As shown in Table 3.2, the team received this bridge site at the end of 2019, and the construction started in January 2020. The first site visit was taken on January 27, 2020 and continued until August 13, 2021. After these dates, there was three additional trips to the site for additional measurements.

Table 3.2: Timeline of Project and Field Instrumentation Records

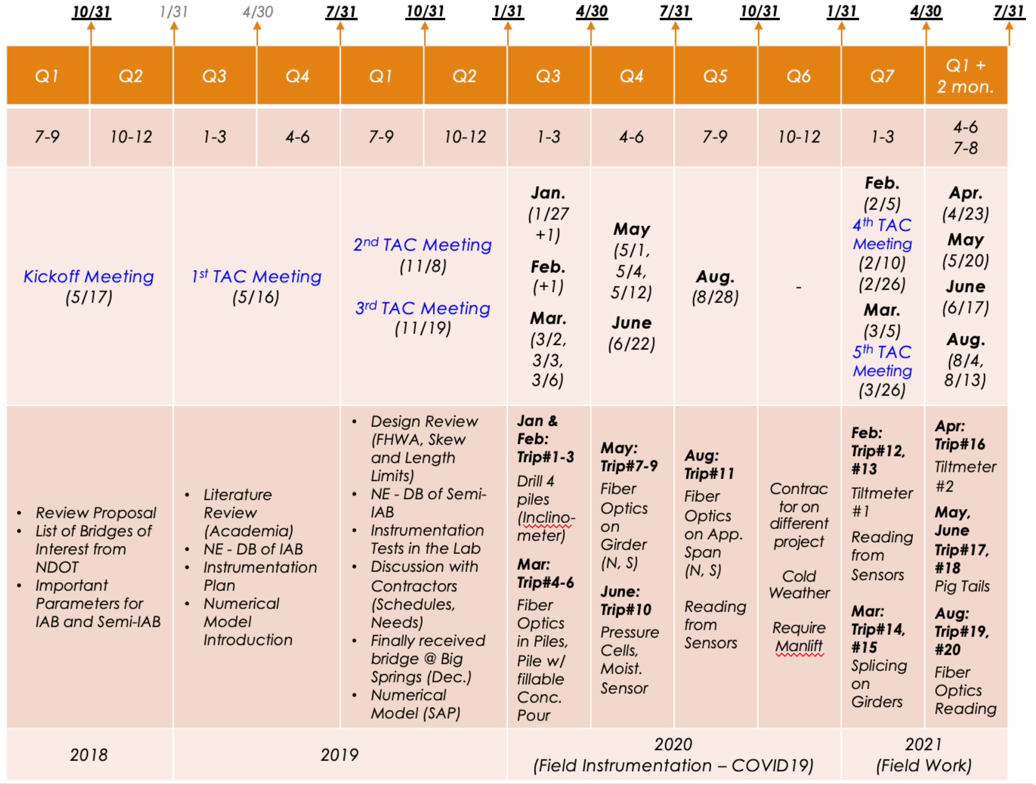

10/31	1/31	4/30	7/31	10/31	1/31	4/30	7/31	10/31	1/31	4/30	7/31
Q1	Q2	Q3	Q4	Q1	Q2	Q3	Q4	Q5	Q6	Q7	Q1 + 2 mon.
7-9	10-12	1-3	4-6	7-9	10-12	1-3	4-6	7-9	10-12	1-3	4-6 7-8
Kickoff Meeting (5/17)		1st TAC Meeting (5/16)		2nd TAC Meeting (11/8) 3rd TAC Meeting (11/19)		**Jan.** (1/27 +1) **Feb.** (+1) **Mar.** (3/2, 3/3, 3/6)	**May** (5/1, 5/4, 5/12) **June** (6/22)	**Aug.** (8/28)	-	**Feb.** (2/5) 4th TAC Meeting (2/10) (2/26) **Mar.** (3/5) 5th TAC Meeting (3/26)	**Apr.** (4/23) **May** (5/20) **June** (6/17) **Aug.** (8/4, 8/13)
• Review Proposal • List of Bridges of Interest from NDOT • Important Parameters for IAB and Semi-IAB		• Literature Review (Academia) • NE - DB of IAB • Instrumentation Plan • Numerical Model Introduction		• Design Review (FHWA, Skew and Length Limits) • NE - DB of Semi-IAB • Instrumentation Tests in the Lab • Discussion with Contractors (Schedules, Needs) • Finally received bridge @ Big Springs (Dec.) • Numerical Model (SAP)		**Jan & Feb: Trip#1-3** Drill 4 piles (Inclino-meter) **Mar: Trip#4-6** Fiber Optics in Piles, Pile w/ fillable Conc. Pour	**May: Trip#7-9** Fiber Optics on Girder (N, S) **June: Trip#10** Pressure Cells, Moist. Sensor	**Aug: Trip#11** Fiber Optics on App. Span (N, S) Reading from Sensors	Contractor on different project Cold Weather Require Manlift	**Feb: Trip#12, #13** Tiltmeter #1 Reading from Sensors **Mar: Trip#14, #15** Splicing on Girders	**Apr: Trip#16** Tiltmeter #2 **May, June Trip#17, #18** Pig Tails **Aug: Trip#19, #20** Fiber Optics Reading
2018		2019				2020 (Field Instrumentation – COVID19)				2021 (Field Work)	

4. FIELD MONITORING RESULTS

4.1 Introduction

This chapter includes the measurements after the construction was completed in 2021 and after our instrumentation site visits were completed in August 2021 up to July of 2022 to report the behavior of the full integral curved bridge with one full year weather cycle. All tiltmeters and pressure cells, as well as the supervisor node of the remote data logger are equipped with thermistors to record the ambient temperature. These sensors would have been ideal for monitoring the ambient temperature, however, for an unknown reason, none of them recorded the temperature correctly. Therefore, the temperature of the site was obtained from the weather station nearest to the bridge site (North Platte Station). Figure 4.1 shows this temperature from May 2020 to July 2022. This graph shows the cyclical nature of temperature changes.

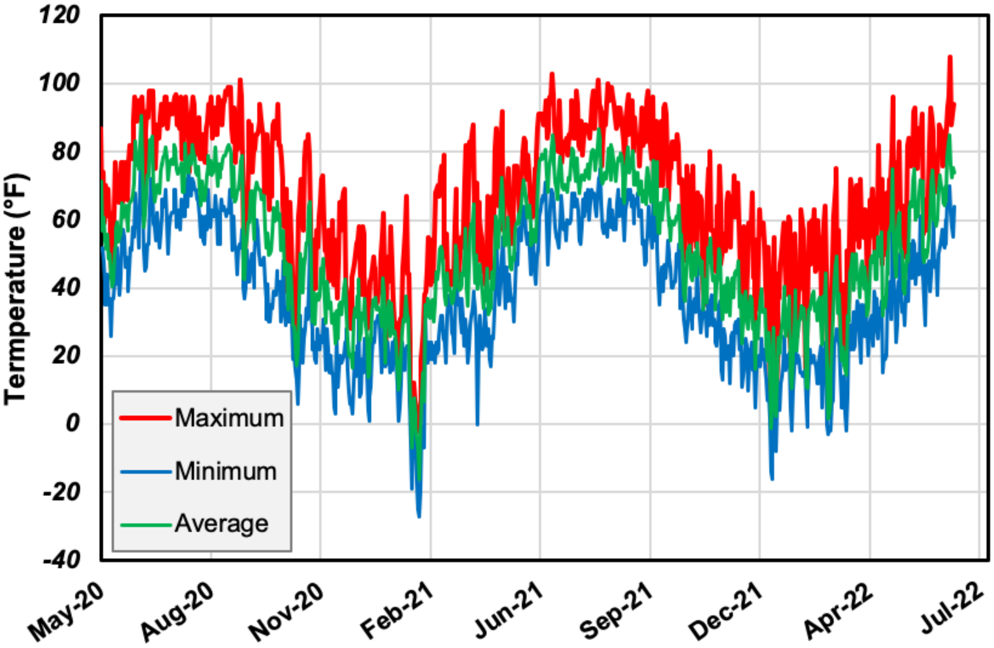

Figure 4.1: Daily Temperature Change of the North Platte Weather Station

As Figure 4.1 shows, the maximum temperatures can reach over 100 °F from June to September, and minimum temperatures can drop below -20 °F between January and February at the bridge site.

4.2 Pressure Cell Measurements

As mentioned in Section 3.2.6, pressure cell readings were made manually at the site prior to installing the remote data logger system. Table 4.1 shows the reading prior to installation of the remote data acquisition system.

Table 4.1: Pressure Cell Readings before Installing the Remote Data Acquisition System

Date	Pressure (psi)					
	North Abutment			South Abutment		
	East–Top	East–Bottom	West–Bottom	East–Top	East–Bottom	West–Bottom
Aug. 2020	46.11	50.81	42.11	NA	NA	NA
Feb. 2021	2.66	2.98	2.14	2.24	2.51	1.89

The remote data acquisition system was installed on April 24, 2021, and since then, data has been collected remotely. Figure 4.2 shows the location of the pressure cells on each abutment. Three different colors (green, blue, and red) are used in Figure 4.2 to indicate the locations where the pressure cells were installed and correlate them with the measurements.

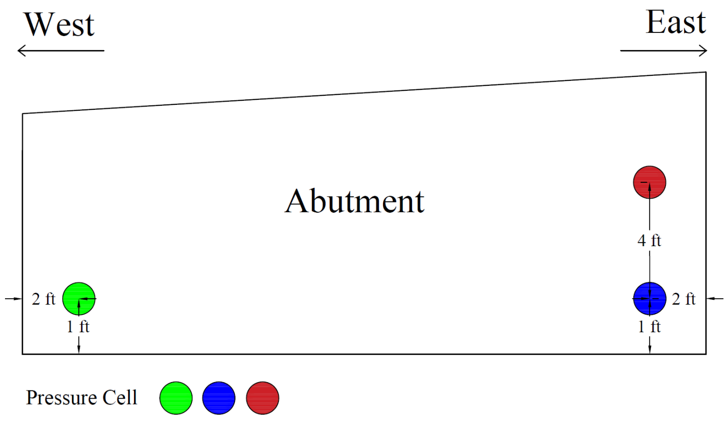

Figure 4.2: Location of Pressure Cells on Each Abutment

The colors red, blue, and green represent the east top, east bottom, and west bottom pressure cells, respectively. In addition, each pressure cell in this figure will have the same color as the line graphs that will appear afterward, making it easier to follow and interpret the trend. Sample readings from both abutments are displayed in Figure 4.3.

☑ Show tooltips on charts

Start: Apr 6, 2021 12:00 am **Stop:** none

(a) north abutment

☑ Show tooltips on charts

Start: Apr 6, 2021 12:00 am **Stop:** none

(b) south abutment

Figure 4.3: Pressure Cell and Tiltmeter Readings

Note that these are raw data graphs that have not been processed. The research team noticed that for both pressure cells and tiltmeters, there are occasionally unusual spikes and sudden jumps in the graphs. These readings are unusual since pressure and tilt cannot change over 1,000% in an hour for example. Additionally, at the time of these spikes, the bridge was not in service, so some sort of malfunction must have occurred. Red circles are drawn around some of the spikes in Figure 4.3. As a result, these sharp spikes do not reflect the actual pressure or tilt. Therefore, the research team generated an R code that reads the raw data, calculates the change in each step, and if the change exceeded a threshold, a missing value could be substituted for the data point. To fill in the missing values, a linear interpolation method was used. Considering that the data does not change significantly in each step (an hour), linear interpolation seems appropriate for this dataset. Since April 24, 2021, this remote data acquisition system has been recording data per hour without any issues except for one incident. No data could be saved between March 26, 2022, and April 8, 2022, as both nodes ran out of battery. These data were restored after new batteries were installed. The pressure cell readings from late April 25, 2021, to June 8, 2022, are shown in Figure 4.4. It is unfortunate that three of the six mounted pressure cells were lost a few months after their installation.

According to Figure 4.4, the west bottom pressure cell from the north abutment and the east top and bottom cells from the south abutment have stopped to function. The pressure cells show a cyclic pattern when the data view is zoomed in, since all three readings rise in the daytime as the bridge expands, while at night, when the bridge contracts, all three readings remain nearly constant. This indicates that the abutment has shifted away from the backfill soil where the soil is not pressing against the pressure cell.

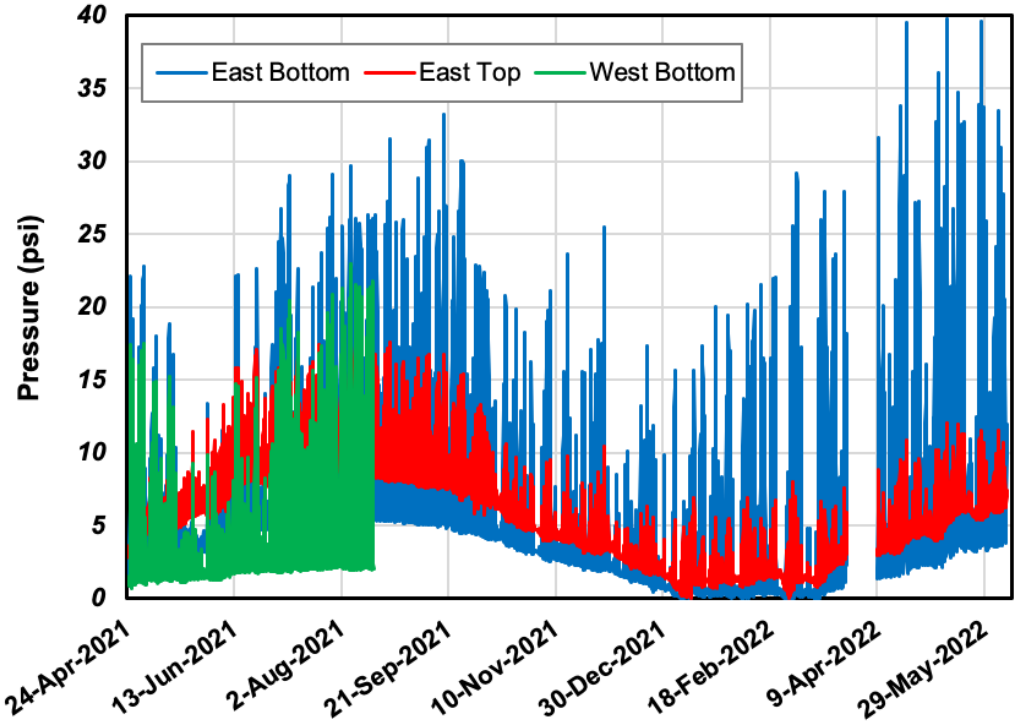

(a) north abutment

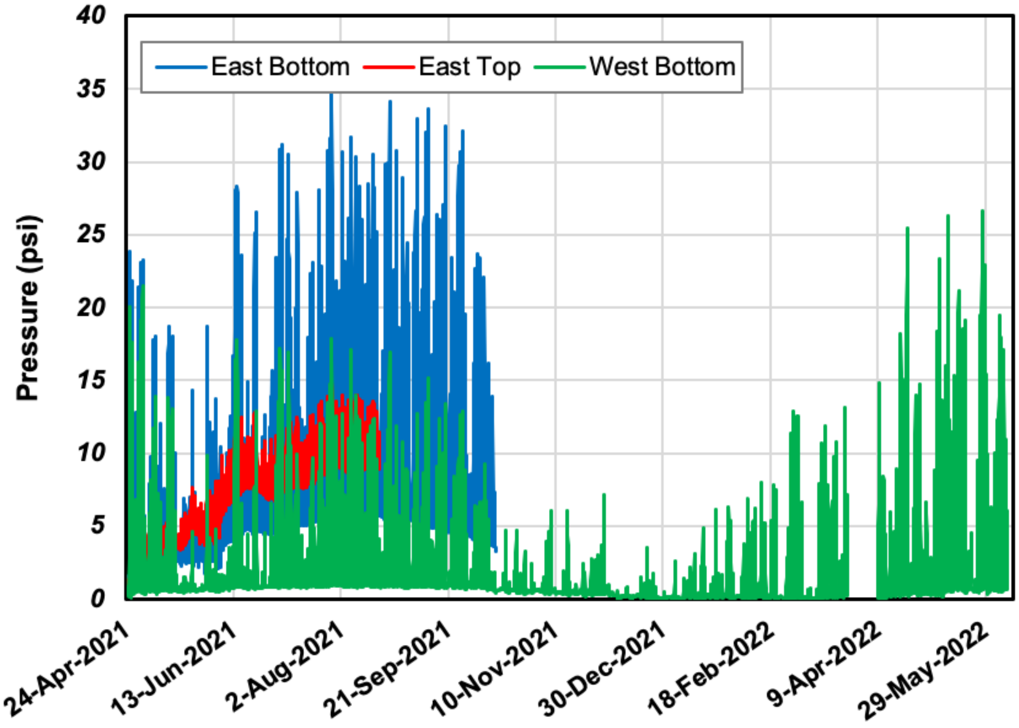

(b) south abutment

Figure 4.4: Pressure Cell Measurements

The effect of temperature dependent rise and fall of the earth pressure is shown in Figure 4.5, where a week of pressure data from all the cells shows the cyclic nature of their behavior. More precisely, the pressure readings start to rise every day at approximately 7 to 9 AM in the morning, reach their maximum between 5 and 7 PM in the evening, and then drop until around midnight, when they enter the constant pressure zone until the next day to follow the similar pattern. This pattern is repeated every day. Pressure readings show a spike whenever the daily temperature fluctuates a lot, and when the temperature does not change much, the pressure difference is not high. According to Figure 4.4 and for both abutments, the east bottom pressure cell has the highest pressure, followed by the west bottom and east top cells. As of June 8, 2022, for the south abutment, the maximum pressure for the east bottom pressure cell was 34.6 psi that occurred on July 28, 2021 at 6 PM, for the west bottom cell, the maximum pressure was 26.3 psi which occurred on May 11, 2022 at 6 PM, and finally, the maximum pressure on the east top cell was 14.9 psi, which was recorded on July 28, 2021 at 7 PM. The research team previously mentioned that the south abutment's east top and bottom pressure cells stopped functioning on August 20 and October 13, respectively, for reasons that are still unknown to the research team. According to Figure 4.4 (b), east top and bottom cells indicate that they are experiencing build-up pressure just a few days after the remote data acquisition installation, and the buildup pressure increases with time. Although this buildup of pressure is not significant, it is still present for the west bottom cell. In addition, this residual pressure is rising up until late August 2021, then declining with the onset of the cold season. Additionally, the east top cell has a higher buildup pressure than the east bottom cell.

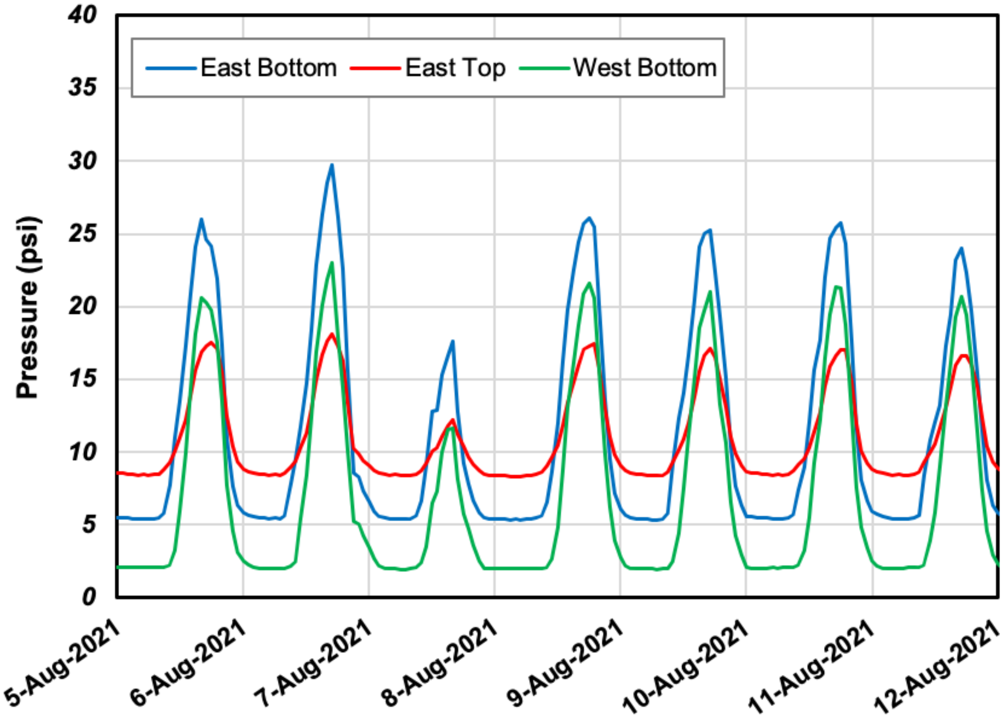

(a) weekly pressure cell data from the north abutment

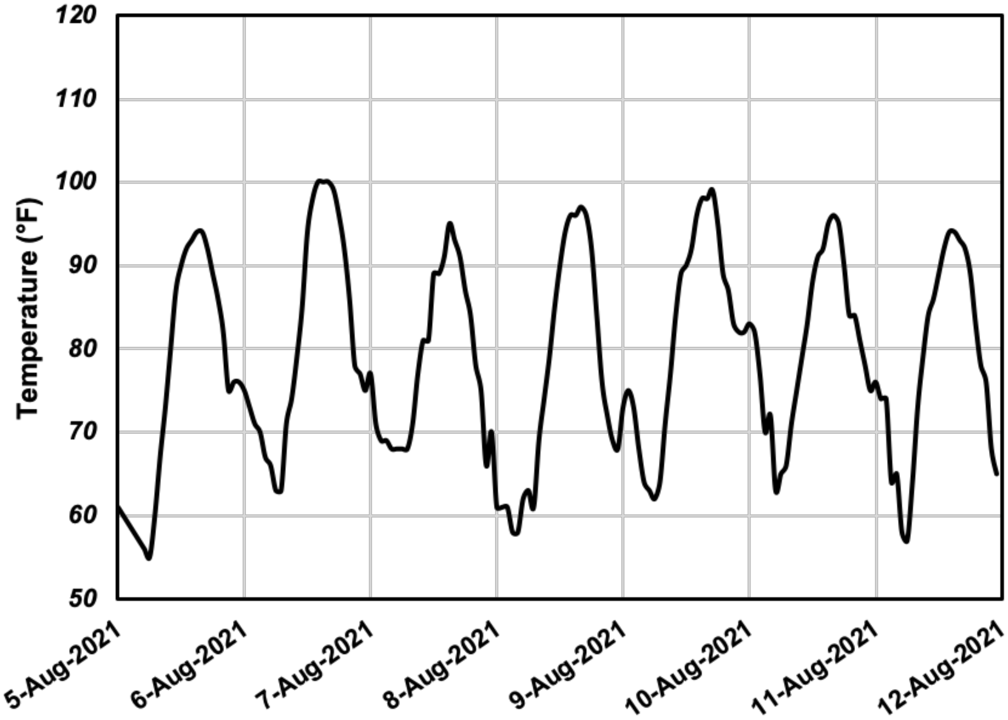

(b) ambient temperature of week when data was collected

Figure 4.5: Cyclic Behavior of the Pressure Cell Measurements

The behavior shown in Figure 4.4 may indicate that the buildup pressure is due to the backfill soil behind the abutment breaking and filling up the gap when the bridge abutments are moving towards each other abutment during contraction and building up pressure when expansion takes place. The highest buildup pressure for the east top cell occurred in August 2021, which is 8.5 psi, meaning that the pressure does not fall below 8.5 psi even at night when the bridge contracts and moves away from the soil. This value is around 5.5 psi for the east bottom, and 0.5 psi for the west bottom cells, both of which occurred in August 2021. When the cold season begins, this buildup pressure declines. In a day, when temperature does not fluctuate much, east top, east bottom, and west bottom cells show the highest pressures, in order. The order is different though when temperature fluctuates a lot throughout the day. Similarly, the north abutment exhibits a comparable pattern (Figure 4.4 (a)). Similar to the south abutment, east bottom, west bottom and east top pressure cells from the north abutment experience the highest pressure to the lowest pressure in order. As shown in this figure, the abutment's west bottom pressure cell stopped working on August 17, 2021, for no apparent reason. As of June 8, 2022, for the north abutment, the maximum pressure for the east bottom pressure cell was 39.8 psi that occurred on May 11, 2022 at 6 PM, for the west bottom cell was 23 psi which occurred on August 6, 2022 at 5 PM, and finally, the highest pressure on the east top cell was 18.5 psi, and that happened on July 28, 2021 at 6 PM. On the north abutment, the buildup pressure follows the same pattern as on the other abutment. A week after the remote data acquisition system was installed, the east top and bottom cells began accumulating pressure. However, it was different for the west bottom pressure cell. In comparison to the other two cells, its buildup began after approximately a month and at a slower rate. The highest buildup pressure for the east top cell occurs in August 2021 which is 8.7 psi. This value is around 5.5 psi for the east bottom, and 2 psi for the west bottom cells, both of which occurred in August 2021. Therefore, this figure indicates that the south abutment experiences slightly higher pressure than the north abutment but comparable trends are observed. Figures 4.6 to 4.8 show a comparison of the identical pressure cell on both abutments.

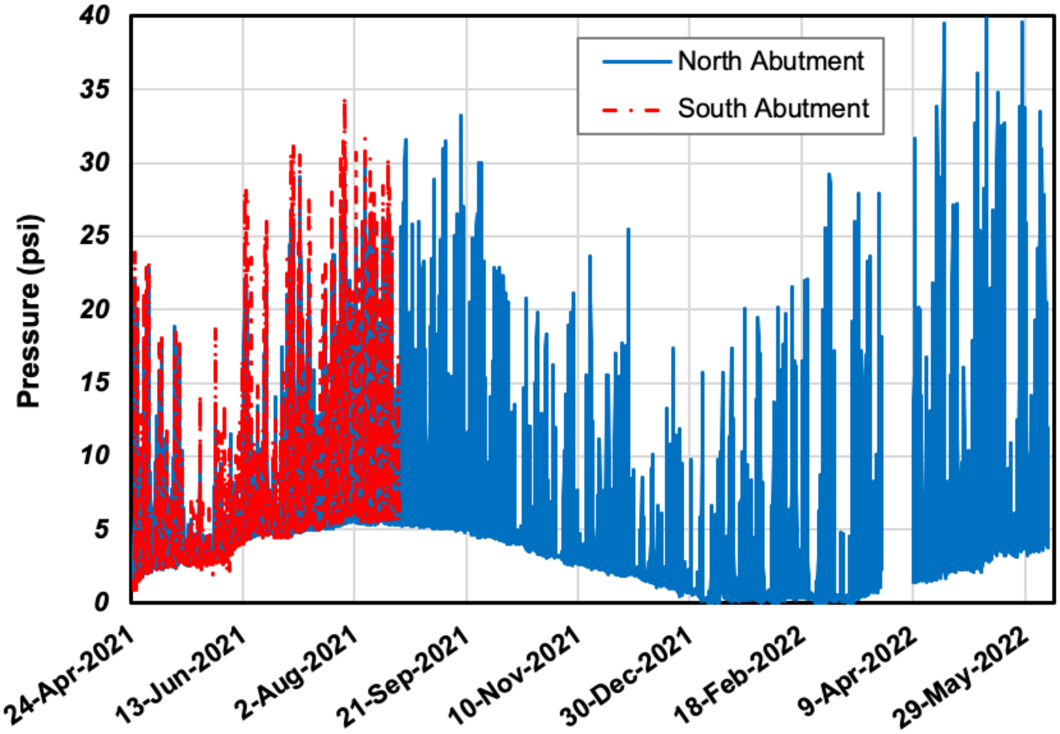

Figure 4.6: East Bottom Pressure Cells on North and South Abutments

Figure 4.6 indicates that the buildup pressure seems to be about the same for both abutments for the east bottom pressure cells before the one on the south abutment stopped functioning. On the other hand, the pressure measured in the south abutment appears to be slightly higher than the measurements in the north abutment. Figure 4.7 shows that the east top pressure cell experiences higher pressures on the north abutment (during the time the cell on the south abutment was still operational).

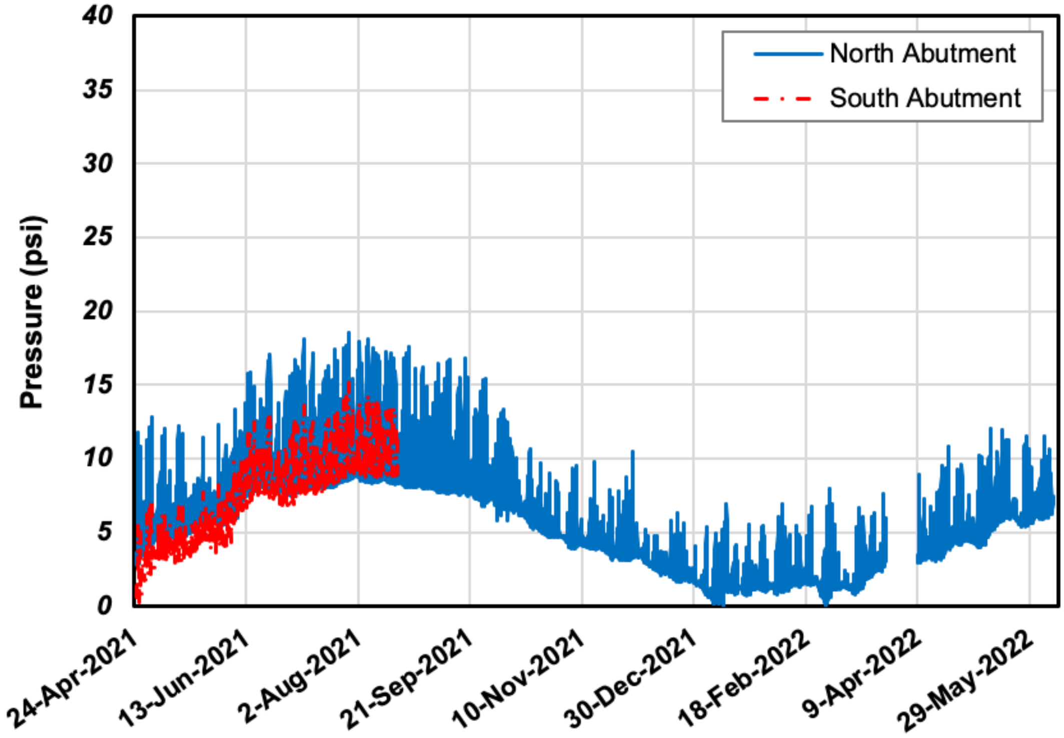

Figure 4.7: East Top Pressure Cells on North and South Abutments

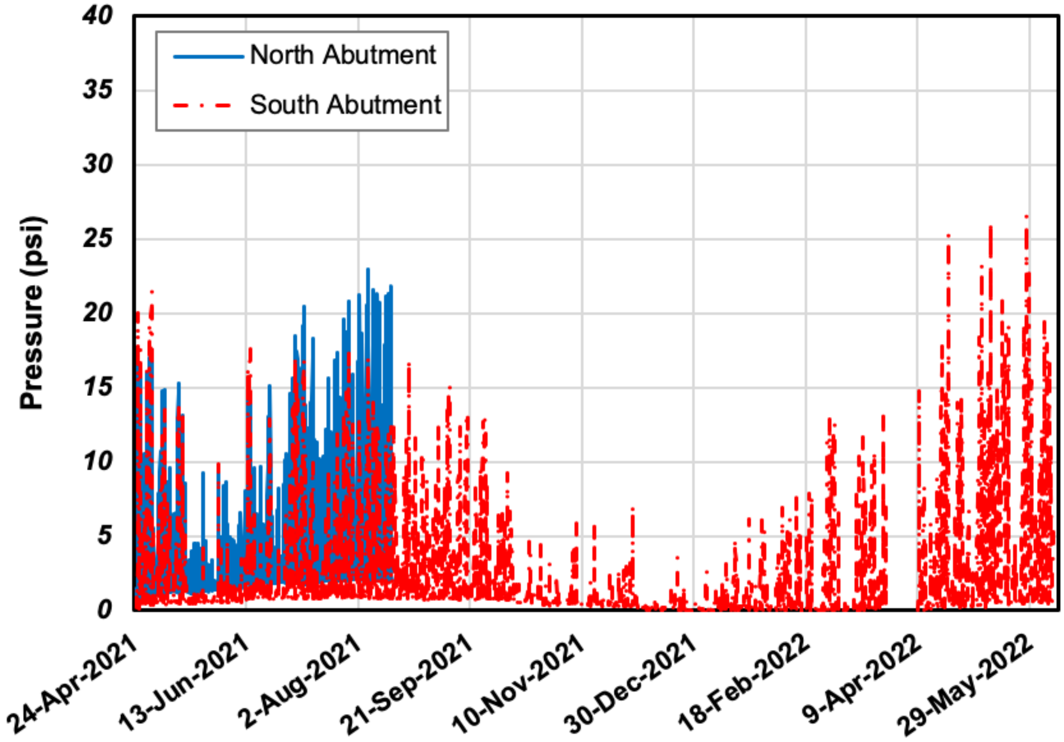

Figure 4.8: West Bottom Pressure Cells on North and South Abutments

The buildup pressure on the north abutment's cell is also generally higher. Finally, Figure 4.8 displays the comparison of the west bottom pressure cells. In comparison with the south abutment, the north abutment has a higher buildup pressure. With the exception of a few days when the south abutment is under more pressure, the north abutment generally experiences more pressure. But it is noted that the repetition of pressures cycles are approximately comparable magnitude, indicating the elastic behavior of soil. However, a continuous monitoring may be required to check the integrity of the bridge and retaining structures.

4.3 Tiltmeter Measurements

A longitudinal tilt is a rotation in the direction of travel (perpendicular to the abutment) whereas a lateral tilt is perpendicular to the travel direction (parallel to the abutment). At the north abutment, the tiltmeter is installed in such a way that its positive longitudinal tilt is towards the south (moving away from the backfill), and its positive lateral tilt is towards the east. For the south abutment, however, the positive longitudinal tilt is towards the north (moving away from the backfill) while the positive lateral tilt is towards the west. To make the positive signs consistent for both abutments, the signs of the lateral and longitudinal tiltmeter reading of the south abutment as well as the north abutment were reversed. The positive tilt for the longitudinal direction is therefore towards the north, while the positive tilt for the lateral orientation is towards the east. Figures 4.9 and 4.10 illustrate the tiltmeter readings for both abutments for longitudinal and lateral tilts, respectively.

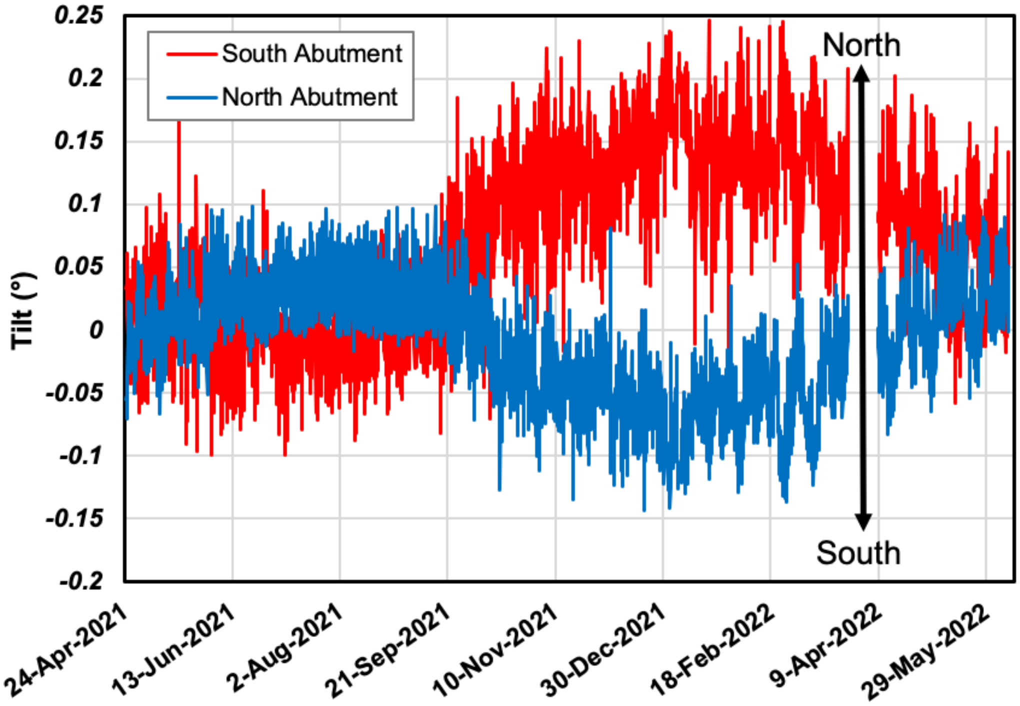

Figure 4.9: Longitudinal Tilts for North and South Abutments

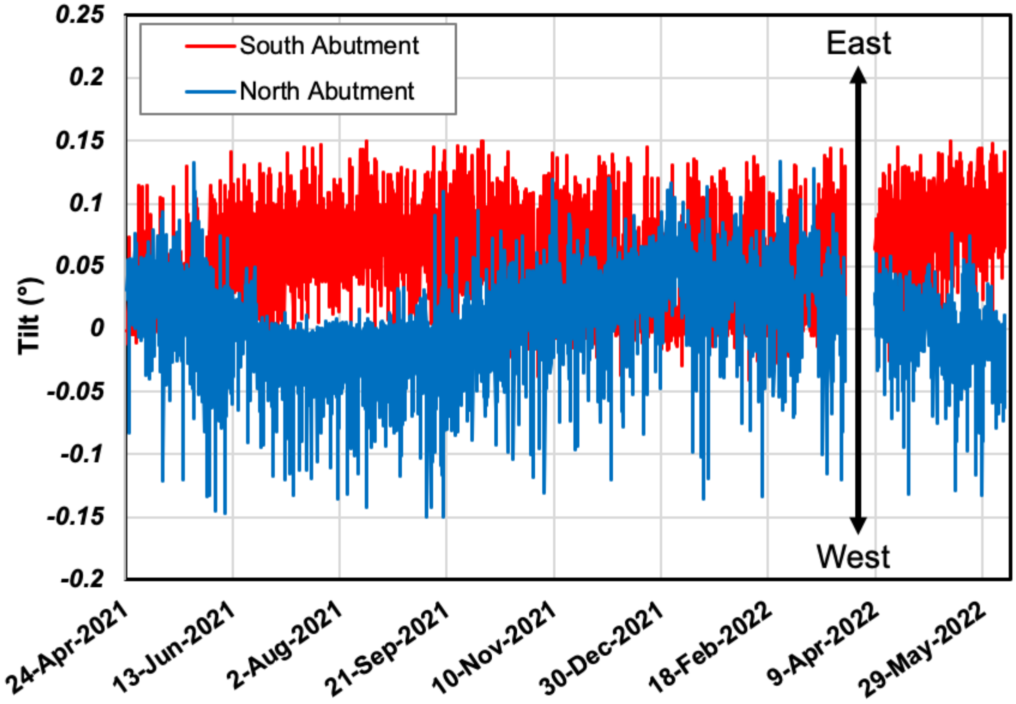

Figure 4.10: Lateral Tilts for North and South Abutments

As shown in Figure 4.9, as of late August 2021, the tiltmeters are experiencing an expansion phase, indicating that both abutments are pushing against the backfill soil. As a consequence, the south abutment tilts towards the south, whereas the north abutment tilts towards the north. Since during the spring and summer seasons, bridge expansion is expected to be the dominant behavior of the bridge, this pattern makes sense. Both abutments, thus, rotate up to 0.1° (north abutment shows slightly higher rotations). From September 2021, the superstructure starts to contract, and it continues until March 2022. In the contraction phase, abutments rotate freely without having to push against any backfill soil, so the range of rotation for this phase is greater than that for the expansion phase. In addition, this figure shows that the north abutment rotates more during contraction phase than the south abutment. While the north abutment's rotation can reach up to 0.25°, the south abutment experiences up to 0.15° of rotation. Both abutments seem to have a different pattern for the lateral tilt. The south abutment will tilt towards east until September 2021, while the north abutment will rotate towards west. This indicates that the entire bridge is horizontally rotating counterclockwise. Their rotations begin to converge after September 2021 which are slightly to the east. They start to diverge again in April 2022, just as they did in 2021. The lateral tilt has a smaller range of rotations compared to the longitudinal tilt. Though the north abutment has similar ranges, the south abutment can tilt longitudinally by as much as 65% more than its lateral extent. In an analogous manner to Figure 4.5, where a relationship between backfill passive pressure and ambient temperature is shown, Figure 4.11 depicts a comparable relationship between longitudinal tilt and ambient temperature. According to this figure, when the daily temperature rises, north and south abutment tiltmeters tilt towards north and south, respectively, which indicates that the bridge is expanding. They reach their highest tilt around 5 to 7 PM every day, when the temperature is at its highest.

However, when the daily temperature starts to drop, north and south abutment tiltmeters begin to rotate towards the south and north, respectively. During a temperature drop, these tiltmeters reach their maximum inward rotation implying that the bridge is contracting. These patterns repeat every day.

4.4 Inclinometer Measurements

During the construction phase, the research team measured deflection of each inclinometer when it was possible, and the team had access to the top of the casings. Following the completion of the construction, all inclinometer deflections were recorded in every visit. As mentioned previously, the research team decided to set the digital probe in a way that its A^+ direction always faces the bridge in order to maintain consistency with our inclinometer readings.

As a result, the B^+ direction for the south abutment faces East, while that for the north abutment faces West. Additionally, each hole has been named based on its location, so it is easier to differentiate them. NE, NW, SE and SW stand for North East, North West, South East, and South West, respectively. These orientations and locations are shown in Figure 4.12.

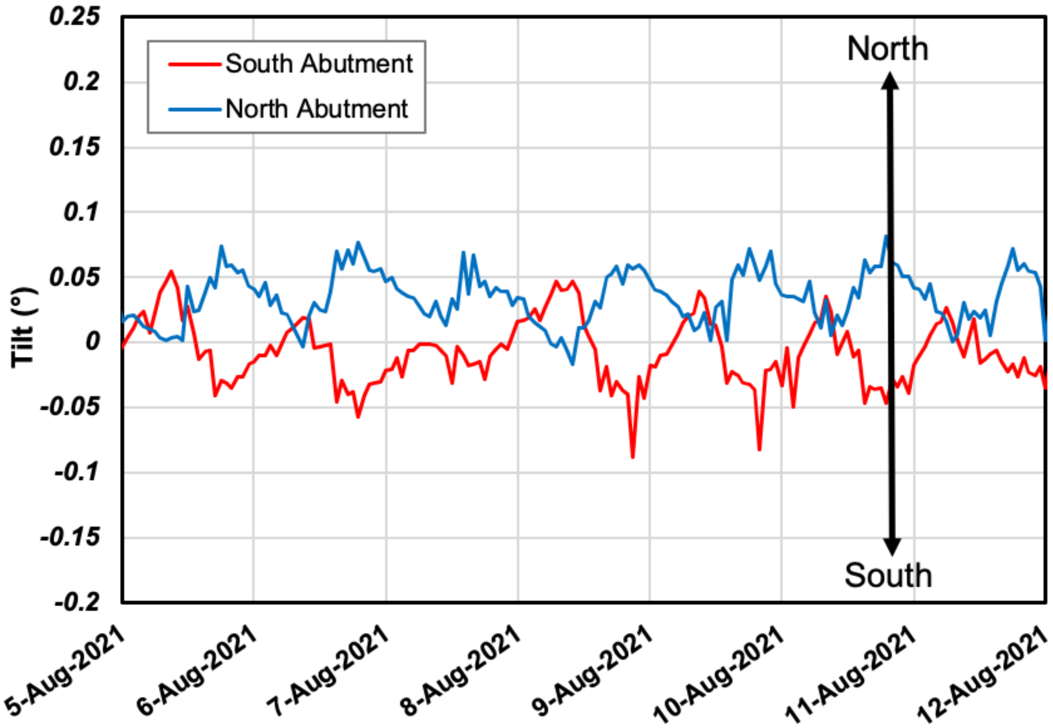

(a) weekly tiltmeter data from the north abutment

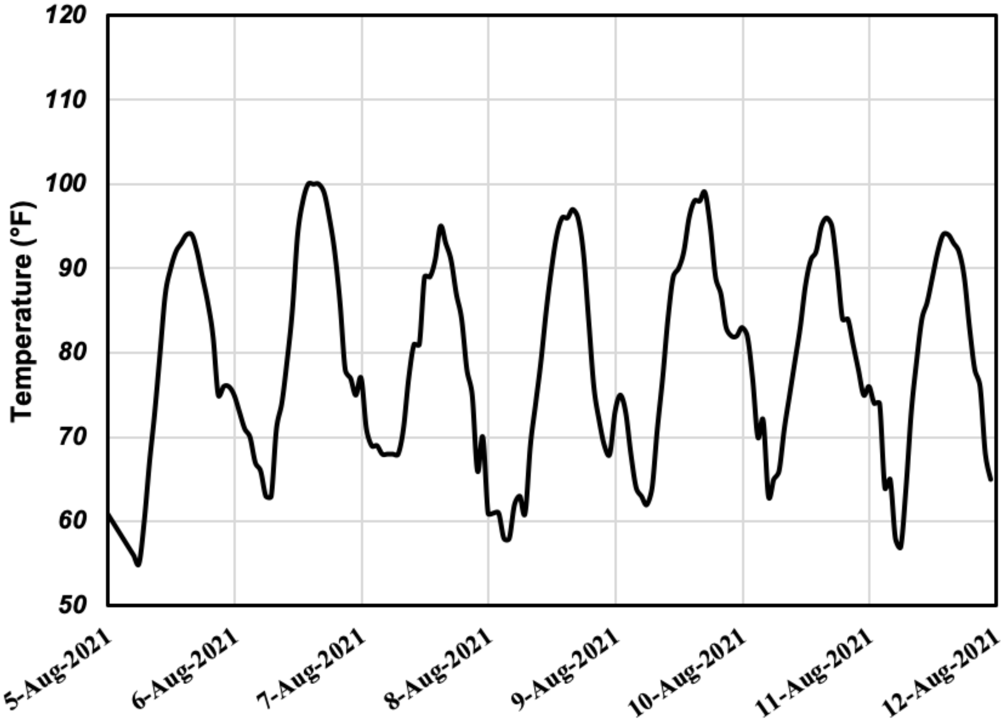

(b) ambient temperature of week when data was collected

Figure 4.11: Cyclic Behavior of the Tiltmeter Measurements

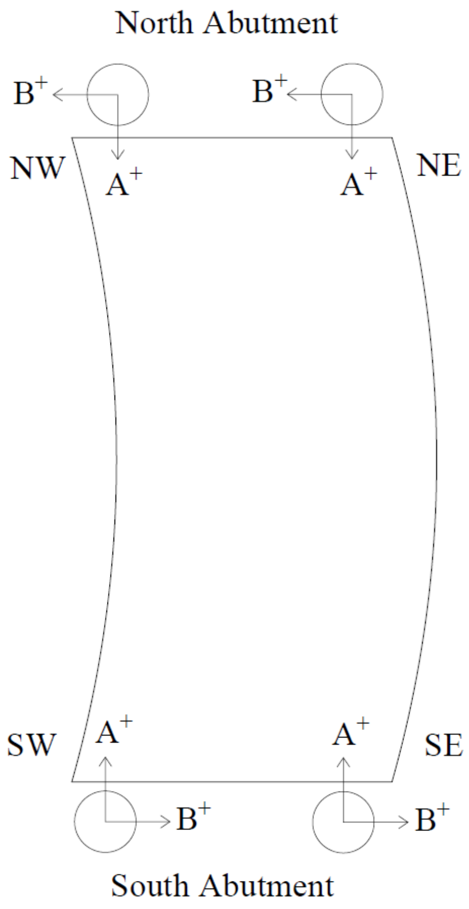

Figure 4.12: Indication of A and B Directions for Each Inclinometer

Therefore, if the longitudinal profile shape or deflection of an inclinometer is positive, it indicates that the bridge is moving inward, but if it is negative, it indicates that the bridge is expanding. However, if one looks at the B direction, which is perpendicular to the A direction, the positive B direction for the south abutment is towards the east, while the positive B direction for the north abutment is towards the west. The final length of each inclinometer casing is given in Table 3.1. As mentioned in the previous chapter, since the digital probe has a length of 4 ft, when we make measurements for the top 4 ft of the casing, the probe begins to come out of the casing, and we can no longer rely on those readings. For that reason, the last reading for each inclinometer is at 4 ft below the surface. So far, there have been 11 readings of each inclinometer, 9 of which were made after the casings were cut to their final height. These readings were taken on the dates listed in Table 4.2.

Table 4.2: Inclinometer Measurement Dates

Reading No.	Date
1	Unknown
2	May 20, 2020
3	August 28, 2020
4	March 5, 2021
5	April 23, 2021
6	May 20, 2021
7	June 17, 2021
8	August 13, 2021
9	August 31, 2021
10	November 17, 2021
11	April 8, 2022

Figures 4.13 to 4.20 illustrate the longitudinal and lateral profiles of each inclinometer reading. In addition, all graphs have been stretched (zoomed in) to make the differences between the results easier to see. Finally, after each graph, there is another graph that zooms in on the top part of the previous graph in order to magnify the behavior of the casings at different points in time. These graphs show the profile of the casing, not the deflection. Accordingly, the horizontal axis does not indicate how much the casing deflected. It only shows the shape of the casing rather than the true value. It is important to choose a benchmark for these profile graphs, and then compare every new reading to that benchmark to see how much the casing deflected. Although there are 11 available readings, the first two readings were made before the casings

were fully extended. Furthermore, the first three readings were measured by different crew, resulting in inconsistent readings, and for this reason, the research team decided to discard these readings and use the fourth reading (March 5, 2021) as the benchmark. Figures 4.13 to 4.14 display the longitudinal and lateral profiles of the north–east inclinometer casing. Our expectation is that the bridge will move longitudinally based on the ambient temperature. If it is warm outside, the bridge will expand; during cold weather, it will contract. However, this pattern does not hold for the longitudinal behavior of the north–east inclinometer. As an example, moving from March 2021 to April 2021 or May 2021 to June 2021 results in an inward movement rather than outward, which was not anticipated. North–east inclinometer lateral movements are very close for all the recordings, and similar to the longitudinal movement, they do not follow a clear pattern with temperature. North–west inclinometer readings are shown in Figures 4.15 to 4.16. According to Figure 4.15, as the temperature goes up, the bridge expands, and as it goes down, it contracts. Similar to the north–east inclinometer lateral reading, this inclinometer's lateral movement also appears to exhibit extremely small deformation with no general pattern. For the south–east readings that are shown in Figures 4.17 to 4.18, both longitudinal and lateral movements appear to follow a pattern based on the ambient temperature. For the longitudinal movement, as is expected, the longitudinal movement of the bridge in warm seasons is inward while it moves outward in cold seasons. In contrast to the north abutment's inclinometers lateral movement, which showed no pattern, the south–east inclinometer lateral movement moves towards the west when temperature rises and to the east as temperature decreases. In summary, inclinometer readings show small strain and elastic behavior of back fill materials for abutments.

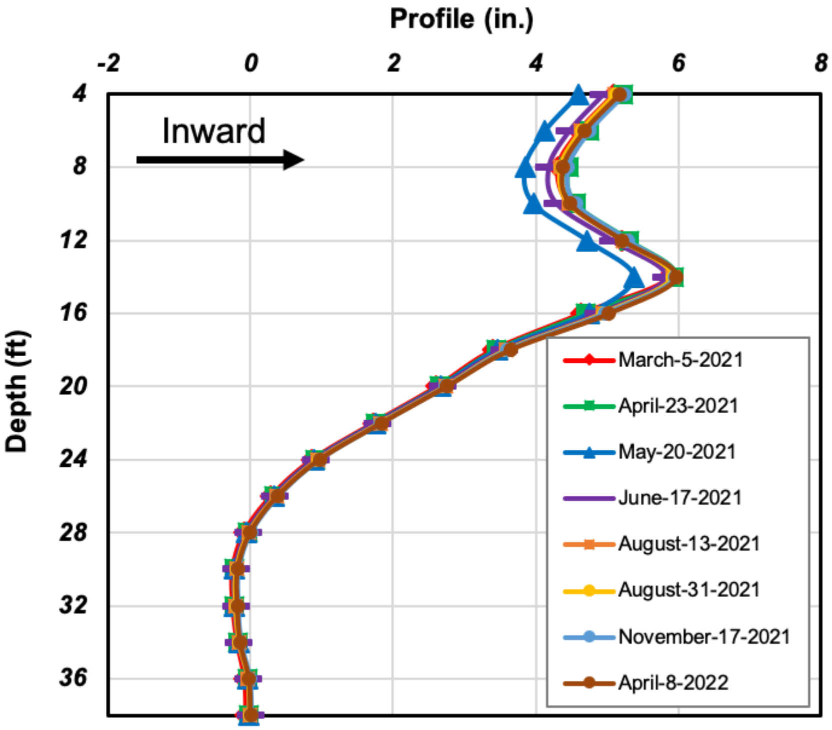

(a) general view

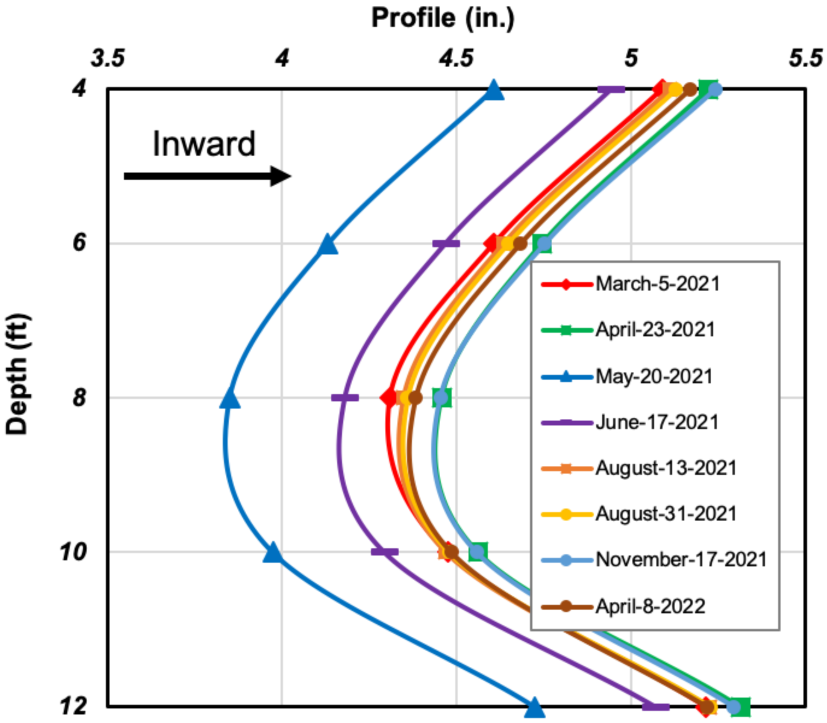

(b) zoomed in view

Figure 4.13: Longitudinal Profile of the North-East Inclinometer

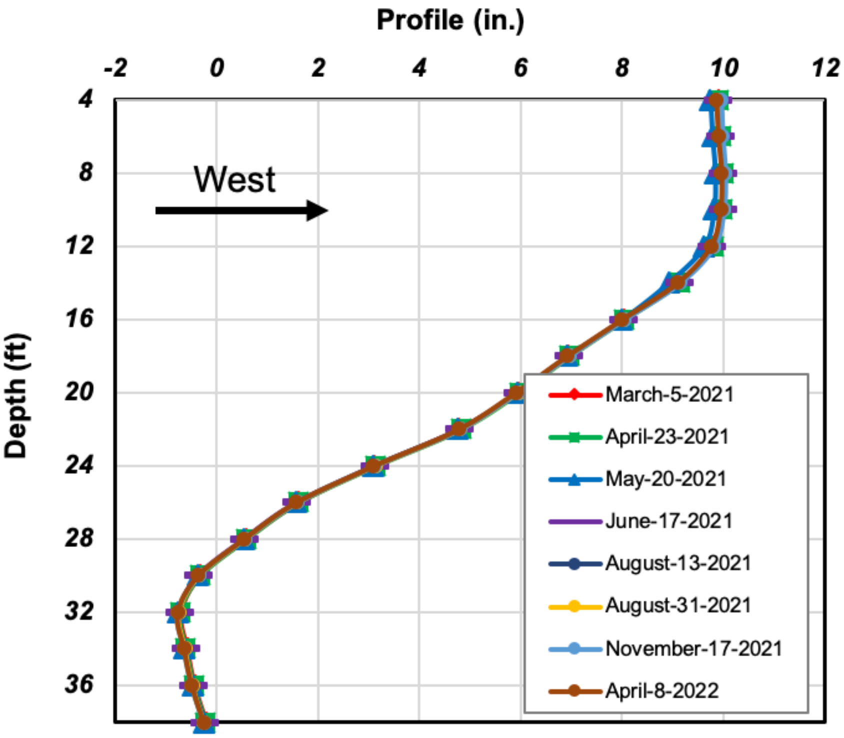

(a) general view

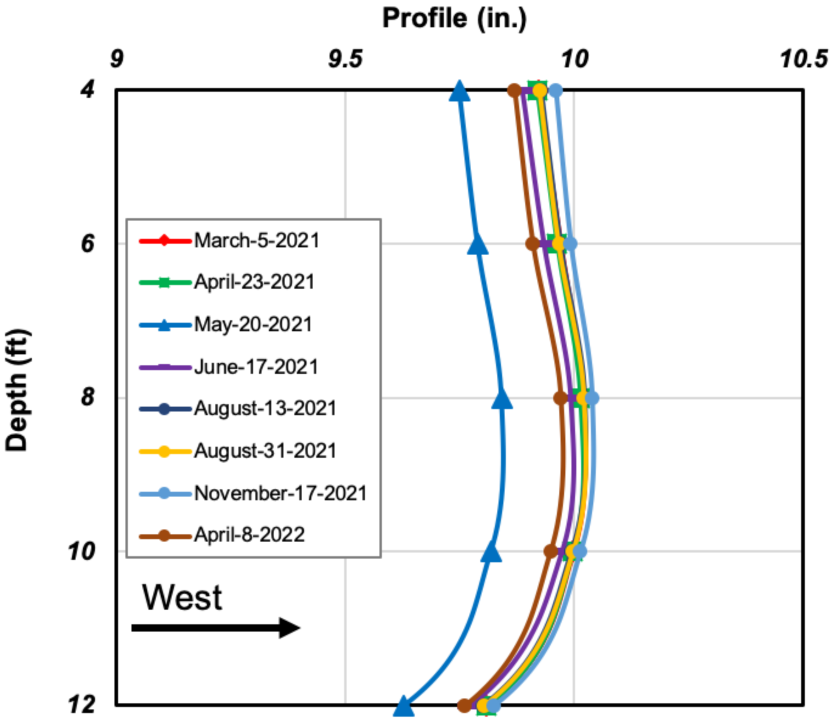

(b) zoomed in view

Figure 4.14: Lateral Profile of the North-East Inclinometer

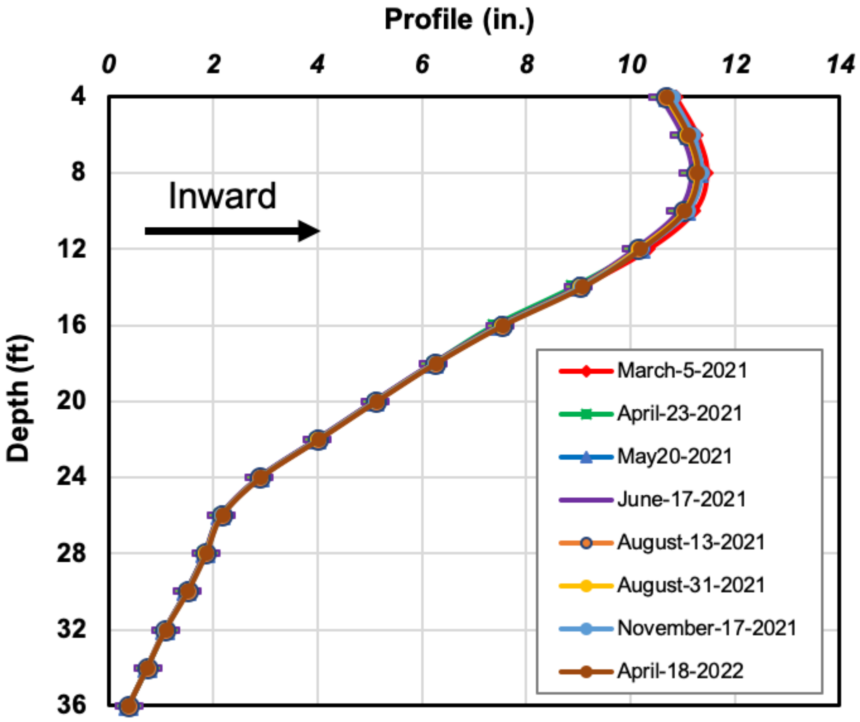

(a) general view

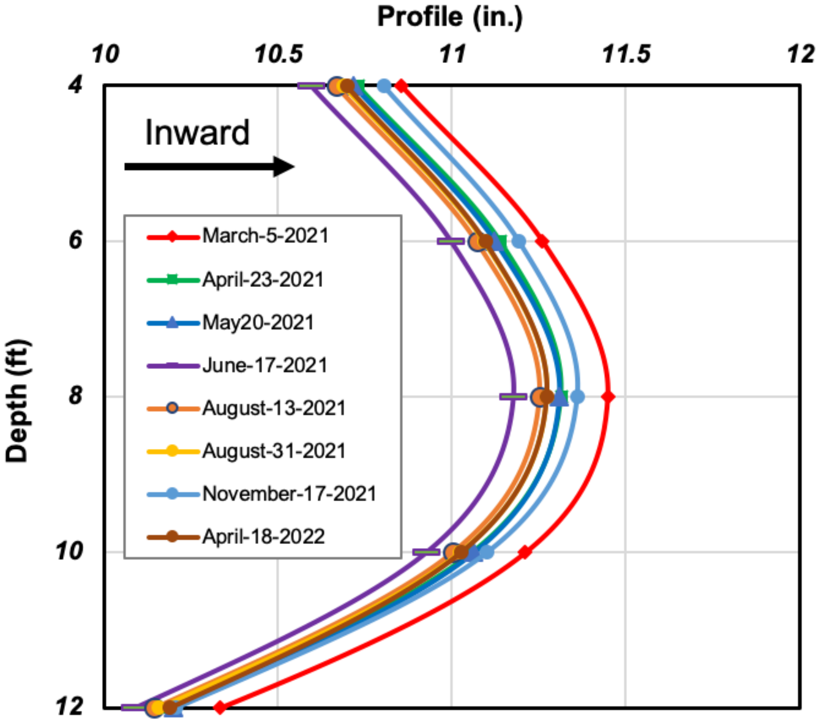

(b) zoomed in view

Figure 4.15: Longitudinal Profile of the North-West Inclinometer

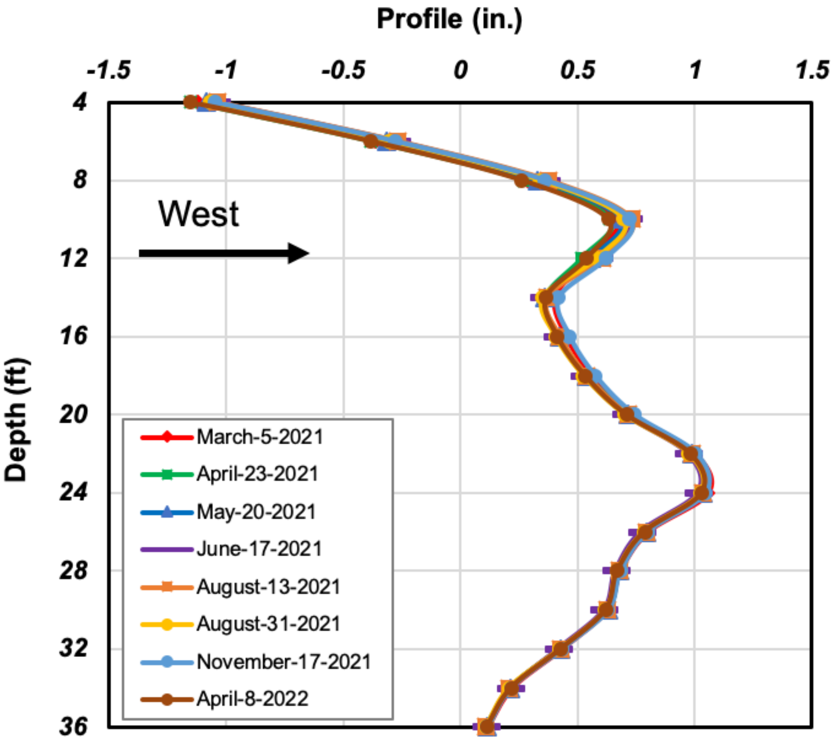

(a) general view

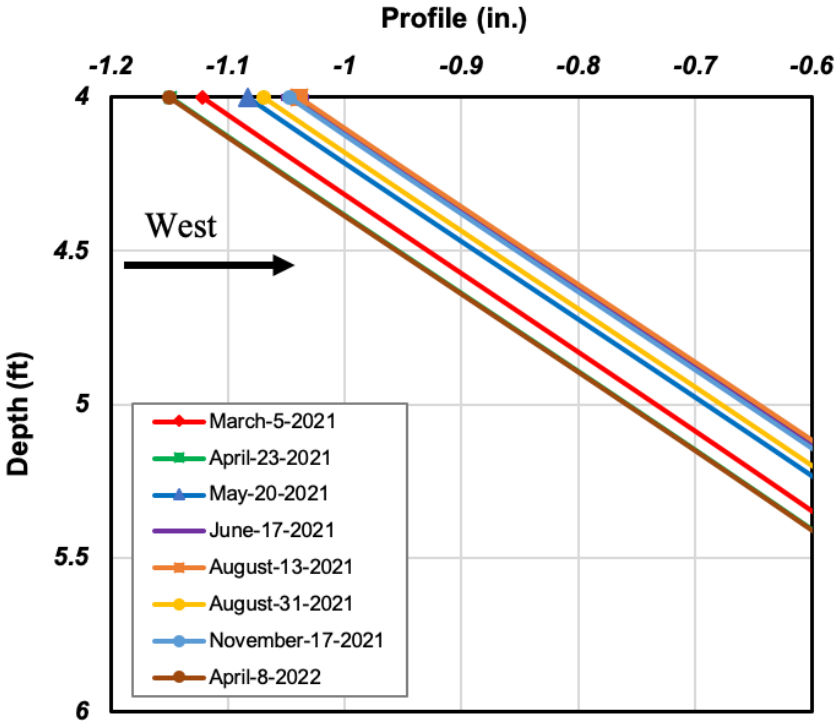

(b) zoomed in view

Figure 4.16: Lateral Profile of the North-West Inclinometer

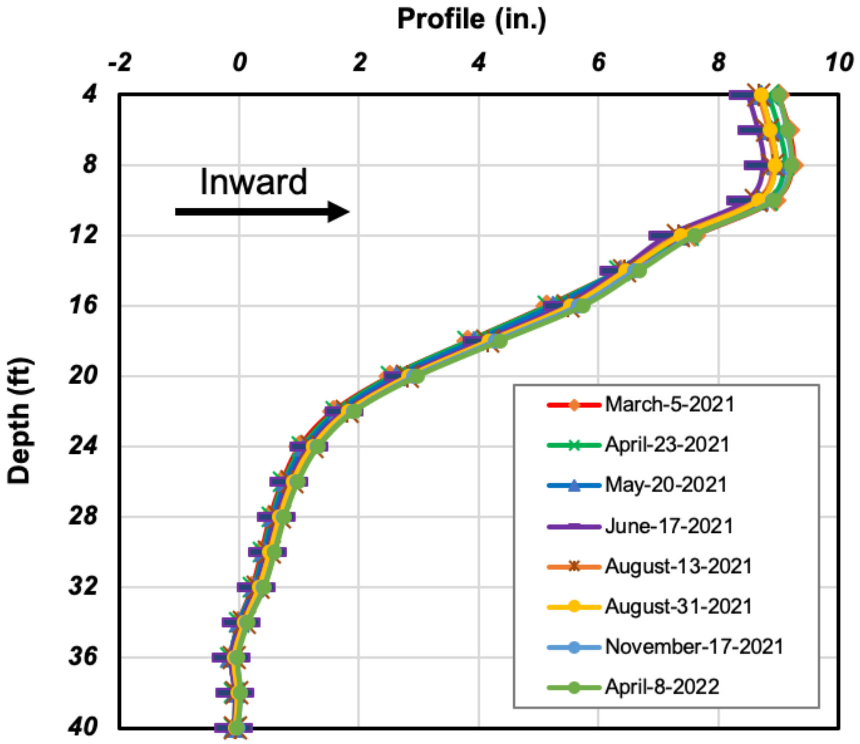

(a) general view

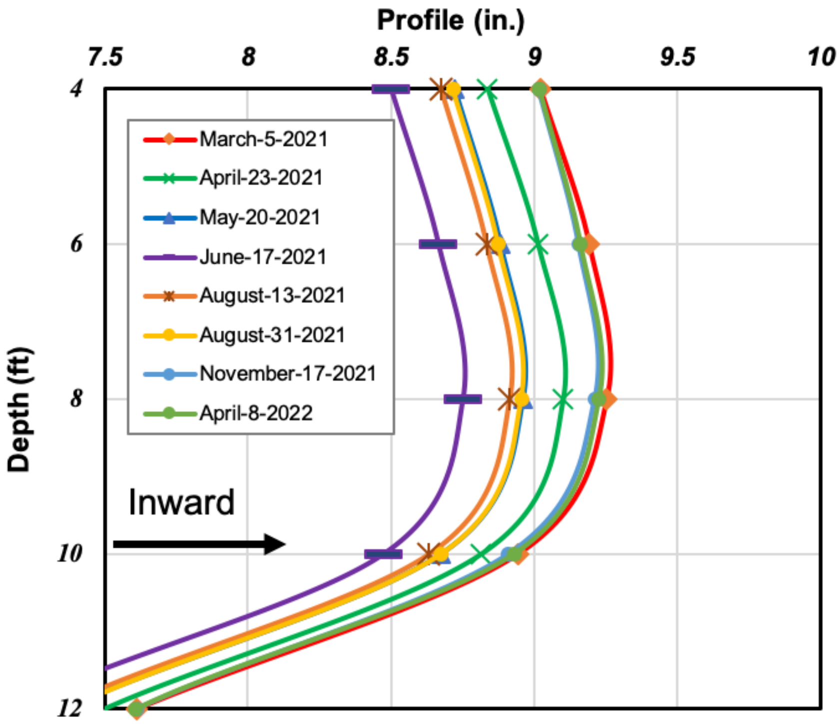

(b) zoomed in view

Figure 4.17: Longitudinal Profile of the South-East Inclinometer

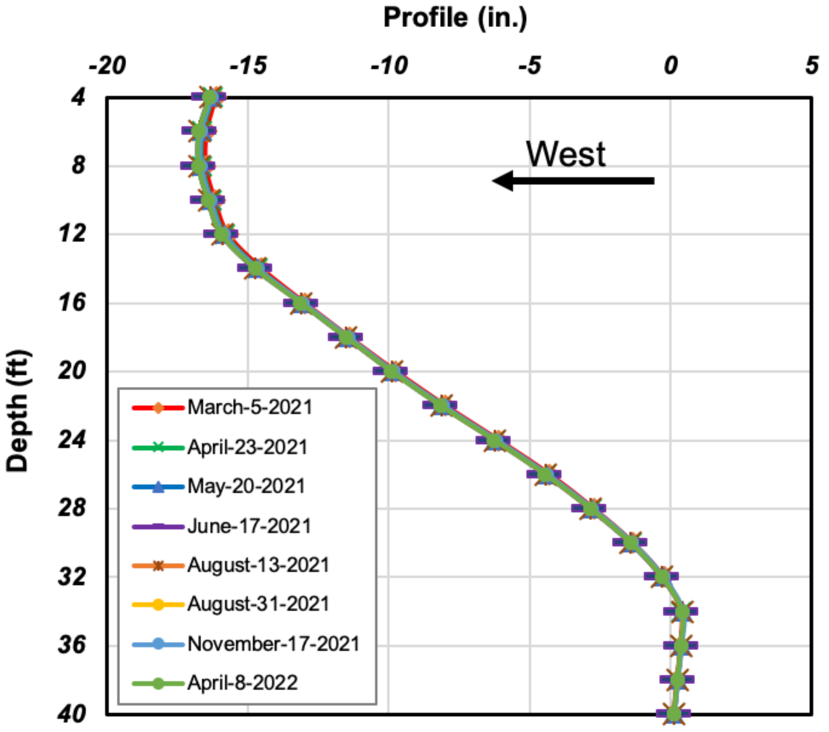

(a) general view

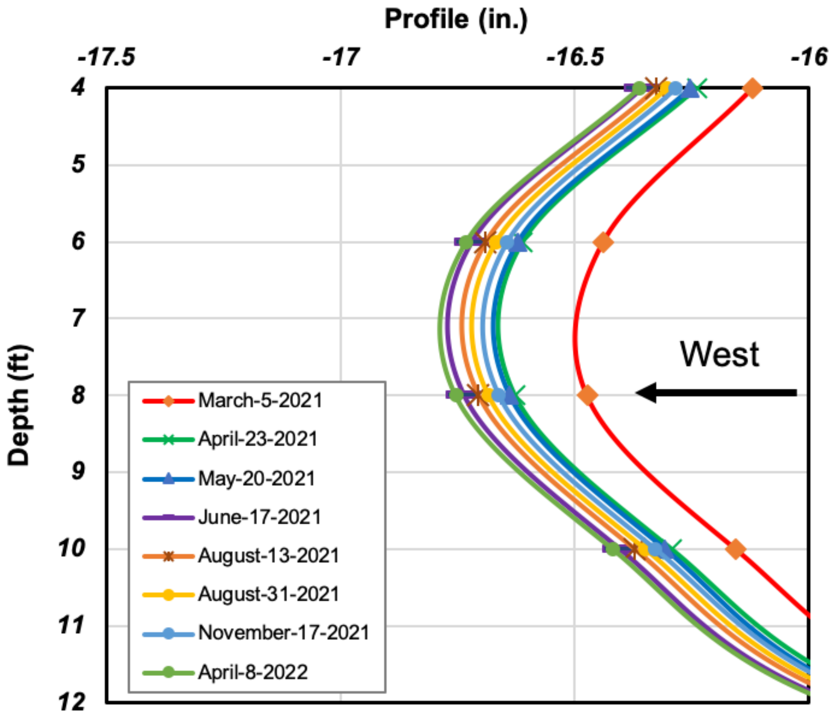

(b) zoomed in view

Figure 4.18: Lateral Profile of the South-East Inclinometer

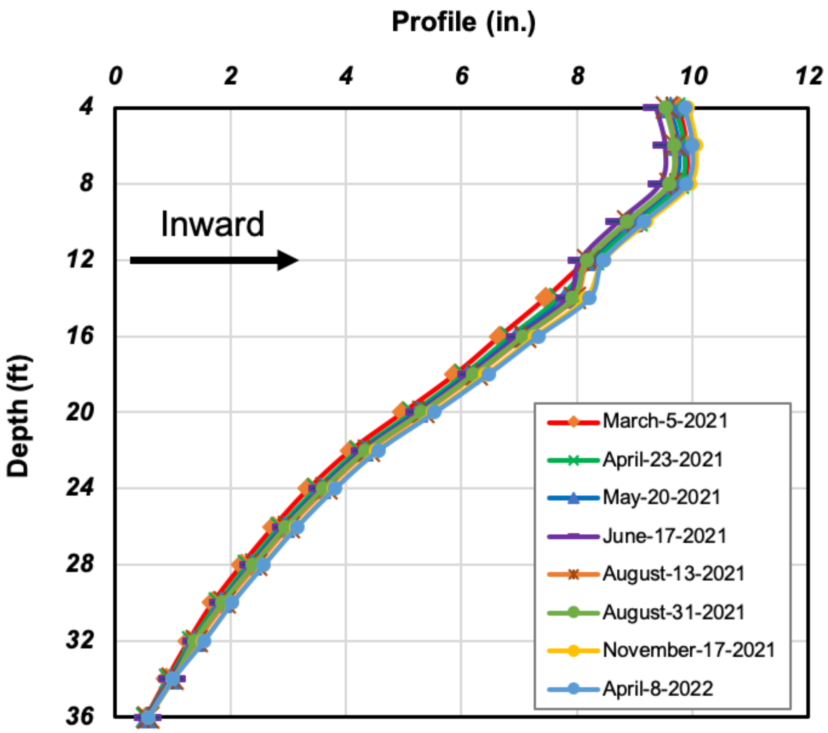

(a) general view

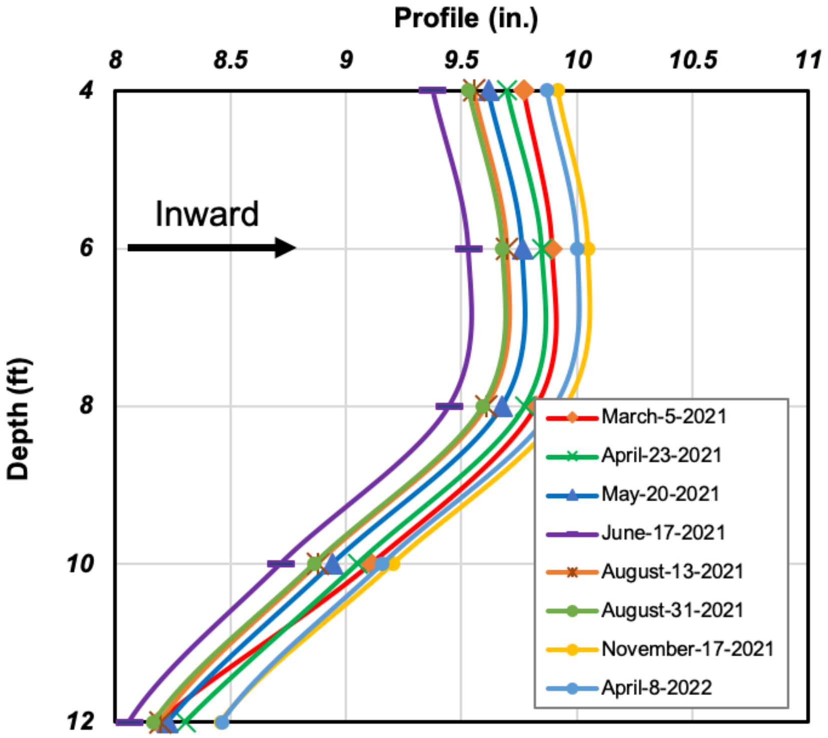

(b) zoomed in view

Figure 4.19: Longitudinal Profile of the South-West Inclinometer

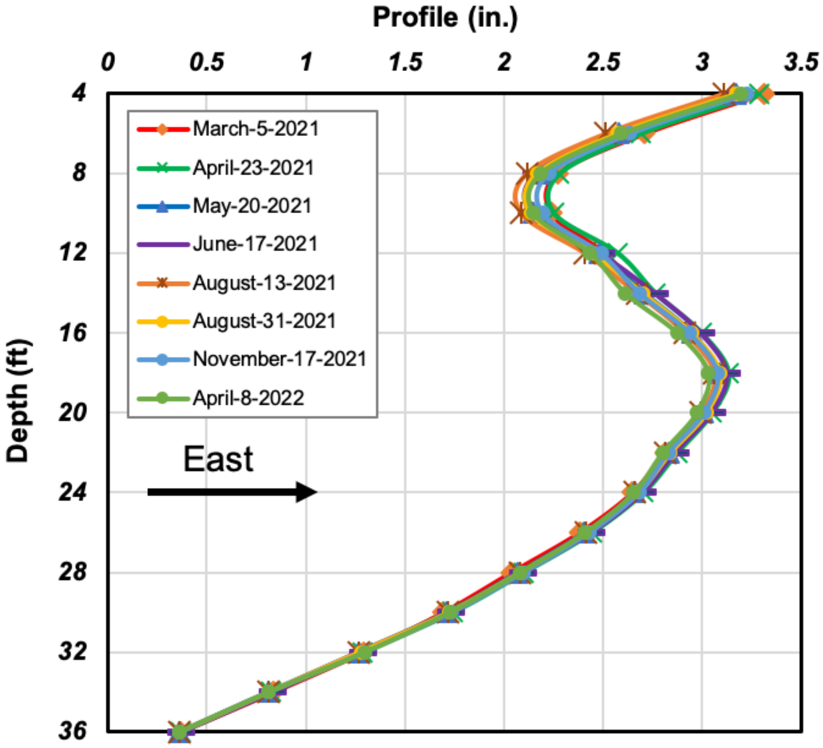

(a) general view

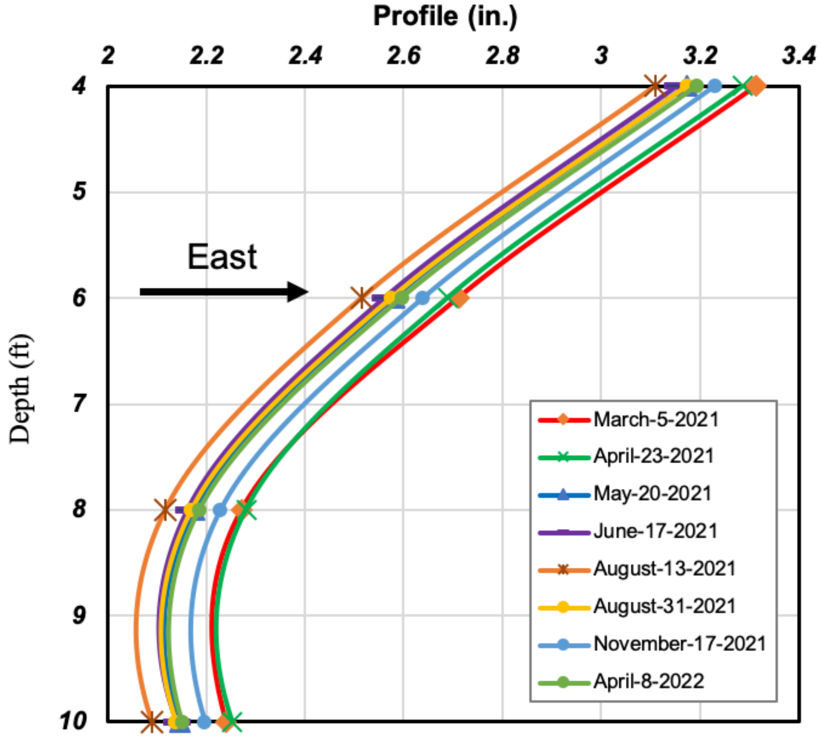

(b) zoomed in view

Figure 4.20: Lateral Profile of the South-West Inclinometer

Finally, the south–west inclinometer movements are similar to those of the south–east inclinometer, meaning that as temperature increases, the bridge expands longitudinally and moves to the west laterally. Figures 4.21 to 4.28 show the deflection of each inclinometer casing. As previously mentioned, the reading on March 5, 2021, served as a benchmark for all subsequent readings. In general, these deflections follow the same trend as their profiles, but here we can see how much each casing deflects. As shown in Figures 4.21 and 4.22, there is an anomaly in the longitudinal and lateral deflections of the May 20, 2021, reading for the north–east inclinometer, since it does not follow the temperature as stated for its profile. In just over a month (April to May 2021), there is a movement of nearly 0.6 inches, which is much higher than other readings. This amount of deflection should not be caused by bridge deformation since it is even higher than the measurement made in June and August 2021. There is a possibility that there were some movements in the backfill that cannot be explained by displacement in the superstructure for this inclinometer. Lateral deflection also has the same problem, where the May 2021 reading differs from other readings. Additionally, other readings are extremely small and are limited to less than 0.05 inches while the May 2021 reading reaches up to 0.2 inches. Figures 4.23 and 4.24 show north–west inclinometer readings. This casing longitudinally expands and contracts with changes in ambient temperature. In June 2021, it experienced the largest longitudinal displacement of around 0.28 inches in the backfill. The lateral movement of this inclinometer, however, does not appear to follow a clear pattern and is limited to 0.1 inches. Figure 4.25 displays a clear pattern of longitudinal deflection of the south–east inclinometer where it experiences a peak outward movement of 0.52 inches in June 2021.

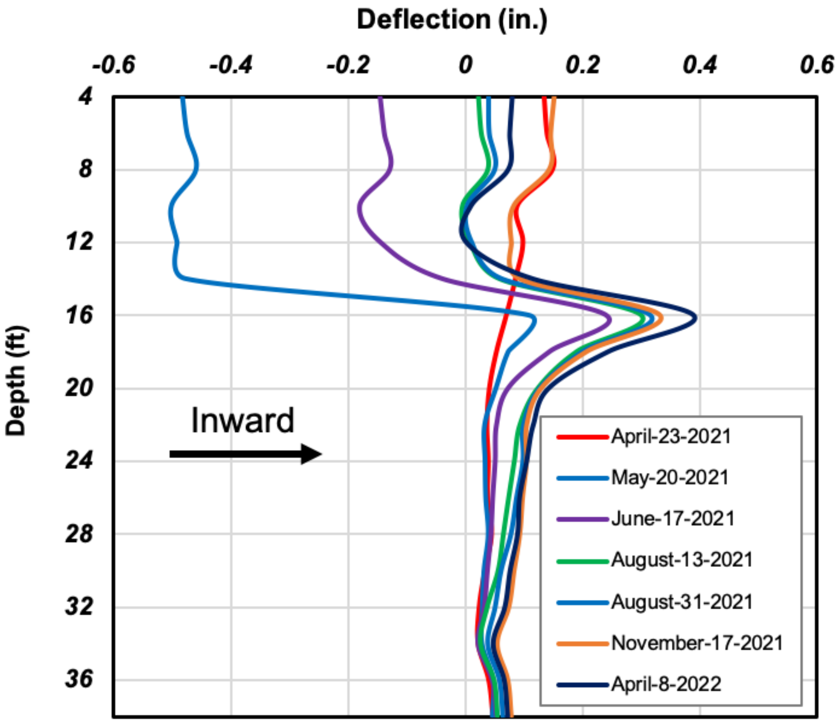

(a) general view

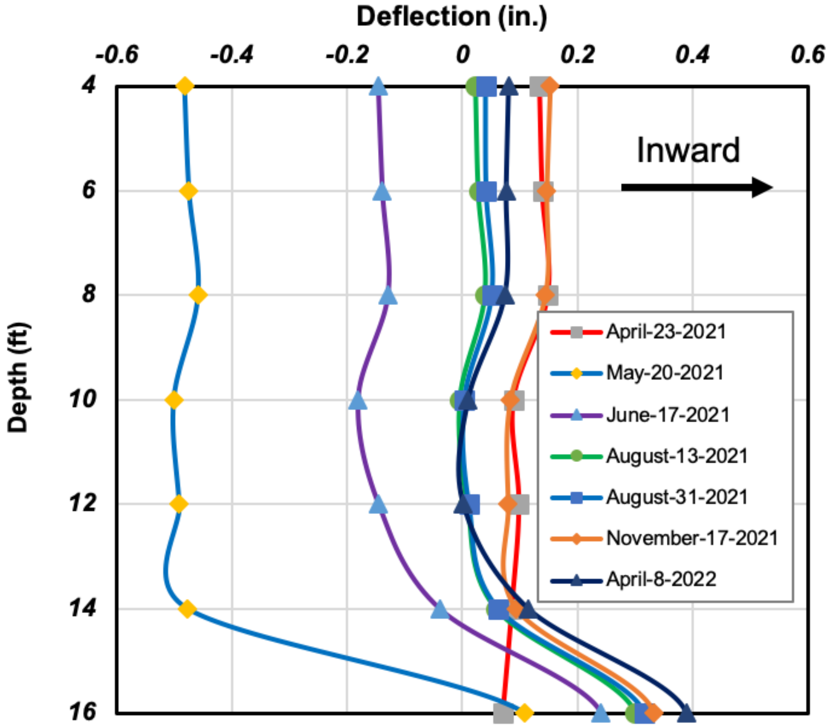

(b) zoomed in view

Figure 4.21: Longitudinal Deflection of the North-East inclinometer

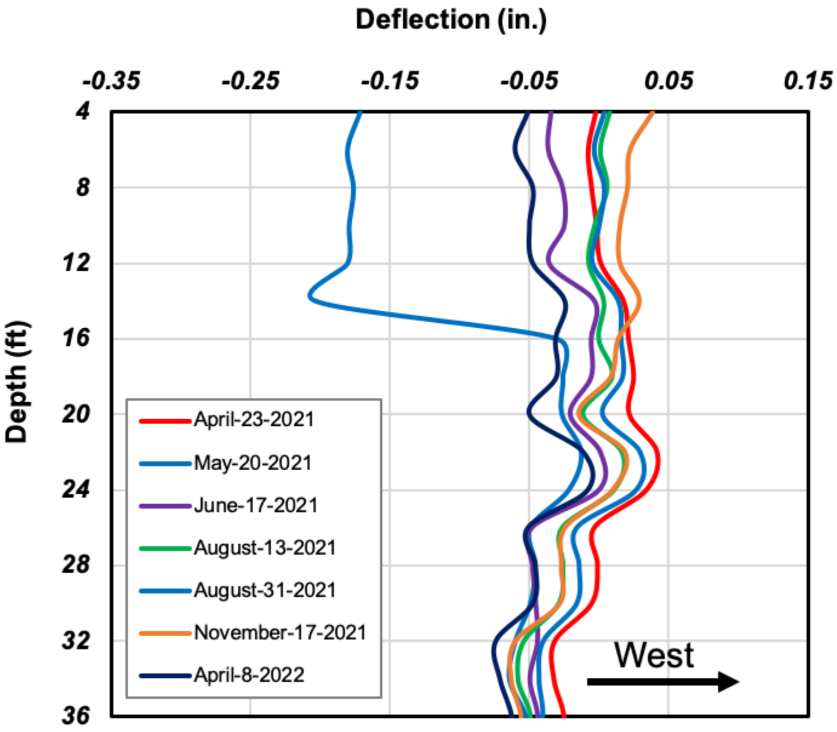

(a) general view

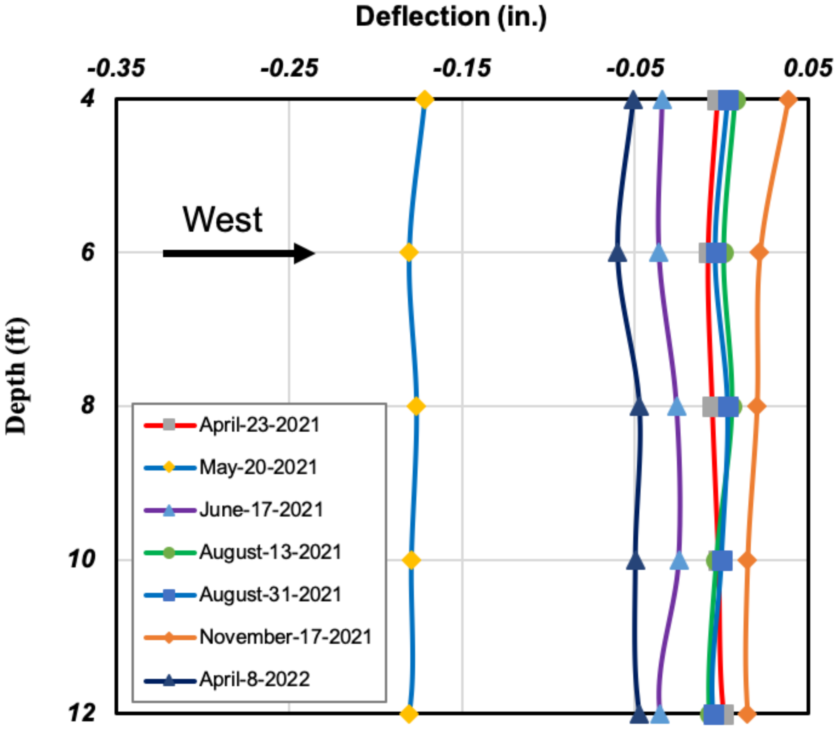

(b) zoomed in view

Figure 4.22: Lateral Deflection of the North-East Inclinometer

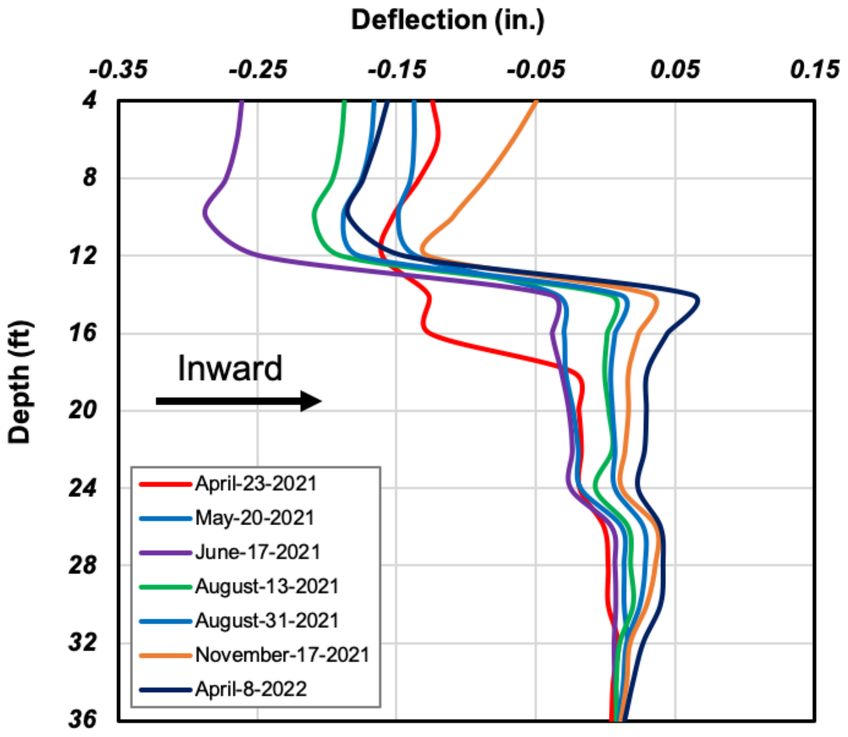

(a) general view

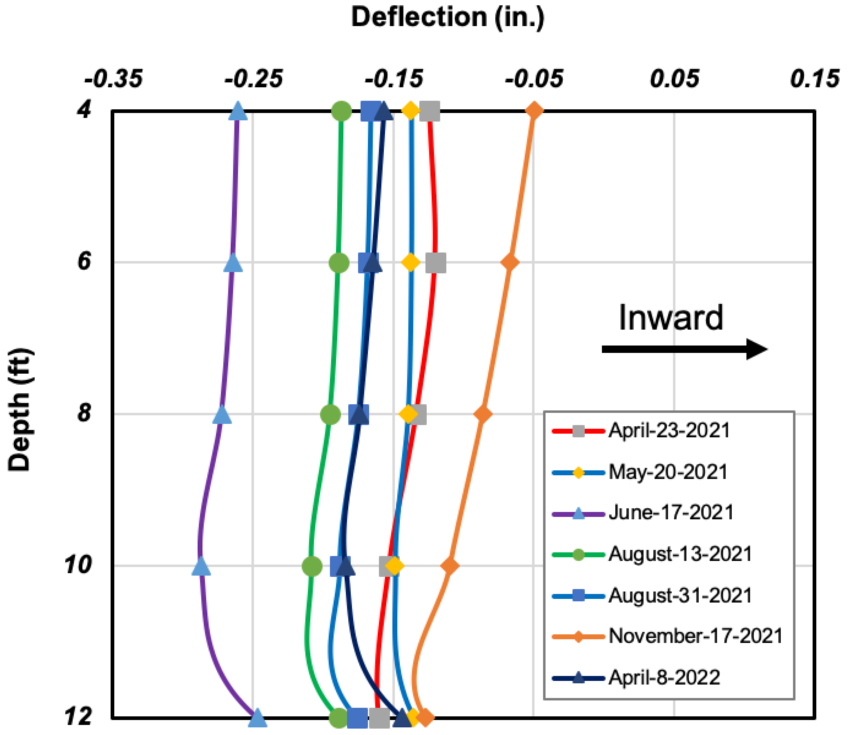

(b) zoomed in view

Figure 4.23: Longitudinal Deflection of the North-West Inclinometer

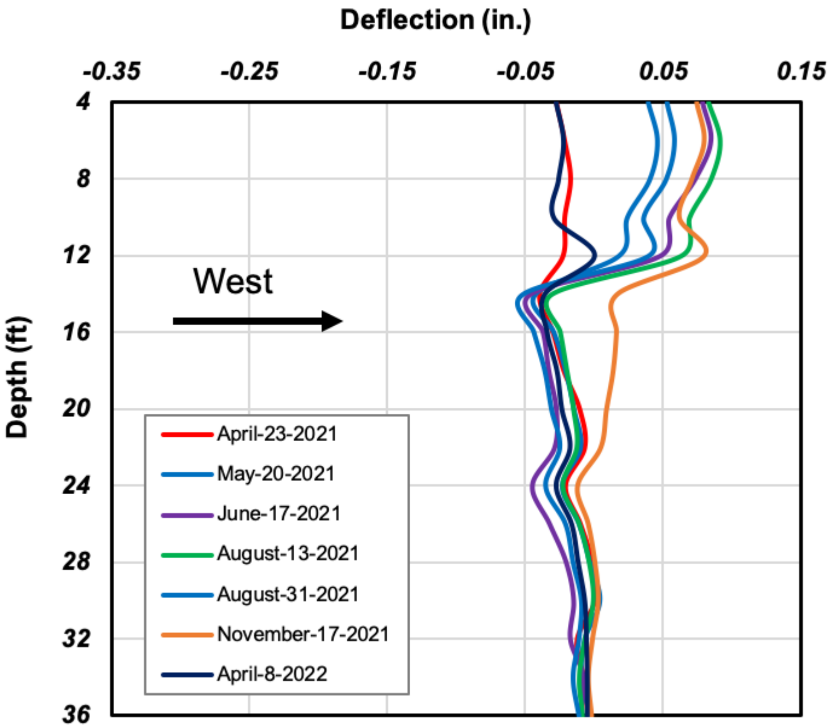

(a) general view

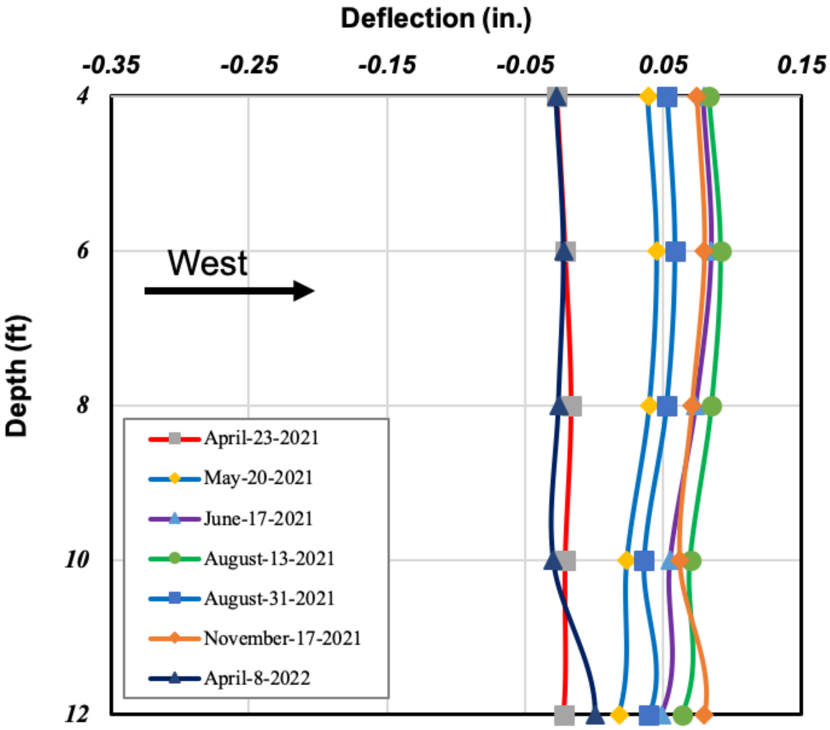

(b) zoomed in view

Figure 4.24: Lateral Deflection of the North-West Inclinometer

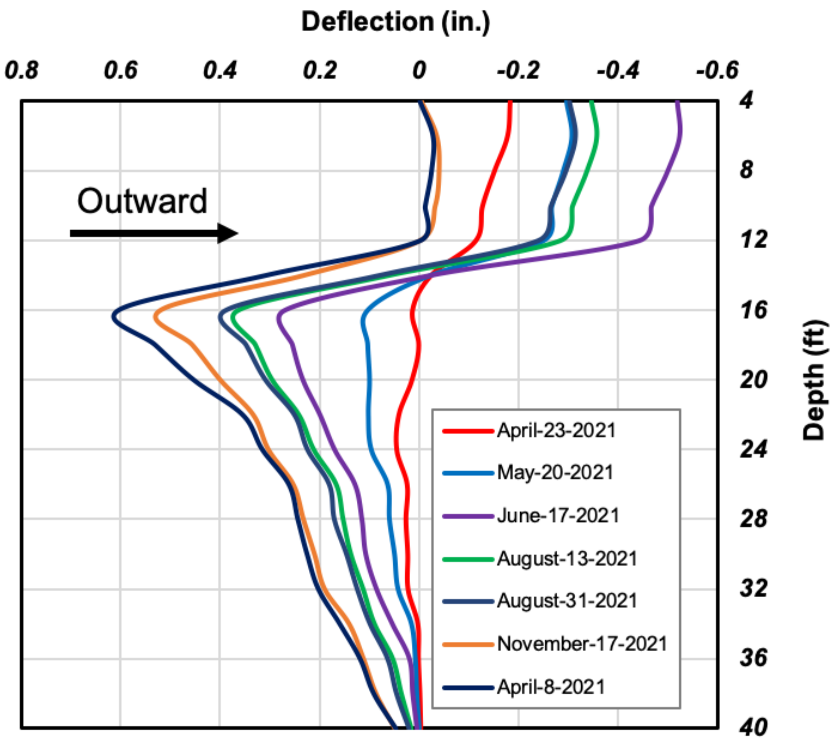

(a) general view

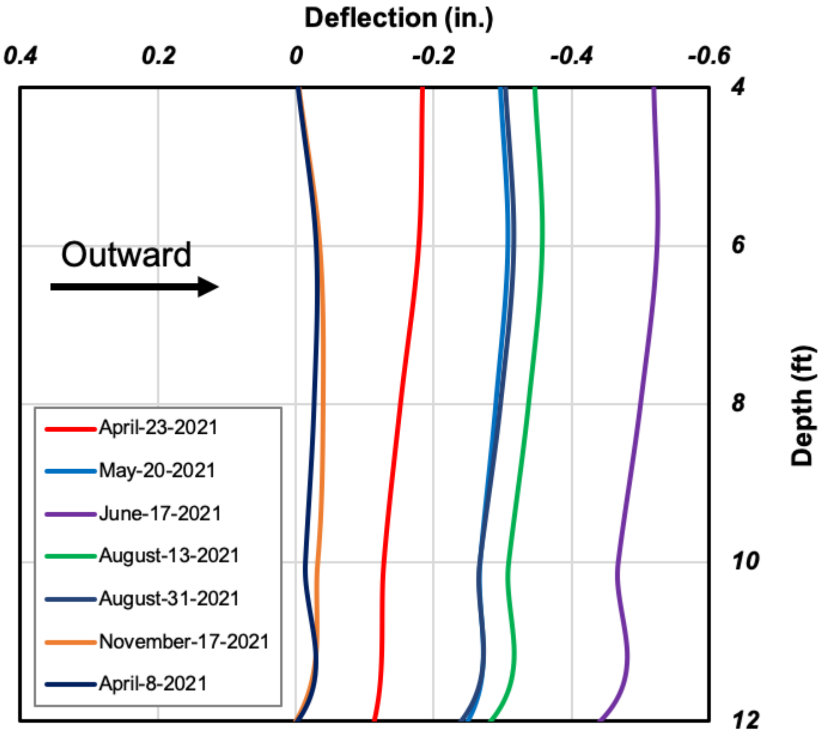

(b) zoomed in view

Figure 4.25: Longitudinal Deflection of the South-East Inclinometer

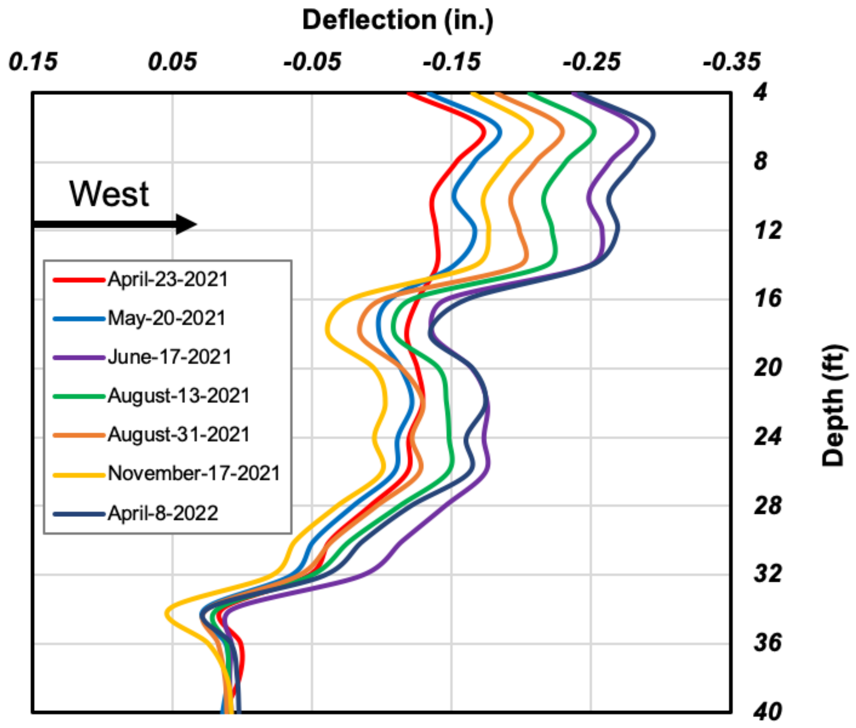

(a) general view

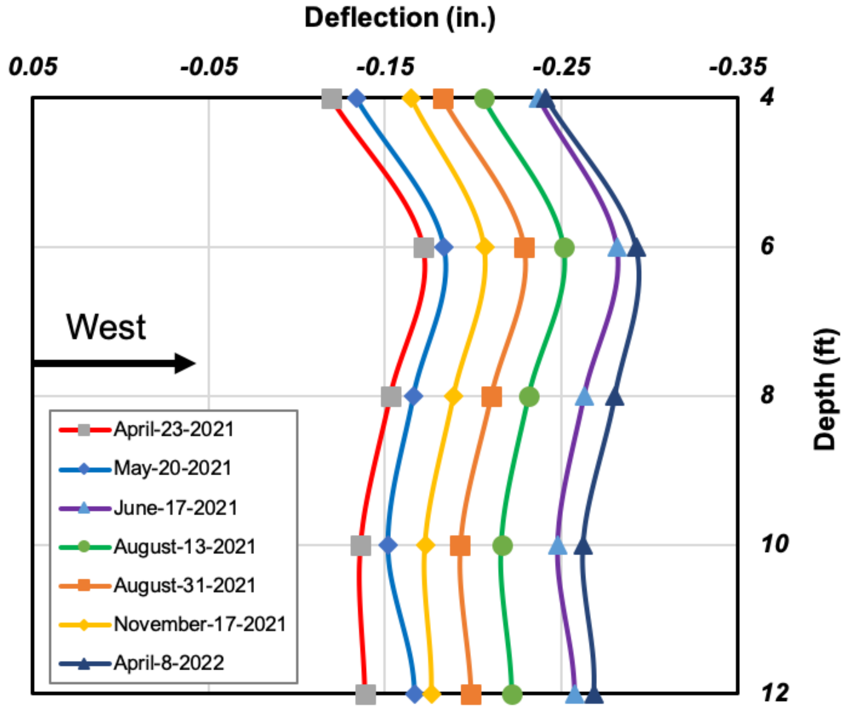

(b) zoomed in view

Figure 4.26: Lateral Deflection of the South-East Inclinometer

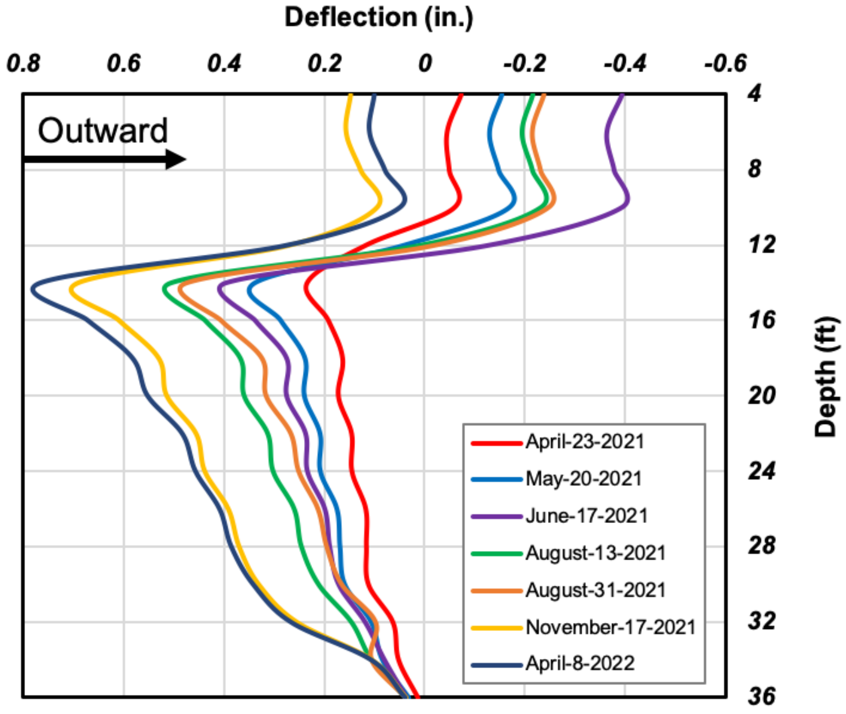

(a) general view

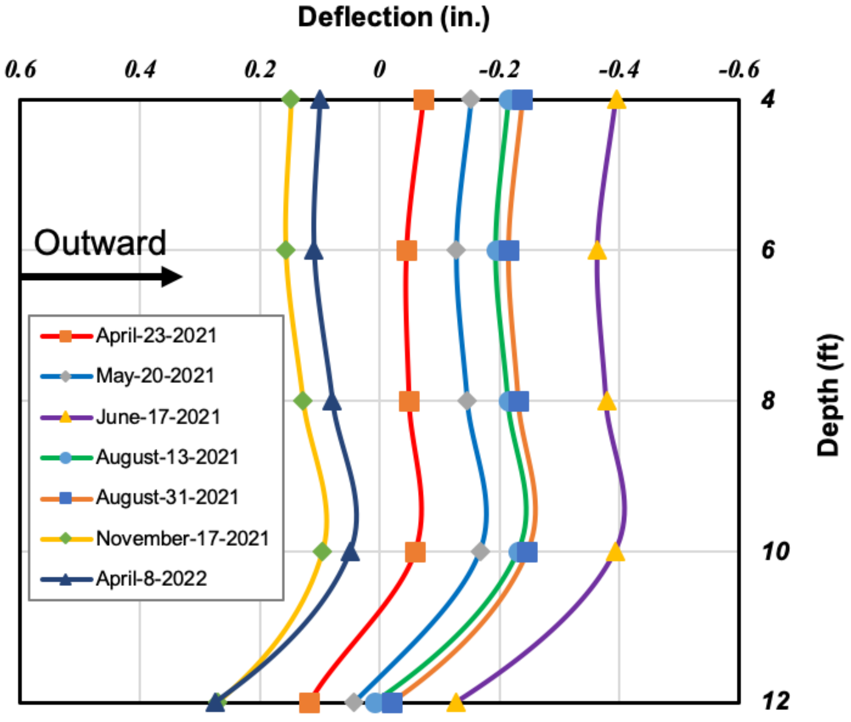

(b) zoomed in view

Figure 4.27: Longitudinal Deflection of the South-West Inclinometer

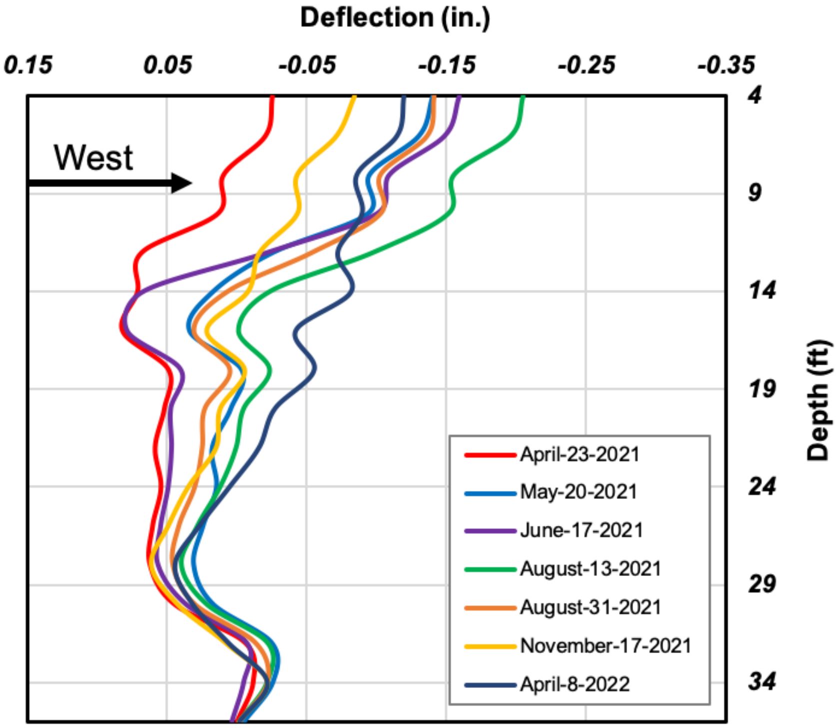

(a) general view

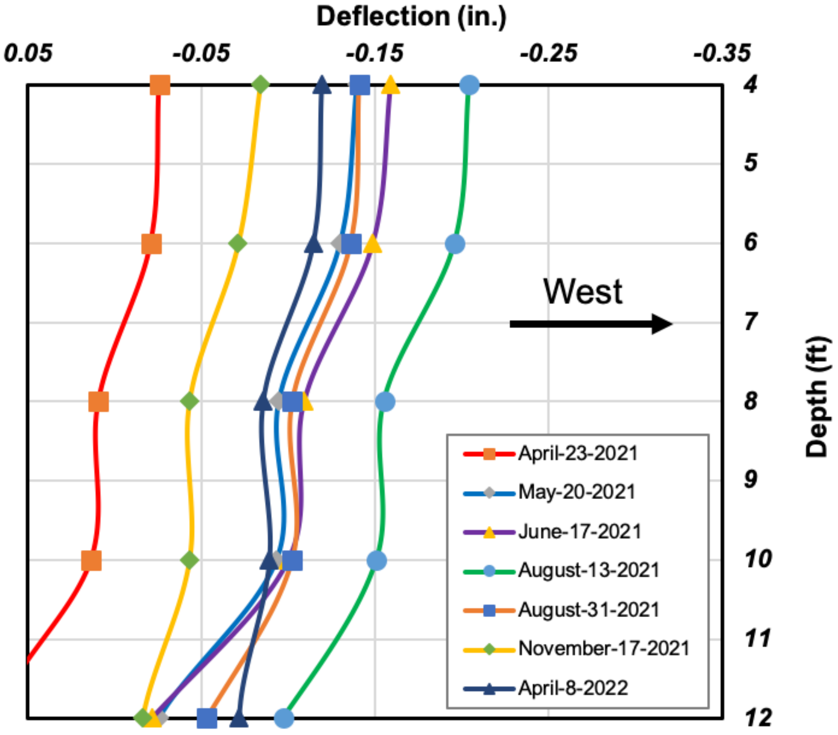

(b) zoomed in view

Figure 4.28: Lateral Deflection of the South-West Inclinometer

Lateral movement which is shown in Figure 4.26 is always to the west, and it can reach 0.3 inches. Finally, the deflections of the south–west inclinometer are shown in Figures 4.25 and 4.26. Similar to the north–east inclinometer, it deflects inward and outward as expected. The maximum outward longitudinal deflection happens in May 2021 where the casing deflects about 0.4 inches. Its lateral deflection is mostly towards west where it reaches its peak of 0.2 inches on August 31, 2021.

Figures 4.29 and 4.30 depict the longitudinal and lateral deflections of the top of each inclinometer (at the depth of 4 feet) over different dates so that we can better understand and compare their behavior. It is obvious from Figure 4.29 that the north–east inclinometer excessively deflected from April to May 2021, as mentioned earlier. In addition, there was a drop from May to June 2021 which is inconsistent with those of other inclinometers.

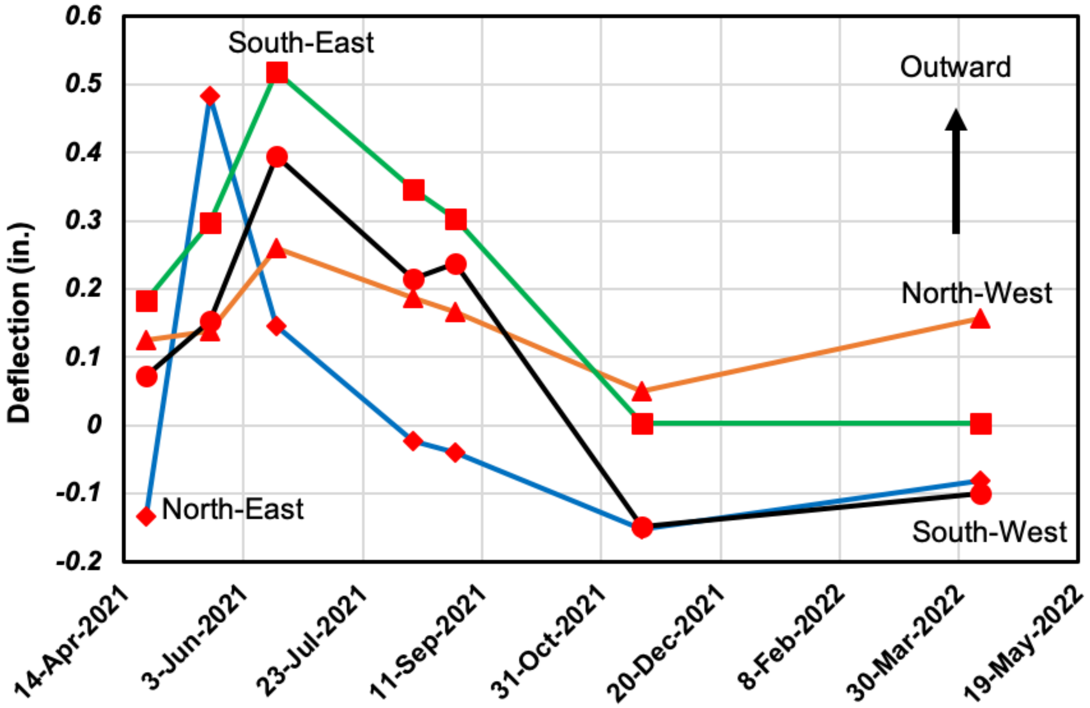

Figure 4.29: Longitudinal Deflection of the Top Inclinometer Readings (4 ft from top)

The south–west inclinometer also shows a higher deflection on August 31, 2021, as compared to August 13, 2021. This is contrary to other inclinometer readings for the same dates. Additionally, the most recent deflection reading of the south–east inclinometer, which was taken in April 2022, remains inward. However, it differs from the behavior of other inclinometers whose last inward deflection reading was in November 2021.

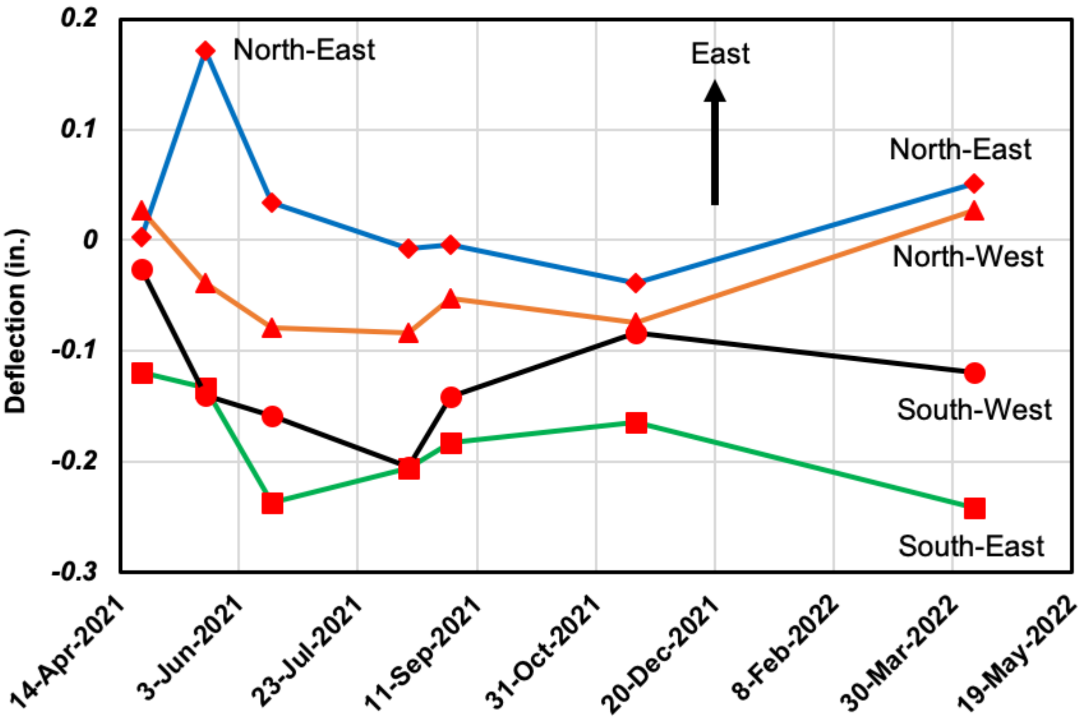

Figure 4.30: Lateral Deflection of the Top Inclinometer Readings (4 ft from top)

Figure 4.30 shows the lateral deflection of the top reading of all inclinometers. It appears that north abutment inclinometers, north–east and north–west, behave very similarly. The lateral deflection is towards the west.

4.5 Moisture Sensor

Two moisture sensors were initially installed behind each abutment at different depths, but one of the sensors behind the south abutment was lost during installation. Despite this, none of the sensors were functioning properly until we realized there was an issue with their batteries. At the end of May 2021, these batteries were replaced, and sensors began to work again.

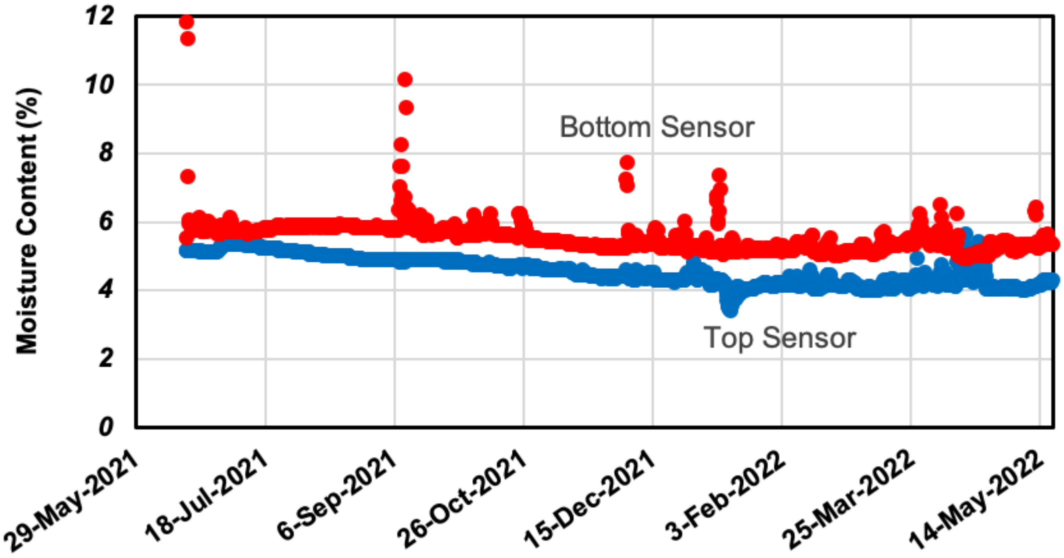

(a) north abutment

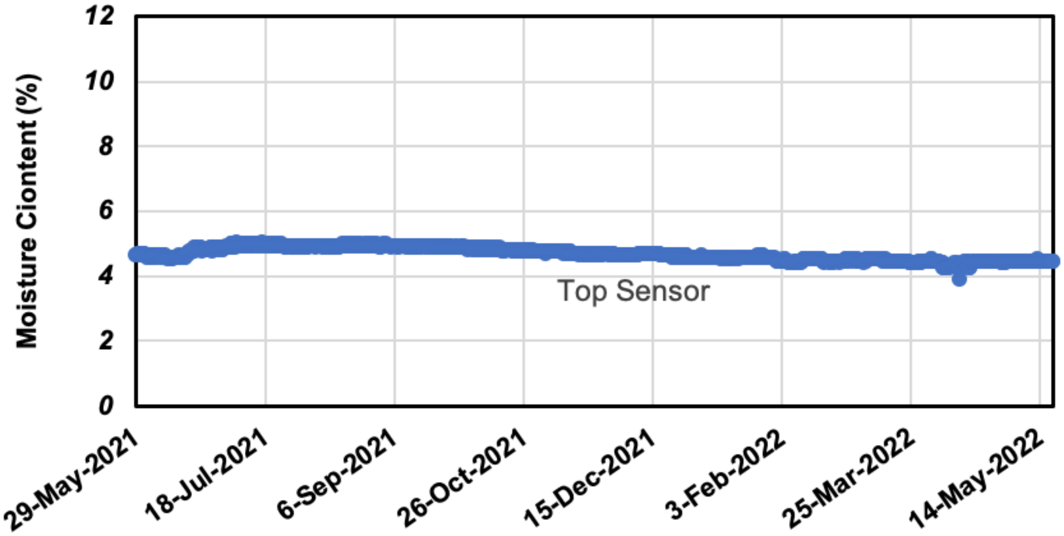

(b) south abutment

Figure 4.31: Moisture Content

Figure 4.31 displays the backfill moisture content behind both abutments. According to this figure, both sides have similar moisture contents on average. It seems that some data points in the bottom sensor of the north abutment are outliers. There have been incidents where moisture content data has jumped dramatically, ranging from 8% to 12% which is significantly higher than the rest of the data. This behavior may indicate the fill materials were temporarily saturated or in high moisture content condition, but the water was quickly drained. The top sensor, however, seems more consistent. Furthermore, Figure 4.31 (a) shows that the moisture content has gradually decreased over time. The average moisture content of the bottom and top sensors was 6% and 5.4%, respectively. Their decline has continued since then, and they are now 5.2% and 4% on average (as of June 2022). Compared to the top sensor, there is a higher moisture content in the bottom sensor as expected. As mentioned before, the bottom sensor of the south abutment was damaged during installation, so the top sensor is the only data we get from the south side. Similar to the top sensor of the north abutment, the average moisture content of the south abutment was around 5% for the first few months, and then its decline started. As of June 2022, the average moisture content of the top sensor of the south abutment is 4.5%.

4.6 Summary

In this chapter, we discussed the results of the sensor measurements installed on the Big Springs I-80 West Bridge in Nebraska. There was an unidentified cause for the failure of three pressure cells out of six that we installed on both abutments. According to the results, there is a good correlation between pressure cell changes and ambient temperature fluctuations.

Furthermore, pressure cells show a build–up of pressure over time, probably caused by backfill soil falling and filling the gap as the bridge contracts. As indicated by the tiltmeter outputs, the maximum tilt for the north and south abutments is 0.25° and 0.15°, respectively, which is expected since the south abutment is connected to a longer span. Based on inclinometer measurements, soil movements at the south abutment are greater than those at the north abutment. In addition, all inclinometer deflection graphs show a jump at a depth of 13–15 ft, which corresponds to the bottom of the abutment movement. Over time, moisture sensors have shown that the moisture content at the backfill soil does not change dramatically. These findings indicated that the abutment behave elastically in general. Lastly, we were unable to measure the strain of the bridge girder of pile. All fiber cables installed on pile were unfortunately damaged while the fiber optic cables installed on approach were cut by the contractors or damaged at the ends. The only portion that was measurable was the cable attached on the girder. However, not all portion of the cable are showing measurements, and the difficulties with the field measurements were due to the high wind in a dusty environment, where the fiber optic cable splicing device and the data acquisition unit was providing error. It is a regret that other measures of conventional strain gauges or meter gages were not installed as a backup plan.

5. NUMERICAL MODEL

5.1 Introduction

A three–dimensional finite element (FE) model is developed to extensively evaluate the field monitoring results presented in Chapter 4. Following validation, this model is extended for a parametric study (Chapter 6) to investigate the effects of different parameters on the performance of curved IABs. The research team modeled the soils around the piles and behind the abutments with simplified nonlinear elastoplastic springs. It needs to be noted that approach slabs were not modeled at the abutments in this research. Although there is not an expansion joint at the connection of abutments to approach slabs, there is still a construction joint due to the fact that the concrete for approach slabs and abutments were not poured together. These two sections are connected through #6 anchorage rebars that are spaced approximately 7.5 in. apart. The research team does not believe this type of abutment-approach slab connection is solid enough to be modeled as part of the jointless bridge. That is why the bridge was modeled without its approach slabs.

IAB deformation is largely due to thermal loading, which was calculated from the site's ambient temperature obtained from a nearby weather station. It needs to be noted that the testbed bridge is a newly constructed bridge, and it was not open to traffic until the spring of 2022. Therefore, prior to spring 2022, the bridge was only affected mostly by thermal loads and creep and shrinkage of concrete bridge deck. Finally, data from the site instrumentation was utilized to calibrate the model's parameters. The research team developed three–dimensional models using CSiBridge, a structural analysis and design software. The details of these FE models are described in this chapter.

5.2 Structural Elements

Cross braces and piles were modeled using frame elements. For the abutments, pier, and pier cap, thick shell elements were used. In contrast, thin shell elements were used to model the deck and girders. Shear studs are placed on top of the girders to ensure continuity between girders and the deck during the superstructure design stage. This continuity can be captured in two different ways in the simulation process. First, a rigid link can be defined between girders and the deck when they are modeled with frame and shell elements, respectively. However, when both the girders and the deck are modeled as shell elements, rigid connectivity is achieved by meshing them at the connection points and matching the mesh nodes. The latter is how rigidity was acquired between the deck and girders in this study through meshing the connection points. In the following sections, each element is discussed in more detail.

5.2.1 Piles

Each abutment is supported by nine 12–in. pipe piles with an overall thickness of 3/8 inches. All piles conform to the requirements of ASTM A252, Grade 2 steel with a 35 ksi yield strength and a modulus of elasticity of 29000 ksi. The top 18 feet of all piles are enclosed inside Corrugated Metal Pipe (CMP) sleeves as shown in Figure 5.1 and the space between them is filled with loose sand (Figure 5.1). The sand will become dense due to the compaction from free fall energy. However, the sand was assumed to be loose due to the shallow depth (18 ft). Consequently, there is little resistance to the movement of the top portion of piles from the loose sand. Therefore, the top 18 feet of the piles were simply modeled without soil around, which indicates that no soil–structure interaction exists. In Chapter 3, it was discussed how corner piles were filled with mortar to hold composite beams with fiber optic cables in place. This means that these corner pile sections may behave like Concrete Filled Tubes (CFT) which must be included in the model. Therefore, the research team transformed these sections into equivalent steel sections with modified properties.

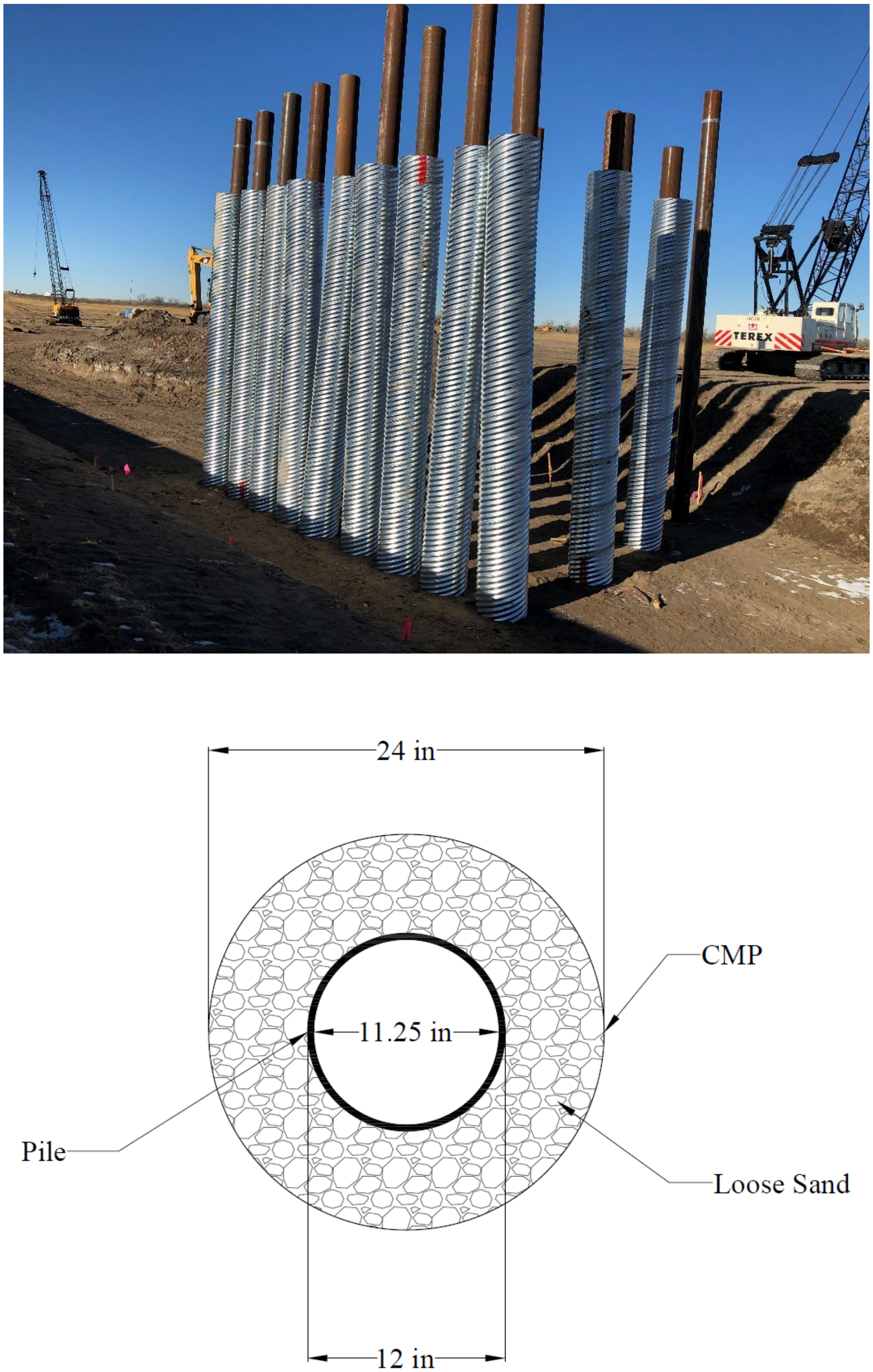

Figure 5.1: CMP Sleeves around Pipe Piles and the Loose Sand in between

To transform the composite section, the team used Equation 5-1 to calculate the modular ratio, n.

$$n = \frac{E_s}{E_c} \tag{5-1}$$

where, E_s (29000 ksi) and E_c ($57000\sqrt{f'_c}$) are the moduli of elasticity of steel and concrete, respectively. According to Figure 5.2, this ratio is then used to calculate the equivalent steel section from the mortar core (O.D. stands for Outer Diameter, and I.D for Inner Diameter).

Lastly, we calculated the moment of inertia of the transformed section by adding the moments of inertia of the steel ring and that of the transformed mortar core using Equations 5-2 to 5-4. Table 5.1 shows the transformed properties of the section.

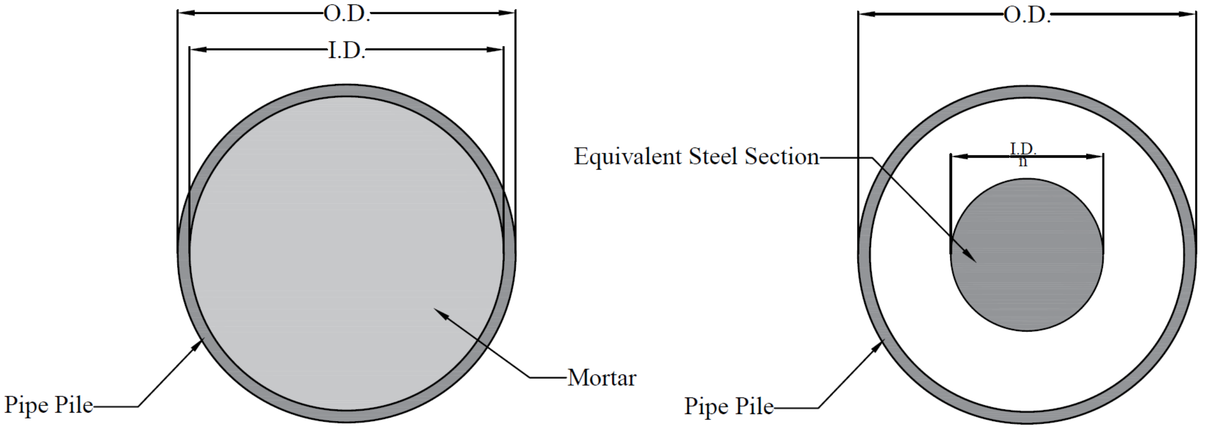

CFT Pile Cross Section

Transformed Cross Sectior

Figure 5.2: CFT Cross Section Transformation

$$I_{total} = I_{ring} + I_{core} \tag{5-2}$$

where

$$I_{ring} = \frac{\pi}{64}(O.D.^4 - I.D.^4) \tag{5-3}$$

$$I_{core} = \frac{1}{4}(\frac{I.D.}{2})^3(\frac{I.D.}{2n}) \tag{5-4}$$

Table 5.1: CFT Transformed Section Properties

Outer Diameter	14 in
Inner Diameter	13 in
Wall thickness	1 in
Moment of Inertia	300 in^4
Area	30 in^2

Regarding piles modeling, there are additional points worth mentioning.

- According to the drawings, the tentative length of the piles was estimated to be 75 feet, but after the test pile driving process, it was modified to 80 feet for each abutment.
- Piles are assumed to be fixed at their base.
- Piles are assumed to be vertical when the bridge becomes integral.

5.2.2 Girders

The four girders were modeled as thin shell elements based on Kirchhoff's formulation that ignores transverse shear deformations (CSI, 2016). As Figure 5.3 illustrates, there are three different girder sections for three parts of the bridge namely, on the bent, and from the bent to the north and south abutment. In the end, each girder was meshed so that it had matching nodes with the deck, ensuring continuity of the deck–girder connection.

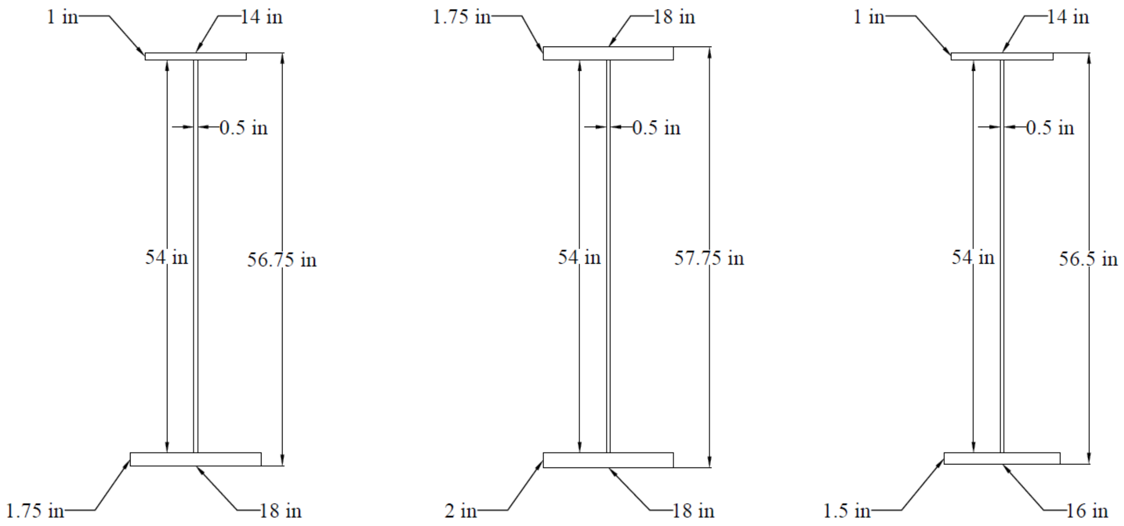

Figure 5.3: Cross Section of Girders at Different Locations

5.2.3 Deck

This bridge contains a 7.5–in. uniform concrete slab between the girders and an 8–in. slab in the deck's overhang. The deck is made of Class 47BD concrete with a 28–day strength of 4000 psi, which is assumed to remain linear elastic during the analysis. To model the deck, a four–node thin shell element was used, and as mentioned previously, the continuity of the girder–deck connection was ensured through the shared mesh nodes between girders top flange and the deck. Cross section of the concrete deck is displayed in Figure 5.4.

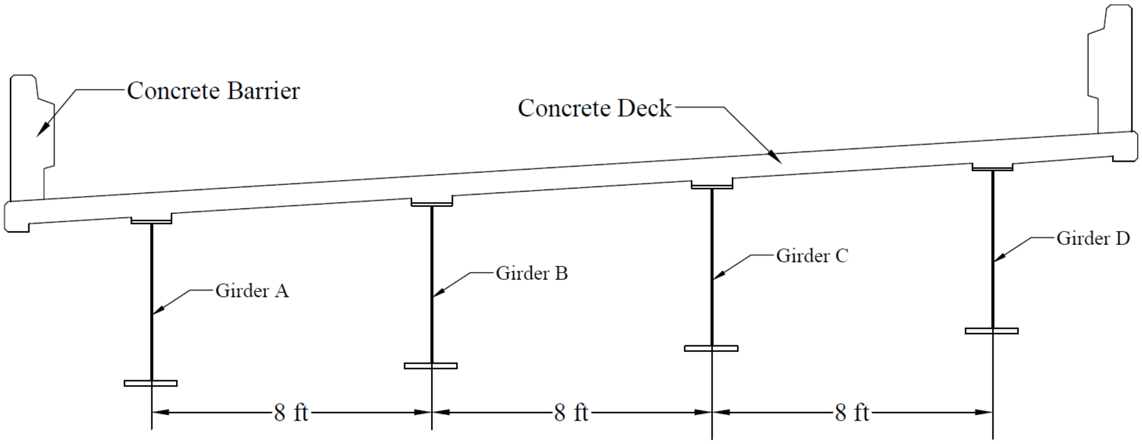

Figure 5.4: Concrete Slab Cross Section

5.2.4 Abutments

Different from the deck, abutments were modeled using 4–node thick shell elements that simulate transverse shearing. Since this is an IA bridge, all structural elements intersecting at the abutment are fully integrated meaning that the abutment, piles, girders and the deck are rigidly connected. Because piles are modeled as frame elements, the continuity of the pile–abutment connection is achieved by connecting their end nodes to an abutment mesh node. Figure 5.5 illustrates the abutment cross section with its girders and piles.

5.2.5 Bent

The bent cap is supported by twenty–eight 45–long pipe piles. In this study, the soil around the piles supporting the pier was not modeled, and the pile tip was assumed to be fixed since the bent is assumed to have negligible movements. Moreover, Figure 5.6 indicates that the bent sitting height differs for each girder. The exact shape of this pier was modeled in CSiBridge.

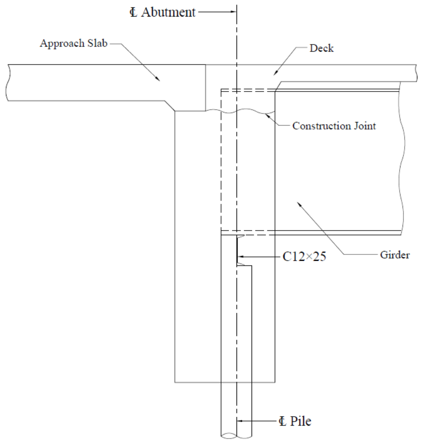

(a) abutment cross sectoin

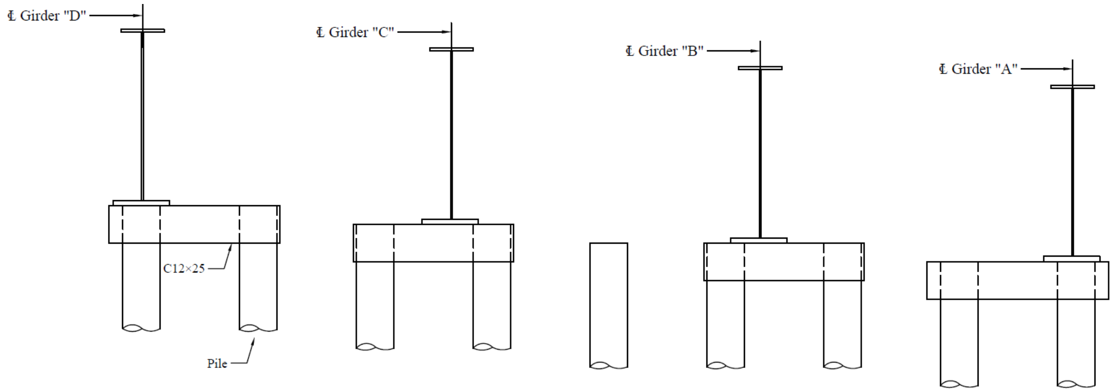

(b) abutment framing details

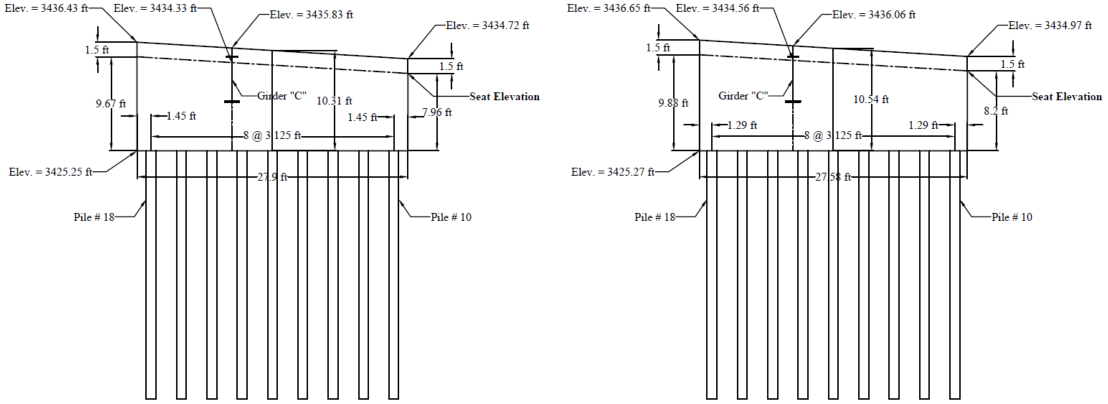

(c) general view of north and south abutments with piles

Figure 5.5: Drawings of Abutments

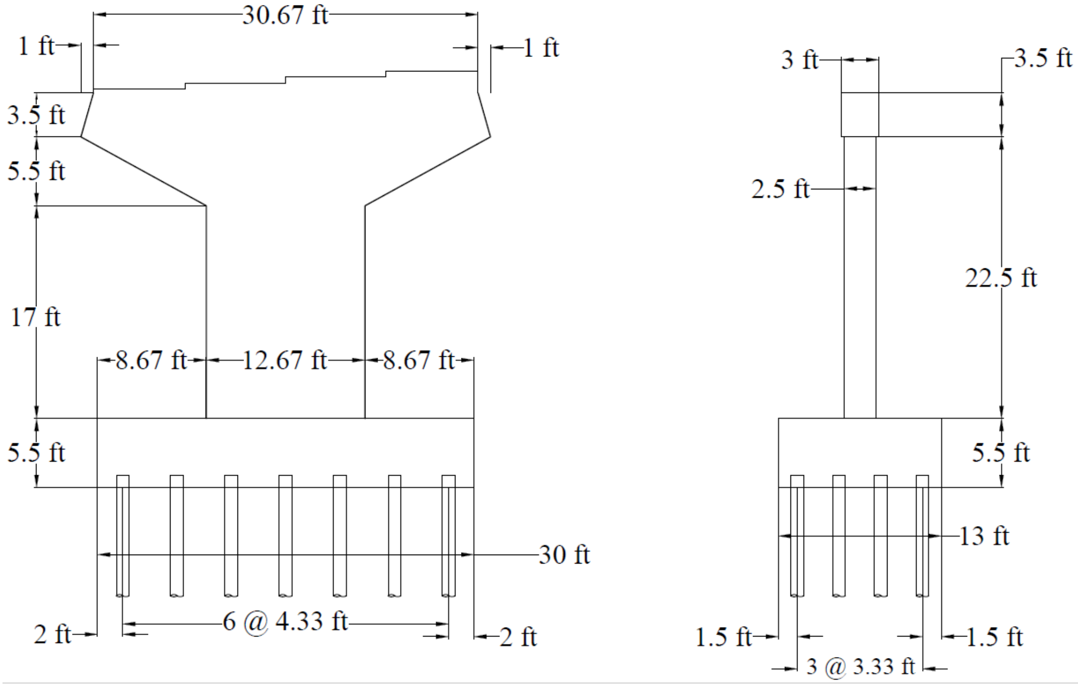

Figure 5.6: Bent, Bent Cap and its Supporting Piles

5.3 Soil Elements

A pile might be designed only to support the vertical load when the horizontal load acting on the pile is relatively small. Particularly, when the horizontal load is not negligible, however, the pile must be designed for vertical, horizontal load and a combination of them. It can be challenging since not only will the soil resistance be affected by the lateral deflection of the pile, the pile deflection, itself, will also be affected by the soil reaction around it because these components are inter-coupled (Figure 5.7 retrieved from Isenhower et al. 2020; LPILE 2019 Technical Manual). This is a classic soil–structure interaction problem. When a pile is driven into a soil medium (axially loaded piles), the soil adjacent to the pile is most affected by its vertical load, while for a laterally loaded pile, deflection can lead to stresses and strains as far away as several pile diameters. Among the four types of lateral loading, static, short–term, cyclic, and dynamic, the one caused by temperature variations can be categorized as cyclic loading.

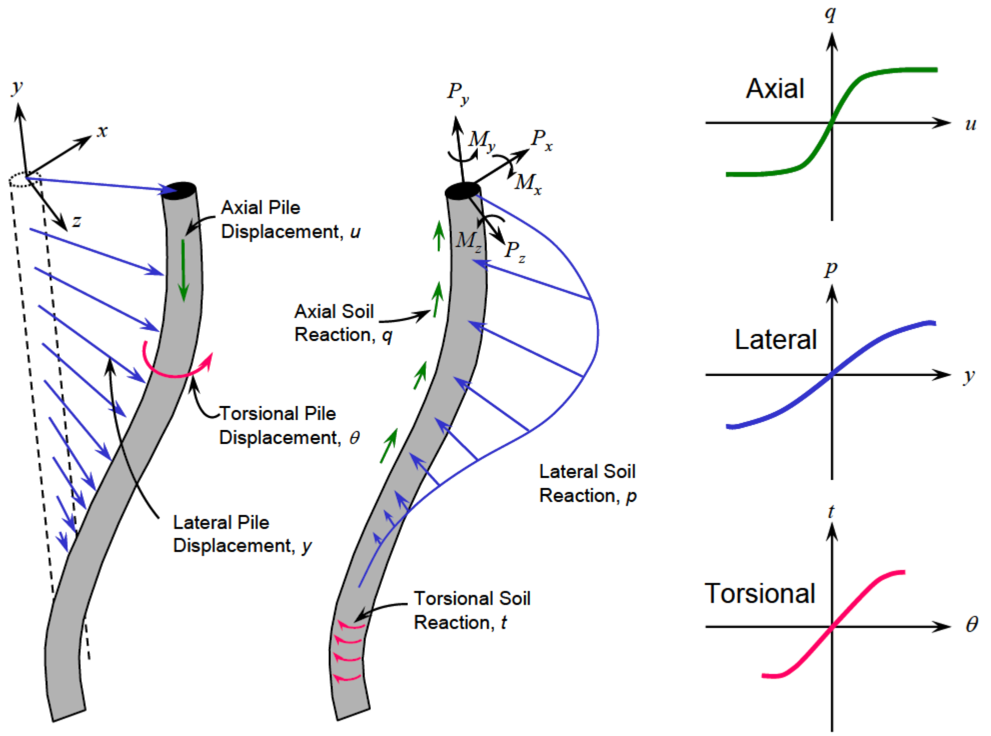

(a) Three-dimensional pile displacements

(b) Pile reactions

(c) Nonlinear load-transfer curves

Figure 5.7: Three-Dimensional Soil-Pile Interaction (retrieved from LPILE 2019 Technical Manual)

5.3.1 P–y Curves

Load–deflection curves, also known as P–y curves, are the analytical models that are widely used for soil–pile interaction analyses. If there is no lateral deflection in the pile, as shown in Figure 5.8 (a), lateral stresses will be uniformly distributed around it. However, when deflection (y) is introduced into the equation (Figure 5.8 (b)), the stress distribution will become non–uniform with decreased stresses on the backside of the pile while increased stresses are experienced on the front side. In order to determine the lateral load acting in the opposite direction of pile deflection, it is necessary to integrate the unit stresses surrounding the pile's circumference. The P–y curve in Figure 5.9 displays how LPILE models soil–pile interaction. Piles' head is loaded in two dimensions by a vertical load (P), a lateral load (V), and an overturning moment (M).

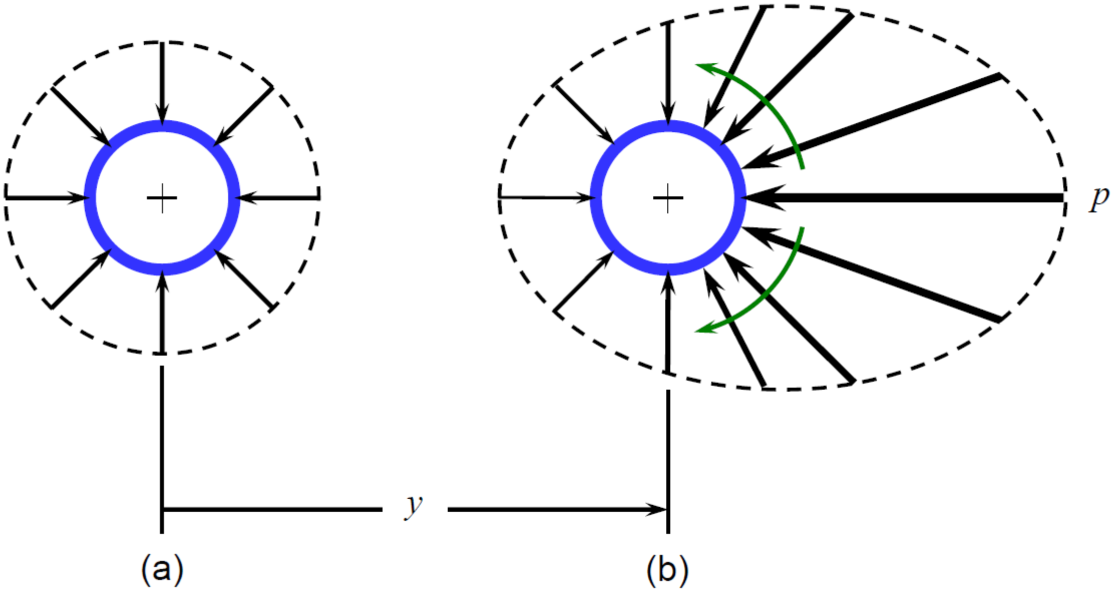

Figure 5.8: Distribution of Stresses around a Pile, (a) Before Lateral Deflection, (b) After Lateral Deflection (retrieved from LPILE 2019 Technical Manual)

Discrete nonlinear springs replace the surrounding soil at discrete points, representing the soil resistance (P) as a function of soil deflection (y). Based on this figure, it can be seen that the shape and intensity of P–y curves change with depth, which can be attributed to different soil layers and also to different vertical stresses at different depths.

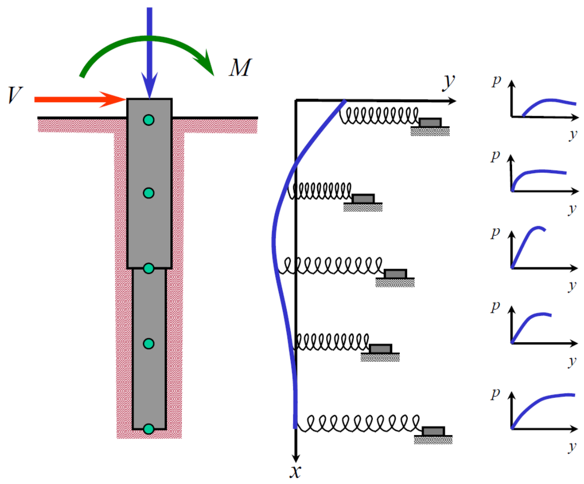

Figure 5.9: Soil–Pile Model used by LPILE and P–Y curves (retrieved from LPILE 2019 Technical Manual)

5.3.2 Soil Properties

In Figure 5.10, we see the soil profiles provided by NDOT that include information on the soil type, layer thickness, water level, and Standard Penetration Test (SPT) number for every layer. Therefore, SPT numbers were used to determine each layer's cohesion (c_u) and internal friction angle (φ'). Usage of the soil properties is addressed in the next section.

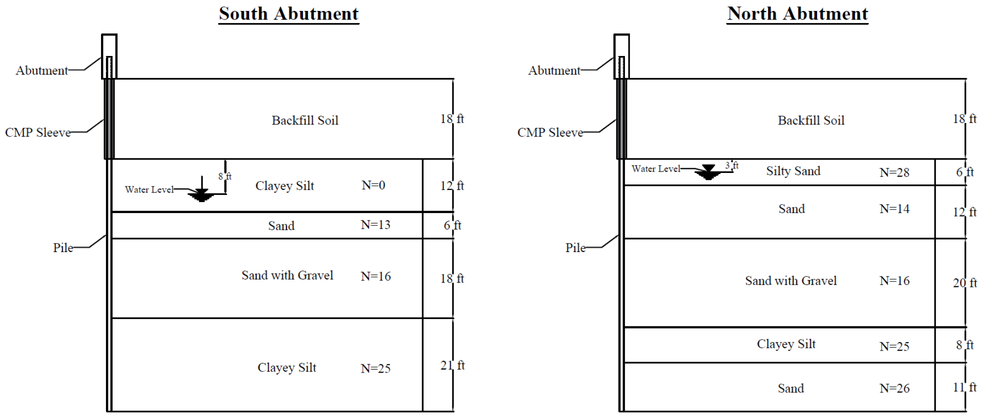

Figure 5.10: Soil Properties at the North and South Abutments

5.4 Soil–Pile Interaction

In this section, the research team explains how soil properties are determined. On the basis of Tables 5.2 and 5.3, the team selected the dry unit weight of the soil based on each layer's soil type. Then, Table 5.4 is used to compute the unconfined compression strength for layers with cohesive soils. Taking the south abutment's top layer with a clayey silt as an example, its SPT is equal to 0. Table 5.4 shows that it is categorized as a very soft layer with an approximate q_u of 500 lb/ft^2. Finally, using the equation below, the undrained cohesion is obtained.

$$c_u = \frac{q_u}{2} \tag{5.5}$$

Table 5.2: Dry Unit Weight for Typical Soils in Natural State (retrieved from Table 3.1 of Das and Sivakugan 2019).

Type of soil	**Dry unit weight, γ_d (lb/ft^3)**
Loose uniform sand	92
Dense uniform sand	115
Loose angular–grained silty sand	102
Dense angular–grained silty sand	121
Stiff clay	108
Soft clay	73 – 93
Loess	86
Soft organic clay	38 – 51
Glacial till	134

Table 5.3: Typical Dry Densities for Different Soil Groups (retrieved from Table 35.10 of Lindeburg 2014)

Class Group Symbol	Description	Range of Maximum Dry Densities (lb/ft^3)
GW	Well–graded, clean gravels, gravel–sand mixtures	125–135
GP	Poorly graded clean gravels, gravel–sand mixtures	115–125
GM	silty gravels, poorly graded gravel–sand silt	120–135
GC	Clayey gravels, poorly graded gravel–sand-clay	115–130
SW	Well-graded clean sands, gravelly sands	110–130
SP	Poorly graded clean sands, sand–gravel mix	100–120
SM	Silty sands, poorly graded san–silt mix	110–125
SM–SC	Sand–silt–clay mix with slightly plastic fines	110–130
SC	Clayey sands, poorly graded sand–clay mix	105–125
ML	Inorganic silts and clayey silts	95–120
ML–CL	Mixture of organic silt and clay	100–120
CL	Inorganic clays of low–to–medium plasticity	95–120
OL	Organic silts and silt–clays, low plasticity	80–100
MH	Inorganic clayey silts, elastic silts	70–95
CH	Inorganic clays of high plasticity	75–105
OH	Organic and silty clays	65–100

Table 5.4: Approximate Correlation among SPT number, Consistency, and Unconfined Compression Strength in Cohesive soil (retrieved from Table 17.4 of Lovell 2010)

SPT number, N_{60}	Consistency	Unconfined compression strength, q_u (lb/ft^2)
< 2	Very soft	500
2 to 8	Soft to medium	500 to 1700
8 to 15	Stiff	1700 to 3100
15 to 30	Very stiff	3100 to 8400
> 30	Hard	8400

For the layers with granular soils, on the other hand, we need to first calculate the effective overburden pressure (σ') of the target layer since SPT is highly correlated with it. Therefore,

$$\gamma' = \gamma_{sat} - \gamma_w \tag{5-6}$$

where γ_{sat}, γ_w and γ' are the saturated unit weight of soil, the unit weight of water and the effective unit weight of soil, respectively. Afterwards, this effective unit weight is used to calculate the effective stress for each soil layer.

$$\sigma' = \gamma' \frac{h}{2} + \gamma'_{top} h_{top} \tag{5-7}$$

where h is the thickness of the soil layer, γ'_{top} is the average effective unit weight of the soil layers on top, h_{top} is the thickness of top layers and σ' is the effective overburden pressure. Using the SPT number and overburden pressure, the next step is to calculate the approximate relative density of each layer. Meyerhof (1957) developed a formula for this purpose which will be used here.

$$D_r(\%) = \sqrt{\frac{N_{60}}{17 + 24\left(\frac{\sigma'}{P_a}\right)}} \times 100 \tag{5-8}$$

where D_r is the relative density of the soil layer, and P_a is the atmospheric pressure. Next, a soil layer's qualitative description can be determined using this relative density (Table 5.5).

Table 5.5: Qualitative Description of Granular Soil Deposits (retrieved from Table 3.2 of Das and Sivakugan 2019)

Relative density (%)	Description of soil deposit
0–15	Very loose
15–50	Loose
50–70	Medium
70–85	Dense
85–100	Very Dense

Finally, the drained angle of friction was calculated based on the SPT number (N_{60}), the overburden pressure (σ'), and the atmospheric pressure (P_a). Equation 5-9, developed by Kulhawy and Mayne (1990) is used for this purpose.

$$\varphi = \left(\frac{N_{60}}{12.2 + 20.3\left(\frac{\sigma'}{P_a}\right)}\right)^{-0.34} \tag{5-9}$$

Tables 5.6 and 5.7 show the properties of soils behind each abutment. These tables also show which soil model was used in LPILE to model the soil–pile interaction behavior.

Table 5.6: South Abutment Soil Properties

Soil Type	Layer Thickness (ft)	SPT No.	LPILE Soil	c_u (psf)	φ' (°)
Clayey Silt	8	0	Soft Clay (Matlock)	250	0
Clayey Silt	4	0	Soft Clay (Matlock)	250	0
Sand	6	13	Sand (Reese)	0	39.7
Sand with Gravel	18	16	Sand (Reese)	0	38.9
Clayey Silt	21	25	Silt	3317	39.7

Table 5.7: North Abutment Soil Properties

Soil Type	Layer Thickness (ft)	SPT No.	Lpile Soil	C_u (psf)	φ' (°)
Silty Sand	3	28	Sand (Reese)	0	51.6
Silty Sand	3	28	Sand (Reese)	0	49.8
Sand	12	14	Sand (Reese)	0	40.6
Sand with Gravel	20	16	Sand (Reese)	0	38.3
Clayey Silt	8	25	Silt	3316.5	40.1
Sand	11	26	Sand (Reese)	0	39.2

As shown in these tables, the Reese model was selected for sand, silty sand and sand with gravel while the Matlock and Silt models were used for clayey silt layers. The procedure Reese et al. (1974) developed to compute P–y curves in sand can be used for both static and cyclic loadings of vertical piles driven in a flat ground (LPILE 2019 Technical Manual). The P–y curve developed by this procedure is shown in Figure 5.11.

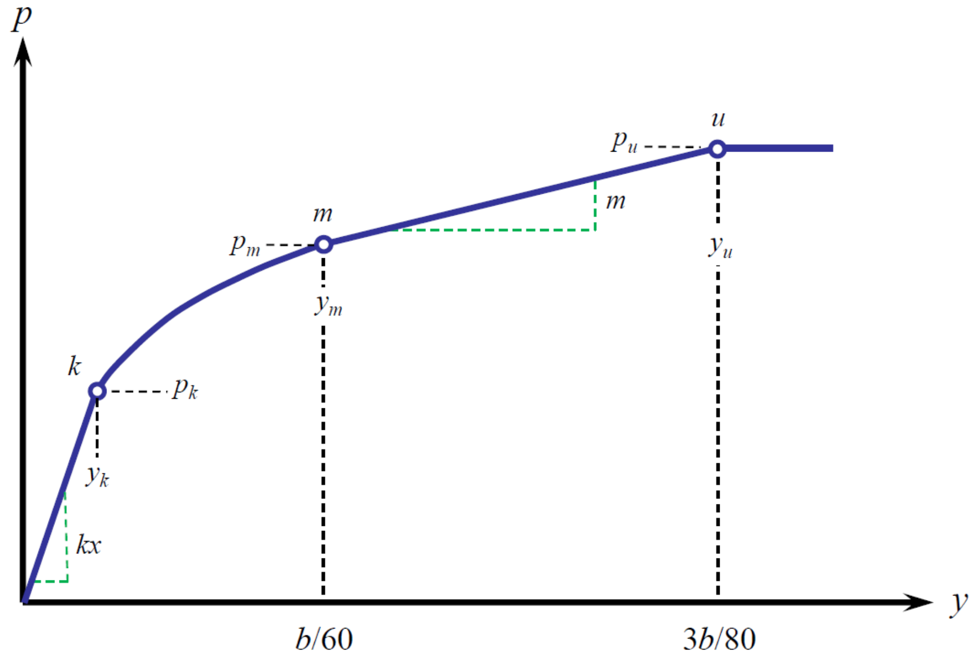

Figure 5.11: Characteristic Shape of P-y Curves in Sand (retrieved from Figure 3-27 of LPILE 2019 Technical Manual)

Calculation of P–y curves for soft clay follows the Matlock (1970) procedure. He performed lateral load tests in soft clay in the presence of water (LPILE v2019 Technical Manual). Figure 5.12 displays the P–y curve in soft clay (Matlock) for cyclic loading.

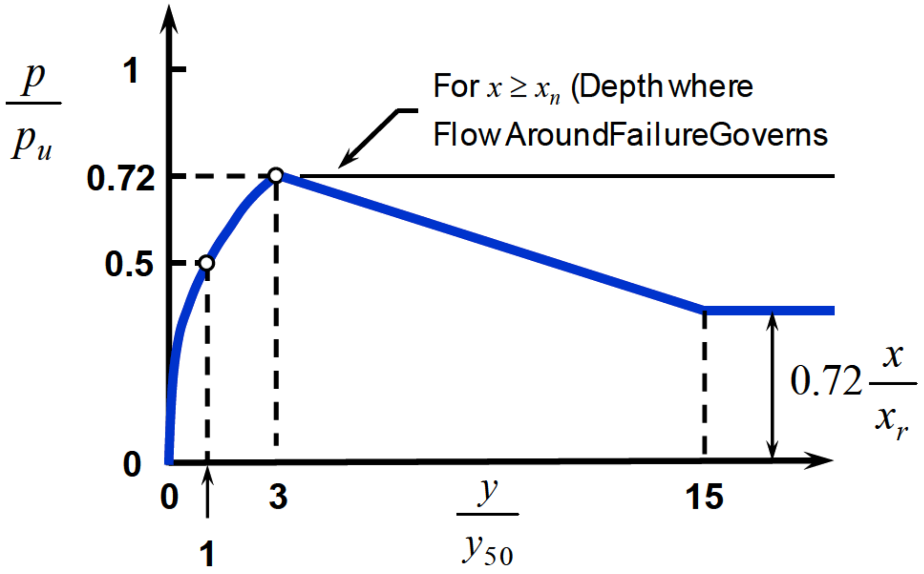

Figure 5.12: Matlock P–y curve in soft clay for cyclic loading (retrieved from Figure 3-12 LPILE 2019 Technical Manual)

The LPILE technical manual states that for soils with both cohesion and internal friction (e.g., clayey silt), the P–y curve is calculated according to the Reese et al. procedure mentioned earlier. In fact, c–φ soils behave more like cohesionless soil in terms of stress–strain characteristics. LPILE's Sand (Reese) model takes three parameters into account. These parameters are the effective unit weight (Tables 5.2 and 5.3) and friction angle (Tables 5.6 and 5.7). The third parameter, *k*, is the slope of the initial straight line of the P-y curve in Figure 5.11. LPile technical manual contains tables of recommended *k* values that are specified for levels both below and above the water table (Tables 5.8 and 5.9).

Table 5.8: Recommended Values of k for Fine Sand below the Water Table (retrieved from Table 3-6 of LPILE 2019 Technical Manual)

Recommended k (pci)	Relative Density		
	Loose	Medium	Dense
	20	60	125

Table 5.9: Recommended Values of k for Fine Sand above the Water Table (retrieved from Table 3-7 of LPILE 2019 Technical Manual)

Recommended k (pci)	Relative Density		
	Loose	Medium	Dense
	25	90	225

LPILE will automatically determine the *k* value from the description of the soil if it is left equal to zero. It is completed using the graph shown in Figure 5.13. In the case where φ exceeds 45°, a limiting *k* value which corresponds to $\varphi = 45°$ will be used. Similar to the Sand (Reese) model, a Soft Clay (Matlock) model is defined by three parameters, including the effective unit weight (Tables 5.2 and 5.3), the undrained cohesion (Tables 5.6 and 5.7) and the strain corresponding to 50% of the maximum principal stress difference (ε_{50}).

Table 5.10 provides the recommended values in the LPile technical manual for ε_{50}. As stated previously, Tables 5.4 and 5.5 present information on the qualitative characteristics and consistency of the soil deposits which will be used to select the appropriate value of ε_{50} from Table 5.10. Additionally, the strain factor will also be replaced by default values if set to zero, as with the *k* value for granular soils.

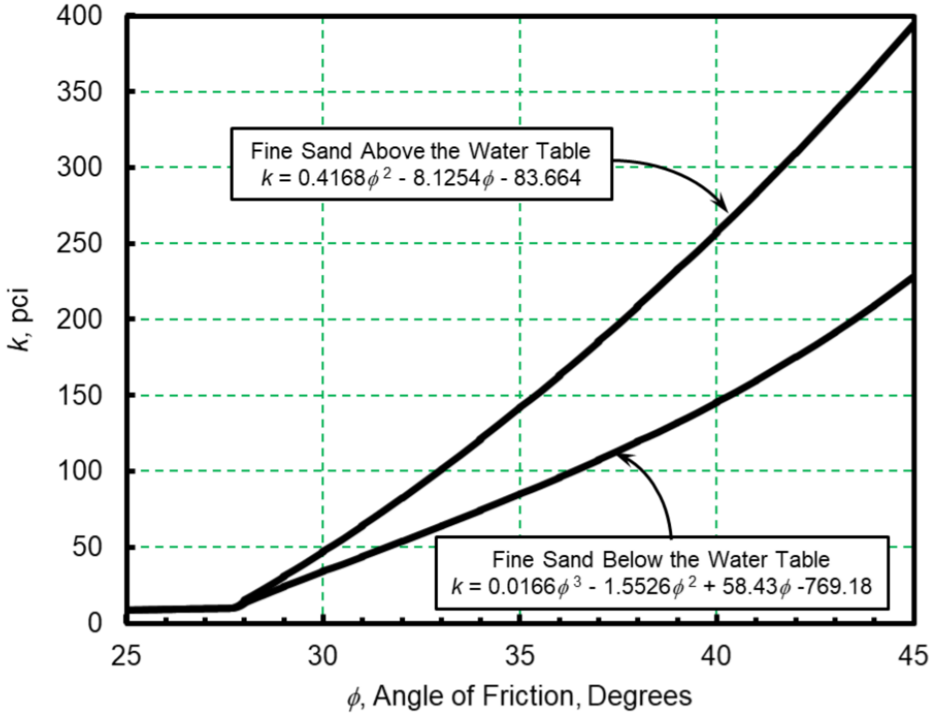

Figure 5.13: *k* values versus Angle of Friction for Fine Sand in LPILE (retrieved from Figure 3-34 of LPILE 2019 Technical Manual)

Table 5.10: Recommended Values of Strain Factor for Clays (retrieved from Table 3-2 of LPILE 2019 Technical Manual)

Consistency of Clay	Strain Factor, ε_{50}
Soft	0.02
Medium	0.01
Stiff	0.005

Finally, five parameters are needed to define c–φ soils including the effective weight, undrained cohesion (c), friction angle (φ), strain factor (ε_{50}) and k. We have already discussed how these five parameters can be determined.

In order to model the soil–pile interaction for all the piles supporting each abutment, P–y curves are used in this study. In the analytical modeling, the top 18 feet of the piles are modeled and analyzed assuming that there is no soil (nonlinear springs) surrounding them. As previously explained, this is because the top portion of each pile is enclosed in a CMP sleeve, which is then filled with loose sand. In order to illustrate the behavior of soils at different depths and levels, nonlinear springs are attached every 2 feet along the pile (starting at the depth of 18 feet and continuing down until the tip of the pile). The load–displacement curves of these nonlinear springs are derived from the P–Y analysis in LPILE. These springs are arranged along the pile in two orthogonal directions, parallel and perpendicular to the abutment's wall. In order to calculate the stiffness of the nonlinear springs in CSiBridge, the soil resistance (P) derived from LPILE is multiplied by the distance between adjacent springs (2 feet). The soil–pile interaction analysis in CSiBridge will be based on these load–displacement curves. A typical load–displacement curve of a nonlinear soil–pile spring is displayed in Figure 5.14.

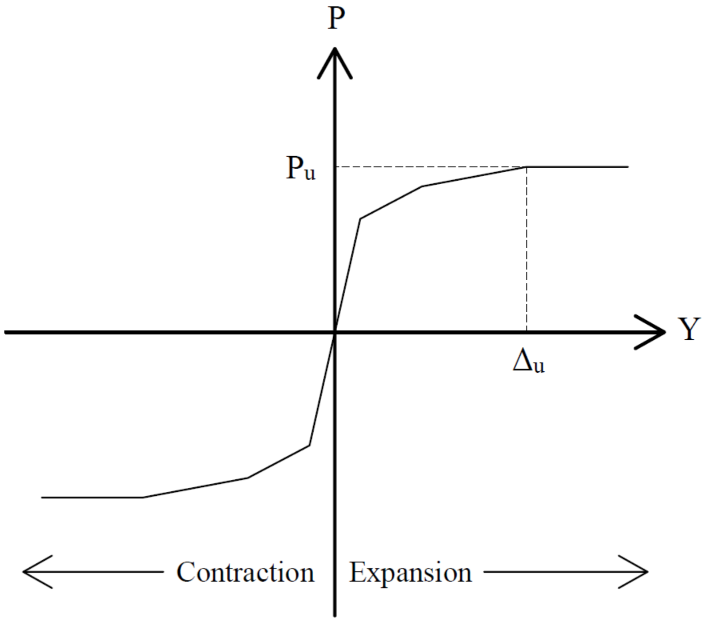

Figure 5.14: Typical Load–Displacement Curve for Nonlinear Springs around a Pile

5.5. Soil – Abutment Interaction

In contrast to modeling soil–pile interaction, soil–abutment interaction is similar but different. Consequently, the technique presented in the previous section is not applied. In an IAB, abutments behave more like retaining walls. Hence, pertinent formulas should be used. As the bridge expands, passive pressure develops behind the abutment. During the contraction phase, abutments will start to move away from the soil which will result in a drop in passive pressure. Based on this inward displacement, the pressure can reach zero, indicating that the soil and the abutment have completely separated. This trend can be viewed from two perspectives: daily and seasonal temperature fluctuations. From a daily perspective, as the temperature rises during the day, passive pressure is built up behind the abutment, and when it drops at night, the superstructure contracts. Every day, this pattern repeats itself. When viewed on a broader scale, instead of days and nights, one may think of warm and cold seasons, Spring–Summer and Fall–Winter, respectively. In general, during warm seasons, the tendency will be for the superstructure to expand with an increase of passive pressure, and during cold seasons, it may contract as the pressure drops. During cold months, it is generally assumed that the temperature decrease may completely detach the abutment from the soil, resulting in zero pressure between the two. Therefore, zero pressure condition could be applied to soil–abutment interaction problems. It is possible to implement it in the same way as nonlinear springs in soil–pile interactions, however, the load–displacement curve will differ. In the field of earth pressure theories, the Rankine theory is the one that is very well known. In this theory, the interface friction between the two media (wall and soil) is ignored, resulting in a slightly underestimated passive pressure. The Coulomb's theory is another very well–known earth pressure theory. Although this theory takes into account the interface friction along the wall and soil, its predictions have been proved to be too extreme. Therefore, the research team decided to use the Rankine's theory for this study. Based on these theories, the team determined the maximum passive pressure that will be incorporated in the load–displacement curve of the nonlinear spring representing the soil behind the abutment.

5.5.1 Rankine's Theory and Computation of the Spring Constant

Rankine's theory provides a slightly higher active earth pressure and slightly lower passive earth pressure. This method is easy to implement and works reasonably well for granular soils. According to Figure 5.15, this theory assumes that a wedge of soil is formed behind the abutment.

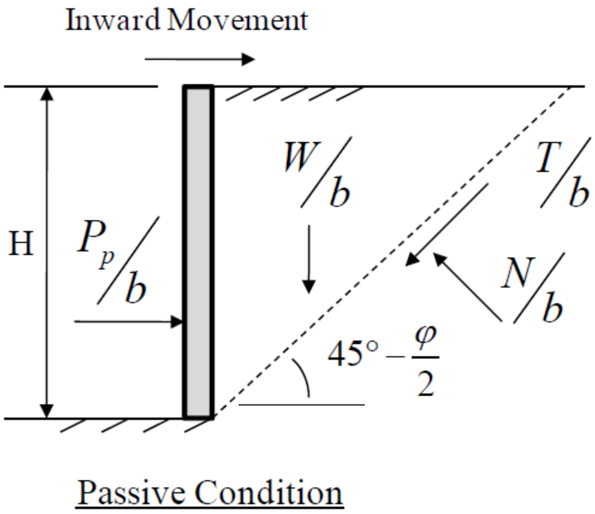

Figure 5.15: Rankine's Solution to Passive Pressure (retrieved from Lovell, 2010)

Then one can solve for the equilibrium of the forces acting on the wedge including the wall lateral resistance, friction and normal forces on the slip line and the soil weight. The research team assumed that there is a triangular distribution of pressure on the wall with the condition of a homogeneous soil condition (Figure 5.16).

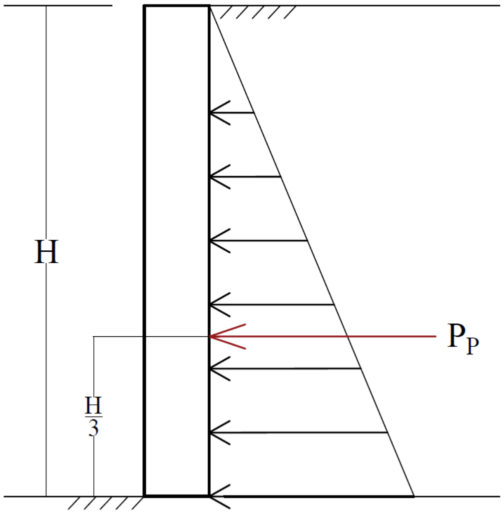

Figure 5.16: Lateral Pressure Distribution on the Abutment's Wall

In this study, active pressures were not considered because the passive pressure would be higher in magnitude and potentially causing a more critical condition. In order to calculate the lateral passive earth pressure at any depth of the abutment, the vertical effective stress needs to be multiplied by the lateral earth pressure coefficient which is shown in Equation 5-10. In addition, the rainwater was not considered because the wall was on higher elevation than surrounding area.

$$\sigma_p(z) = K_p \sigma'_z(z) \tag{5-10}$$

where

$K_p = tan^2(45° + \frac{\varphi}{2})$ = Coefficient of lateral passive earth pressure

$\sigma'_z = \gamma' z$ = vertical effective stress at depth z

z = depth from the surface

γ' = soil effective unit weight

φ = internal friction angle

Additionally, Equation 5-11 shows how to calculate the total passive force acting on the abutment's wall. According to Figure 5.16, this force acts at the triangle's center of gravity, which is one third of the abutment's height from the bottom.

$$P_p = \frac{1}{2}\sigma_p BH \tag{5-11}$$

where

P_p = Total passive force acting on the abutment

σ_p = Passive earth pressure at the bottom of the abutment

B = Abutment width

H = Abutment height

Theories such as Rankine provide equations to calculate lateral earth pressure but does not specify when the full passive pressure is mobilized. To reach full passive pressure, Coduto (2001) recommends an approximate horizontal movement of 2% of a retaining wall's height (Figure 5.17).

This movement may, however, lead to high pressures in the numerical study. According to Jesse (2012), an abutment needs to move horizontally 2 to 3.5% of its height to mobilize the full passive pressure. To lower the FE backfill pressure results, the research team used the upper limit of this range (3.5%). Then, the stiffness of the soil–abutment spring can be obtained by dividing the passive force acting on the wall (P_p) by the horizontal movement needed for the soil to reach the full passive pressure (0.035H). This is demonstrated in Equation 5-12.

$$K_{soil} = \frac{P_p}{0.035H} \tag{5-12}$$

where

K_{soil} = stiffness of the lateral spring behind the abutment (perpendicular to the abutment)

P_p = Total passive force acting on the abutment wall

H = Abutment height

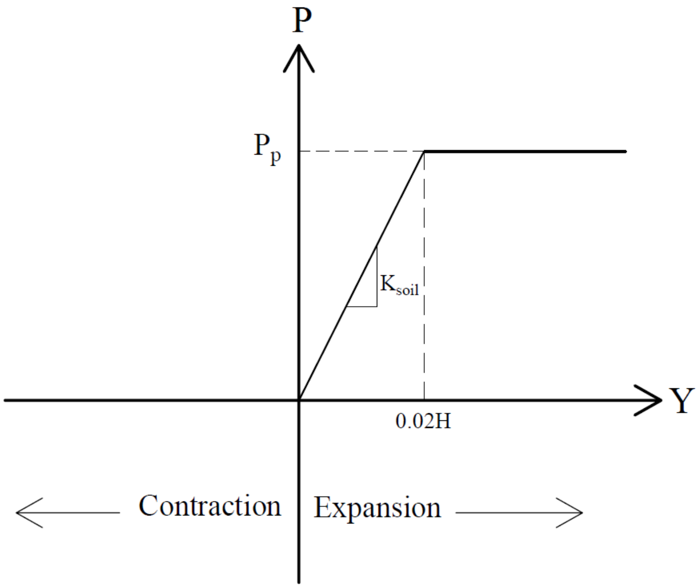

Figure 5.17: Typical Load–Displacement Curve for the Abutment's Backfill Soil

For the analysis, it is assumed that the well graded gravel backfill has an effective unit weight of 100 lb/ft^3 and an internal friction angle of 30°. While north and south abutments differ slightly in height and width, they are assumed to have the same dimensions when calculating the stiffness of the soil–abutment spring. Accordingly, the total passive force for the model was:

$$P_p = \frac{1}{2} K_p \gamma' Z B H \qquad (5\text{-}13)$$

where

P_p = Total passive force acting on the abutment wall

K_p = 3 = Coefficient of lateral passive earth pressure

γ' = 100 $^{lb}/_{ft^3}$ = Effective unit weight of the backfill

Z = 10.5 ft = Depth of the abutment wall

B = 29 ft = Abutment width

H = 10.5 ft = Abutment height

Based on Equation 5-14 (soil stiffness per unit length of wall), and considering that the abutment is required to move 4.41 in. (3.5% of 10.5 ft) to mobilize the maximum passive force, the abutment–backfill spring will have a stiffness of:

$$K_{soil} = \frac{479.6\ kip}{4.41\ in} = 108.7\ ^{kip}/_{in} \qquad (5\text{-}14)$$

The soil medium behind the abutment is typically represented by a single spring at the center of the abutment. The approach may work on straight bridges, but curved bridges cannot normally be analyzed in this way since their lateral movements are not uniform, and the arching effect should not be disregarded. In this study, therefore, three springs are used for each abutment, one at the center of the abutment, and two at each side below the exterior girders' center lines. Figure 5.18 shows the plan view of the bridge with its nonlinear backfill soil links.

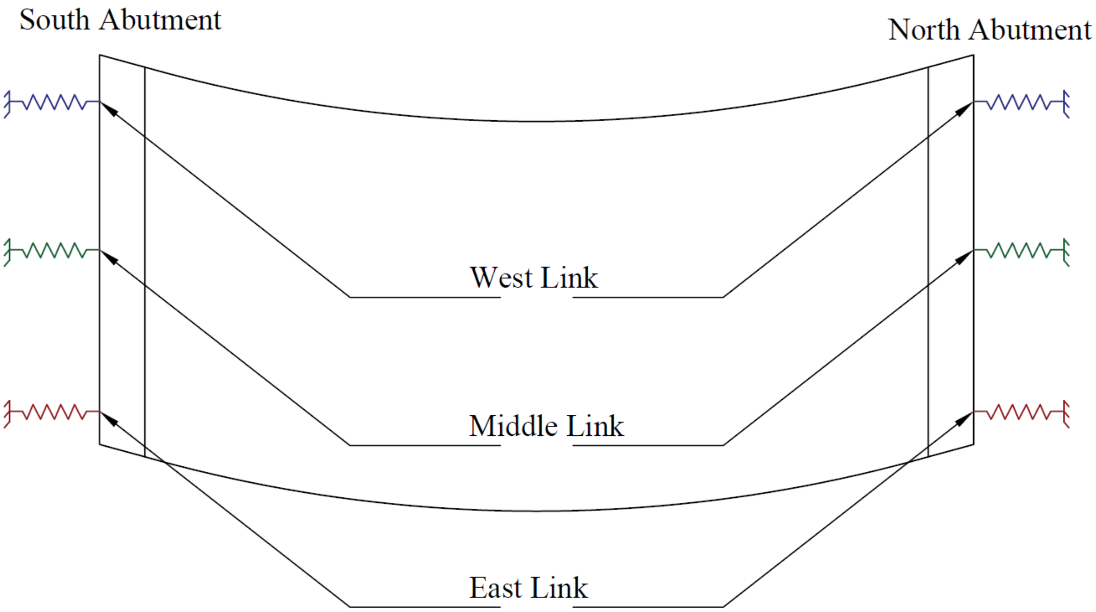

Figure 5.18: Location of the Nonlinear Links on Each Abutment

5.6 Loading

IABs performance is most influenced by temperature fluctuation and shrinkage during their lifetime. Unlike traditional bridges which have expansion joints to accommodate temperature changes, in IABs, the entire substructure and superstructure are affected by these temperature variations. The main loads affecting the bridge's performance are self–weight, temperature, and shrinkage.

5.6.1 Temperature

The closest weather station was used to obtain the temperature data (data from Big Springs, NE weather stations; data retrieved from https//wunderground.com). From the week when the superstructure became integral, Table 5.11 shows the station's maximum, minimum and average weekly temperatures.

Table 5.11: Weekly Max., Min. and Average Temperature at Big Springs Weather Station

Year	Week	Average Weekly Temperature (°F)		
		Maximum	Average	Minimum
2020	Week#1	70	58	44
	Week#2	58	47	36
	Week#3	71	58	48
	Week#4	75	62	47
	Week#5	89	74	57
	Week#6	86	73	60
	Week#7	93	79	63
	Week#8	86	70	57
	Week#9	92	77	62
	Week#10	93	78	63
	Week#11	88	73	61
	Week#12	88	78	69
	Week#13	87	75	67
	Week#14	83	69	58
	Week#15	92	76	63
	Week#16	91	75	60
	Week#17	98	80	64
	Week#18	85	70	54
	Week#19	75	61	47
	Week#20	80	61	46
	Week#21	87	68	52
	Week#22	75	58	40
	Week#23	81	58	37
	Week#24	76	56	39
	Week#25	56	43	32
	Week#26	41	29	17
	Week#27	74	48	27
	Week#28	56	43	31
	Week#29	62	41	25
	Week#30	51	37	23
	Week#31	49	30	12
	Week#32	61	37	20
	Week#33	37	24	12
	Week#34	49	33	19

Year	Week	Average Weekly Temperature (°F)		
		Maximum	Average	Minimum
	Week#35	41	26	14
2021	Week#1	44	32	21
	Week#2	46	35	25
	Week#3	44	30	19
	Week#4	26	21	15
	Week#5	47	30	20
	Week#6	16	9	1
	Week#7	8	-1	-14
	Week#8	42	30	18
	Week#9	59	39	22
	Week#10	67	45	26
2021	Week#11	45	39	33
	Week#12	55	43	33
	Week#13	61	45	27
	Week#14	75	54	33
	Week#15	54	41	22
	Week#16	50	38	25
	Week#17	72	54	38
	Week#18	74	60	43
	Week#19	64	51	38
	Week#20	72	62	55
	Week#21	77	65	55
	Week#22	72	58	47
	Week#23	91	79	66
	Week#24	94	77	61
	Week#25	86	73	58
	Week#26	82	70	58
	Week#27	90	76	64
	Week#28	85	72	60
	Week#29	88	75	65
	Week#30	95	81	68
	Week#31	88	74	61
	Week#32	96	78	61
	Week#33	90	76	64
	Week#34	88	74	64
	Week#35	87	74	65
	Week#36	84	68	55
	Week#37	89	71	58
	Week#38	80	64	50
	Week#39	83	64	47
	Week#40	79	59	44
	Week#41	70	54	40
	Week#42	65	46	31
	Week#43	62	49	36
	Week#44	54	40	31
	Week#45	64	47	32
	Week#46	58	41	25
	Week#47	58	38	22

Year	Week	Average Weekly Temperature (°F)		
		Maximum	Average	Minimum
	Week#48	66	43	27
	Week#49	49	36	21
	Week#50	52	33	19
	Week#51	48	30	17
	Week#52	47	30	16
2022	Week#1	26	11	-2
	Week#2	45	27	13
	Week#3	44	27	14
	Week#4	42	29	19
	Week#5	44	26	12
	Week#6	56	34	17
	Week#7	47	32	15
	Week#8	38	21	8
	Week#9	57	34	16
	Week#10	34	23	10
	Week#11	51	37	21
	Week#12	61	43	27
	Week#13	54	41	29
	Week#14	59	46	32
	Week#15	63	46	27
	Week#16	64	48	32
	Week#17	75	57	40
	Week#18	58	47	38
2022	Week#19	83	65	49
	Week#20	83	66	49
	Week#21	64	52	41
	Week#22	80	65	49
	Week#23	83	69	54
	Week#24	93	76	61

A graph of temperature fluctuations for the given time period in Table 5.11 is shown in Figure 5.19. The actual field temperature change could be higher. A nonlinear staged construction load case was used to assign the average weekly temperatures of Table 5.11 to the bridge superstructure.

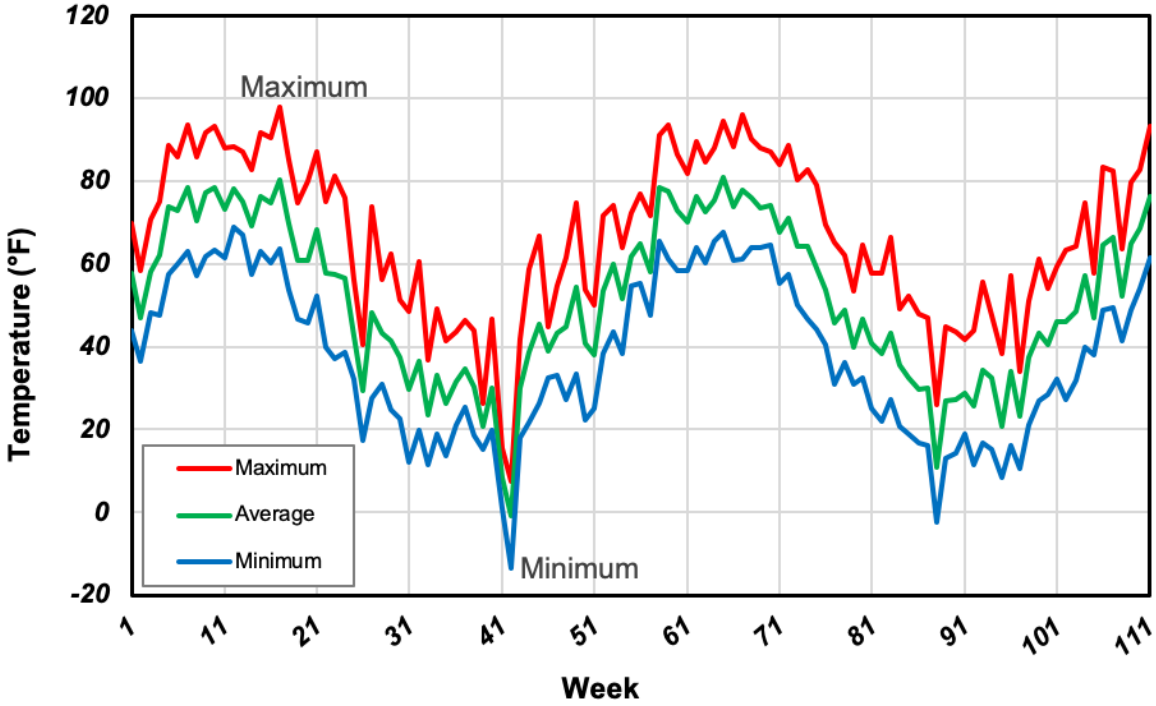

Figure 5.19: Weekly Ambient Temperature at the Big Springs Site

5.6.2 Shrinkage

It is important to note that shrinkage, a time–dependent decrease in concrete deck volume, can greatly influence the long–term performance of IABs. According to Lovell (2010), shrinkage strains account for the net inward movement of IABs. According to Lovell (2010), CEB MC90 is the best shrinkage model to use for IABs, both in terms of magnitude and rate. Therefore, this shrinkage strains were applied to the superstructure with 7–day increments during nonlinear Staged Construction loading.

5.7 Model Verification

With the unavailability of fiber optic DSS cable data that would have shown the bridge's deflection and displacement, the research team instead utilized the inclinometer deflection data as the back-up measurement to verify to the CSiBridge pile deflection. Furthermore, the research team compared the backfill soil pressures and tiltmeter measurements with our numerical simulation results.

5.7.1 Backfill Soil Pressure

A comparison between east and west backfill measured pressure for the south abutment is shown in Figure 5.20. It appears that for the first two cycles, the maximum pressure on the east link is about 44 and 36 psi, respectively while it is 23 and 15 psi for the west link. Therefore, there is almost twice as much backfill pressure on the east link as on the west link. Both east and west links experience a decline in pressure with each cycle. Concrete deck shrinkage strain can explain this behavior. Despite seasonal temperature fluctuations, this shrinkage strain results in a net inward movement of the bridge.

This figure also shows that pressure closely follows ambient temperature. During cold months, the pressure remains zero since as Figure 5.17 shows, there is no pressure defined for the active pressure zone. The FE (Finite Element) staged construction nonlinear analysis was performed since the bridge became integral in May 2020. However, the remote monitoring started a year later, in April 2021. Thus, the results of the second cycle of FE analysis was compared to those of the first cycle of field instrumentation which is shown in Figure 5.21. It can be seen from this figure that the FE pressure trend and range are consistent with those recorded in the field for the considered period of time. It is also noted that the measured pressure shows quite busy fluctuation while the FE based pressure has less noise. This difference is due to the relatively lower intervals of the FE simulation compared to the real case for the measured pressures.

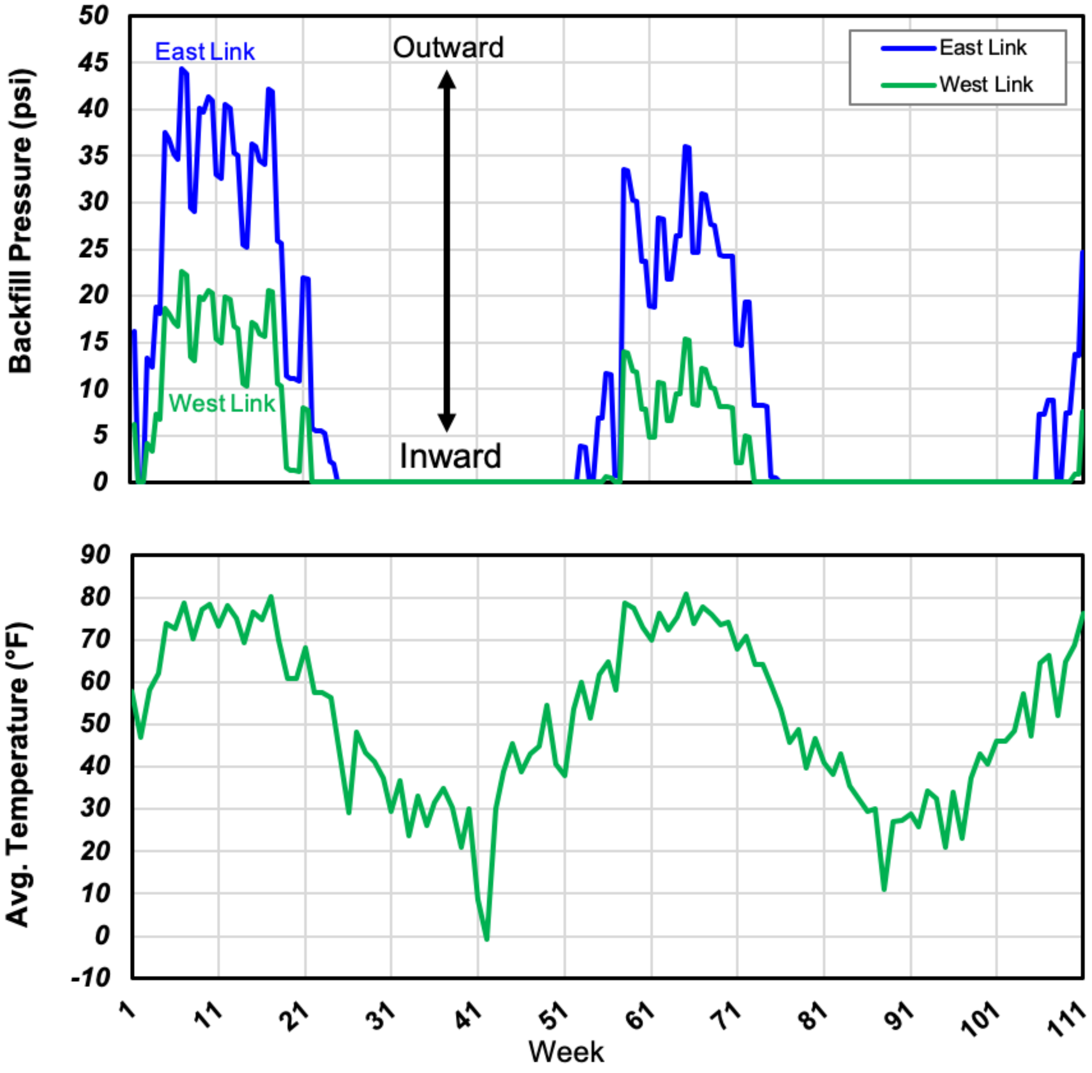

Figure 5.20: Pressure and Average Temperature Variation of the Nonlinear Links on the South Abutment

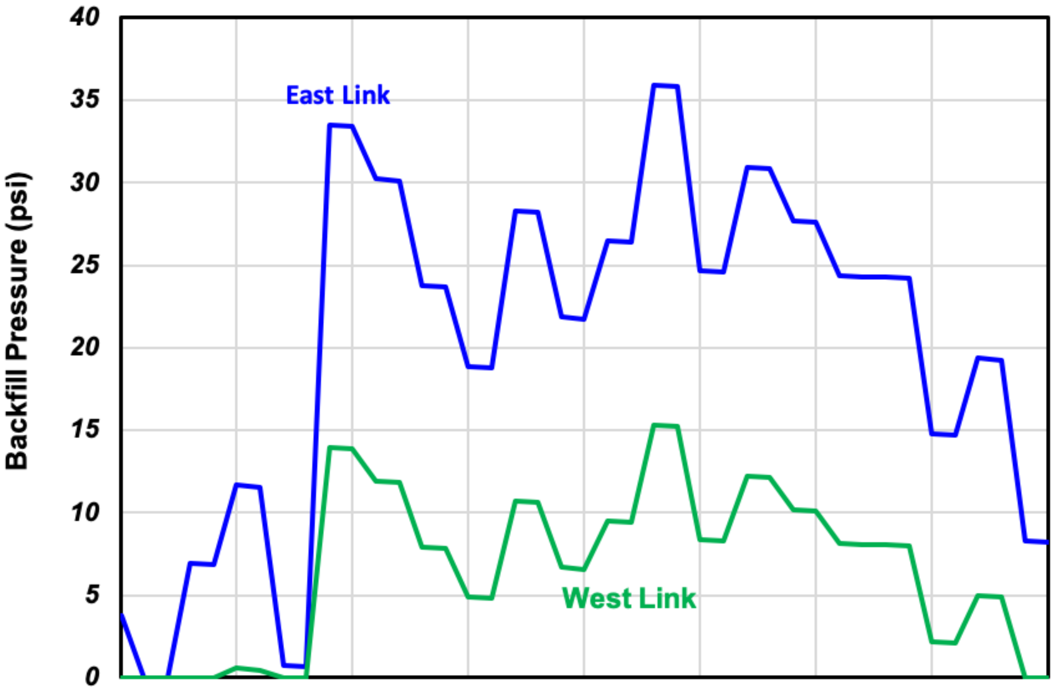

(a) finite element model

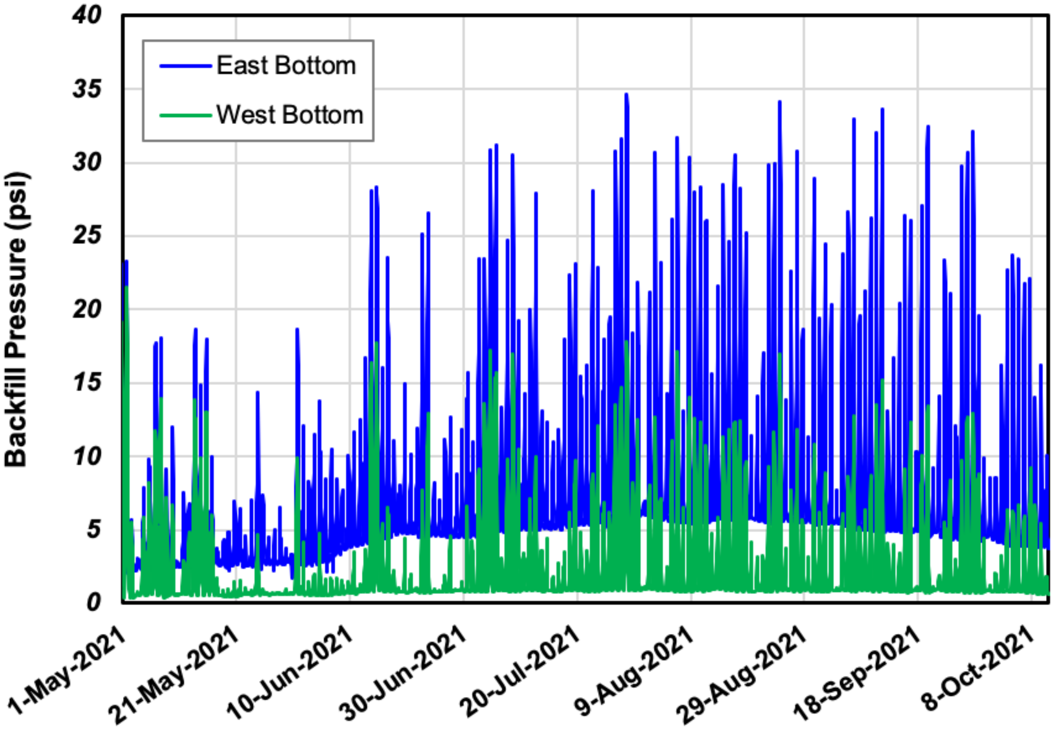

(b) field measurements

Figure 5.21: Comparisons between the South Abutment Backfill Pressures

However, comparing the FE pressure cell results with the field data, the research team found that the overall behavior of backfill pressure change does not match. While the FE pressure results decline with each cycle due to shrinkage strains, the field pressure data seems to increase over time. A bridge contraction may cause the backfill soil near the abutment wall to become loose, drop, and fill the gap. Then, with smaller outward displacements, higher backfill pressures can be reached in the next cycle.

Figure 5.22 displays the FE results for the pressure acting on the north abutment. There is a similar trend to the south abutment (decline over time), with the east link experiencing higher pressures than the west link. During the first two cycles, the east link's maximum pressure was 44 and 31 psi, while the west link's maximum pressure was 34 and 18 psi, respectively. Compared to the south abutment, the east and west pressures on the north abutment are closer. During the first cycle, once summer is over, the pressure drops to zero (week 22 for the west link and week 24 for the east link) and remains zero until when the winter is over (week 56 for the west link and week 52 for the east link). At the end of the warm season, the west link's pressure drops faster than the east link while the east link experiences pressures faster in the beginning of the warm season. This trend is also evident from the field data shown in Figure 4.4. Figure 5.23 shows the comparison between the second cycle of the FE numerical modeling and the first cycle of the field data. Similar to the south abutment, both trend and range are in acceptable conformity.

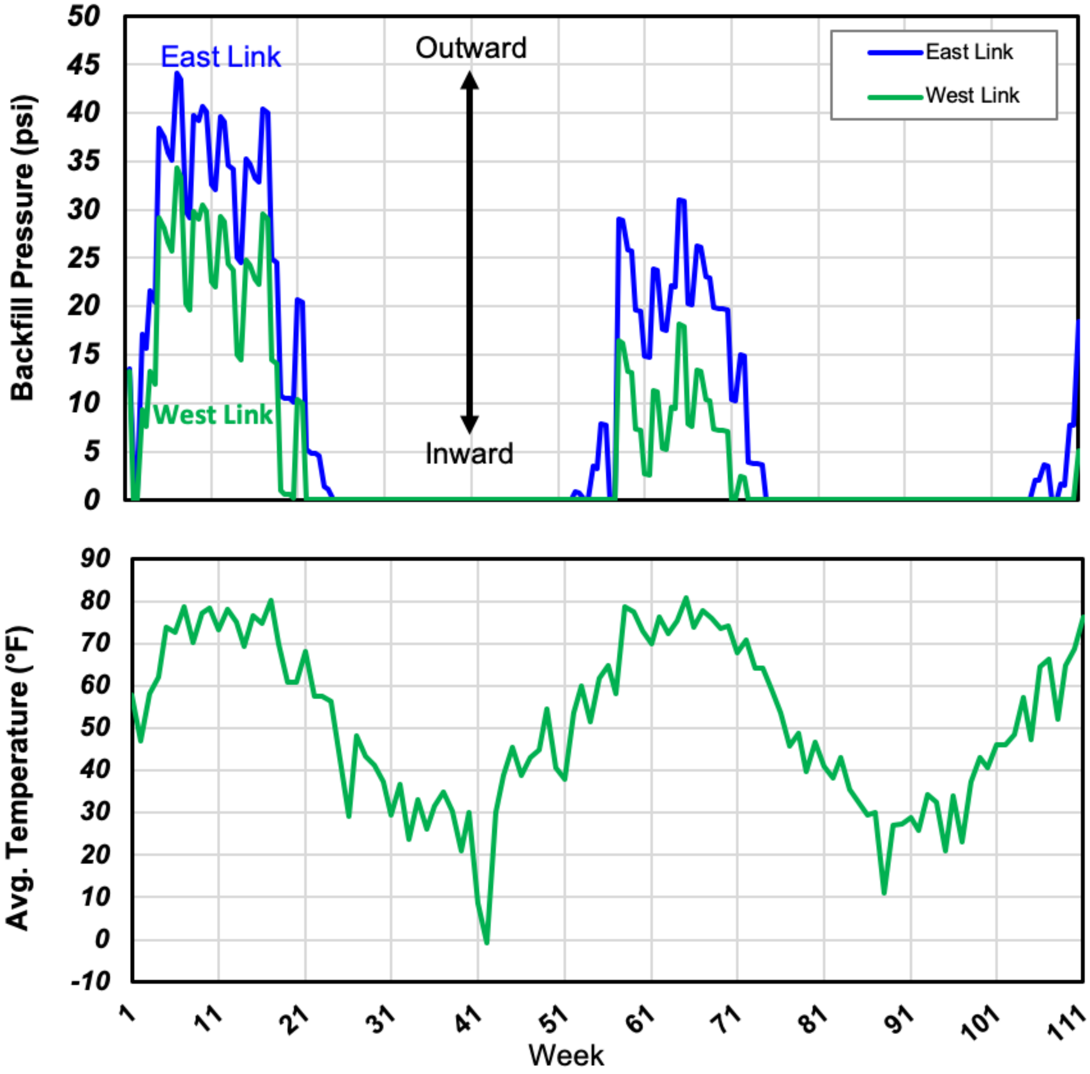

Figure 5.22: Pressure and Average Temperature Variation of the Nonlinear Links on the North Abutment

5.7.2 Pile Deflection

Due to the loss of all fiber optic cables attached to the piles, it is essential to compare pile deformations with inclinometer deformations. While these two are not supposed to be exactly identical because inclinometers measure soil deformations and this is different from pile deflections. However, their intensity should be in the same range because they are only two to three feet apart from each other.

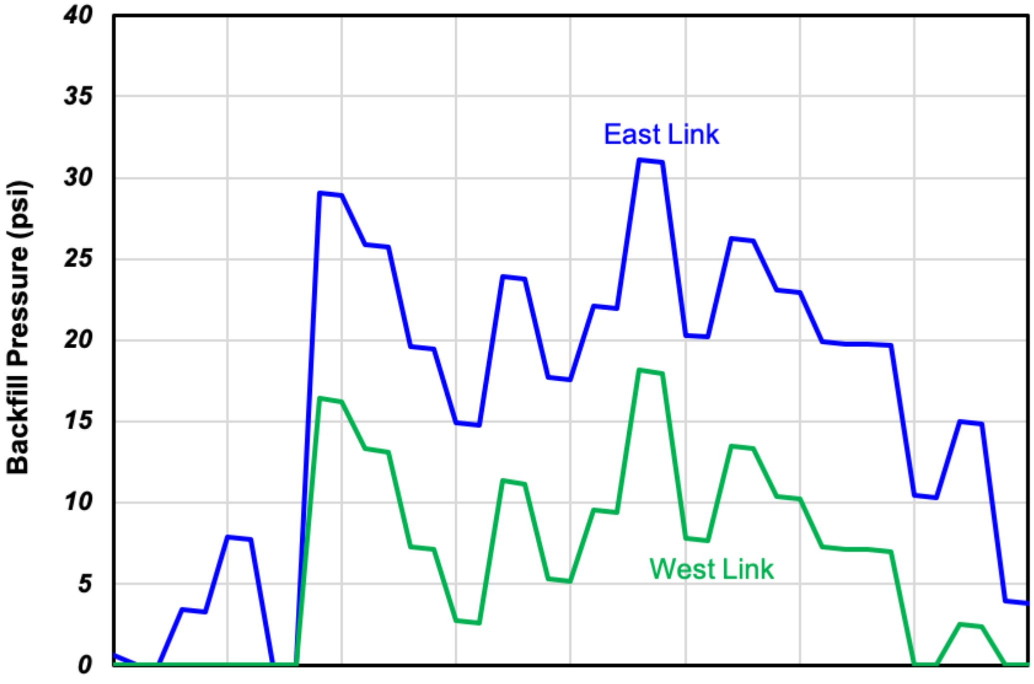

(a) finite element model

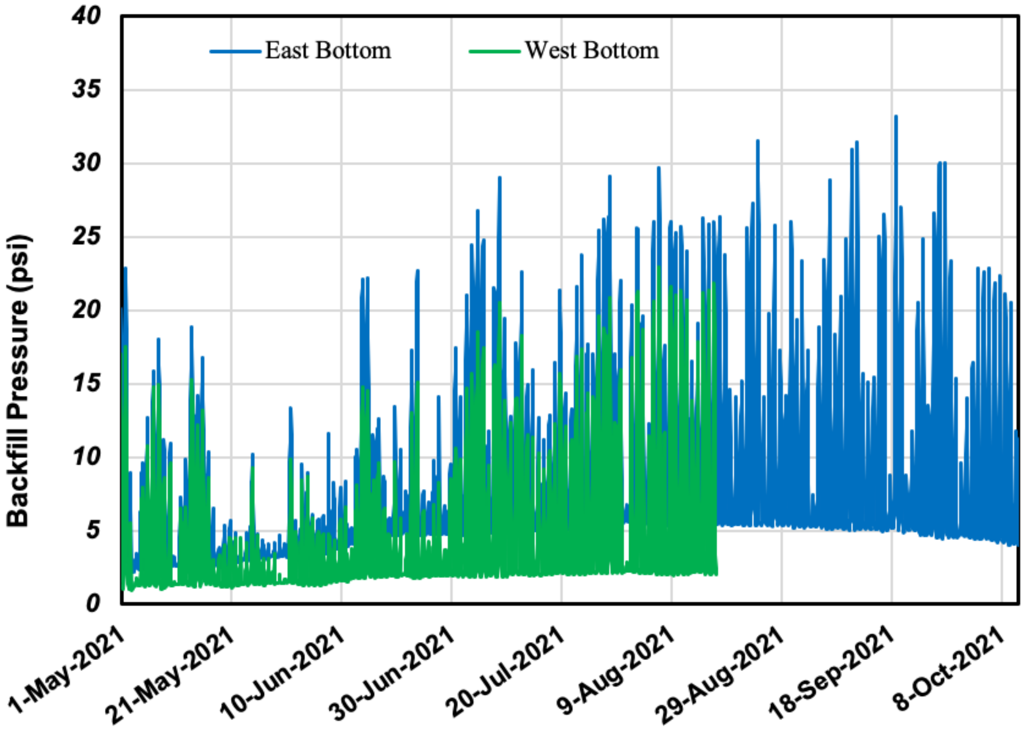

(b) field measurements

Figure 5.23: Comparisons between the North Abutment Backfill Pressures

The March 5, 2021 deflections was used as a benchmark, in line with the previous chapter's assumption. Figures 5.24 through 5.27 compare longitudinal corner pile deflections with longitudinal inclinometer readings for June 17, 2021, where the inclinometer readings were highest. Depth 0 in these figures represents the top of the pile where it goes into the abutment. Figure 5.24 shows that these two deflections are completely different, as one would expect. Due to the movement of the abutment and consequently the backfill behind it, there is always a jump in deflection at around 10 feet depth (here 6 feet since the top 4 feet are not shown) in the inclinometer readings which cannot be seen in the pile deflection. However, the longitudinal inclinometer reading at the bottom of the abutment (depth = 0) in this case is 0.44 in. which is close to 0.42 in. derived from the FE analysis.

Similar comparisons are shown in Figure 5.25 for the southwest inclinometer and pile. Similar to the southeast inclinometer, this inclinometer has a similar deflection. There is a 0.44 in. deflection at the top of the pile, and a 0.38 in. deflection at the same depth for the inclinometer measurements. Because the north abutment's span length is shorter, longitudinal pile and inclinometer deformations are smaller than those on the south abutment which was expected. As Figure 5.26 displays, top of the corner pile on the east side of the north abutment deflects 0.2 in. while the inclinometer reading shows a 0.18 in. deflection.

Finally, Figure 5.27 shows this comparison for the northwest inclinometer and its corresponding corner pile. The top of the pile and inclinometer at the same height deflect 0.25 and 0.27 in., respectively, as shown in this figure. Despite the difference in the deflection profiles of these piles and the inclinometer readings for June 17, 2021, the deflection at the top of the pile and the inclinometer at the same height are comparable.

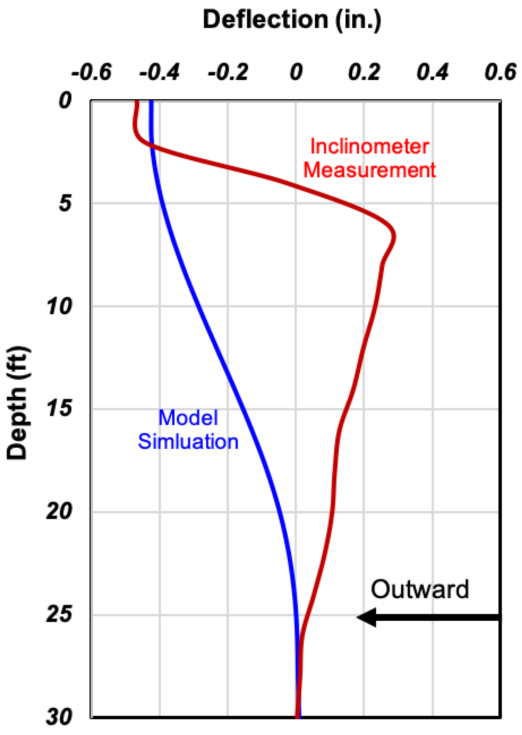

Figure 5.24: Comparisons between Simulated Longitudinal Pile Deflection and Inclinometer Measurements for June 17, 2021 (Southeast Sensor)

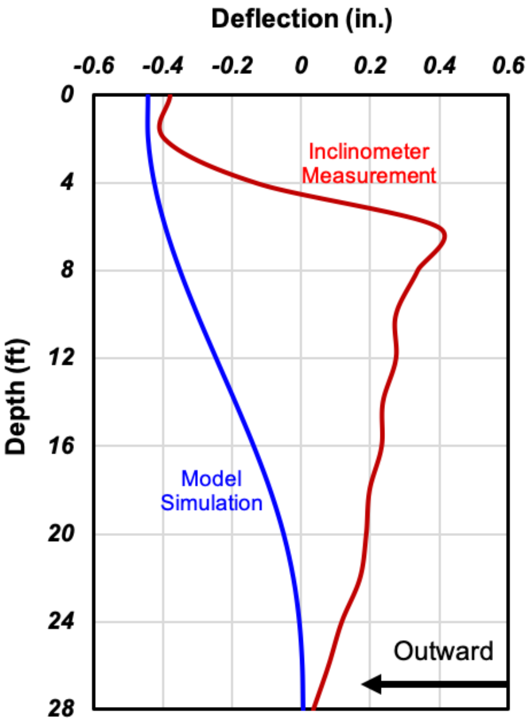

Figure 5.25: Comparisons between Simulated Longitudinal Pile Deflection and Inclinometer Measurements for June 17, 2021 (Southwest Sensor)

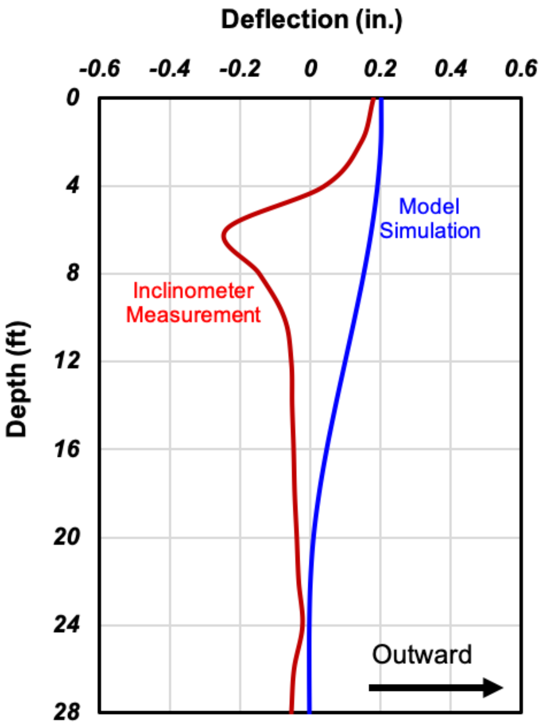

Figure 5.26: Comparisons between Simulated Longitudinal Pile Deflection and Inclinometer Measurements for June 17, 2021 (Northeast Sensor)

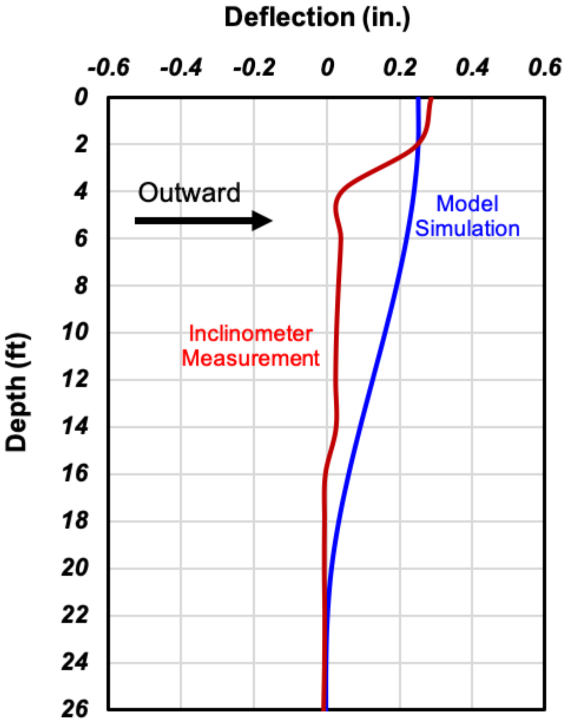

Figure 5.27: Comparisons between Simulated Longitudinal Pile Deflection and Inclinometer Measurements for June 17, 2021 (Northwest Sensor)

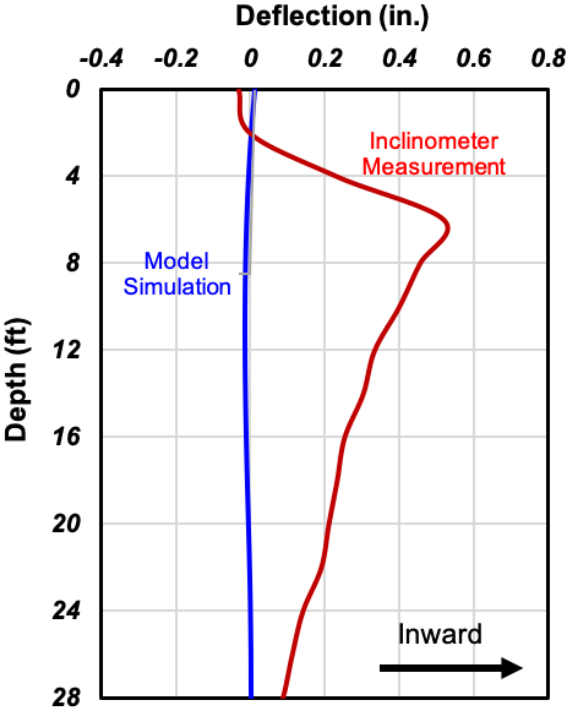

Figure 5.28: Comparisons between Simulated Longitudinal Pile Deflection and Inclinometer Measurements for November 17, 2021 (Southeast Sensor)

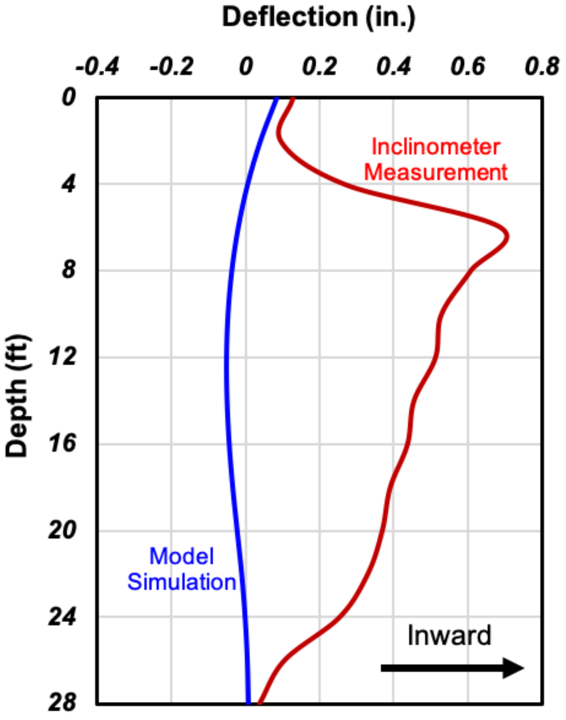

Figure 5.29: Comparisons between Simulated Longitudinal Pile Deflection and Inclinometer Measurements for November 17, 2021 (Southwest Sensor)

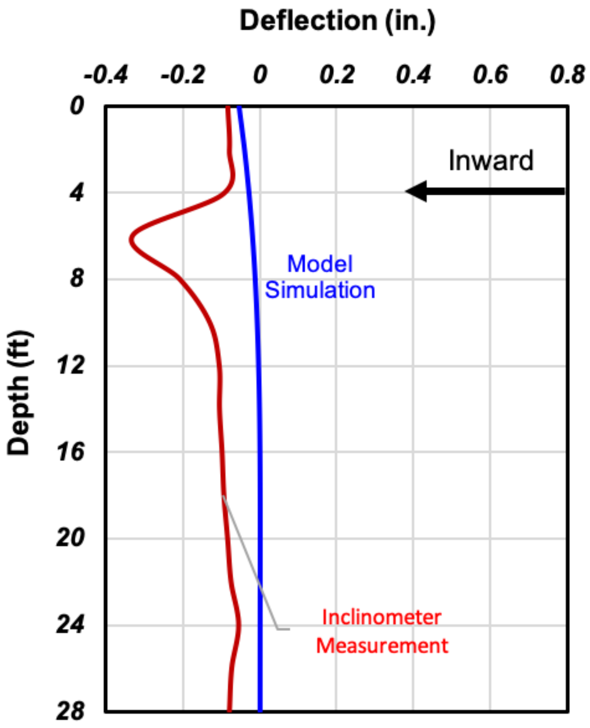

Figure 5.30: Comparisons between Simulated Longitudinal Pile Deflection and Inclinometer Measurements for November 17, 2021 (Northeast Sensor)

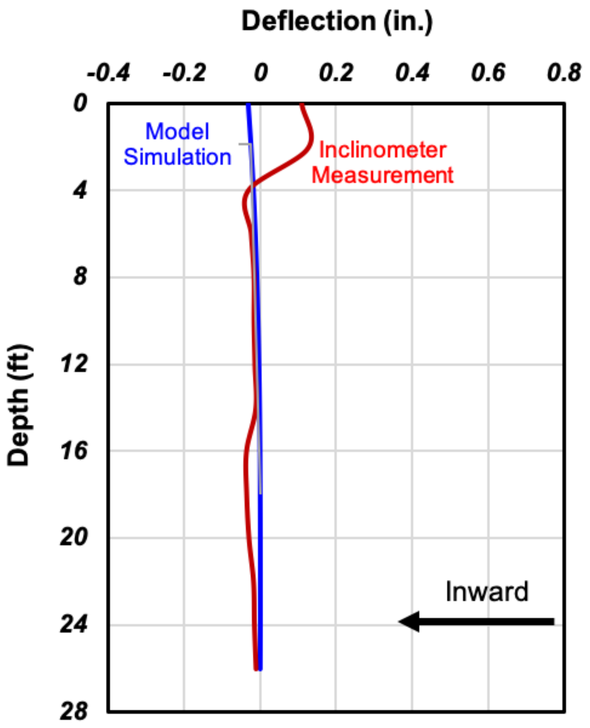

Figure 5.31: Comparisons between Simulated Longitudinal Pile Deflection and Inclinometer Measurements for November 17, 2021 (Northwest Sensor)

Figures 5.28 to 5.31 show the same comparisons but for November 17, 2021, when the inclinometers experience the largest contraction. It should be noticed that there is a difference between contraction and expansion deflections in inclinometers. The reason is that due to the expansion of the bridge, abutments push away the backfill soil, causing the top part of the inclinometer to deflect. The inclinometer cannot be pulled inward by the bridge when it contracts, however. These four figures show that except for the northwest case, top of the pile and the corresponding inclinometer readings are close. The above reasoning may be used to explain a 0.14–in. difference between the northwest inclinometer and pile readings.

5.7.3 Tiltmeter

The results of FE simulation are presented in this section, along with comparisons with the field data. For this comparison, a point on each abutment, 4 feet below the top, was selected to be consistent with the field data readings. According to Figure 5.32, south abutment shows a greater longitudinal tilt than its north counterpart since it is connected to a longer span. Furthermore, for both abutments, contraction tilts are larger than expansion tilts since soil resistance is absent when the bridge contracts. Last but not least, notice how closely the tilts follow the ambient temperature.

In the previous section, we discussed the need to compare the second cycle of FE simulation results with the first cycle of field data. This comparison is shown in Figure 5.33 for the south abutment. In winter, the bridge contracts resulting in a maximum tilt of 0.2° in the FE model, while the field data shows a tilt of almost 0.25°. The maximum tilts for the bridge expansion are 0.085° and 0.1°, respectively, based on numerical simulations and field data. According to these results, the numerical simulation under predicts the field data by 15–20%.

Despite this, the overall trend and range of the data are comparable. Similarly, Figure 5.34 shows that for the north abutment, the maximum contraction tilts are very close. It is 0.13° for the numerical simulation while 0.14° for the field data. In contrast, the FE model underestimates the expansion tilt by 30% (0.1° versus 0.07° for the FE model and field data, respectively). In the same way as the south abutment, FE simulations and field data show similar trends and ranges.

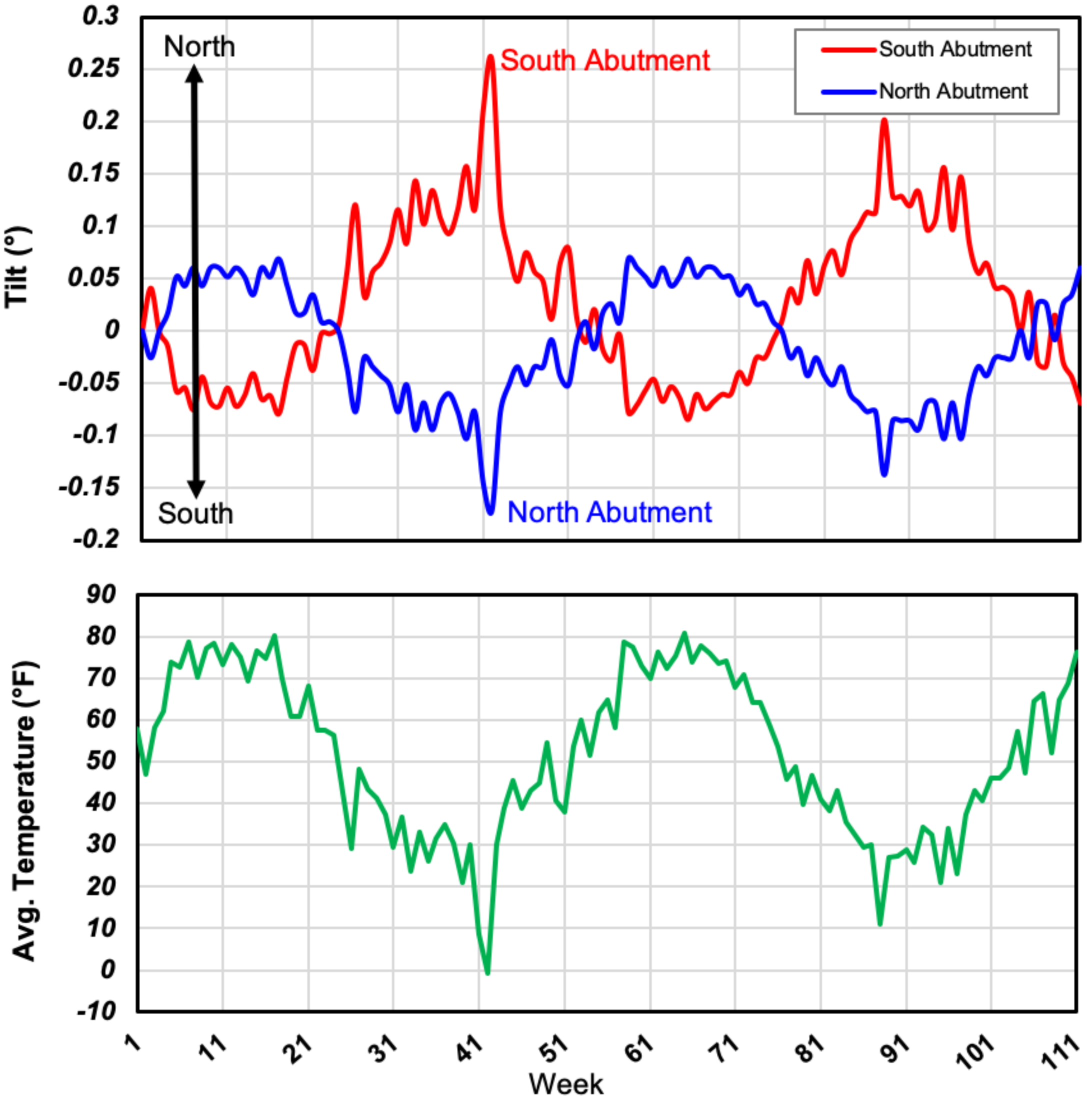

Figure 5.32: Model Simulation Results of North and South Abutments Tilts and Corresponding Weekly Average Temperature

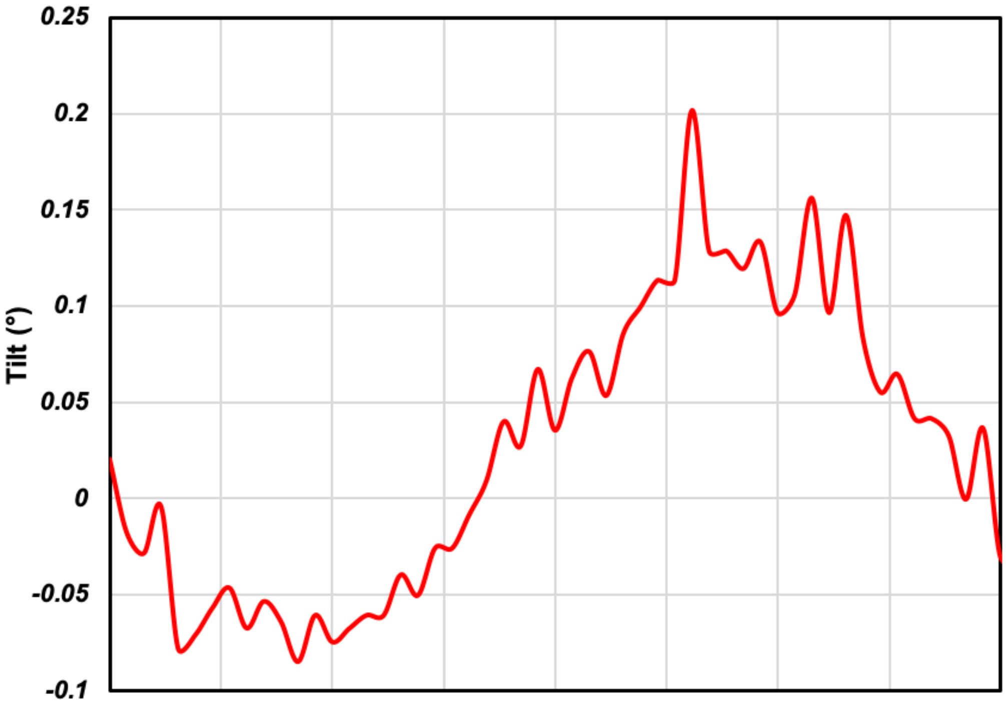

(a) finite element model

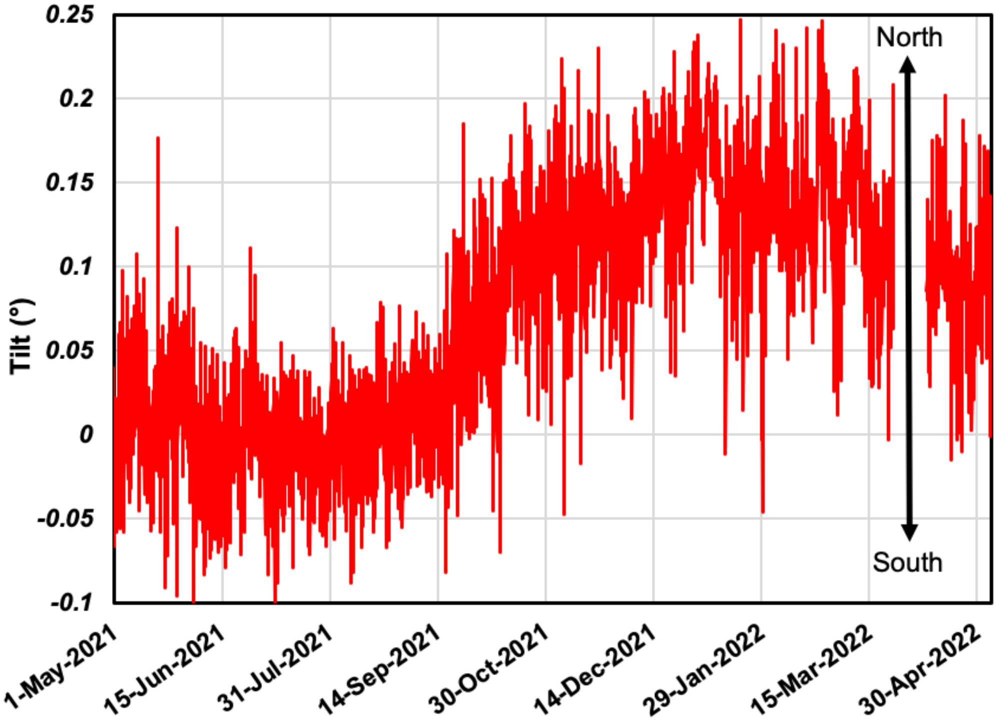

(b) field measurement data

Figure 5.33: Longitudinal Tilt of the South Abutment

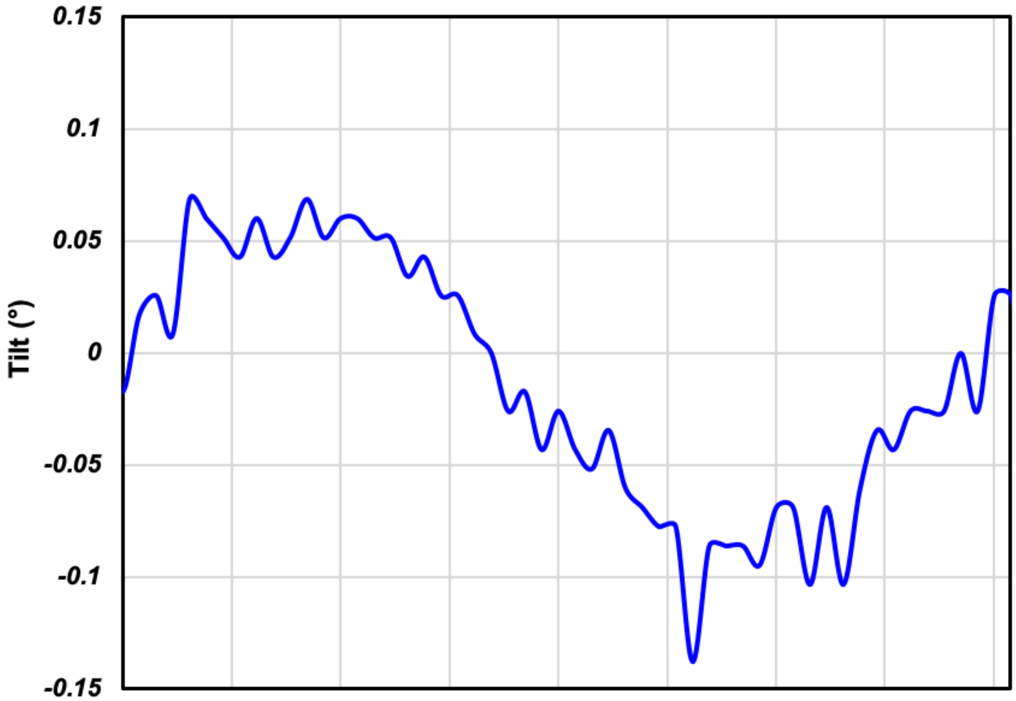

(a) finite element model

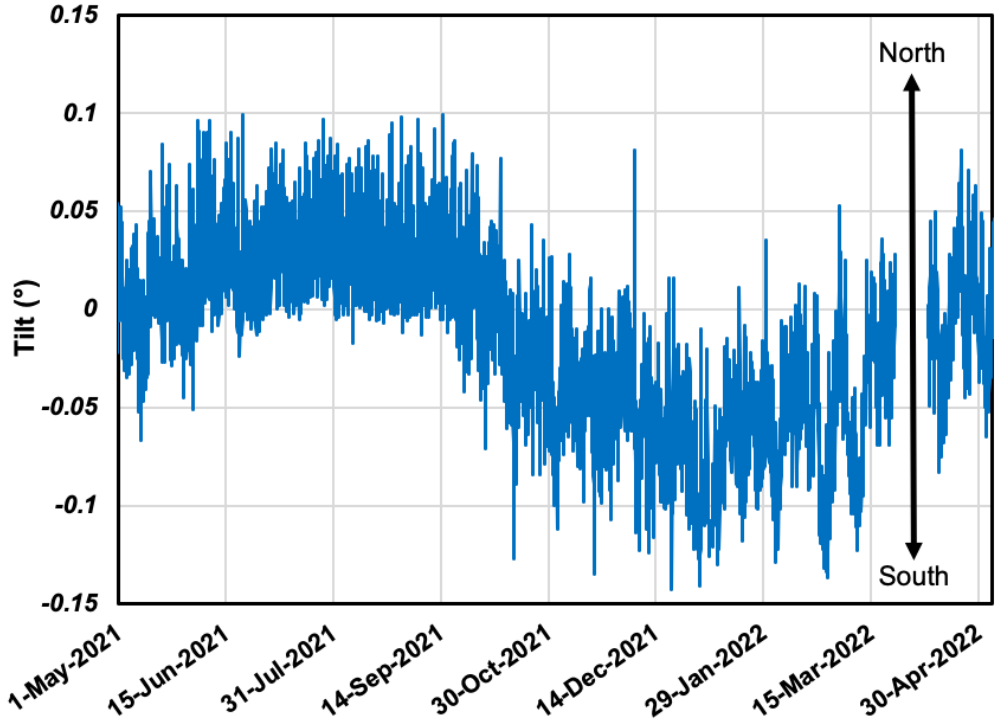

(b) field measurement data

Figure 5.34: Longitudinal Tilt of the North Abutment

5.8 Summary

This chapter describes the steps involved in generating an FE model for the Big Springs bridge. Following the modeling process, the FE model was analyzed under temperature and shrinkage loads to compare with the results obtained in the field. Our comparisons were based on pressure cells, tilt meters, and inclinometer measurements, as we were unable to measure deflection of the bridge. According to this comparison, the FE pressures follow a different pattern than the field pressure cells. The overall FE pressure trend is decreasing due to shrinkage, while the field data indicates a build-up pressure. In spite of this difference, the magnitudes of the pressures are comparable. Comparison of inclinometer deflections with pile deflections gives us a sense of whether FE deflections are close to field data. These deflections, however, measure different things, so they aren't supposed to be the direct comparison, but the trend can be compared. However, although their overall deflection profiles are different, their deflections at the bottom of the abutment (top of the pile) have acceptable similarities and is comparable. Finally, FE abutment tilts tend to be 20-25% off from field tilt meters on average, while the general trend is similar. In addition, this degree of matching is promising, considering the field soils are natural materials with high variability. With the pressure behind the abutment and the displacement at the top of the pile in good agreement with the field measurements, parametric studies were conducted to investigate the limits of the curved full integral abutment bridges and the details of the studies are included in the next chapter. In addition, the tilts that closely follow the ambient temperature change, is also well captured in the three-dimensional finite models developed through this study.

6. PARAMETRIC STUDY

6.1 Introduction

To better understand and predict how various parameters and conditions affect the performance of curved IABs, a parametric study was conducted. As shown in Table 6.1, fifty-eight different FE models were generated with unique various geometry and characteristics. A total of six lengths are listed in Table 6.1, ranging from 200 to 1,200 ft in 200–ft increments. For every bridge length, a span length of 100 ft was considered. Finally, various radii of curvature are taken into account for each combination of total and span length. There is a wide range of radii between 200 and 1,800 ft in 600–ft increments representing severe to moderate bridge curvatures. The maximum degree of curvature allowed for all bridges is 90°, so longer bridges cannot have shorter curvatures (e.g., 200– and 600–ft curvatures are not included in 1,000– and 1,200–ft long bridge models). There is a radius of infinity at the end of each combination, which indicates a straight bridge, in order to see how straight and curved bridges perform differently. The main loads affecting the long–term performance of IABs are temperature fluctuations and concrete shrinkage of the deck. Therefore, the research team will focus only on these two loads for this parametric study.

Table 6.1: Geometric Parameters of the Numerical Models

No.	Total Length (ft)	Span Length (ft)	No. of Spans	Radius (ft)	Degree of Curvature (°)
1	200	100	2	200	57.3
2				600	19.1
3				1,000	11.5
4				1,400	8.2
5				1,800	6.4
6				∞	0
7	200	200	1	200	57.3
8				600	19.1
9				1,000	11.5
10				1,400	8.2
11				1,800	6.4
12				∞	0
13	400	100	4	600	38.2
14				1,000	22.9
15				1,400	16.4
16				1,800	12.7
17				∞	0
18	400	200	2	600	38.2
19				1,000	22.9
20				1,400	16.4
21				1,800	12.7
22				∞	0
23	600	100	6	600	57.3
24				1,000	34.4
25				1,400	24.6
26				1,800	19.1
27				∞	0
28	600	200	3	600	57.3
29				1,000	34.4
30				1,400	24.6
31				1,800	19.1
32				∞	0
33	800	100	8	600	76.4
34				1,000	45.8
35				1,400	32.7
36				1,800	25.5
37				∞	0
38	800	200	4	600	76.4

No.	Total Length (ft)	Span Length (ft)	No. of Spans	Radius (ft)	Degree of Curvature (°)
39				1,000	45.8
40				1,400	32.7
41				1,800	25.5
42				∞	0
43	1,000	100	10	1,000	57.3
44				1,400	40.9
45				1,800	31.8
46				∞	0
47	1,000	200	5	1,000	57.3
48				1,400	40.9
49				1,800	31.8
50				∞	0
51	1,200	100	12	1,000	68.8
52				1,400	49.1
53				1,800	38.2
54				∞	0
55	1,200	200	6	1,000	68.8
56				1,400	49.1
57				1,800	38.2
58				∞	0

6.2 Bridge Properties

The Big Springs bridge model that was discussed in Chapter 5 is the baseline of most of the properties of the bridge models in this chapter, such as steel girders, concrete deck, pipe piles, granular backfill, shrinkage loads, CMP sleeves and soil around piles, unless stated otherwise. The only differences are that the bridge width is 36 ft, and each pier has two circular concrete columns. To make these bridges symmetrical, soil–pile springs on both abutments are similar to the soil–pile springs on the north abutment of the Big Springs bridge site.

6.3 Shrinkage Load

CSiBridge includes a variety of shrinkage model, some of which are displayed in Figure 6.1. In this figure, the cumulative strain is represented over the first 2,000 days after construction and shrinkage has begun. Based on this figure, the shrinkage models differ in terms of the initial rates of how shrinkage changes over time and total strain values. Therefore, selecting the most appropriate shrinkage model is important. Lovell (2010) concluded that the CEB–FIP 90 shrinkage model performs best for capturing the IABs long–term inward (contraction) movements. In this study, the CEB-FIP 90 shrinkage model will be used as the default model in the parametric study since the weather in Nebraska is similar to Indiana following the conclusions of Lovell's study. Due to the high initial rate and total strain after 2,000 days, ACI 209R–92 model was selected as the second shrinkage model in the parametric study. The strain values for these two models are shown in Table 6.2.

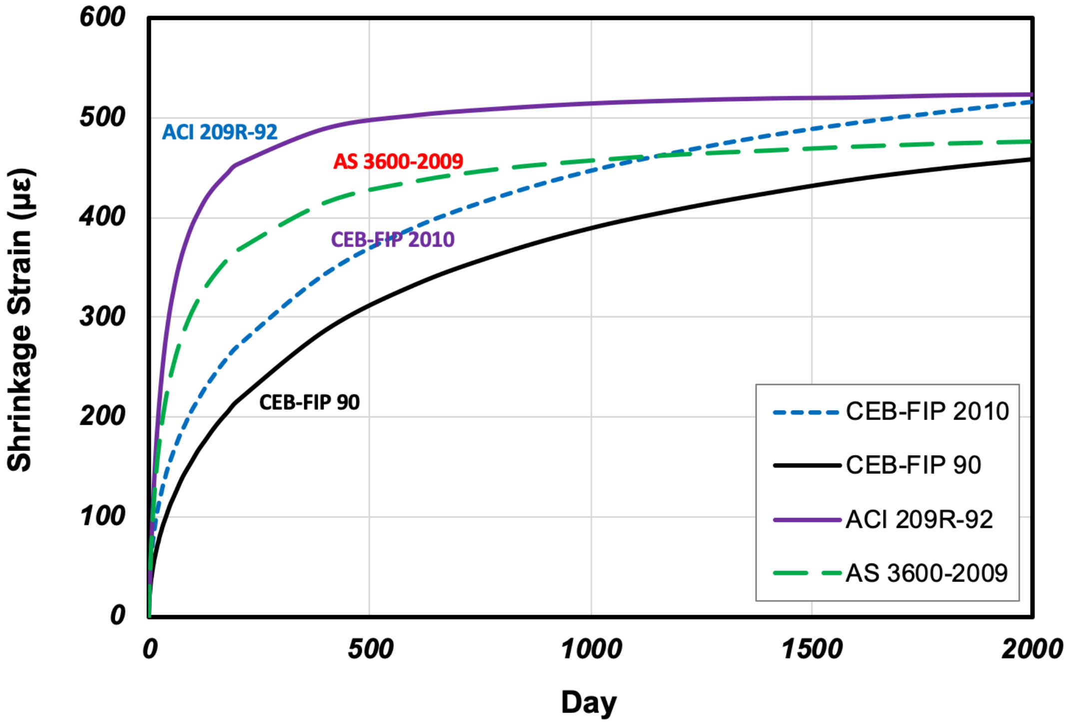

Figure 6.1: Shrinkage Models in CSiBridge

Table 6.2: Shrinkage Strains and Temperature Fluctuations used in the Parametric Study

Date	Days	Shrinkage Model				Temperature (°F)	ΔT (°F)
		ACI 209R–90		CEB–FIP 90			
		Total Strain, ε (ft/ft)	Δε (×10^6) (ft/ft)	Total Strain, ε (ft/ft)	Δε (×10^6) (ft/ft)		
May, 2020	0	0	0	0	0	60	0
Aug, 2020	124	4.15E-04	414.5	1.75E-04	174.7	120	60
Feb, 2021	307	4.72E-04	57.5	2.54E-04	79.2	-10	-130
Aug, 2021	490	4.95E-04	23	3.07E-04	53.2	120	130
Feb, 2022	673	5.05E-04	10	3.44E-04	36.7	-10	-130
Aug, 2022	856	5.11E-04	5.7	3.71E-04	27.4	120	130
Feb, 2023	1039	5.14E-04	3.6	3.93E-04	21.6	-10	-130
Aug, 2023	1222	5.17E-04	2.6	4.10E-04	17.4	120	130
Feb, 2024	1405	5.19E-04	1.9	4.25E-04	14.5	-10	-130
Aug, 2024	1588	5.20E-04	1.5	4.37E-04	12.1	120	130
Feb, 2025	1771	5.21E-04	1.1	4.47E-04	10.3	-10	-130

6.4 Temperature Load

According to the Nebraska DOT Bridge Office Policies and Procedures (2016), steel bridges with concrete decks should be designed for a temperature range of 130 °F (-10 °F to 120 °F). This range falls between the two temperature ranges that AASHTO recommends for moderate and cold climates (0 °F to 120 °F for moderate and -30 °F to 120 °F for cold). Based on this recommendation, a seasonal temperature fluctuation of 130 °F was used in this study. In addition, the research team assumed that all bridge models were built in May 2020 (following the construction schedules of Big Springs bridge site) at an ambient reference temperature of 60 °F. Table 6.2 shows these temperature changes.

6.5 Soil-Pile Springs

Based on what was discussed previously, the default backfill soil and soil around the piles will have similar soil conditions as those in the Big Springs bridge site. In addition, we examined the effects of various soil conditions on the performance of curved IABs by including four additional types of soil in the models, including: Loose Sand, Dense Sand, Very Soft Clay and Very Dense Clay. Griemann et al. (1987) proposed expressions for soil ultimate resistance (P_u) and initial soil modulus (E_s) for both cohesive and non–cohesive soils. For soft clay, these two parameters are as follows:

$$E_s(z) = \frac{P_u}{y_{50}} \tag{6.1}$$

$$P_u(z) = min\begin{Bmatrix} \left[3 + \frac{\gamma}{C_u} z + \frac{0.5}{B} z\right] c_u B \\ 9 c_u B \end{Bmatrix} \tag{6.2}$$

and for very stiff clay,

$$E_s(z) = \frac{P_u}{2y_{50}} \tag{6.3}$$

$$P_u(z) = min\begin{Bmatrix} \left[3 + \frac{\gamma}{C_u} z + \frac{2}{B} z\right] c_u B \\ 9 c_u B \end{Bmatrix} \tag{6.4}$$

where:

P_u = soil ultimate resistance, kip/ft

c_u = soil shear strength (cohesion), psf

γ = soil unit weight, lbs/ft^3

B = dimension of the pile parallel to the axis of bending, ft

z = depth from the surface, ft

y_{50} = displacement at half ultimate soil resistance, ft

very soft clay → 2.5 B $\boldsymbol{\varepsilon_{50}}$

very stiff clay → 2 B $\boldsymbol{\varepsilon_{50}}$

$\boldsymbol{\varepsilon_{50}}$ = axial strain at half peak stress from the tri–axial test

very soft clay → 0.02

very stiff clay → 0.005

They proposed the following equations for sand:

$$E_s(z) = \frac{J\gamma}{1.35} z \tag{6.5}$$

$$P_u(z) = 3\gamma B K_p B \tag{6.6}$$

where:

J = 200 for loose sand ($\varphi = 30°$)

= 1500 for dense sand ($\varphi = 40°$)

φ = soil internal angle of friction, degrees

γ = soil unit weight, pcf

z = depth from the surface, ft

B = dimension of pile (outer diameter of pipe piles) parallel to the axis of bending, ft

K_p = coefficient of passive pressure

The soil properties for the four soil types are shown in Table 6.3. In addition, the parameter B represents the outer diameter of pipe piles (12 in.). Finally, soil stiffness is calculated by multiplying the calculated soil modulus by spring spacing (2 ft).

Table 6.3: Soil Properties for the Parametric Study

Soil	**Consistency**	**Soil Unit Weight, pcf (γ)**	**Internal Angle of Friction, degrees (ϕ)**	**Undrained Shear Strength, psf (C_u)**
Sand	Loose	110	30	
	Dense	130	40	
Clay	Very Soft	110		250
	Very Stiff	130		3000

Similar to the Big Springs bridge site, it is assumed that the top 18 ft of each abutment piles are enclosed within a CMP sleeve covered with loose sand. Therefore, springs are not modeled for this portion of the piles. Tables 6.4 and 6.5 show lateral spring stiffnesses that we used to model Loose and Dense sand as well as Very Soft and Very Dense Clay, respectively. In addition, Table 6.5 shows that the soil stiffness is constant for both Very Soft and Very Dense clay regardless of depth. This is because the expression $9c_uB$ of Equations 6.2 and 6.4 becomes the minimum after depths of 4 and 8 ft for Very Stiff and Very Soft clay, respectively. Lastly, Figure 6.2 illustrates a typical bilinear force–displacement curve used to model soil–pile springs.

Table 6.4: Soil Stiffness for Loose and Dense Sand

Pile Depth (ft)	Lateral Soil–Pile Spring Stiffness (kip/in)	
	Loose Sand	Dense Sand
18	49	433
20	54	481
22	60	530
24	65	578
26	71	626
28	76	674
30	81	722
32	87	770
34	92	819
36	98	867
38	103	915
40	109	963
42	114	1011
44	120	1059
46	125	1107
48	130	1156
50	136	1204
52	141	1252
54	147	1300
56	152	1348
58	158	1396
60	163	1444
62	168	1493
64	174	1541
66	179	1589
68	185	1637
70	Fixed	Fixed

Table 6.5: Soil Stiffness for Very Soft and Very Stiff Clay

Pile Depth (ft)	Lateral Soil–Pile Spring Stiffness (kip/in)	
	Very Soft Clay	Very Stiff Clay
18	15	225
20	15	225
22	15	225
24	15	225
26	15	225
28	15	225
30	15	225
32	15	225
34	15	225
36	15	225
38	15	225
40	15	225
42	15	225
44	15	225
46	15	225
48	15	225
50	15	225
52	15	225
54	15	225
56	15	225
58	15	225
60	15	225
62	15	225
64	15	225
66	15	225
68	15	225
70	Fixed	Fixed

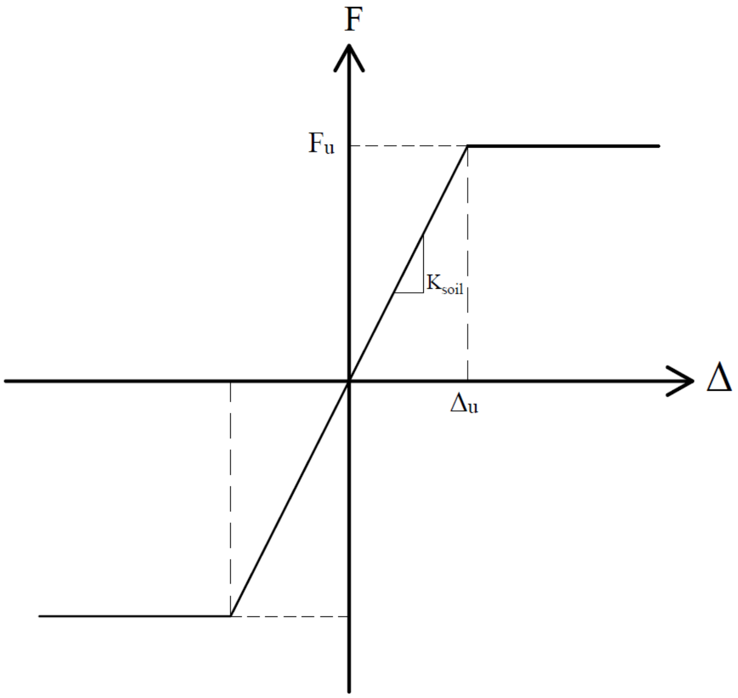

Figure 6.2: Bilinear Force Displacement Relationship of Soil–Pile Springs

6.6 Bearings

Figure 6.3 shows the default bearing configuration for all the bridge models. This figure shows that all girders are mounted on roller bearings except for the middle girder, which sits on a longitudinal roller (guided roller). Throughout this chapter, we will refer to this configuration as the Mixed bearing configuration. A longitudinal roller has restrictions against its lateral movement. As a result, it can only move along the tangent line at the pier location (perpendicular to the radius). Three additional bearing configurations including Rollers, Longitudinal Rollers, and Fixed bearings are added to our models in order to better understand the impact of intermediate bearings on curved IABs. Fixed bearings are restrained against all movements but can rotate. Figures 6.4 to 6.6 illustrate these configurations.

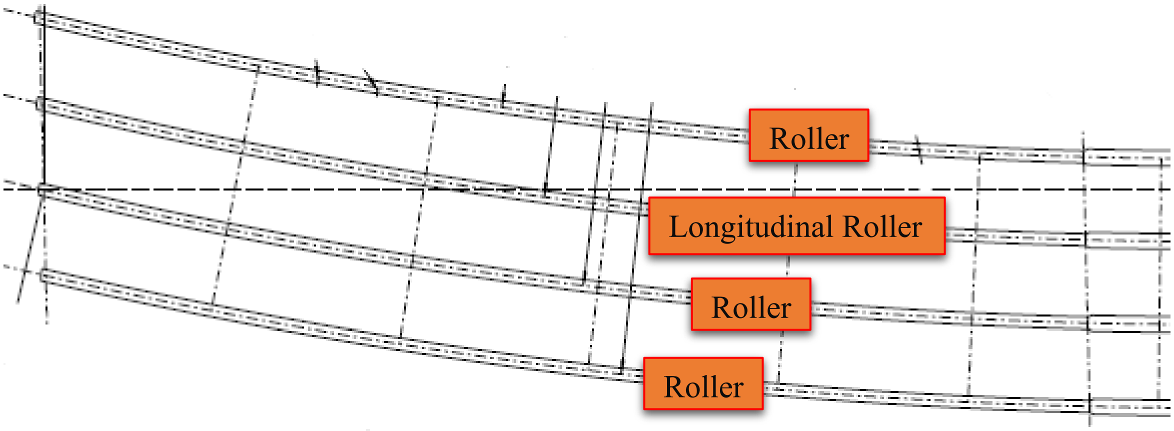

Figure 6.3: Default Bearing Configuration over All Piers

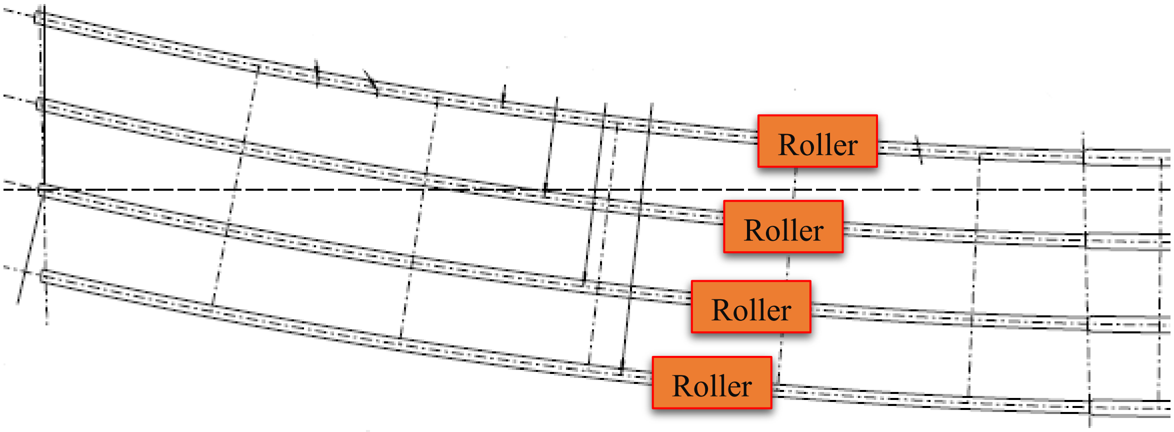

Figure 6.4: Roller Bearing Configuration over All Piers

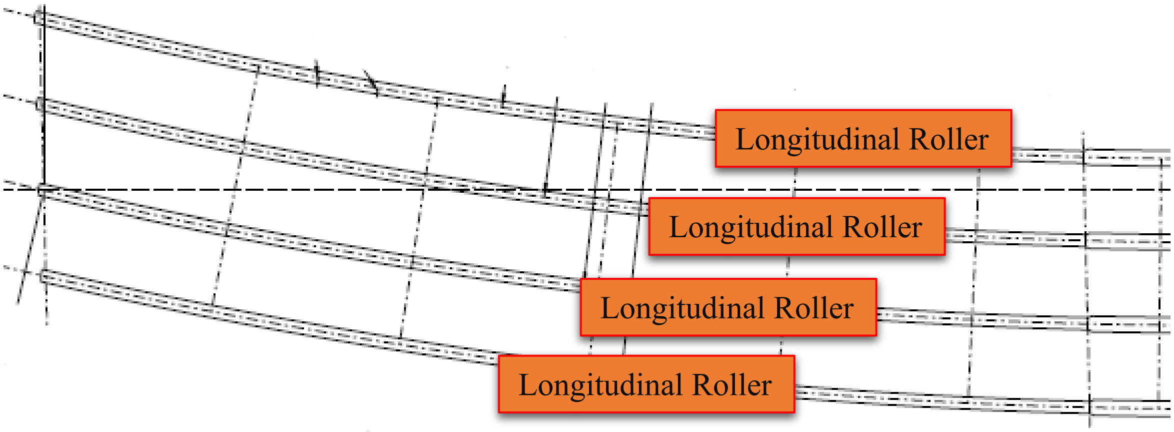

Figure 6.5: Longitudinal Roller Bearing Configuration over All Piers

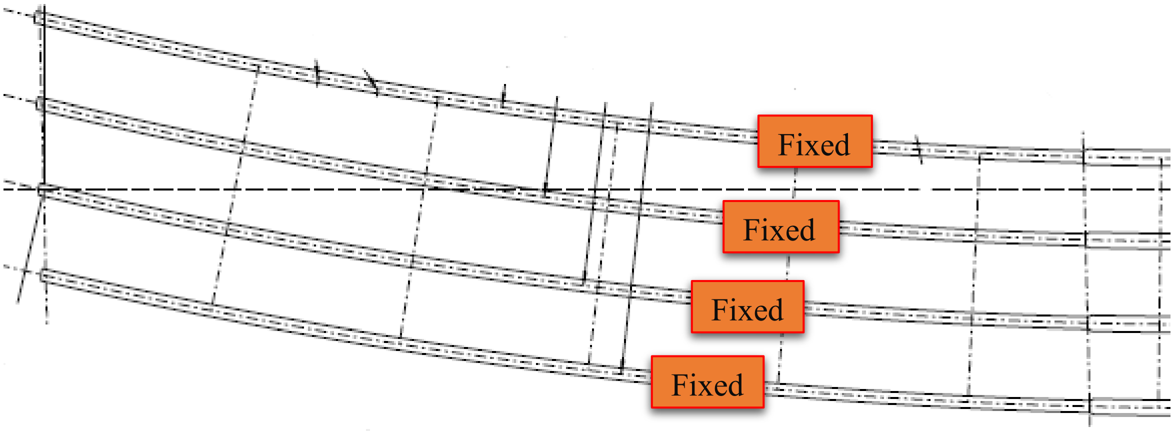

Figure 6.6: Fixed Bearing Configuration over All Piers

6.7 Parametric Study Results

Our method of evaluating the performance of curved IABs with different parameters involves measuring the displacements and stresses at the pile–abutment–girder connections. As mentioned in the previous sections, all properties are default values unless stated otherwise. When examining alternative parameters, however, the research team only considered a 400 ft long bridge with different radii of curvature. Table 6.6 shows the parameters in this study.

Table 6.6: Primary and Secondary Parameters

Primary Variables						
Length (ft)	200	400	600	800	1,000	1,200
Radius of Curvature (ft)	200	600	1,000	1,400	1,800	∞
Secondary Variables						
	Control	**Alternate**				
Temperature (°F)	-10 to +120					
Shrinkage Model	CEB–FIB 90	ACI 209R				
Pile Section	Pipe	HP (Strong Axis)	HP (Weak Axis)			
Bearing	Mixed	Roller	Longitudinal Roller	Fixed		
Soil Stiffness	Big Springs North Abutment	Very Soft Clay	Very Stiff Clay	Loose Sand	Dense Sand	

6.7.1 Length and Curvature

Length and curvature are the two primary variables that we considered in this study. Understanding how the combination of these two factors can influence the overall behavior of curved IABs is essential. We will refer to interior and exterior piles as well as decks in this chapter by using Figure 6.7. Figures 6.8 to 6.15 show the longitudinal and lateral displacements of interior and exterior pile heads and two corners of the deck after 5 years of temperature and shrinkage loading. Because the soil conditions behind the abutments were kept identical in numerical studies of all the bridges, only the results of one abutment are shown in the following sections.

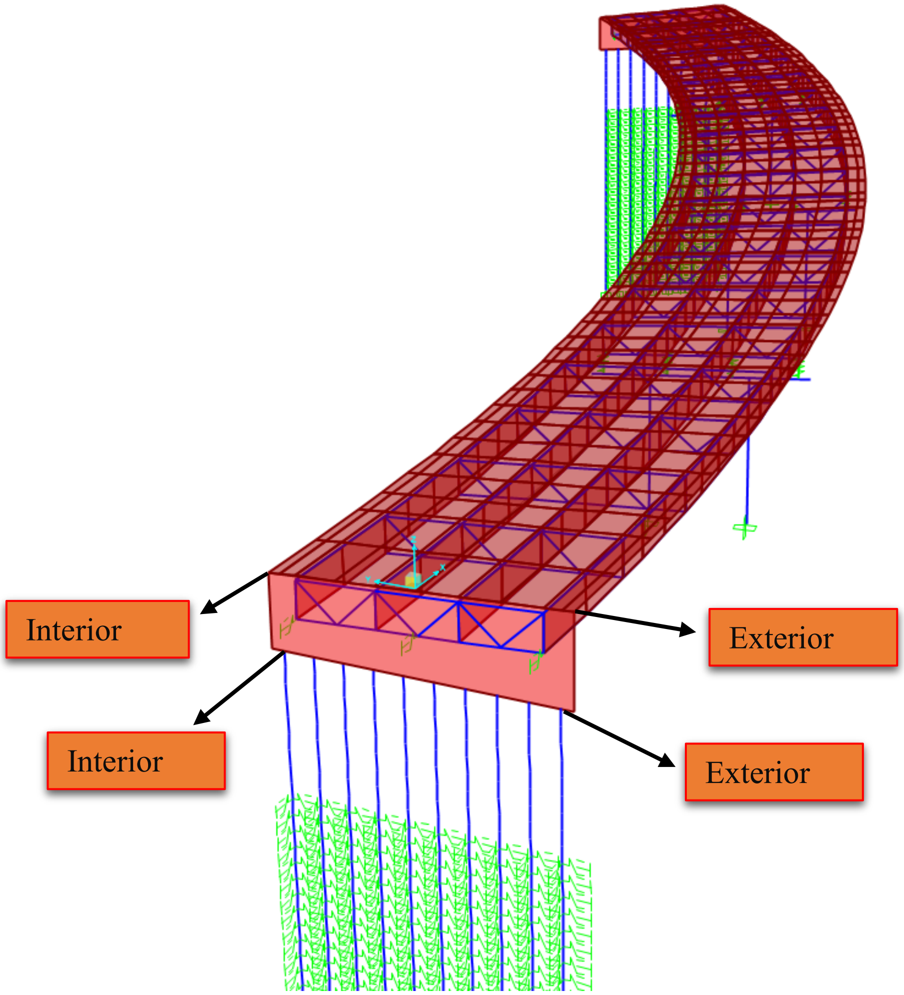

Figure 6.7: Location of Interior and Exterior Pile and Deck Readings

Table 6.7: Interior and Exterior Pile Head and Deck Movements (CEB–FIP 90)

Length (ft)	**Radius of Curvature (ft)**	**Pile Head Longitudinal Movement (in)**		**Pile Head Lateral Movement (in)**		**Deck Longitudinal Movement (in)**		**Deck Lateral Movement (in)**	
		Interior	**Exterior**	**Interior**	**Exterior**	**Interior**	**Exterior**	**Interior**	**Exterior**
200	**200**	0.21	0.09	0.37	0.34	0.76	0.73	0.31	0.41
	600	0.14	0.00	0.15	0.12	0.75	0.74	0.09	0.19
	1,000	0.55	0.46	0.10	0.08	0.94	0.94	0.05	0.14
	1,400	0.27	0.15	0.10	0.07	0.80	0.82	0.04	0.13
	1,800	0.55	0.47	0.08	0.05	0.94	0.95	0.02	0.11
	∞	0.45	0.45	0.05	0.02	0.88	0.88	-0.01	0.08
400	**600**	0.88	0.73	0.35	0.32	1.49	1.48	0.29	0.39
	1,000	1.27	1.17	0.21	0.18	1.72	1.72	0.15	0.25
	1,400	1.28	1.19	0.17	0.14	1.73	1.73	0.11	0.20
	1,800	1.28	1.19	0.14	0.11	1.73	1.73	0.08	0.17
	∞	1.24	1.24	0.05	0.02	1.73	1.73	-0.01	0.08
600	**600**	2.01	1.95	0.37	0.35	2.47	2.52	0.32	0.41
	1,000	2.13	2.06	0.24	0.22	2.60	2.63	0.19	0.28
	1,400	2.06	1.97	0.19	0.16	2.52	2.54	0.13	0.22
	1,800	2.11	2.02	0.16	0.13	2.57	2.59	0.10	0.19
	∞	2.03	2.03	0.05	0.02	2.54	2.54	-0.01	0.08
800	**600**	2.70	2.67	0.38	0.35	3.16	3.26	0.32	0.41
	1,000	2.70	2.64	0.25	0.22	3.17	3.23	0.19	0.28
	1,400	3.02	2.96	0.19	0.16	3.50	3.55	0.13	0.22
	1,800	2.86	2.78	0.16	0.13	3.33	3.37	0.10	0.19
	∞	2.79	2.80	0.05	0.02	3.33	3.33	-0.01	0.08
1,000	**1,000**	3.46	3.42	0.25	0.23	3.94	4.03	0.20	0.29
	1,400	3.77	3.72	0.20	0.17	4.26	4.33	0.14	0.23
	1,800	3.65	3.59	0.16	0.14	4.15	4.20	0.11	0.20
	∞	3.42	3.42	0.05	0.02	3.96	3.96	-0.01	0.08
1,200	**1,000**	4.40	4.39	0.24	0.21	4.90	5.02	0.18	0.27
	1,400	4.47	4.43	0.21	0.18	4.98	5.06	0.15	0.24
	1,800	4.44	4.39	0.17	0.14	4.94	5.01	0.11	0.21
	∞	4.42	4.42	0.05	0.02	4.99	4.99	-0.01	0.08

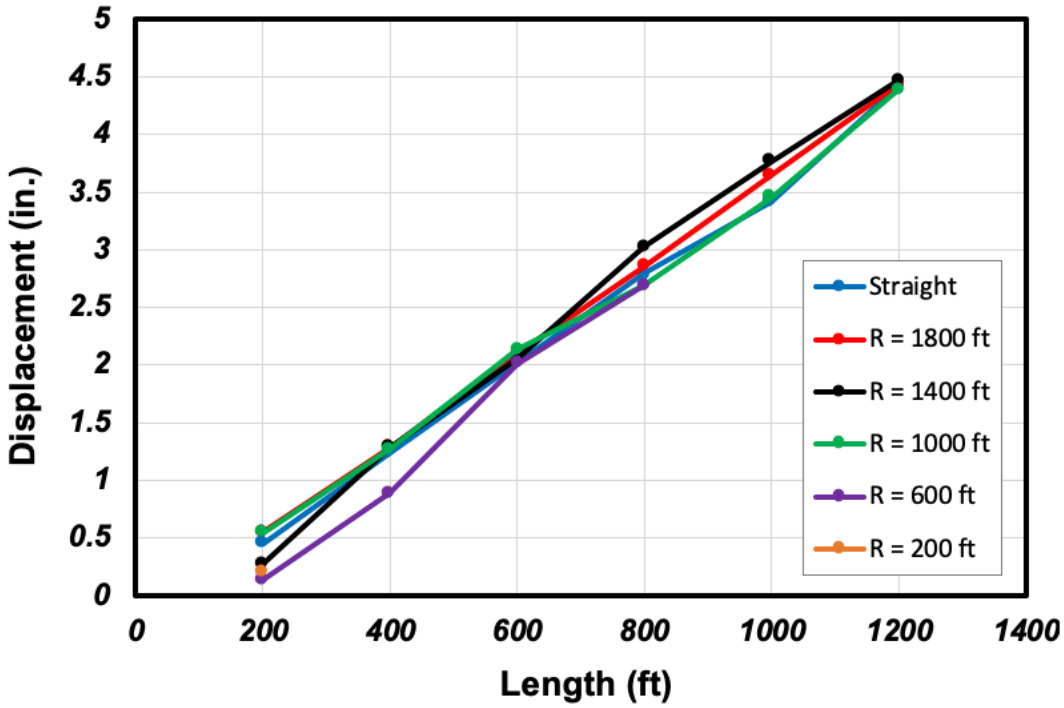

Figure 6.8: Interior Pile Head Longitudinal Movement (CEB–FIP 90)

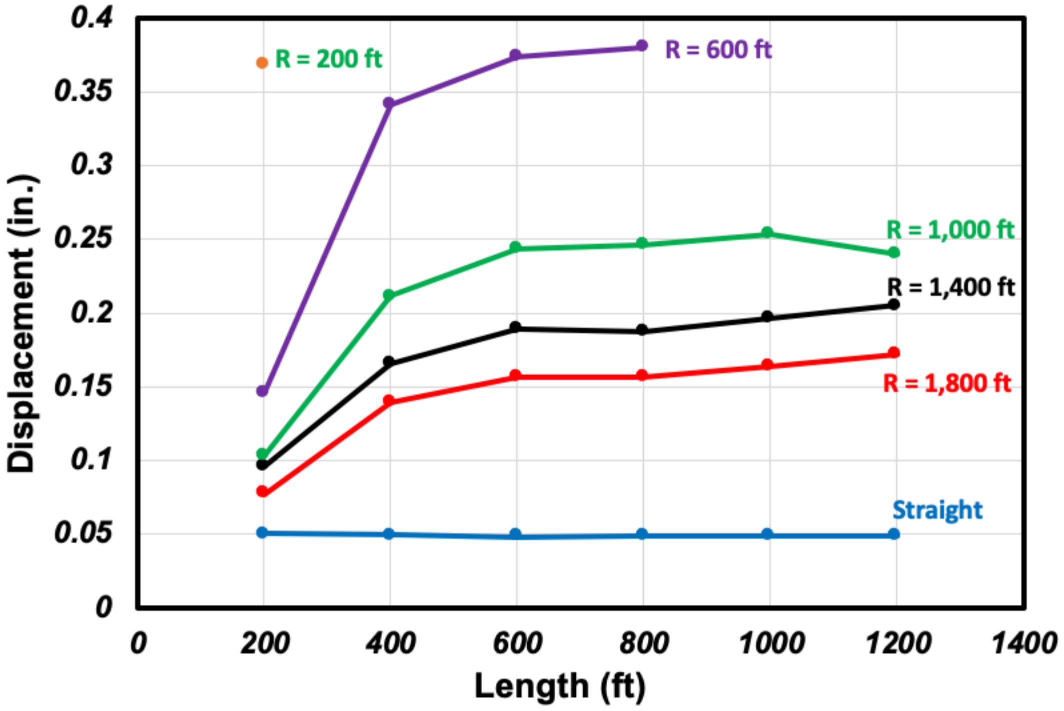

Figure 6.9: Interior Pile Head Lateral Movement (CEB–FIP 90)

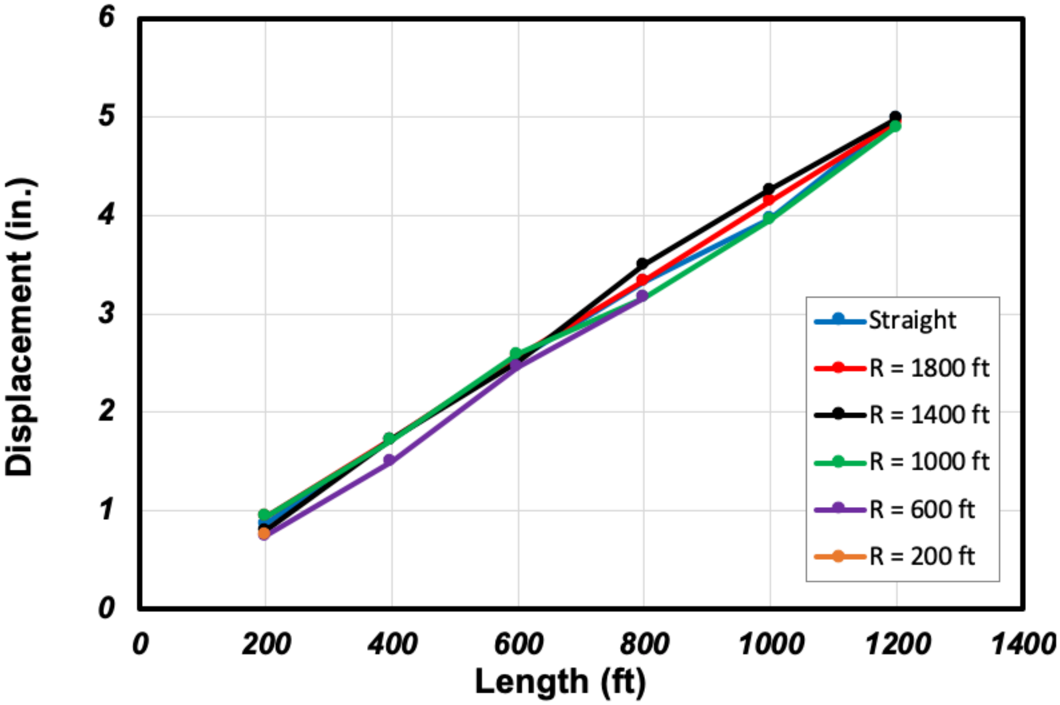

Figure 6.10: Interior Deck Longitudinal Movement (CEB–FIP 90)

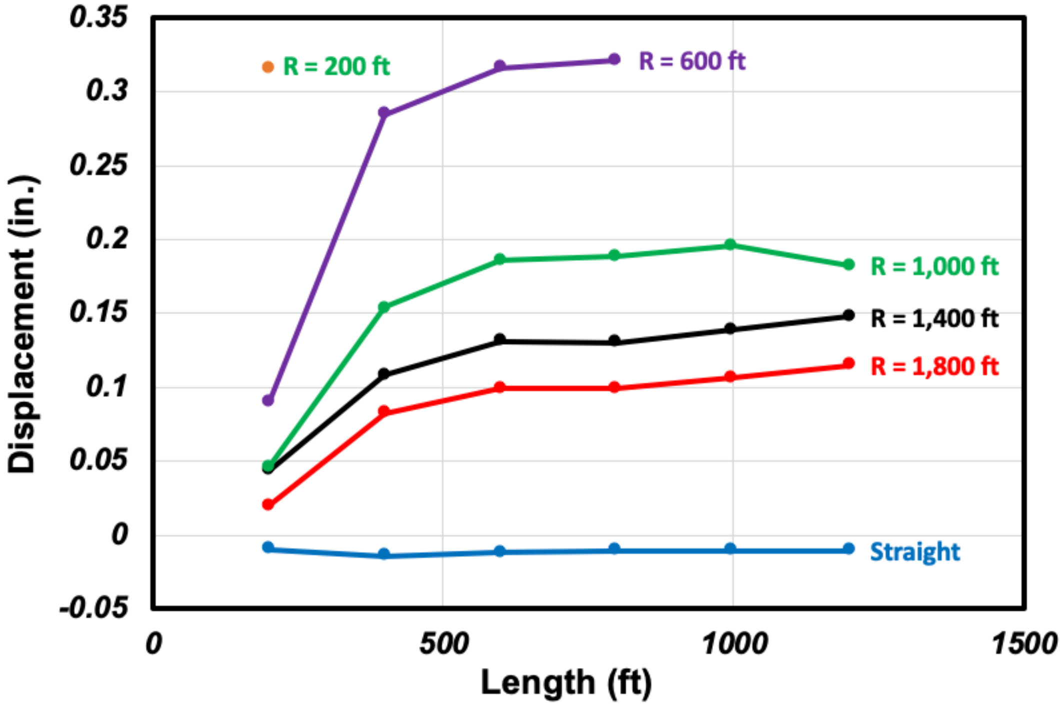

Figure 6.11:Interior Deck Lateral Movement (CEB–FIP 90)

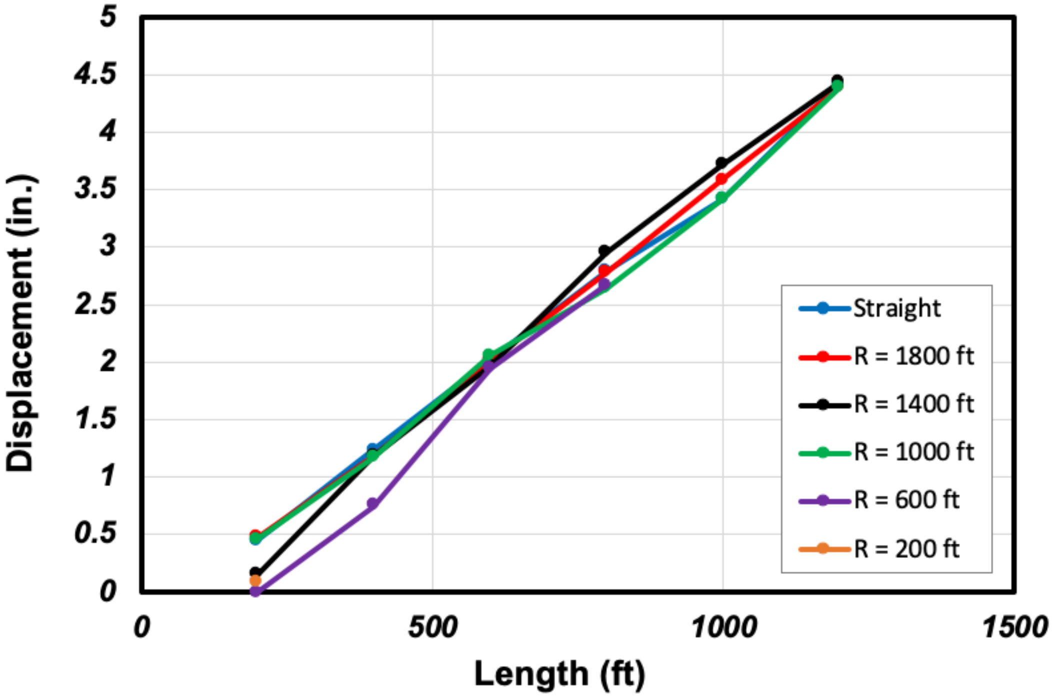

Figure 6.12: Exterior Pile Head Longitudinal Movement (CEB–FIP 90)

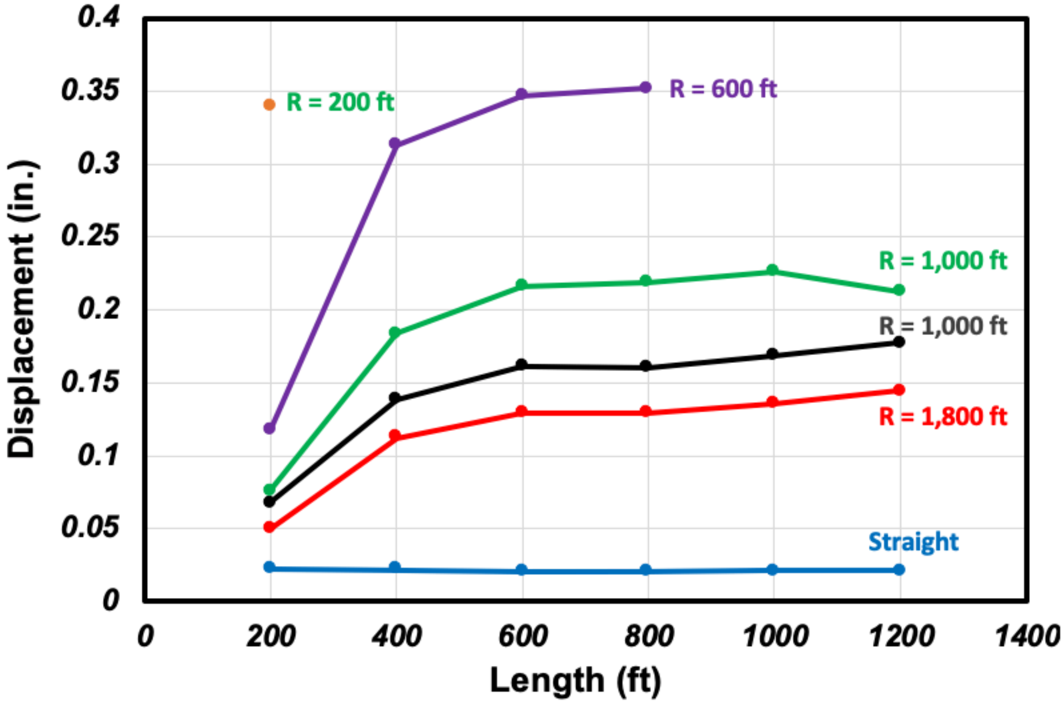

Figure 6.13: Exterior Pile Head Lateral Movement (CEB–FIP 90)

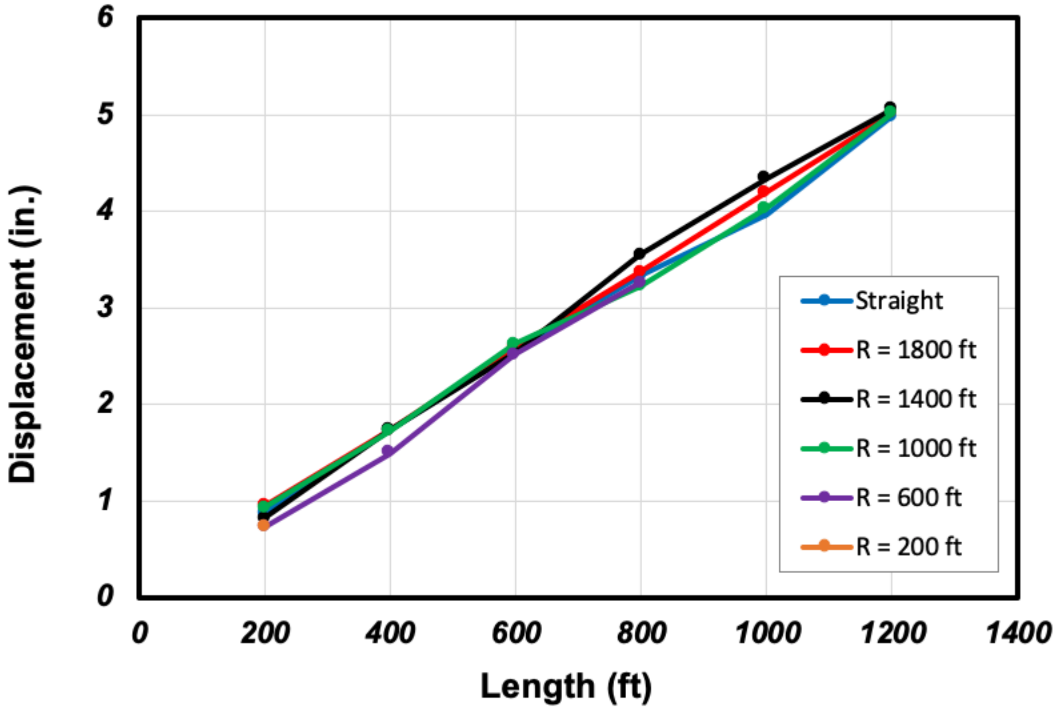

Figure 6.14: Exterior Deck Longitudinal Movement (CEB–FIP 90)

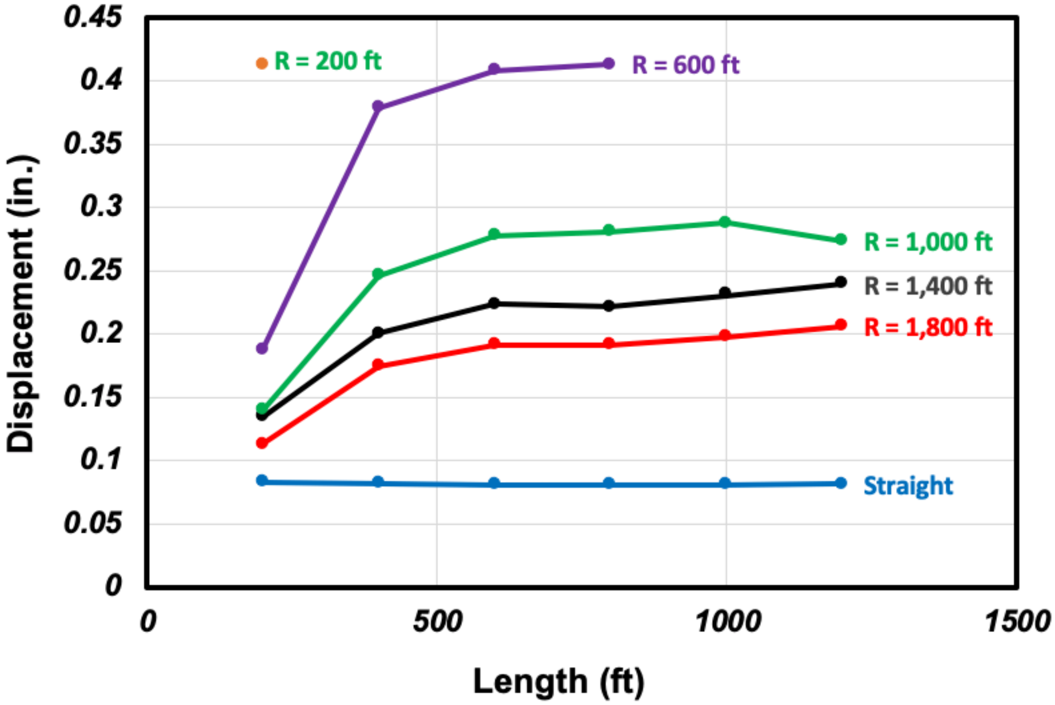

Figure 6.15: Exterior Deck Lateral Movement (CEB–FIP 90)

For all curvatures, Figure 6.8 shows a linear relationship between length and interior pile head longitudinal displacement. The interior pile head longitudinal displacement does not appear to be greatly affected by different radii of curvature despite some displacement differences among various radii for certain lengths (e.g., 200–, 800– and 1,000–ft long bridges). The longitudinal displacement of interior pile heads does not follow a constant pattern for all curvature–length combinations. As an example, the interior pile of a 200–ft long bridge experiences its largest longitudinal movement when the radius of curvature is 1,800 ft while for an 800–ft long bridge, the largest interior pile head movement happens when the radius of curvature is 1,400 ft. The 600–ft long bridge shows only 6% difference in head pile longitudinal movements among various radii of curvature. This difference, however, can go up to 300% for the 200–ft long bridge. In addition, this figure indicates that for all lengths, curved bridges have the largest pile head longitudinal displacement. Figure 6.9 shows the lateral movement of pile heads for all length–curvature combinations. In contrast to the Figure 6.8, there is a clear trend in this figure. All bridge lengths exhibit larger lateral movements when their radius of curvature gets smaller. This figure also shows that, for each radius of curvature, the lateral displacement of the pile head almost always increases as the bridge length increases. The rate of this increase, however, is much higher for the first two length increases (from 200–ft to 400–ft and from 400–ft to 600–ft long bridges). In addition, the straight bridge has a constant lateral movement of the interior pile head, independent of its total length. Due to our assumptions for degree of curvature limits, a 200–ft radius of curvature can only be used on a 200–ft long bridge. That is why there is only one point on the graph for this radius of curvature.

In Figures 6.10 and 6.11, longitudinal and lateral displacements are shown for the interior deck. Even though the trends are similar to those of the interior pile head movements, the values differ slightly. According to Figures 6.8, longitudinal movements at the interior pile head range from 0.2 to 4.5 in., but at the interior deck (Figure 6.10), they range from 0.75 to 5 in. Additionally, for 200–ft long bridges with a 200–ft radius of curvature, it shows that interior deck movements are more consistent than those of interior pile head. As shown in Figures 6.9 and 6.11, interior pile heads move laterally more than interior decks, but their patterns are nearly identical. Movements of exterior pile heads and decks are shown in Figures 6.12 to 6.15. There are many similarities between these figures and those showing interior pile head and deck movements (Figures 6.8 to 6.11). For all lengths and curvatures, pile head displacements are shown in Table 6.7. This table highlights the maximum displacements for each length–curvature combination. It shows that for every length–curvature combination, the interior pile head experiences greater displacements than the exterior pile head. In terms of lateral deck movements, however, the exterior deck exhibits greater displacements than the interior deck. In most cases, the exterior deck moves slightly more longitudinally than the interior deck. In contrast, the exterior deck moves significantly more laterally than the interior deck does. Based on this table, it can also be seen that the maximum movements of the pile head and deck occur at different radii of curvature, depending on the bridge length.

Figures 6.16 through 6.19 show maximum stresses and bending moments at the pile–abutment–girder Connection for piles (among all 10 piles) and girders (among all 4 girders). We have rounded the values of stresses and bending moments to the nearest whole number throughout this chapter. Figure 6.16 shows the pile maximum von Mises stress at the pile–abutment connection. Compared to other lengths, the 200–foot long bridge seems to behave differently. Other than the change between 200 to 400 ft, as the bridge length increases the stress in the pile increases. Interestingly, the maximum pile stress for a 200–ft long bridge appears to be greatly influenced by the radius of curvature while this dependency cannot be observed for other lengths. However, for bridges over 200–ft long and for all curvatures, bridge length is almost linearly related to bridge pile stress. In order words, as the bridge becomes longer, the maximum pile head stress increases. In contrast, the bridge maximum pile head stress drops when the length of the bridge increases from 200 to 400 ft (for R = 600 and 1400 ft) or slightly increases (for R = 1000, 1800, and ∞ ft). It is clear from Figure 6.17 that the bending moment values closely follow the maximum stress graph of the pile head (Figure 6.16). Figures 6.18 and 6.19 show the maximum von Mises stress at the girder–abutment connection point for girder bottom and top flanges, respectively. Figure 6.18 shows that this stress increases almost linearly with bridge length. For curved bridges longer than 400 ft, this stress becomes quite similar among different radii of curvature. In addition, this figure shows that the girder bottom flange of a straight bridge experiences the highest stresses at the abutment's face compared to curved bridges. Lastly, Figure 6.19 shows that shorter bridges experience higher stresses in their girder top flanges at the point of connection between the girder and abutment. Increasing bridge length decreases these stresses, and for bridges exceeding 600 ft, there is no difference in stress among different curvature radii. The 200–ft long bridge with a radius of curvature of 200 ft experiences the highest girder top flange stress which is very close to its yield stress. Compared to a straight bridge, this stress is 190% higher.

Figures 6.20 to 6.31 show similar pile head and deck movements as well as pile and girder stresses but for the ACI 209R shrinkage model. Although the results between the two models differ, the general trends are very similar. The bridge movement is shown in Table 6.8 based on the ACI 209R shrinkage model with the maximum displacement for each length–curvature combination highlighted.

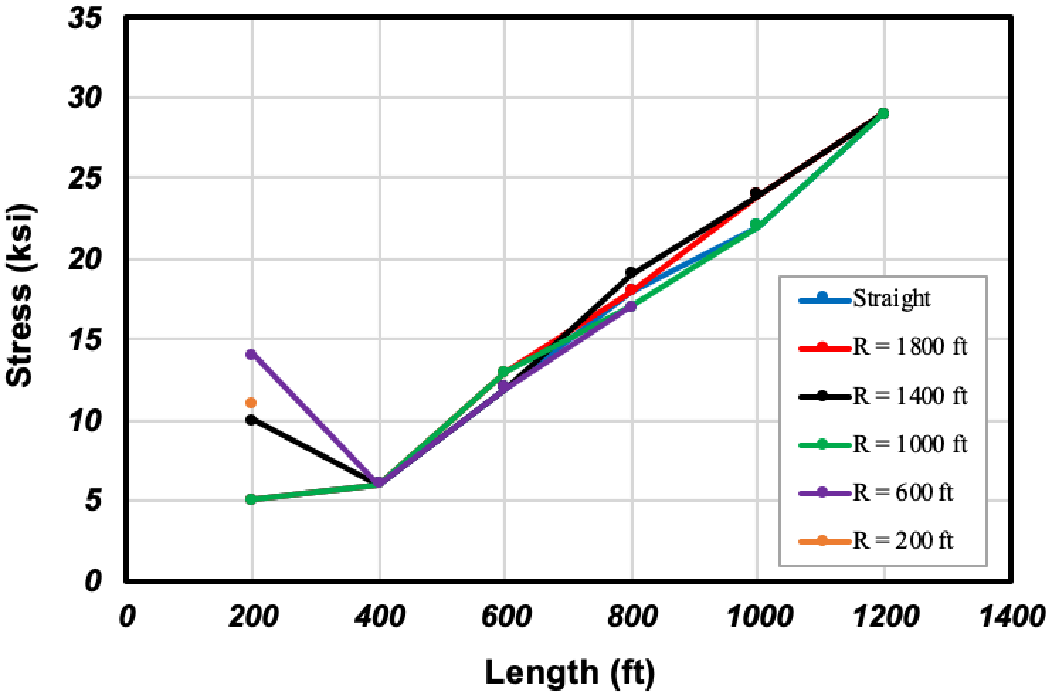

Figure 6.16: Pile Max. von Mises Stress at the Pile–Abutment Connection (CEB–FIP 90)

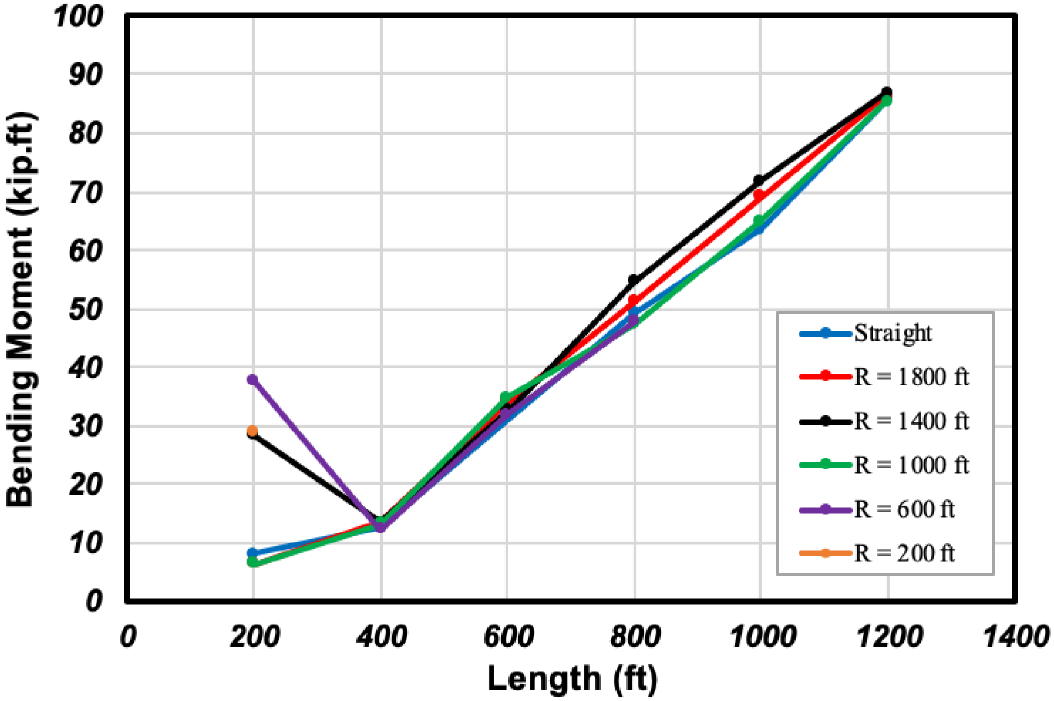

Figure 6.17: Pile Max. Bending Moment at the Pile–Abutment Connection (CEB–FIP 90)

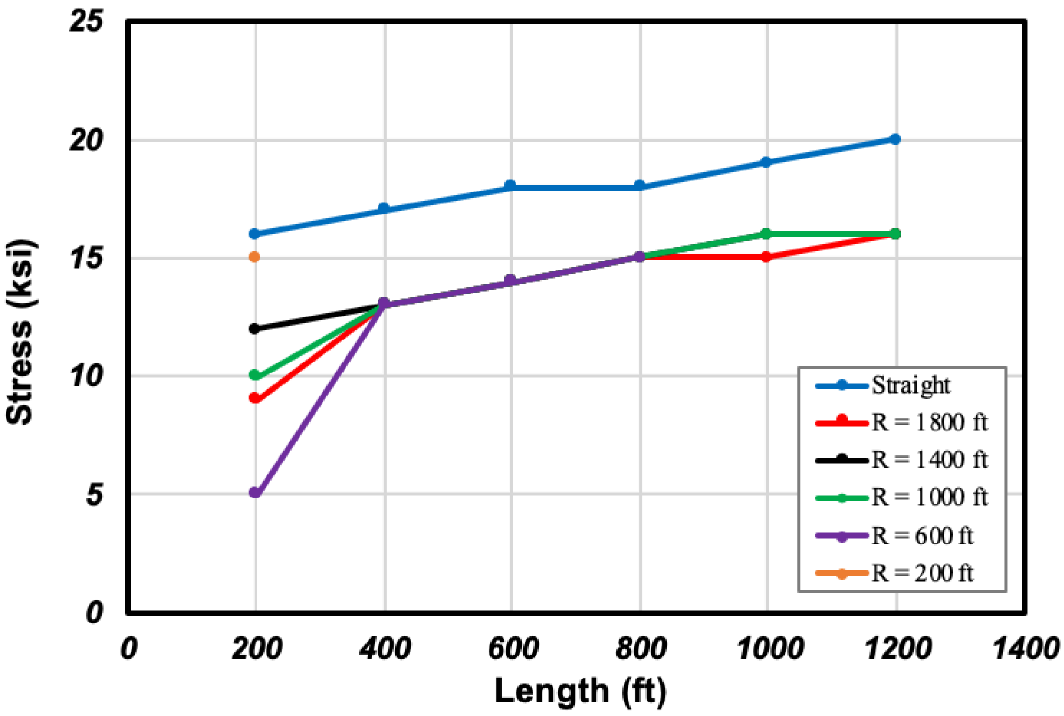

Figure 6.18: Girder Bottom Flange Max. von Mises Stress at the Girder–Abutment Connection (CEB–FIP 90)

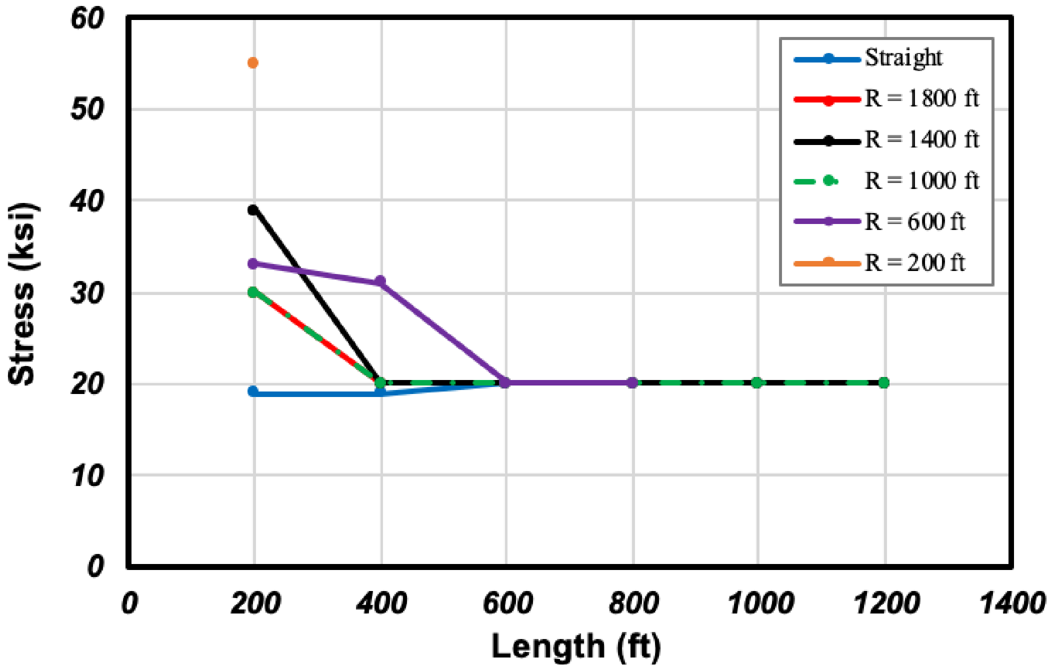

Figure 6.19: Girder Top Flange Max. von Mises Stress at the Girder–Abutment Connection (CEB–FIP 90)

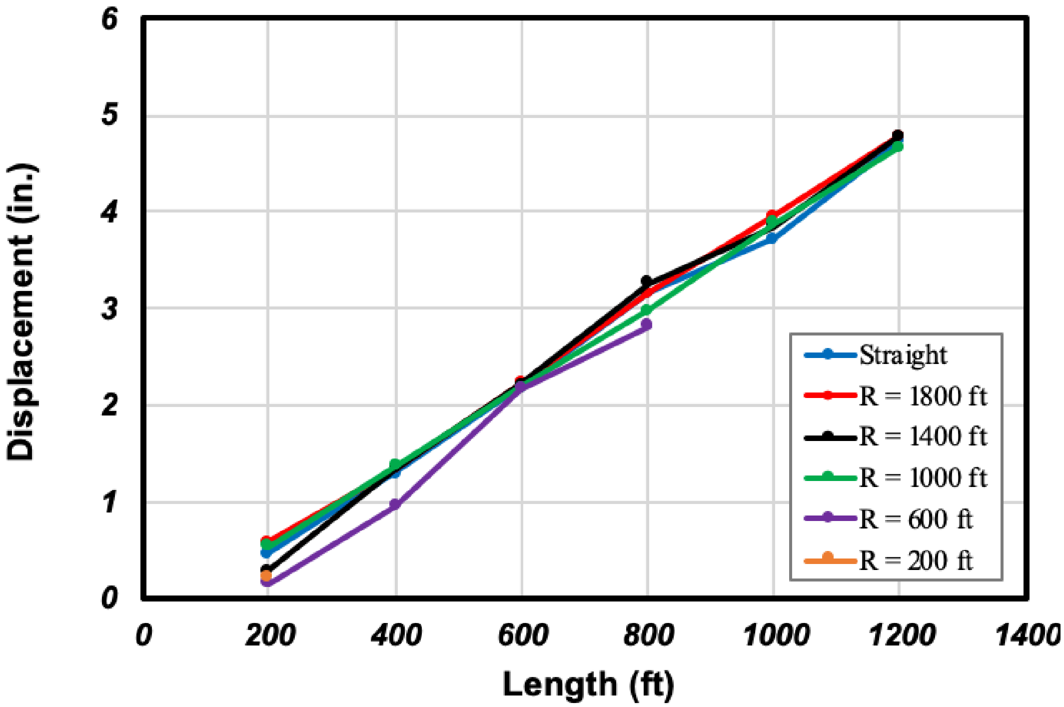

Figure 6.20: Interior Pile Head Longitudinal Movement (ACI 209R)

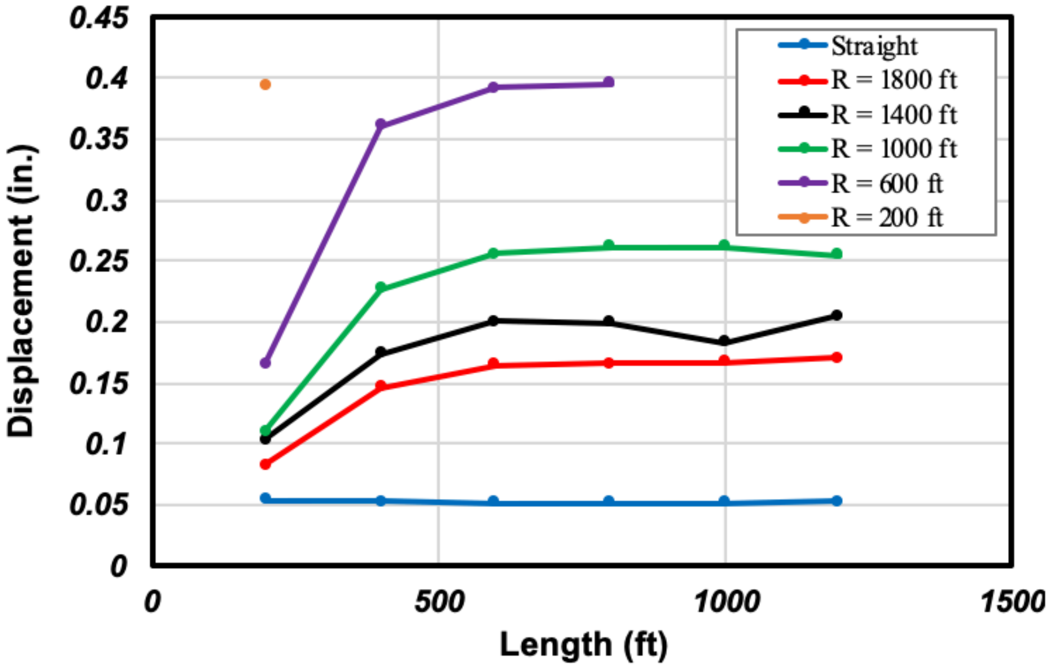

Figure 6.21: Interior Pile Head Lateral Movement (ACI 209R)

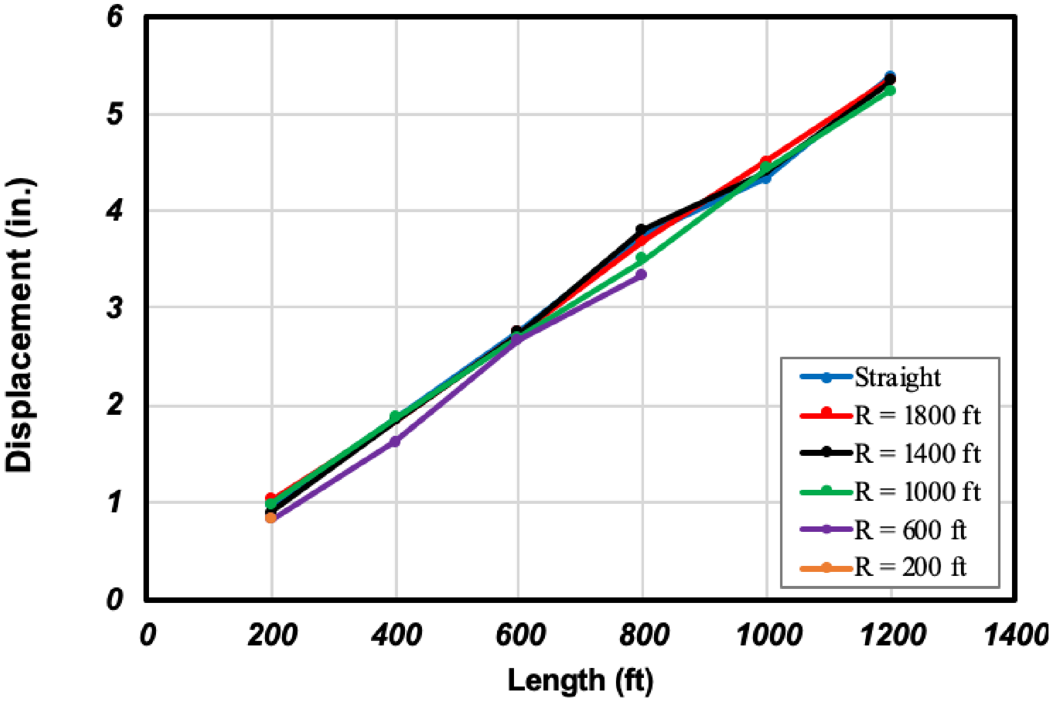

Figure 6.22: Interior Deck Longitudinal Movement (ACI 209R)

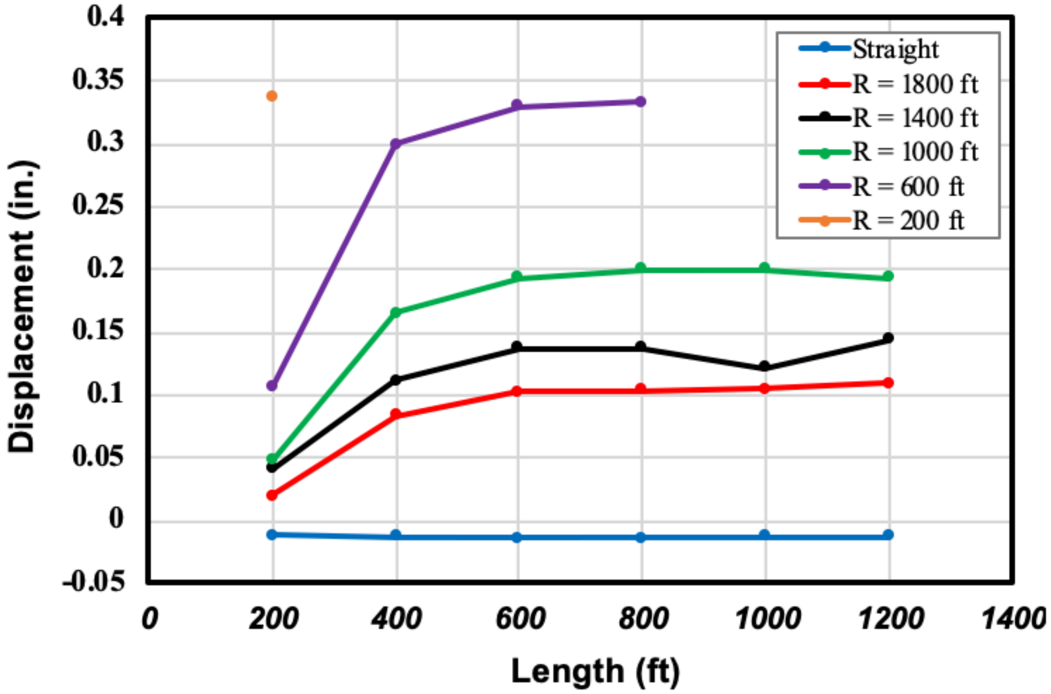

Figure 6.23: Interior Deck Lateral Movement (ACI 209R)

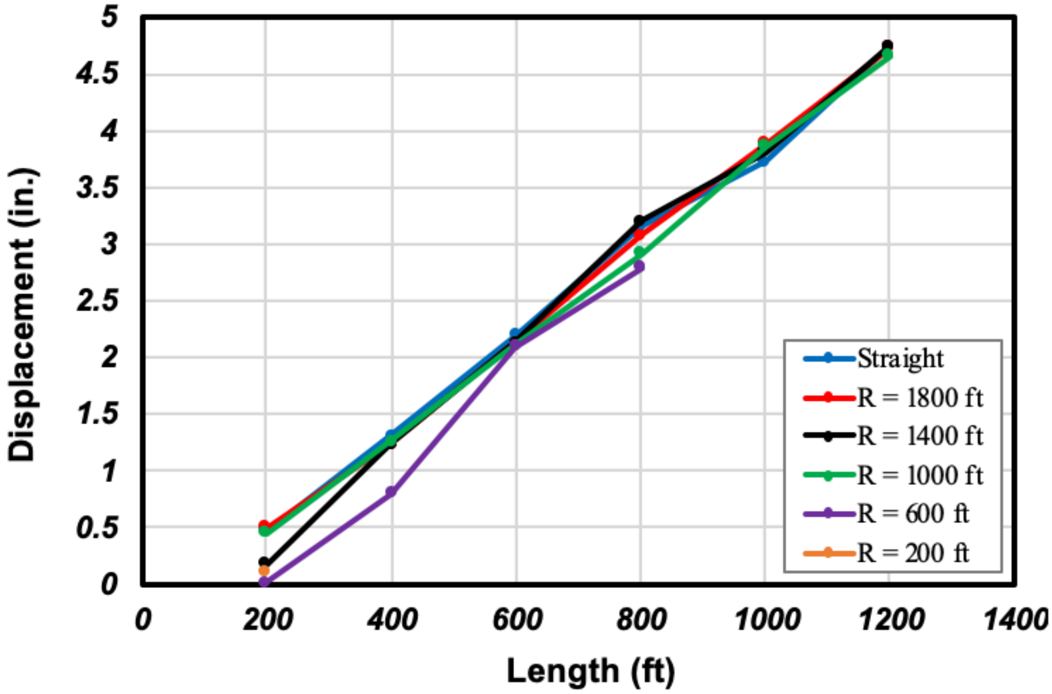

Figure 6.24: Exterior Pile Head Longitudinal Movement (ACI 209R)

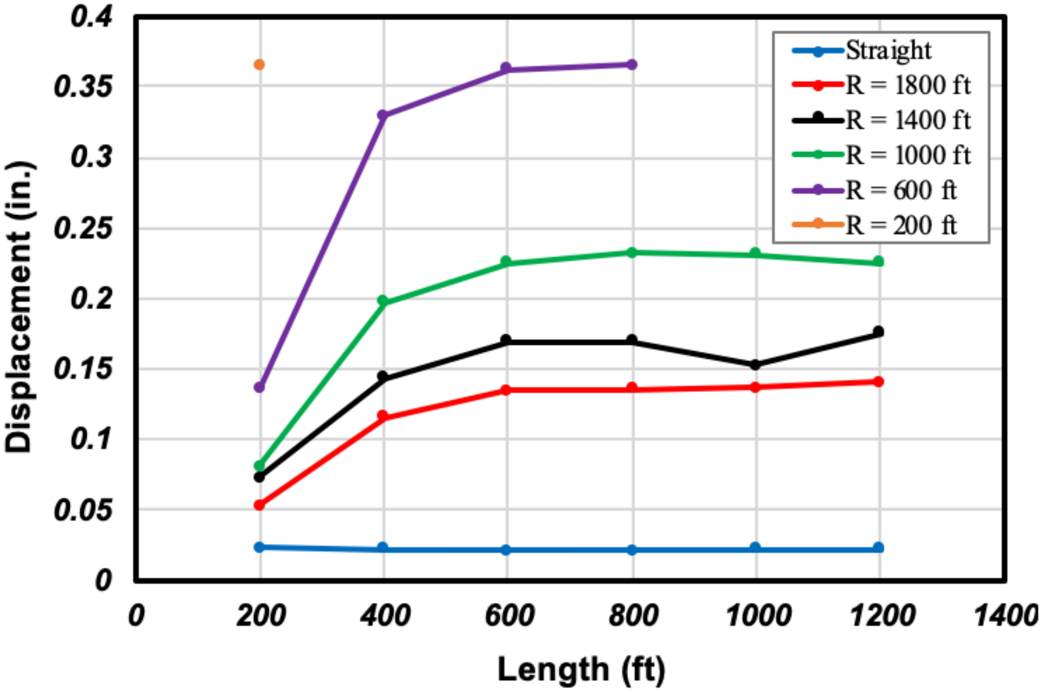

Figure 6.25: Exterior Pile Head Lateral Movement (ACI 209R)

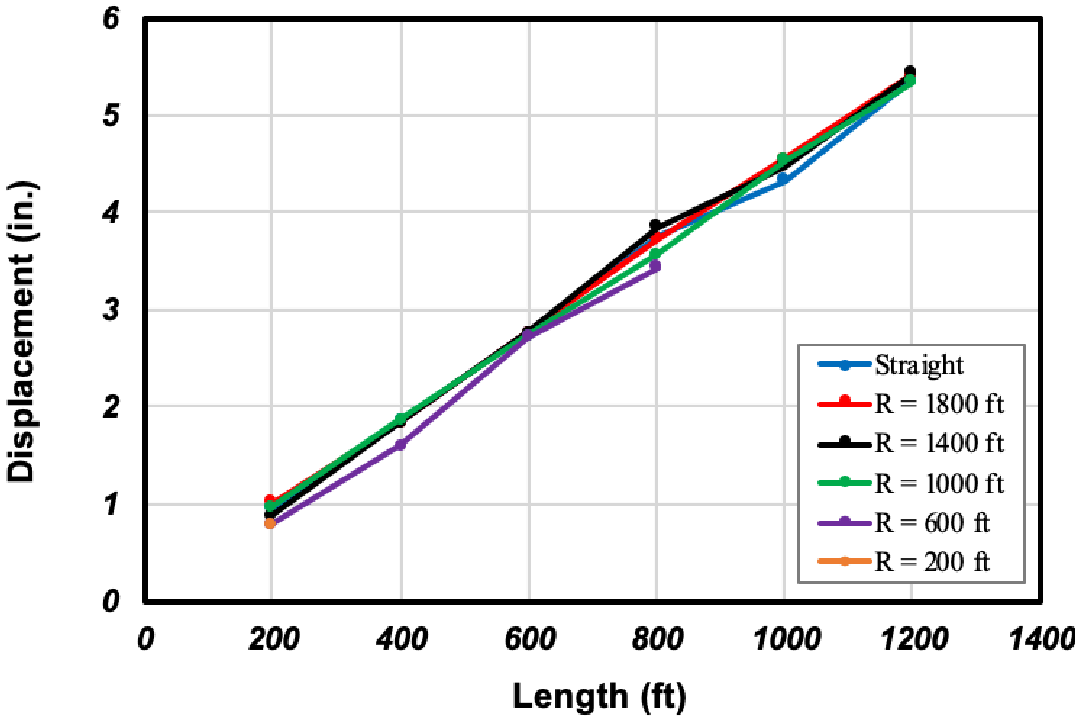

Figure 6.26: Exterior Deck Longitudinal Movement (ACI 209R)

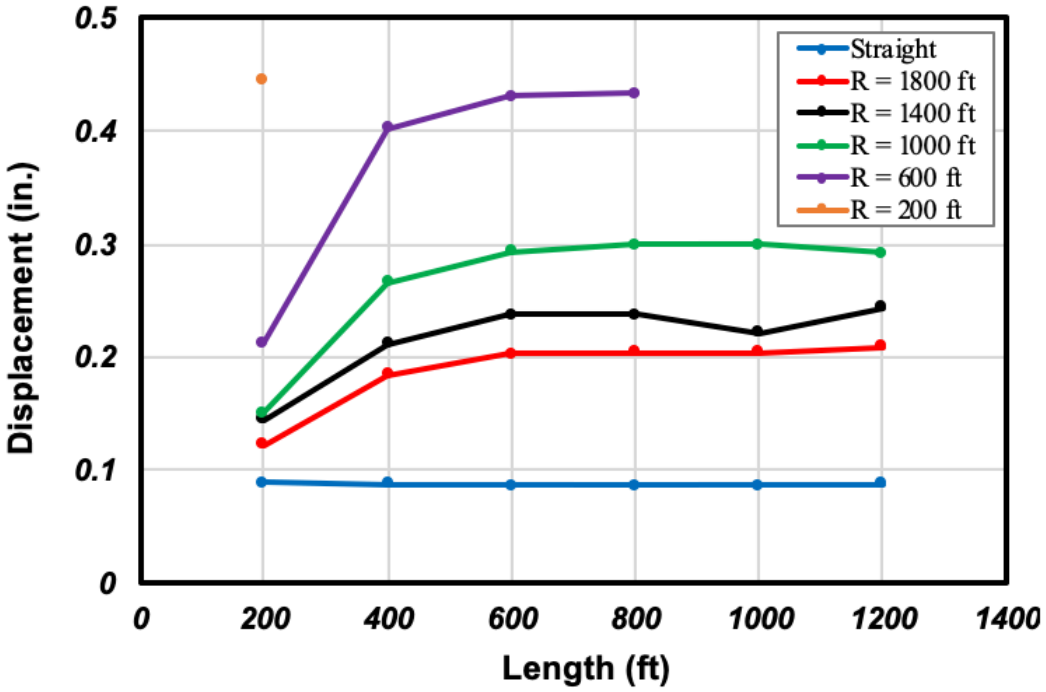

Figure 6.27: Exterior Deck Lateral Movement (ACI 209R)

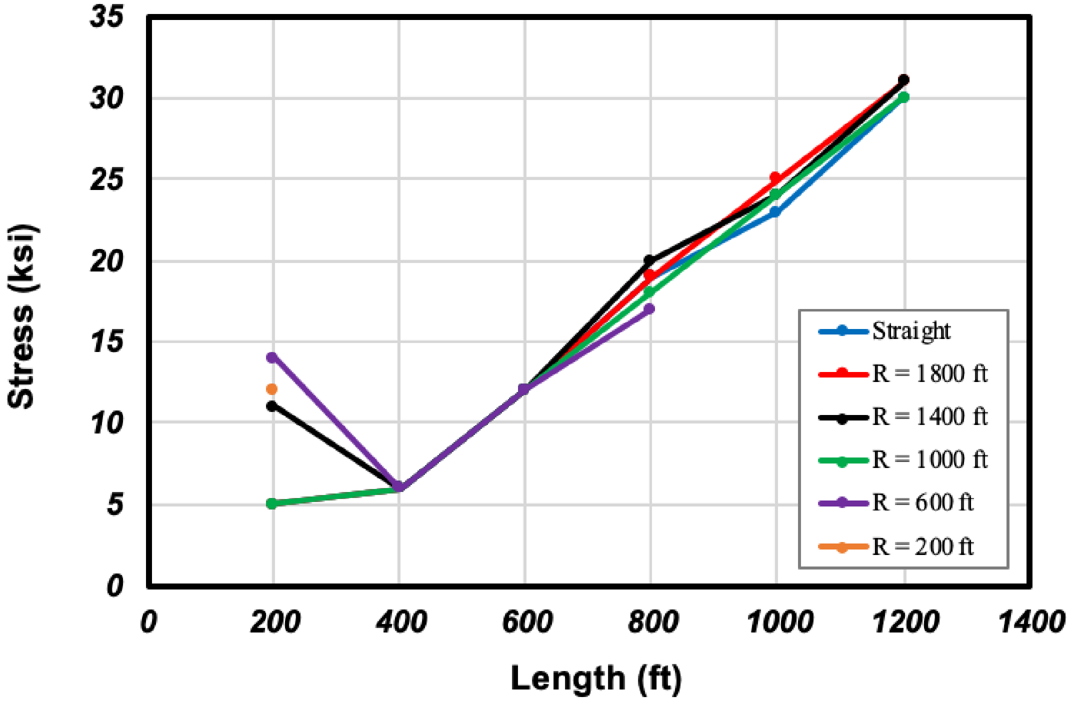

Figure 6.28: Pile Max. von Mises Stress at the Pile–Abutment Connection (ACI 209R)

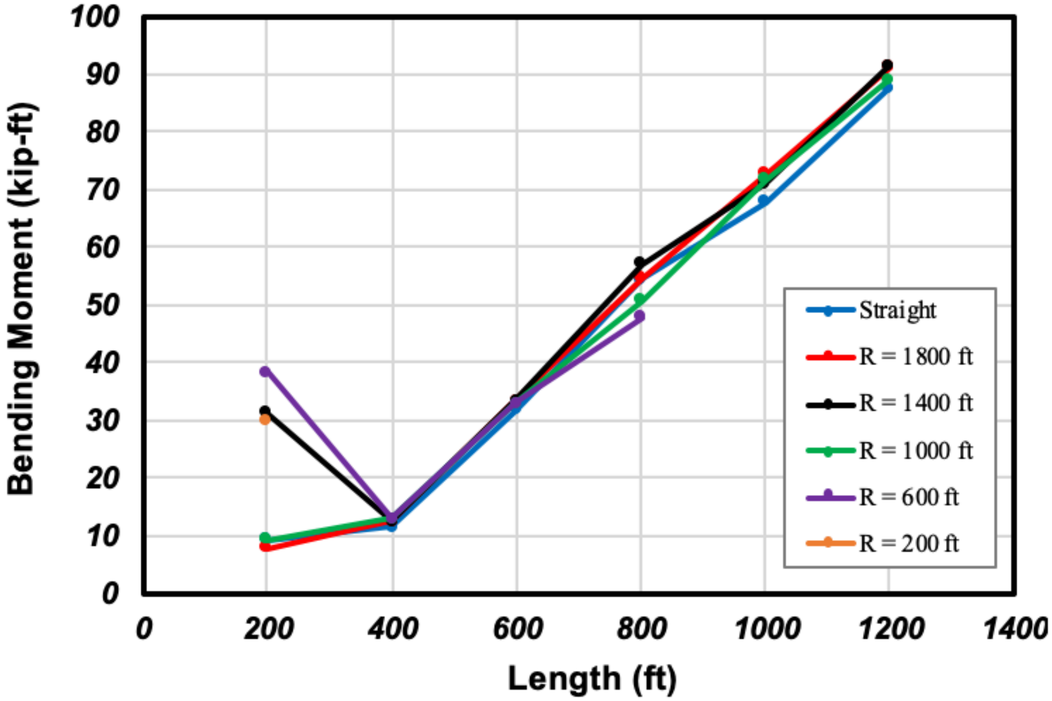

Figure 6.29: Pile Max. Bending Moment at the Pile–Abutment Connection (ACI 209R)

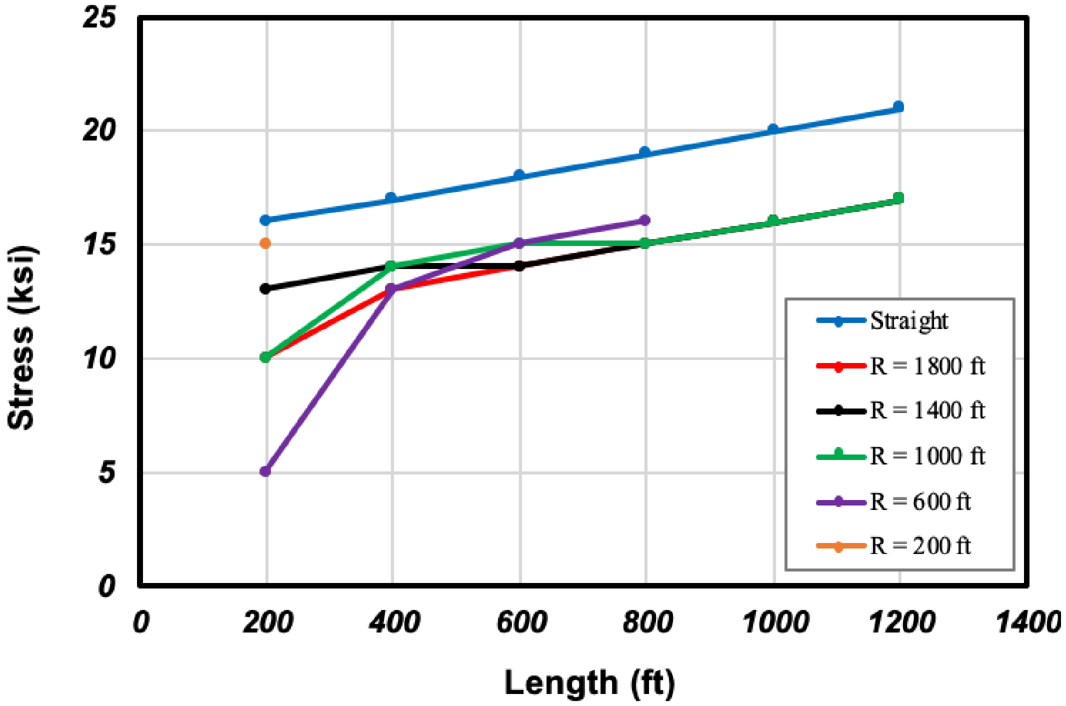

Figure 6.30: Girder Bottom Flange Max. von Mises Stress at the Girder–Abutment Connection (ACI 209R)

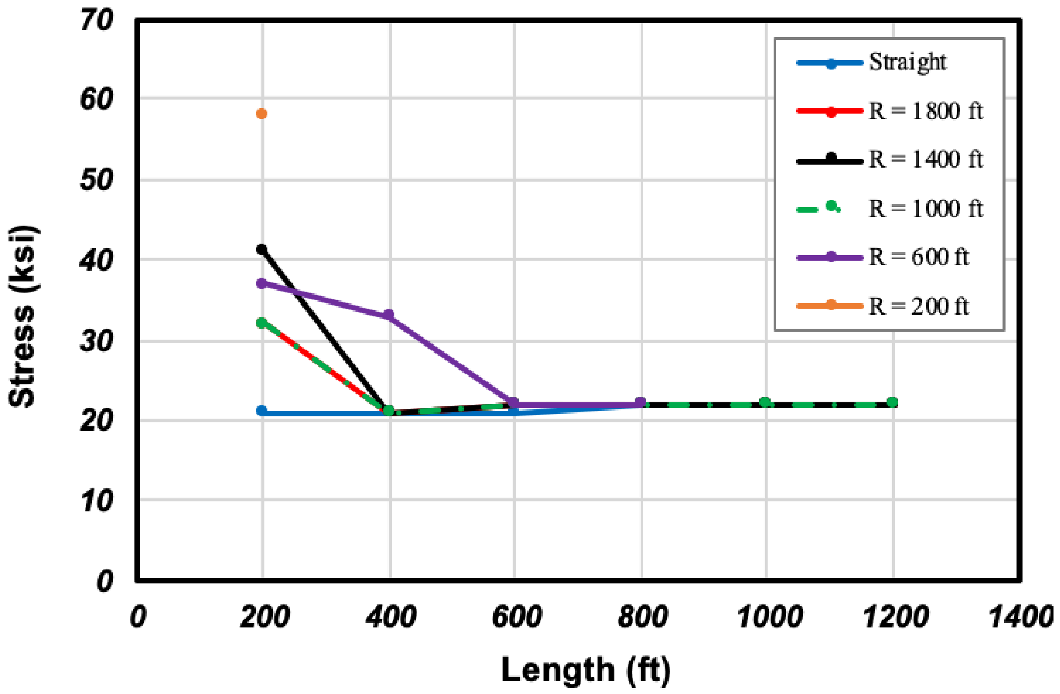

Figure 6.31: Girder Top Flange Max. von Mises Stress at the Girder–Abutment Connection (ACI 209R)

Table 6.8: Interior and Exterior Pile Head and Deck Movements (ACI 209R)

Length (ft)	**Radius of Curvature (ft)**	**Pile Head Longitudinal Movement (in)**		**Pile Head Lateral Movement (in)**		**Deck Longitudinal Movement (in)**		**Deck Lateral Movement (in)**	
		Interior	**Exterior**	**Interior**	**Exterior**	**Interior**	**Exterior**	**Interior**	**Exterior**
200	**200**	0.23	0.11	0.39	0.36	0.82	0.79	0.34	0.44
	600	0.15	0.01	0.17	0.14	0.81	0.80	0.11	0.21
	1,000	0.54	0.45	0.11	0.08	0.98	0.98	0.05	0.15
	1,400	0.29	0.17	0.10	0.07	0.89	0.89	0.04	0.15
	1,800	0.59	0.50	0.08	0.05	1.02	1.02	0.02	0.12
	∞	0.47	0.47	0.05	0.02	0.95	0.95	-0.01	0.09
400	**600**	1.09	0.94	0.36	0.33	1.75	1.76	0.29	0.41
	1,000	1.36	1.26	0.23	0.20	1.86	1.86	0.17	0.27
	1,400	1.34	1.23	0.17	0.14	1.83	1.84	0.11	0.21
	1,800	1.34	1.23	0.15	0.12	1.83	1.84	0.08	0.18
	∞	1.30	1.30	0.05	0.02	1.85	1.85	-0.01	0.09
600	**600**	2.16	2.09	0.39	0.36	2.67	2.73	0.33	0.43
	1,000	2.19	2.10	0.26	0.23	2.70	2.74	0.19	0.29
	1,400	2.22	2.13	0.20	0.17	2.73	2.76	0.14	0.24
	1,800	2.22	2.13	0.17	0.13	2.74	2.76	0.10	0.20
	∞	2.19	2.19	0.05	0.02	2.76	2.76	-0.01	0.09
800	**600**	2.82	2.79	0.40	0.36	3.33	3.43	0.33	0.43
	1,000	2.97	2.91	0.26	0.23	3.50	3.57	0.20	0.30
	1,400	3.27	3.19	0.20	0.17	3.80	3.85	0.14	0.24
	1,800	3.16	3.07	0.17	0.14	3.69	3.73	0.10	0.20
	∞	3.15	3.16	0.05	0.02	3.74	3.75	-0.01	0.09
1,000	**1,000**	3.89	3.86	0.26	0.23	4.43	4.53	0.20	0.30
	1,400	3.86	3.80	0.18	0.15	4.40	4.48	0.12	0.22
	1,800	3.95	3.88	0.17	0.14	4.49	4.55	0.10	0.20
	∞	3.72	3.72	0.05	0.02	4.33	4.33	-0.01	0.09
1,200	**1,000**	4.67	4.66	0.26	0.23	5.22	5.35	0.19	0.29
	1,400	4.78	4.74	0.21	0.18	5.34	5.43	0.14	0.24
	1,800	4.79	4.73	0.17	0.14	5.34	5.42	0.11	0.21
	∞	4.75	4.75	0.05	0.02	5.37	5.37	-0.01	0.09

6.7.2 Shrinkage Model

Because the shrinkage models have different initial slope and total strains, longitudinal and lateral displacements over time for each model was evaluated. The longitudinal and lateral displacements of 400–ft long bridges with different radii of curvature and shrinkage models are shown in Figures 6.32 to 6.65. Since interior and exterior pile and deck responses do not differ in straight bridges, only one result is shown here. In addition, lateral movements are not shown for straight bridges. These graphs show the net inward (contraction) displacement of pile heads and decks both longitudinally and laterally. In the first couple of years after construction, there is a noticeable difference between the ACI 209R model and the CEB–FIP 90 model as a result of the higher initial slope of shrinkage for the ACI 209R model. However, as the time increases, the two models behave more similarly. Figures 6.32 to 6.39 show that longitudinal movements of 400–ft long bridges with 600–ft radius of curvature differs between the two shrinkage models, even after 5 years. On the other hand, both shrinkage models produce nearly identical lateral movements after 5 years. The displacements of the bridge (both longitudinal and lateral) caused by the two shrinkage models nearly converge for 400–ft long bridges with a radius of curvature of 1,000 ft (Figures 6.40 to 6.47). With increasing radius of curvature (less curved bridges), the difference between the two models is less noticeable, and in some cases, their movements are approximately identical after 5 years (Figures 6.48 to 6.65). All of these graphs show that the difference between successive maximums and minimums decreases over time, an indication of the descending shrinkage rate for both models. Tables 6.9 to 6.13 show the displacements for these shrinkage models.

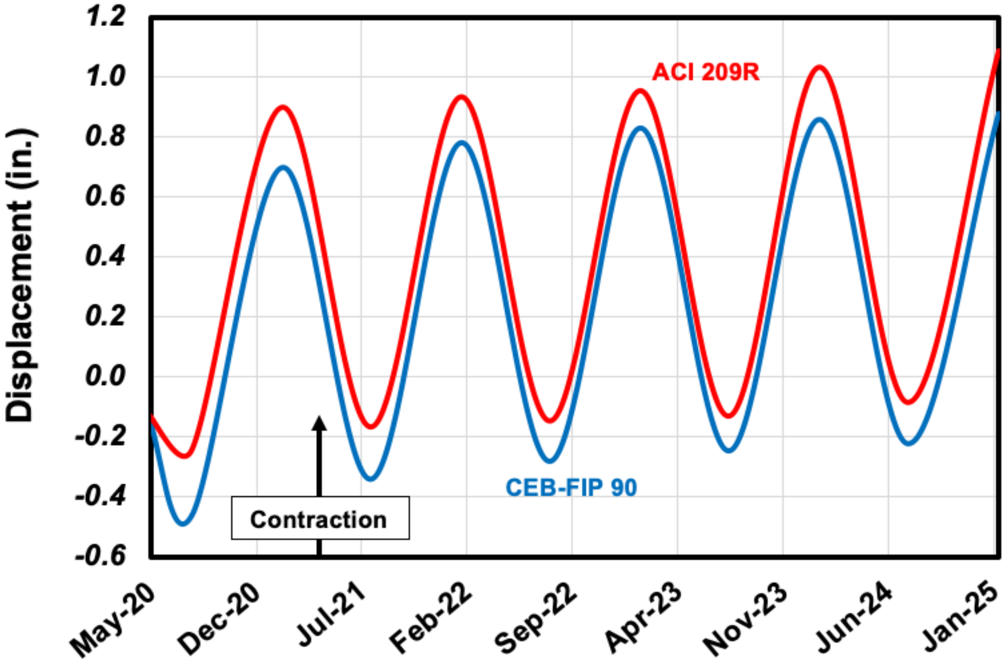

Figure 6.32: Interior Pile Head Longitudinal Movement for the Two Shrinkage Models

(L = 400 ft and R = 600 ft)

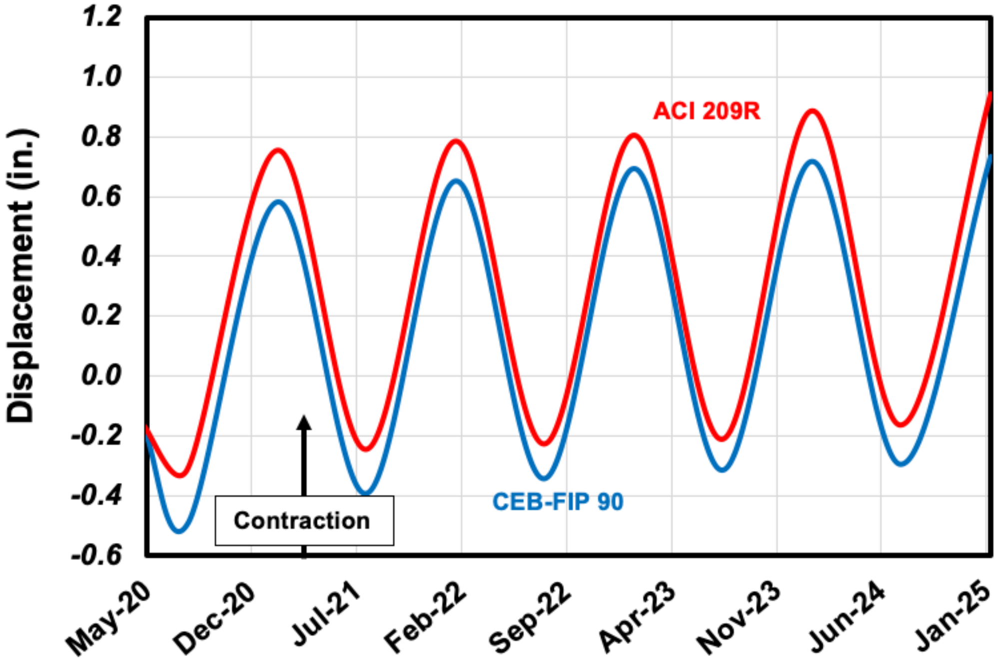

Figure 6.33: Exterior Pile Head Longitudinal Movement for the Two Shrinkage Models

(L = 400 ft and R = 600 ft)

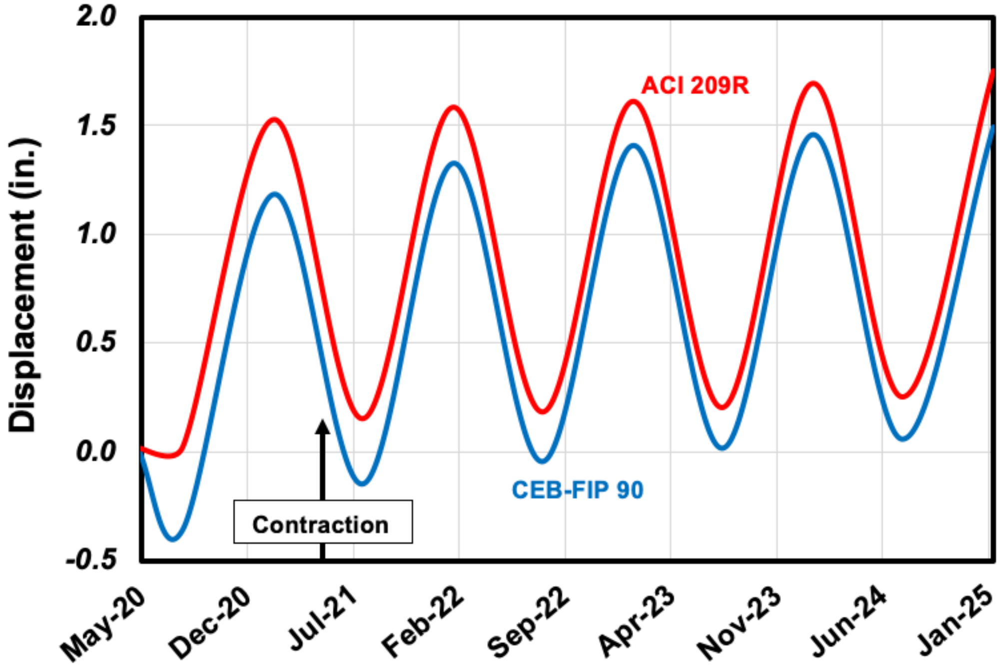

Figure 6.34: Interior Deck Longitudinal Movement for the Two Shrinkage Models

(L = 400 ft and R = 600 ft)

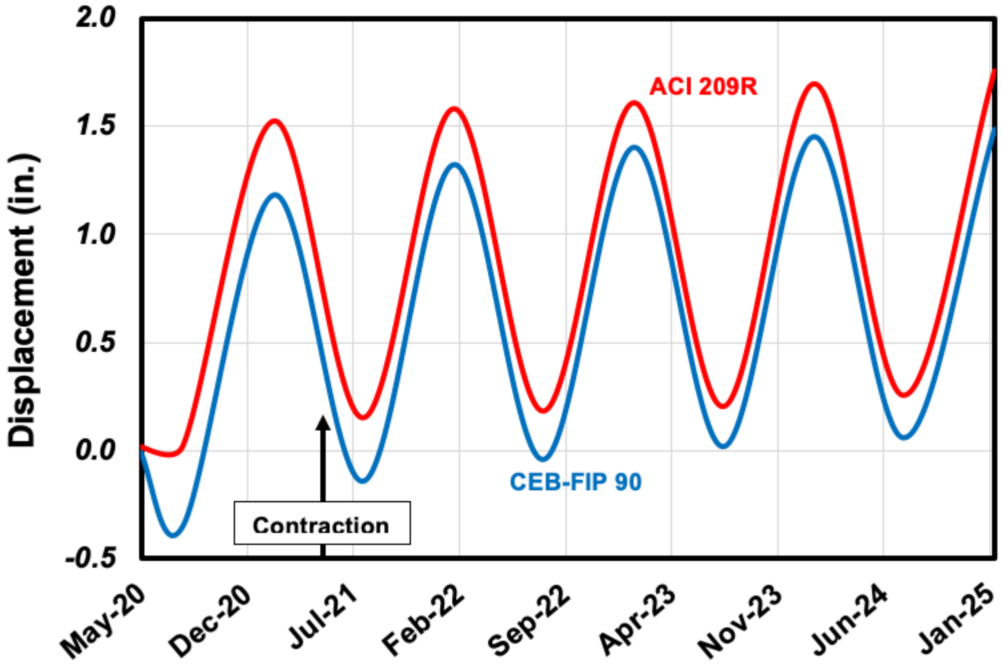

Figure 6.35: Exterior Deck Longitudinal Movement for the Two Shrinkage Models

(L = 400 ft and R = 600 ft)

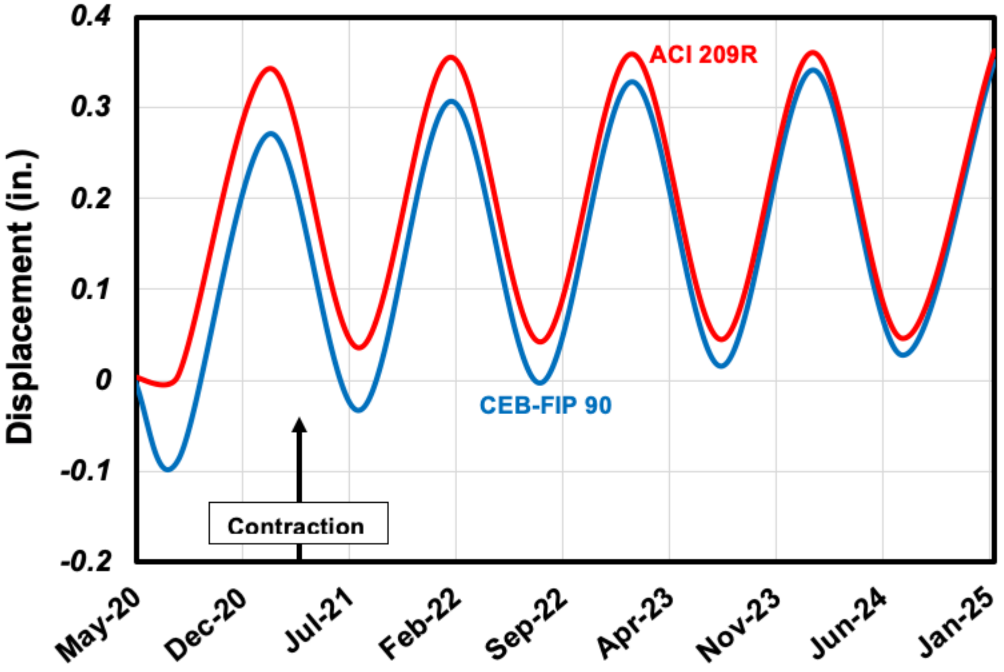

Figure 6.36: Interior Pile Head Lateral Movement for the Two Shrinkage Models

(L = 400 ft and R = 600 ft)

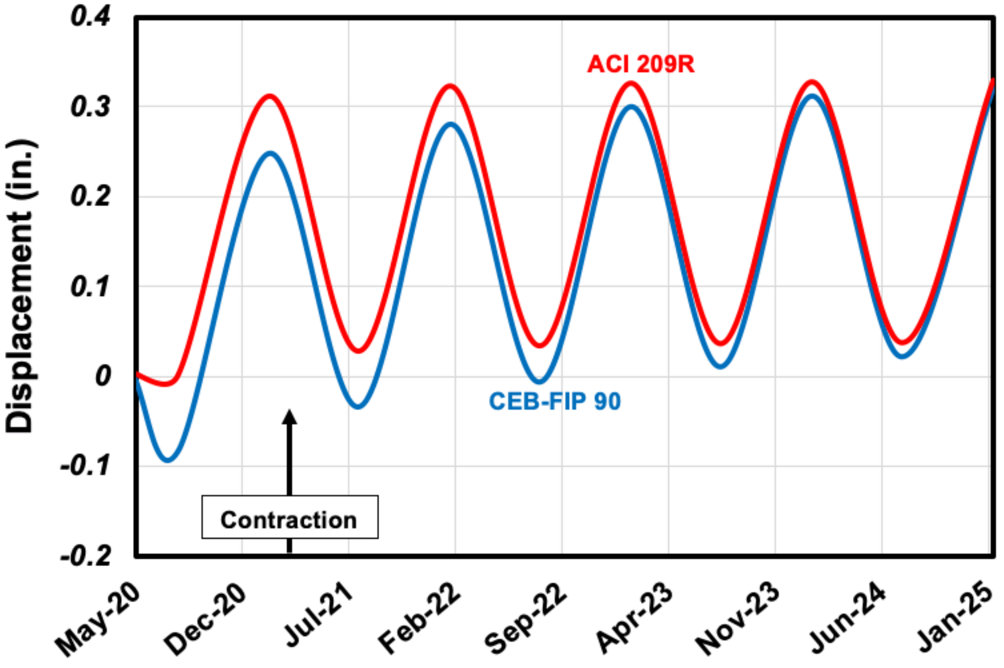

Figure 6.37: Exterior Pile Head Lateral Movement for the Two Shrinkage Models

(L = 400 ft and R = 600 ft)

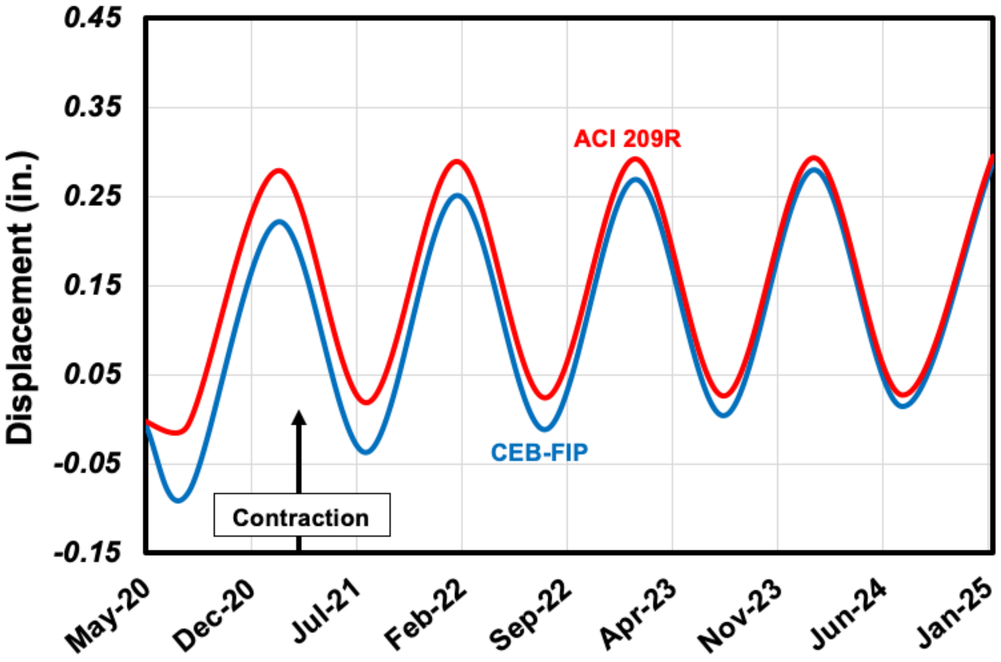

Figure 6.38: Interior Deck Lateral Movement for the Two Shrinkage Models

(L = 400 ft and R = 600 ft)

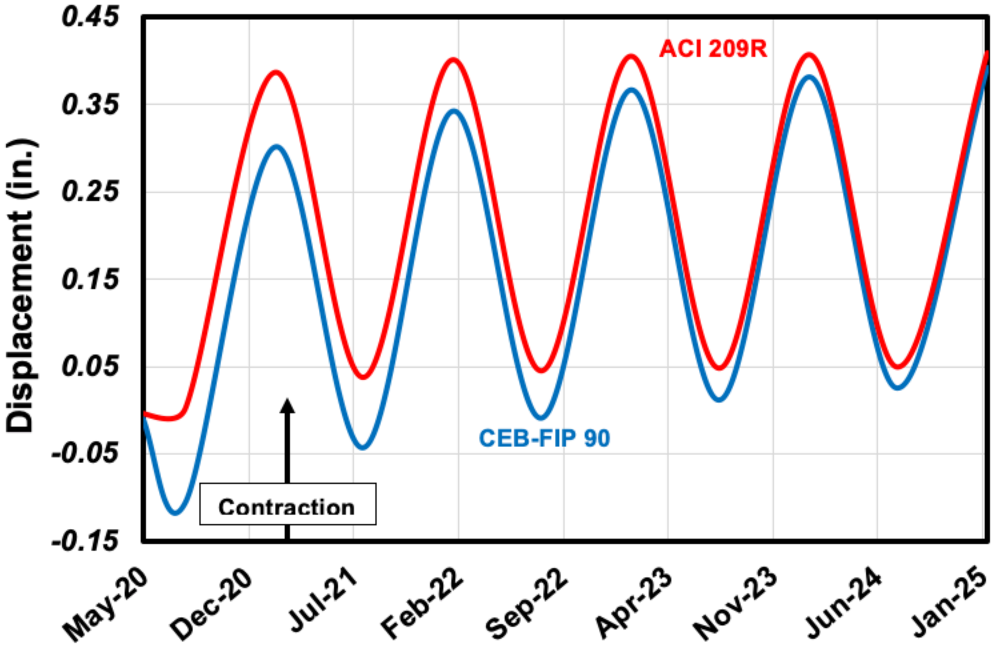

Figure 6.39: Exterior Deck Lateral Movement for the Two Shrinkage Models

(L = 400 ft and R = 600 ft)

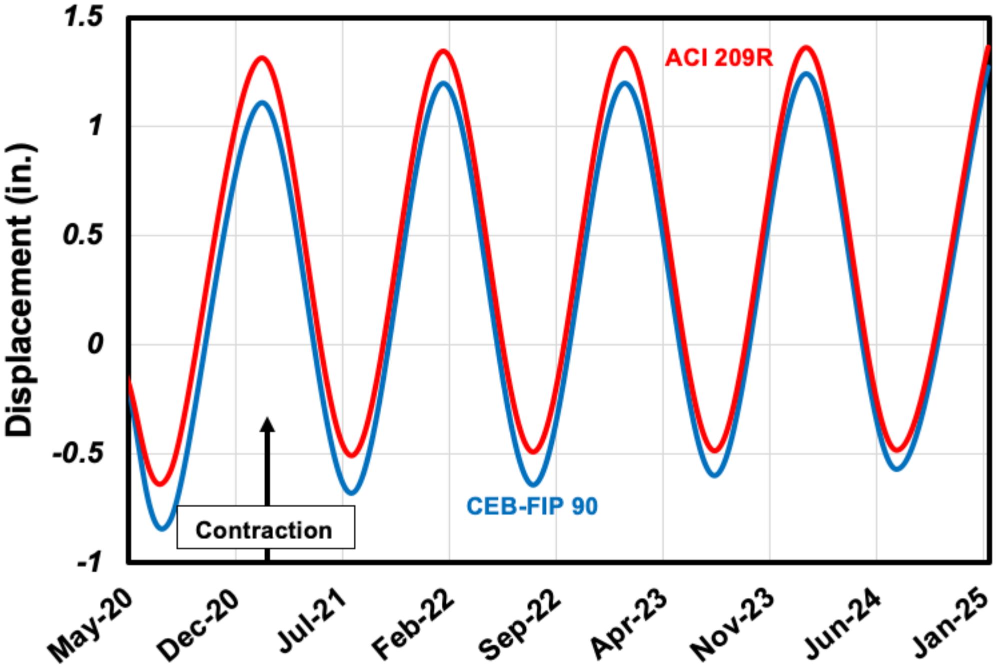

Figure 6.40: Interior Pile Head Longitudinal Movement for the Two Shrinkage Models

(L = 400 ft and R = 1,000 ft)

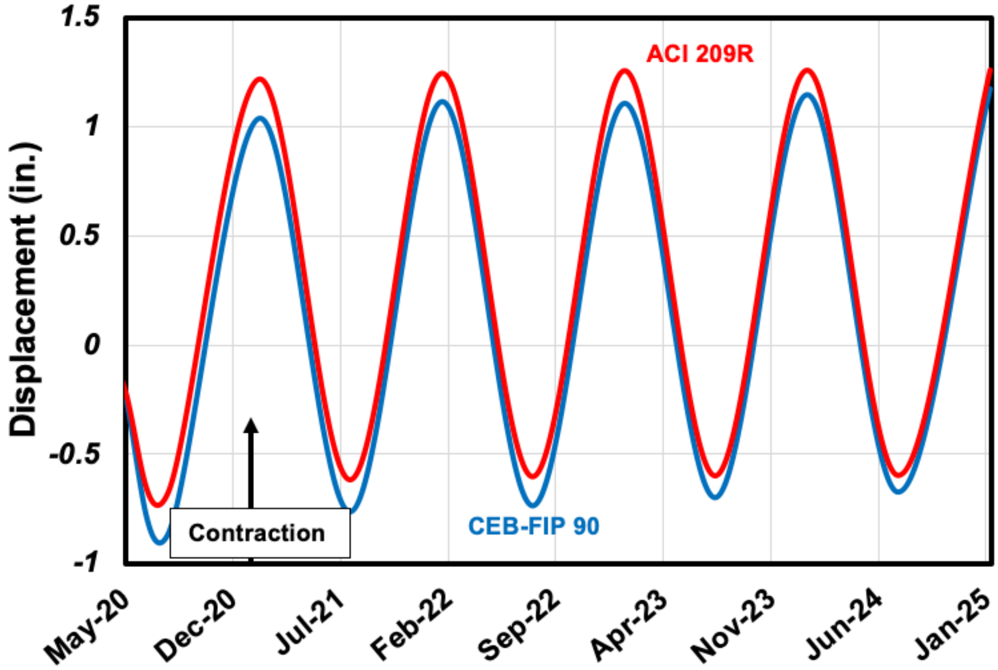

Figure 6.41: Exterior Pile Head Longitudinal Movement for the Two Shrinkage Models

(L = 400 ft and R = 1,000 ft)

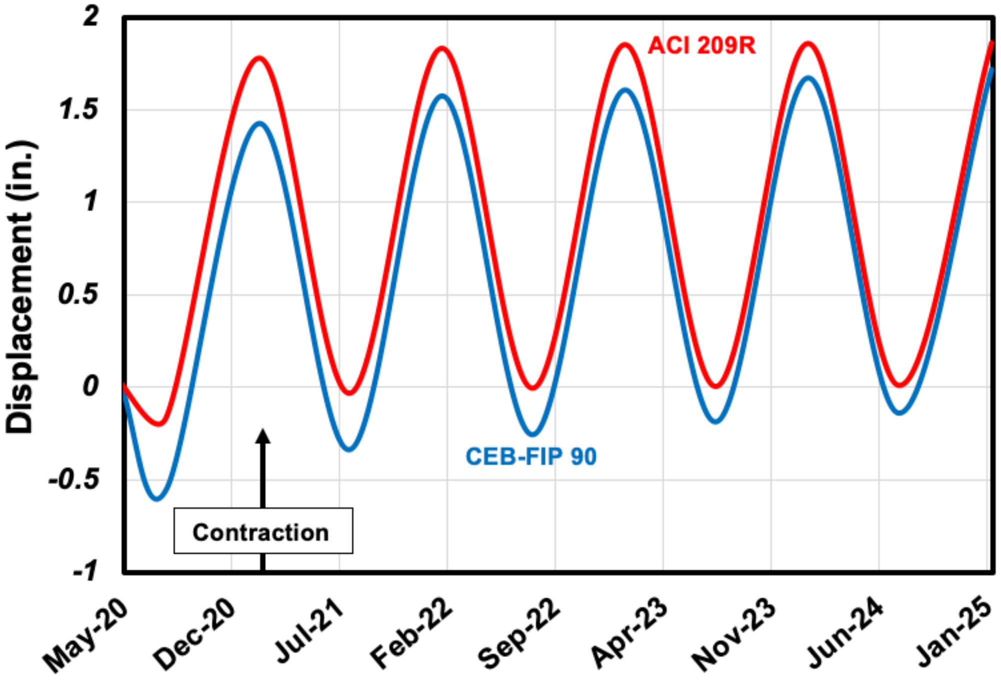

Figure 6.42: Interior Deck Longitudinal Movement for the Two Shrinkage Model

(L = 400 ft and R = 1,000 ft)

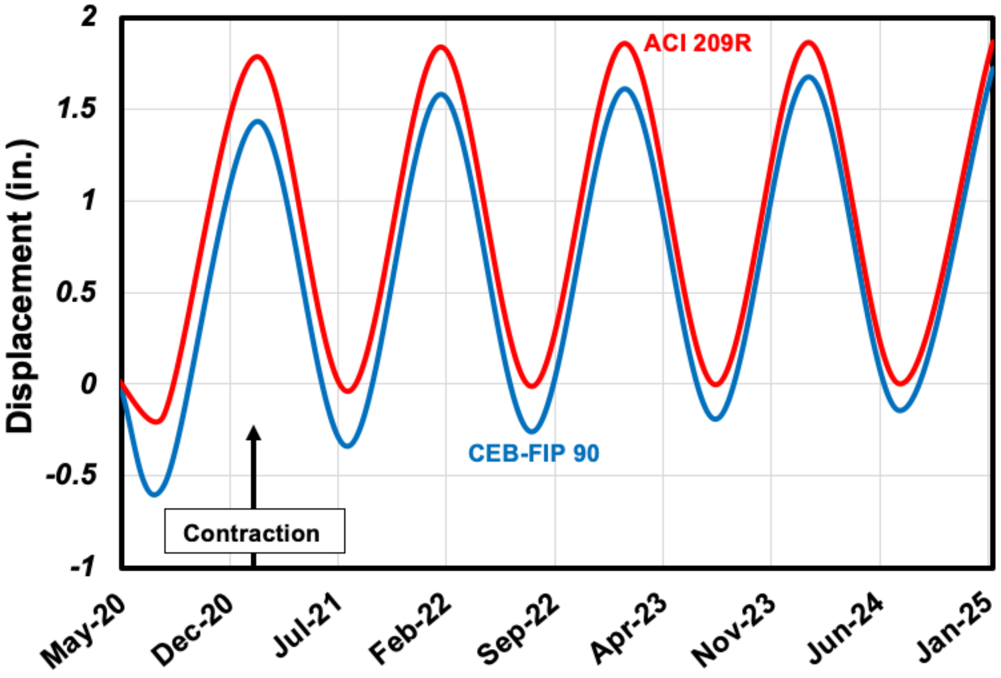

Figure 6.43: Exterior Deck Longitudinal Movement for the Two Shrinkage Models

(L = 400 ft and R = 1,000 ft)

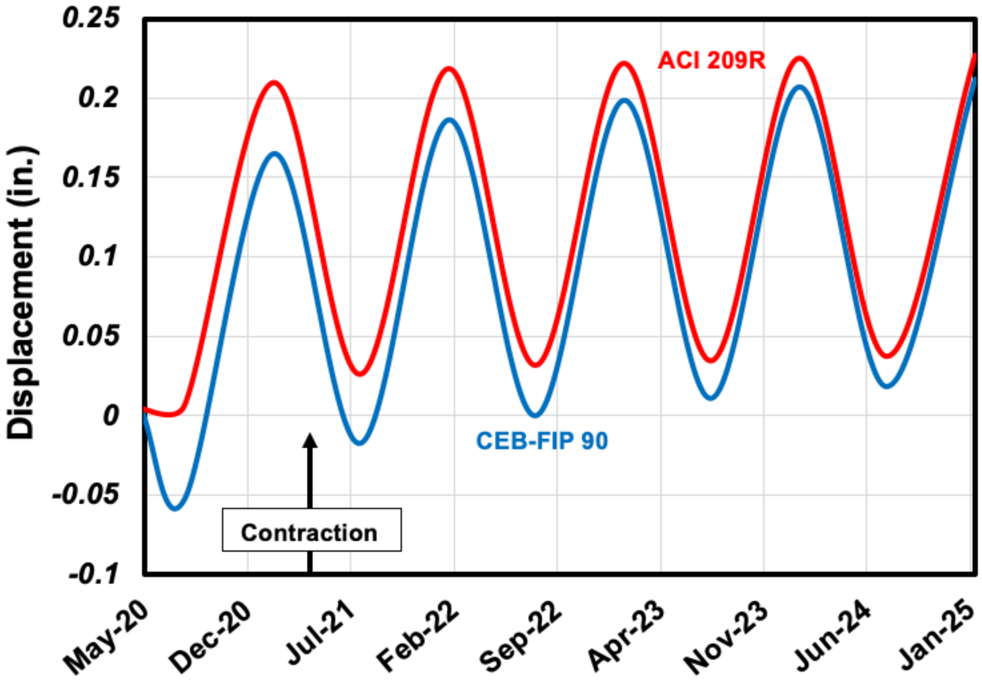

Figure 6.44: Interior Pile Head Lateral Movement for the Two Shrinkage Models

(L = 400 ft and R = 1,000 ft)

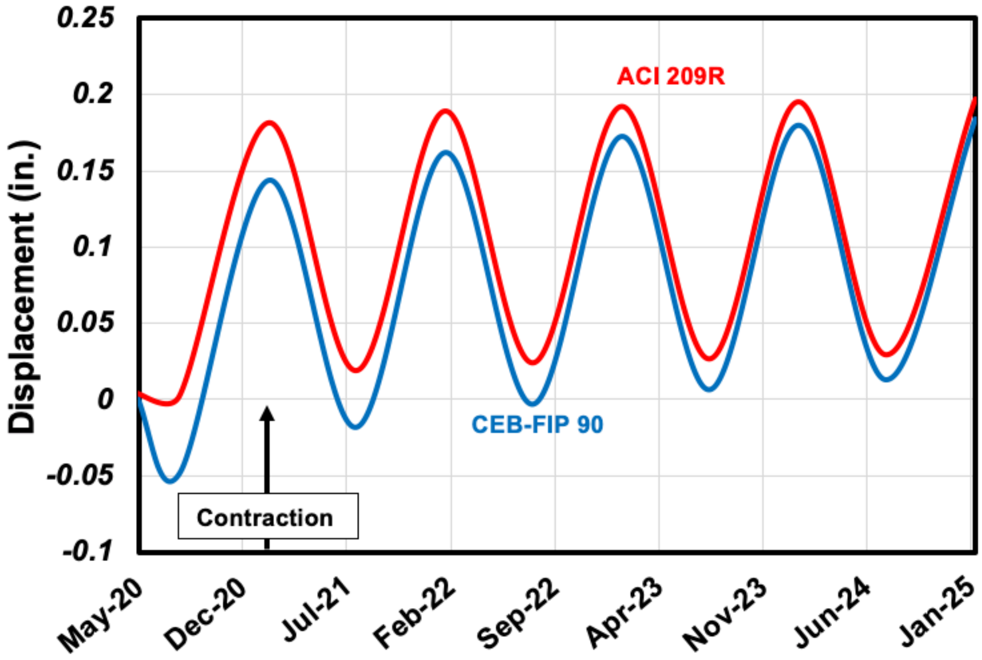

Figure 6.45: Exterior Pile Head Lateral Movement for the Two Shrinkage Models

(L = 400 ft and R = 1,000 ft)

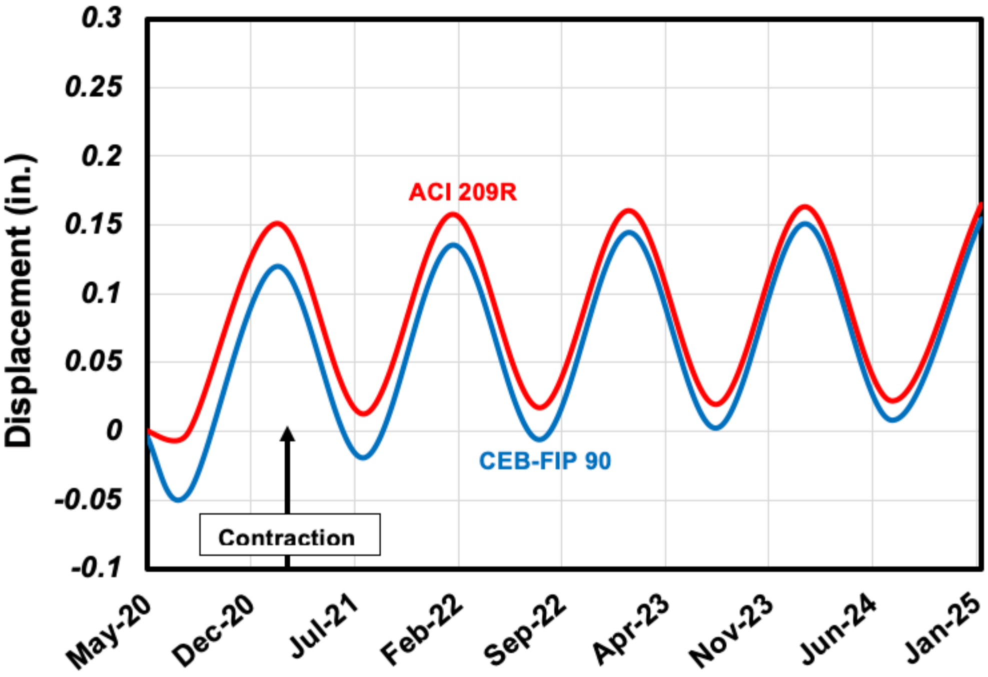

Figure 6.46: Interior Deck Lateral Movement for the Two Shrinkage Models (L = 400 ft and R = 1,000 ft)

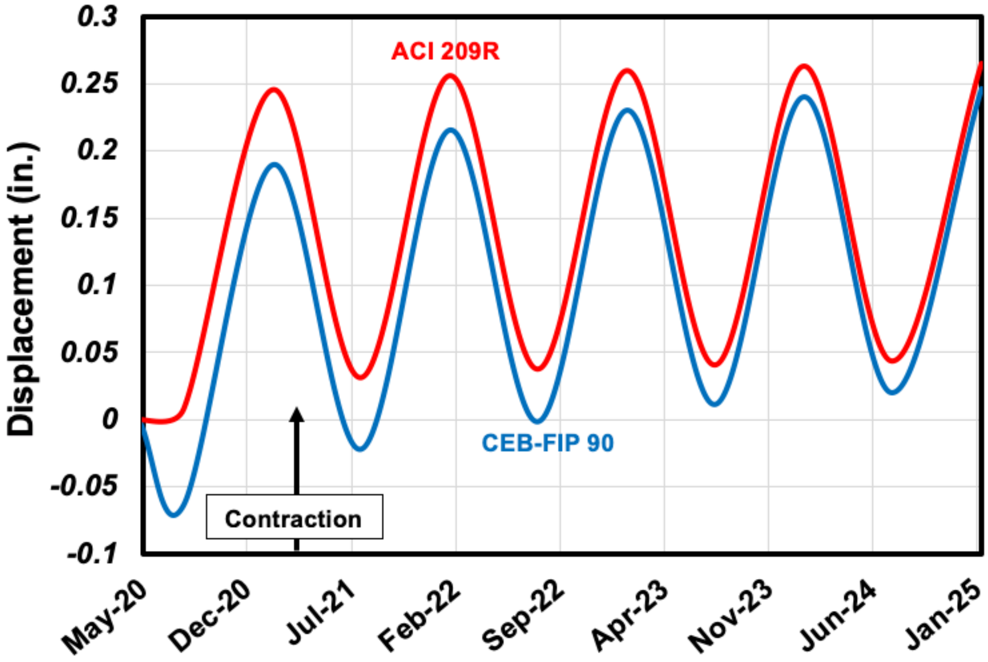

Figure 6.47: Exterior Deck Lateral Movement for the Two Shrinkage Models (L = 400 ft and R = 1,000 ft)

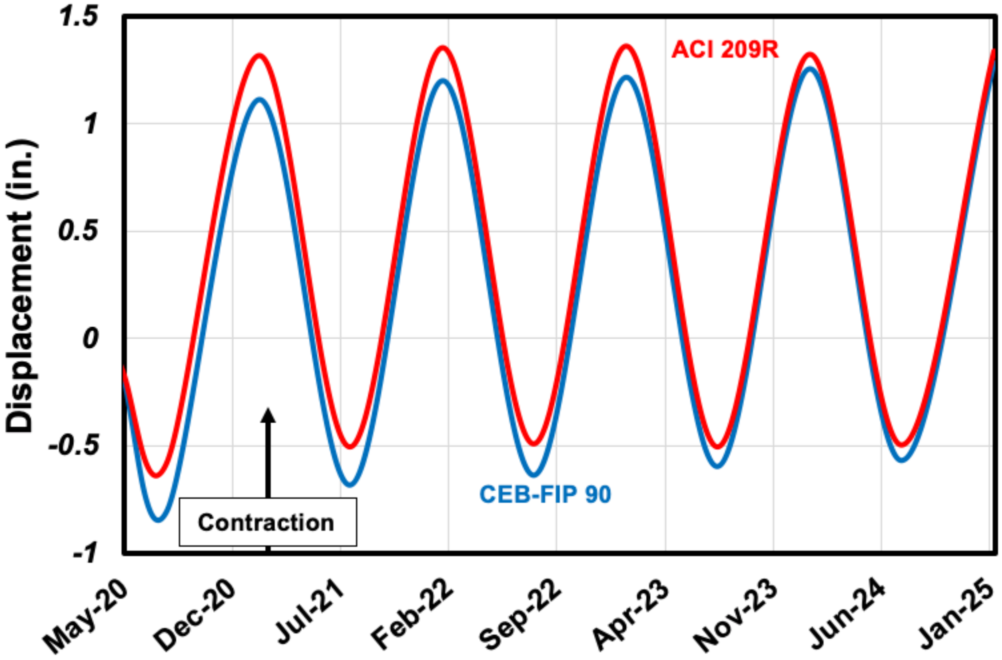

Figure 6.48: Interior Pile Head Longitudinal Movement for the Two Shrinkage Models

(L = 400 ft and R = 1,400 ft)

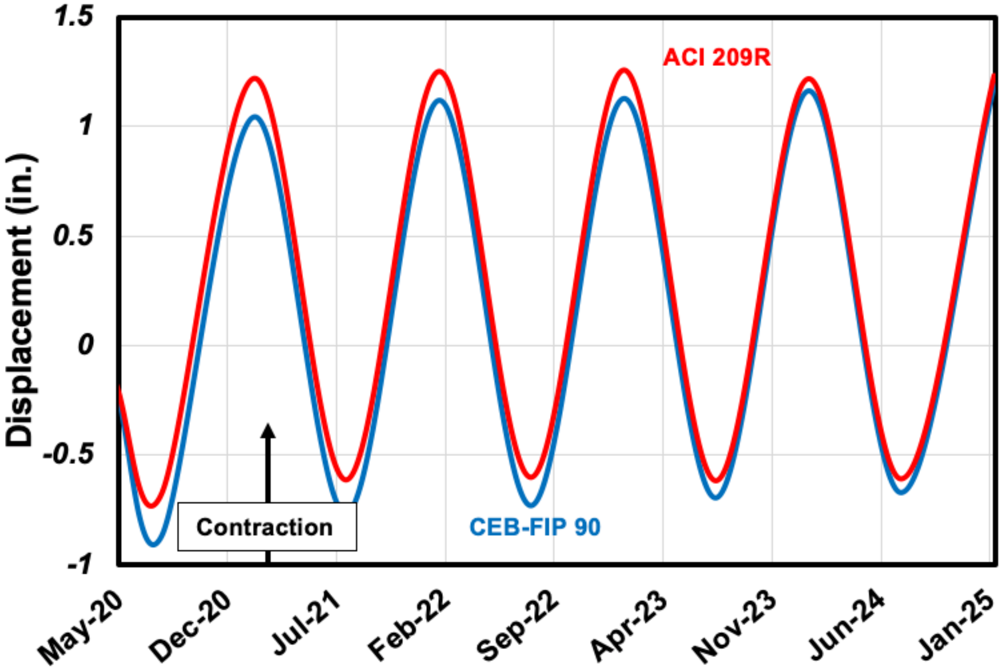

Figure 6.49: Exterior Pile Head Longitudinal Movement for the Two Shrinkage Models

(L = 400 ft and R = 1,400 ft)

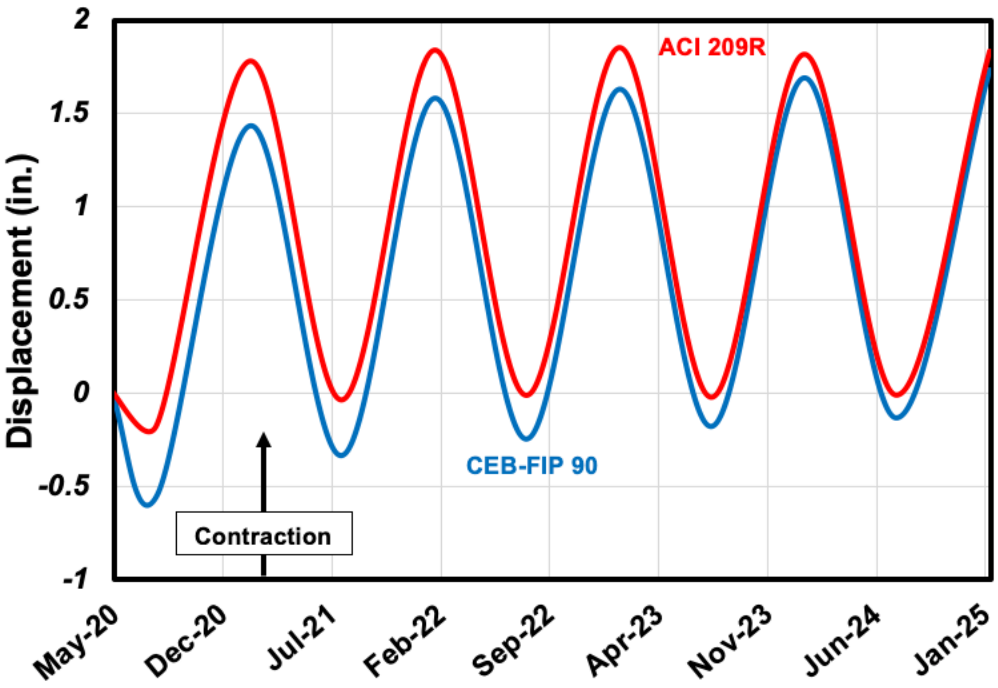

Figure 6.50: Interior Deck Longitudinal Movement for the Two Shrinkage Models

(L = 400 ft and R = 1,400 ft)

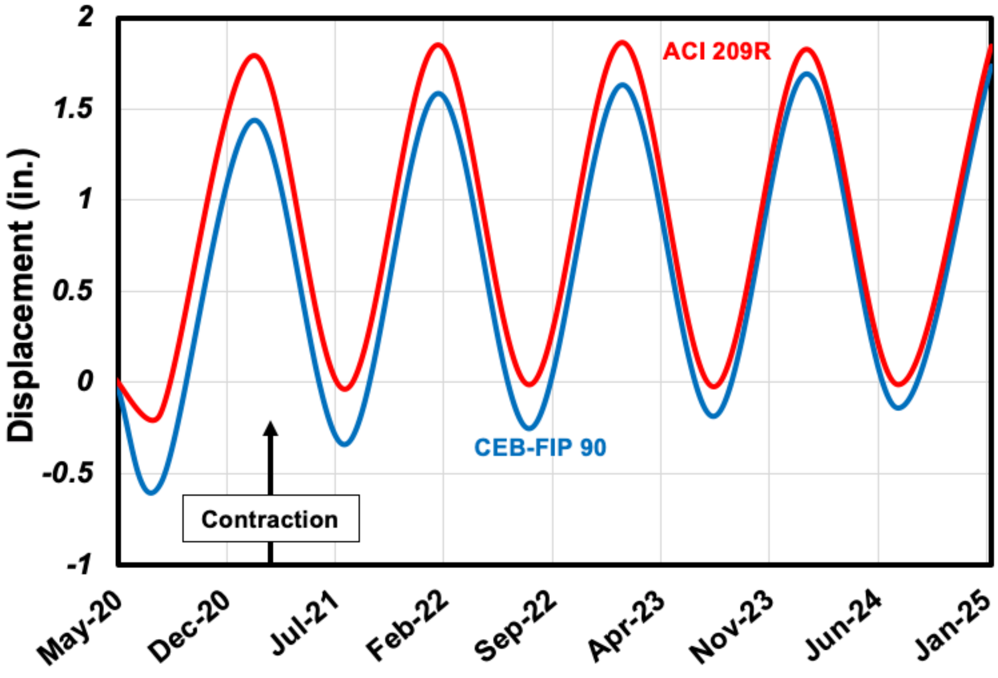

Figure 6.51: Exterior Deck Longitudinal Movement for the Two Shrinkage Models

(L = 400 ft and R = 1,400 ft)

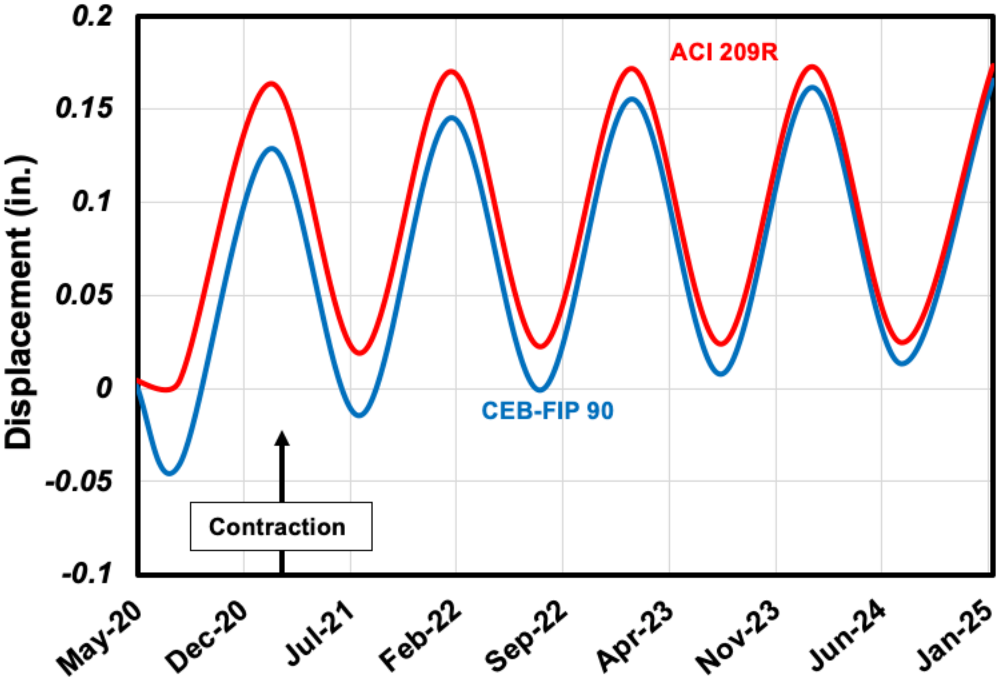

Figure 6.52: Interior Pile Head Lateral Movement for the Two Shrinkage Models

(L = 400 ft and R = 1,400 ft)

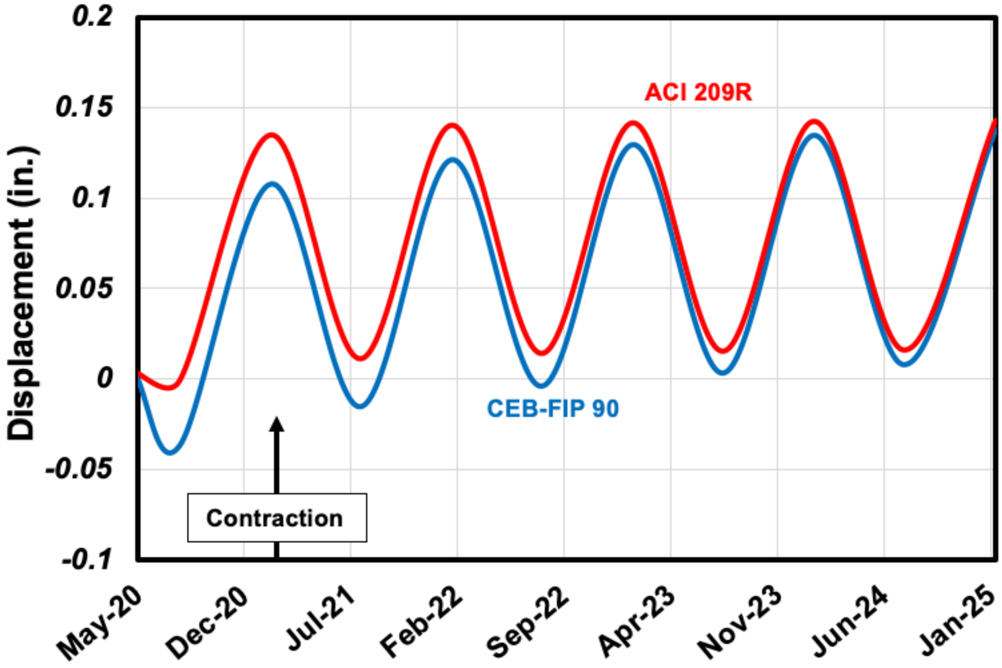

Figure 6.53: Exterior Pile Head Lateral Movement for the Two Shrinkage Models

(L = 400 ft and R = 1,400 ft)

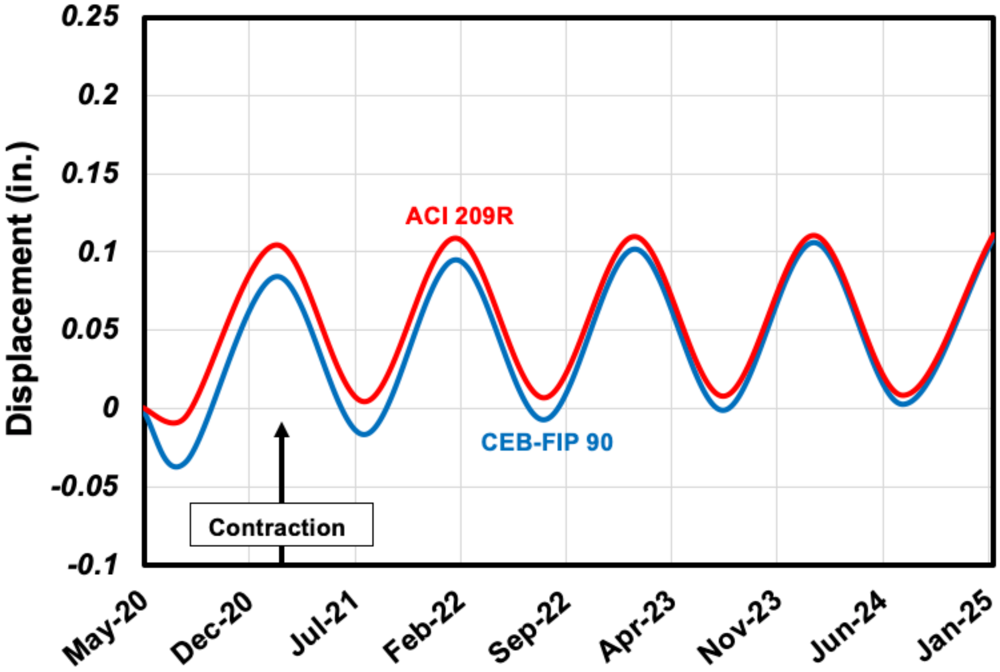

Figure 6.54: Interior Deck Lateral Movement for the Two Shrinkage Models

(L = 400 ft and R = 1,400 ft)

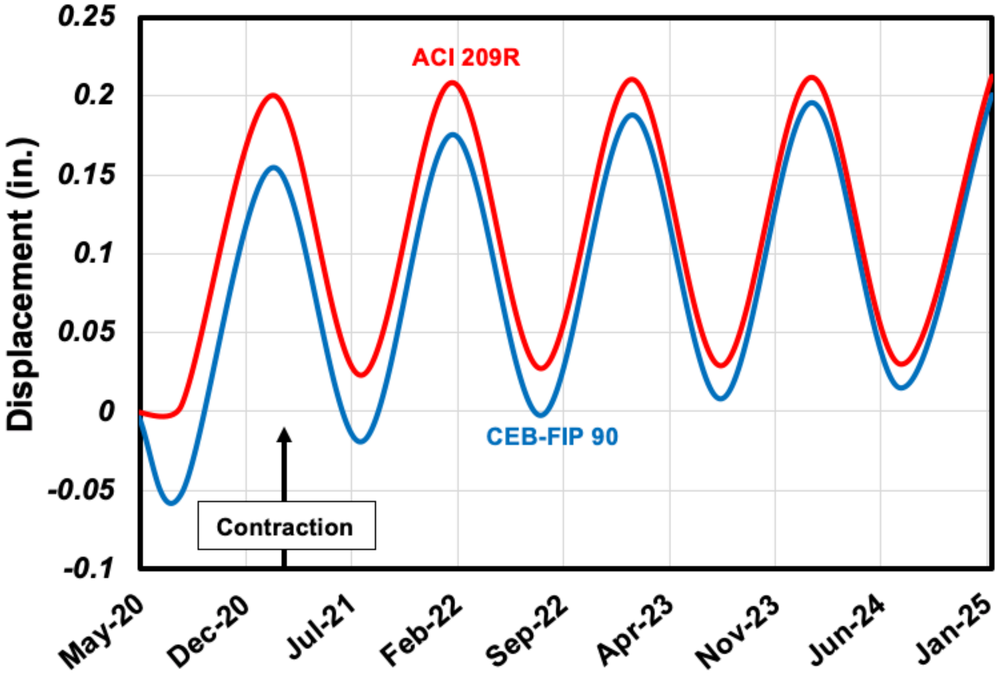

Figure 6.55: Exterior Deck Lateral Movement for the Two Shrinkage Models

(L = 400 ft and R = 1,400 ft)

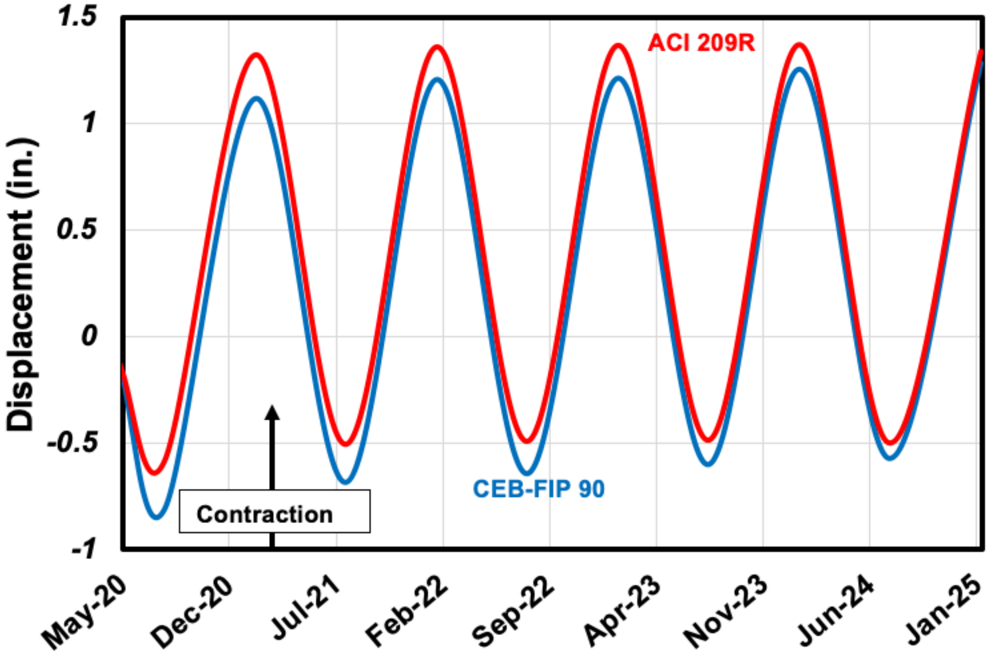

Figure 6.56: Interior Pile Head Longitudinal Movement for the Two Shrinkage Models (L = 400 ft and R = 1,800 ft)

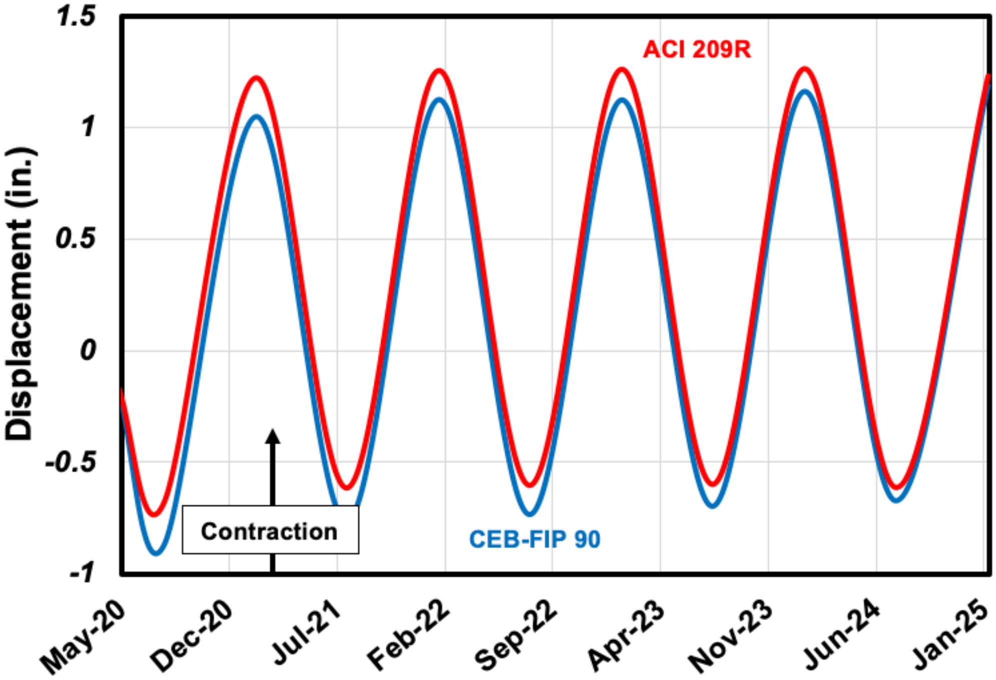

Figure 6.57: Exterior Pile Head Longitudinal Movement for the Two Shrinkage Models (L = 400 ft and R = 1,800 ft)

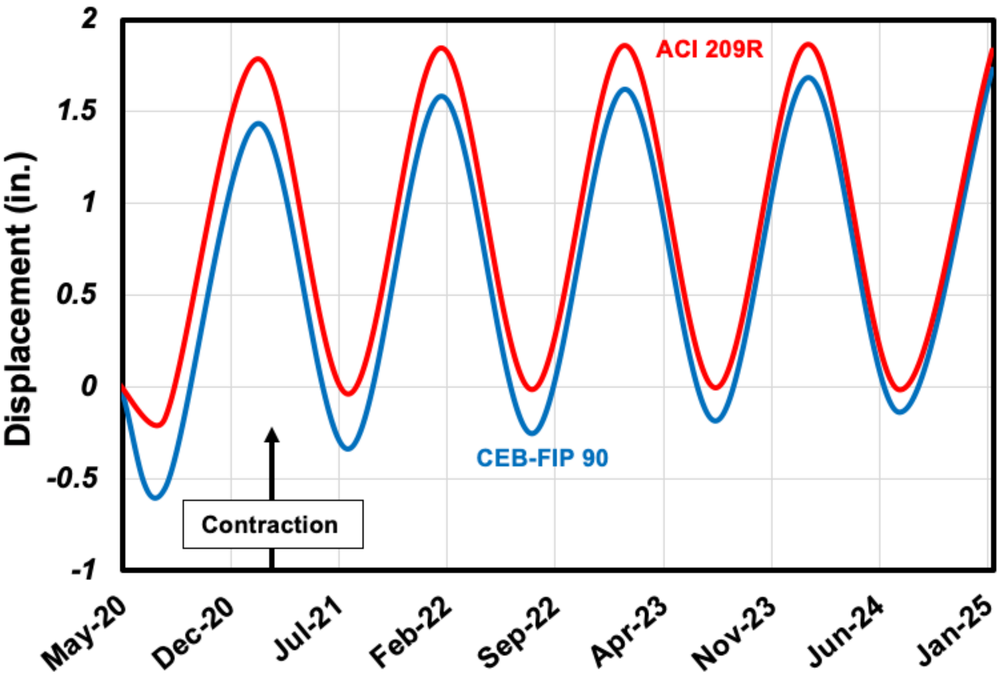

Figure 6.58: Interior Deck Longitudinal Movement for the Two Shrinkage Models

(L = 400 ft and R = 1,800 ft)

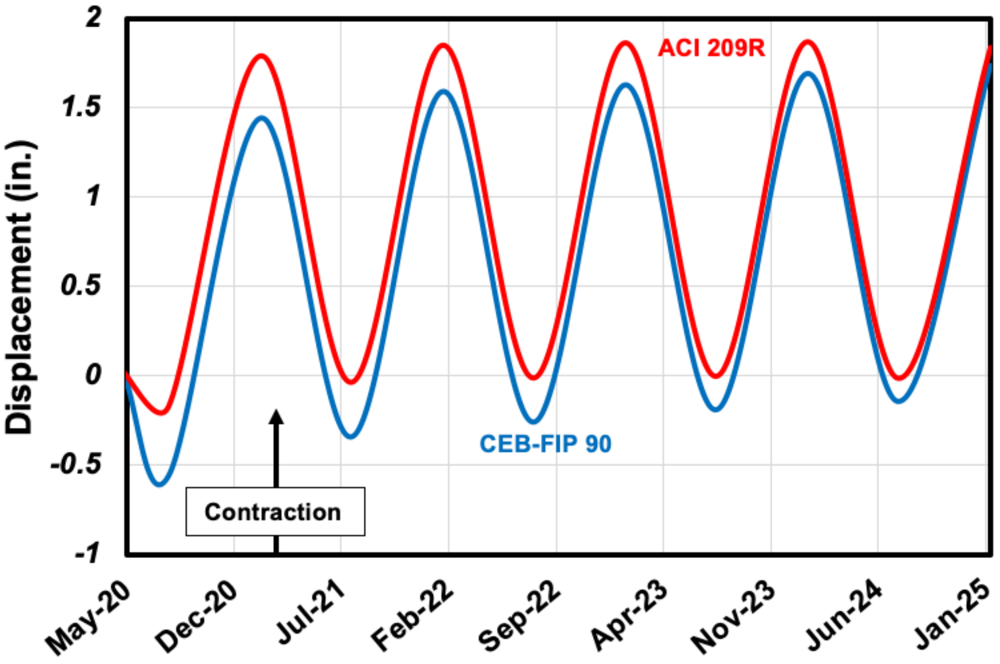

Figure 6.59: Exterior Deck Longitudinal Movement for the Two Shrinkage Models

(L = 400 ft and R = 1,800 ft)

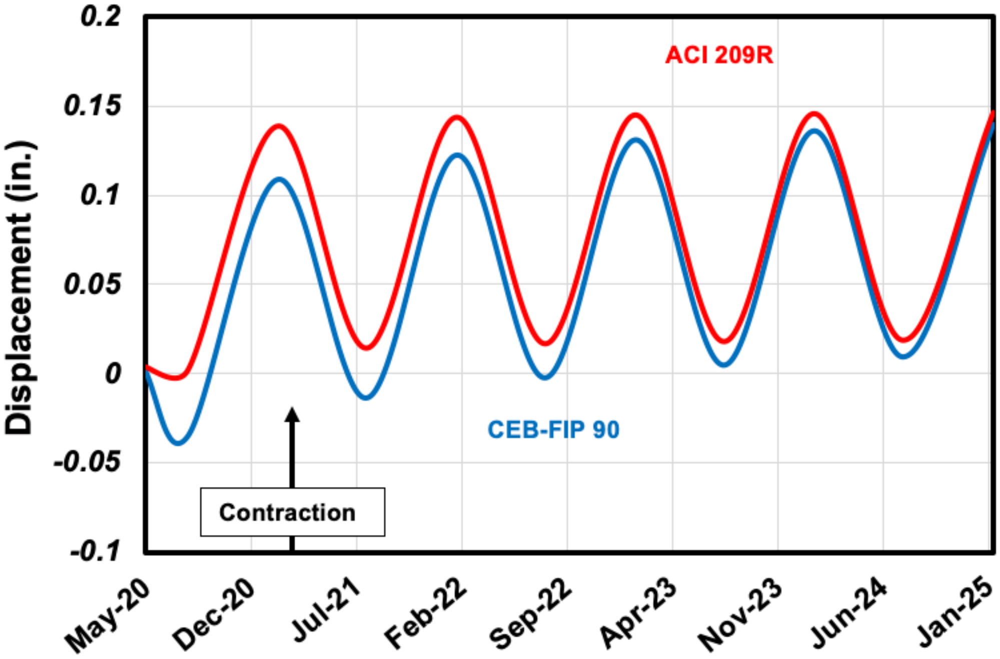

Figure 6.60: Interior Pile Head Lateral Movement for the Two Shrinkage Models

(L = 400 ft and R = 1,800 ft)

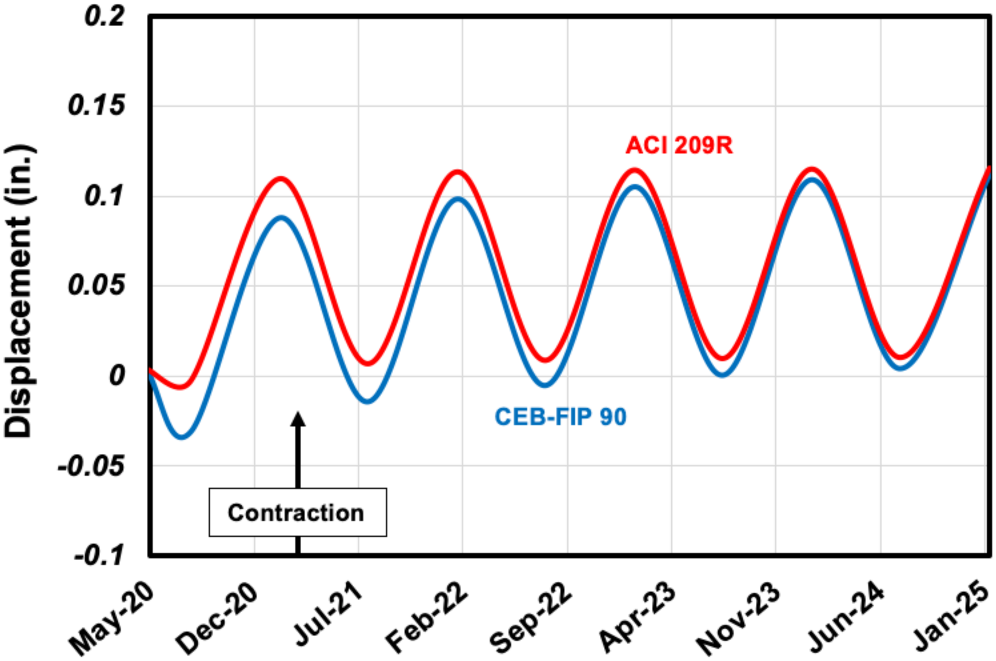

Figure 6.61: Exterior Pile Head Lateral Movement for the Two Shrinkage Models

(L = 400 ft and R = 1,800 ft)

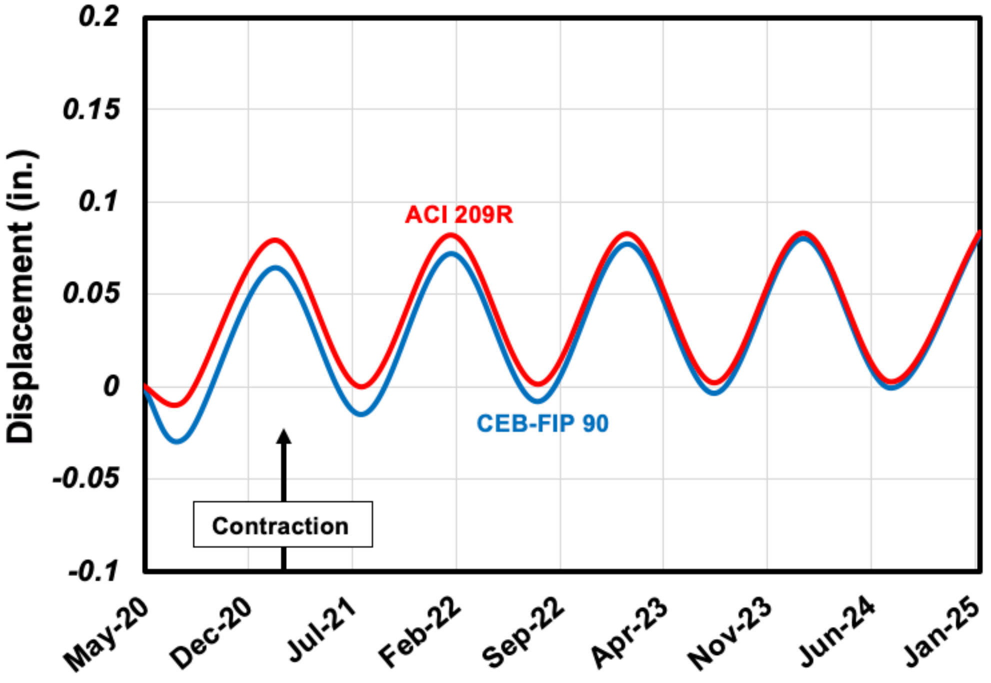

Figure 6.62: Interior Deck Lateral Movement for the Two Shrinkage Models

(L = 400 ft and R = 1,800 ft)

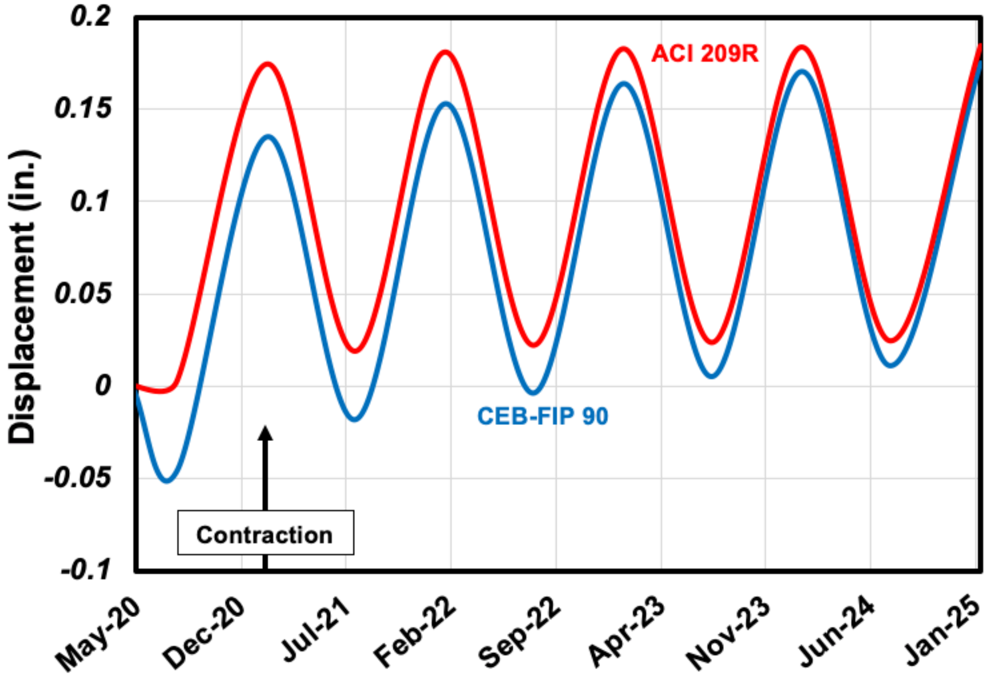

Figure 6.63: Exterior Deck Lateral Movement for the Two Shrinkage Models

(L = 400 ft and R = 1,800 ft)

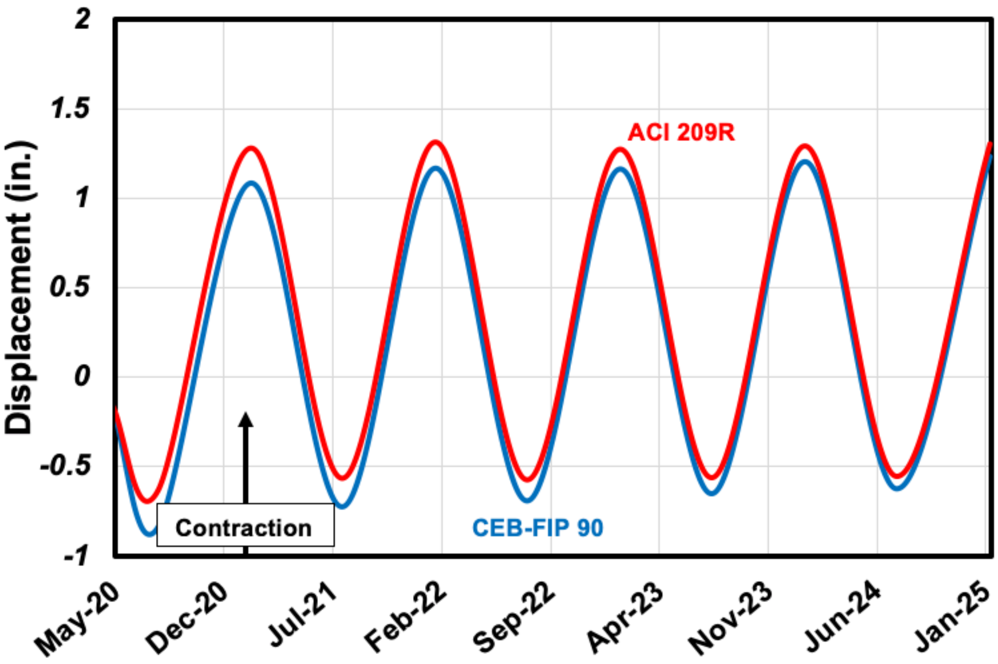

Figure 6.64: Pile Head Longitudinal Movement for the Two Shrinkage Models

(L = 400 ft and R = ∞ ft)

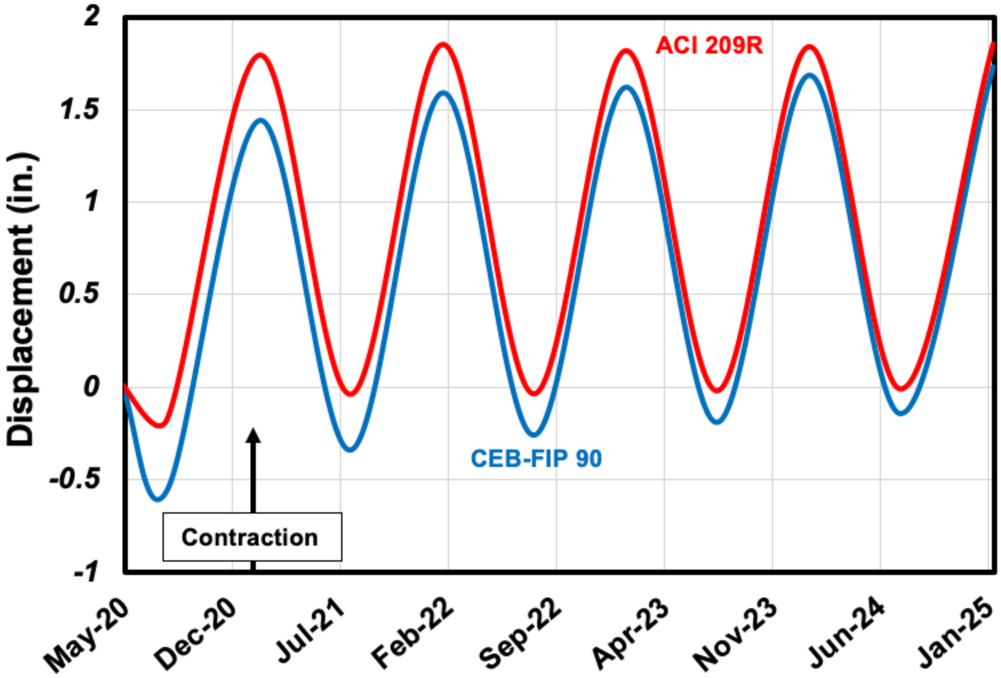

Figure 6.65: Deck Longitudinal Movement for the Two Shrinkage Models

(L = 400 ft and R = ∞ ft)

Table 6.9: Bridge Displacements for Shrinkage Models (L = 400 ft and R = 600 ft)

Date	Displacement (in.)															
	Longitudinal								Lateral							
	Pile Head				Deck				Pile Head				Deck			
	Interior		Exterior		Interior		Exterior		Interior		Exterior		Interior		Exterior	
	CEB-FIP 90	ACI 209R	CEB-FIP 90	ACI 209R	CEB-FIP 90	ACI 209R	CEB-FIP 90	ACI 209R	CEB-FIP 90	ACI 209R	CEB-FIP 90	ACI 209R	CEB-FIP 90	ACI 209R	CEB-FIP 90	ACI 209R
May 2020	-0.12	-0.12	-0.16	-0.16	0.02	0.02	0.02	0.02	0.005	0.005	0.004	0.004	-0.001	-0.001	-0.003	-0.003
Aug. 2020	-0.46	-0.24	-0.49	-0.31	-0.36	0.02	-0.35	0.03	-0.088	0.005	-0.083	0.001	-0.082	-0.006	-0.104	0.003
Feb. 2021	0.70	0.90	0.58	0.76	1.18	1.53	1.18	1.52	0.271	0.343	0.248	0.312	0.222	0.279	0.302	0.387
Aug. 2021	-0.34	-0.17	-0.39	-0.24	-0.15	0.15	-0.14	0.15	-0.033	0.036	-0.033	0.028	-0.037	0.019	-0.042	0.038
Feb. 2022	0.78	0.93	0.65	0.79	1.33	1.59	1.32	1.58	0.307	0.356	0.280	0.323	0.251	0.289	0.343	0.402
Aug. 2022	-0.28	-0.15	-0.34	-0.23	-0.04	0.18	-0.04	0.18	-0.003	0.042	-0.006	0.034	-0.011	0.025	-0.008	0.046
Feb. 2023	0.83	0.95	0.69	0.81	1.41	1.61	1.40	1.61	0.329	0.359	0.300	0.326	0.269	0.292	0.367	0.406
Aug. 2023	-0.25	-0.13	-0.31	-0.21	0.02	0.20	0.02	0.21	0.015	0.045	0.011	0.036	0.005	0.027	0.013	0.049
Feb. 204	0.86	1.03	0.72	0.89	1.46	1.70	1.45	1.70	0.342	0.361	0.312	0.327	0.280	0.293	0.382	0.408
Aug. 2024	-0.22	-0.09	-0.29	-0.16	0.06	0.25	0.06	0.26	0.028	0.046	0.022	0.038	0.015	0.028	0.026	0.050
Feb. 2025	0.88	1.09	0.73	0.94	1.49	1.75	1.48	1.76	0.351	0.363	0.320	0.329	0.288	0.295	0.393	0.410

Table 6.10: Bridge Displacements for Shrinkage Models (L = 400 ft and R = 1,000 ft)

Date	Displacement (in.)															
	Longitudinal								Lateral							
	Pile Head				Deck				Pile Head				Deck			
	Interior		Exterior		Interior		Exterior		Interior		Exterior		Interior		Exterior	
	CEB-FIP 90	ACI 209R	CEB-FIP 90	ACI 209R	CEB-FIP 90	ACI 209R	CEB-FIP 90	ACI 209R	CEB-FIP 90	ACI 209R	CEB-FIP 90	ACI 209R	CEB-FIP 90	ACI 209R	CEB-FIP 90	ACI 209R
May 2020	-0.12	-0.12	-0.16	-0.16	0.02	0.02	0.02	0.02	0.005	0.005	0.005	0.005	0.001	0.001	-0.001	-0.001
Aug. 2020	-0.81	-0.58	-0.87	-0.68	-0.55	-0.17	-0.55	-0.17	-0.052	0.007	-0.048	0.003	-0.046	-0.002	-0.064	0.008
Feb. 2021	1.11	1.31	1.04	1.22	1.42	1.77	1.43	1.78	0.165	0.210	0.144	0.182	0.120	0.151	0.190	0.246
Aug. 2021	-0.68	-0.51	-0.76	-0.62	-0.34	-0.04	-0.34	-0.04	-0.017	0.026	-0.018	0.019	-0.019	0.012	-0.022	0.031
Feb. 2022	1.20	1.35	1.12	1.24	1.57	1.83	1.58	1.84	0.186	0.219	0.162	0.189	0.135	0.158	0.216	0.257
Aug. 2022	-0.64	-0.49	-0.74	-0.60	-0.25	-0.01	-0.26	-0.01	0.000	0.032	-0.003	0.024	-0.006	0.017	-0.002	0.037
Feb. 2023	1.20	1.36	1.11	1.25	1.61	1.85	1.61	1.86	0.198	0.222	0.173	0.192	0.144	0.160	0.230	0.260
Aug. 2023	-0.60	-0.49	-0.70	-0.60	-0.19	0.00	-0.19	-0.01	0.011	0.035	0.007	0.027	0.002	0.019	0.011	0.040
Feb. 204	1.24	1.36	1.15	1.26	1.67	1.85	1.68	1.86	0.207	0.225	0.180	0.195	0.151	0.163	0.240	0.264
Aug. 2024	-0.57	-0.48	-0.67	-0.60	-0.14	0.01	-0.14	0.00	0.019	0.038	0.013	0.029	0.008	0.022	0.020	0.043
Feb. 2025	1.27	1.36	1.17	1.26	1.72	1.86	1.72	1.86	0.212	0.227	0.184	0.197	0.154	0.165	0.246	0.266

Table 6.11: Bridge Displacements for Shrinkage Models (L = 400 ft and R = 1,400 ft)

Date	Displacement (in.)															
	Longitudinal								Lateral							
	Pile Head				Deck				Pile Head				Deck			
	Interior		Exterior		Interior		Exterior		Interior		Exterior		Interior		Exterior	
	CEB-FIP 90	ACI 209R	CEB-FIP 90	ACI 209R	CEB-FIP 90	ACI 209R	CEB-FIP 90	ACI 209R	CEB-FIP 90	ACI 209R	CEB-FIP 90	ACI 209R	CEB-FIP 90	ACI 209R	CEB-FIP 90	ACI 209R
May 2020	-0.12	-0.12	-0.16	-0.16	0.02	0.02	0.02	0.02	0.005	0.005	0.004	0.004	0.001	0.001	0.000	0.000
Aug. 2020	-0.81	-0.58	-0.87	-0.68	-0.55	-0.17	-0.55	-0.17	-0.041	0.004	-0.037	-0.001	-0.034	-0.005	-0.052	0.004
Feb. 2021	1.11	1.32	1.04	1.22	1.43	1.78	1.44	1.79	0.129	0.164	0.108	0.135	0.084	0.105	0.154	0.200
Aug. 2021	-0.68	-0.51	-0.76	-0.61	-0.34	-0.03	-0.34	-0.04	-0.015	0.019	-0.015	0.011	-0.017	0.005	-0.019	0.023
Feb. 2022	1.20	1.36	1.12	1.25	1.58	1.84	1.58	1.85	0.146	0.171	0.121	0.141	0.095	0.109	0.175	0.208
Aug. 2022	-0.64	-0.49	-0.73	-0.60	-0.25	-0.01	-0.25	-0.01	-0.001	0.022	-0.004	0.014	-0.007	0.007	-0.003	0.027
Feb. 2023	1.22	1.36	1.13	1.26	1.63	1.85	1.63	1.86	0.156	0.172	0.130	0.142	0.102	0.110	0.188	0.210
Aug. 2023	-0.60	-0.51	-0.69	-0.62	-0.18	-0.02	-0.19	-0.02	0.008	0.024	0.003	0.016	-0.001	0.008	0.008	0.029
Feb. 204	1.26	1.33	1.16	1.22	1.69	1.82	1.69	1.82	0.162	0.173	0.135	0.143	0.106	0.111	0.196	0.212
Aug. 2024	-0.57	-0.50	-0.67	-0.61	-0.14	-0.01	-0.14	-0.01	0.013	0.025	0.008	0.016	0.003	0.009	0.015	0.030
Feb. 2025	1.28	1.34	1.19	1.23	1.73	1.83	1.73	1.84	0.166	0.174	0.138	0.143	0.108	0.111	0.201	0.212

Table 6.12: Bridge Displacements for Shrinkage Models (L = 400 ft and R = 1,800 ft)

Date	Displacement (in.)															
	Longitudinal								Lateral							
	Pile Head				Deck				Pile Head				Deck			
	Interior		Exterior		Interior		Exterior		Interior		Exterior		Interior		Exterior	
	CEB-FIP 90	ACI 209R	CEB-FIP 90	ACI 209R	CEB-FIP 90	ACI 209R	CEB-FIP 90	ACI 209R	CEB-FIP 90	ACI 209R	CEB-FIP 90	ACI 209R	CEB-FIP 90	ACI 209R	CEB-FIP 90	ACI 209R
May 2020	-0.12	-0.12	-0.16	-0.16	0.02	0.02	0.02	0.02	0.004	0.004	0.004	0.004	0.001	0.001	0.000	0.000
Aug. 2020	-0.81	-0.59	-0.87	-0.68	-0.55	-0.17	-0.56	-0.17	-0.035	0.002	-0.031	-0.003	-0.028	-0.007	-0.046	0.003
Feb. 2021	1.12	1.32	1.05	1.22	1.43	1.78	1.44	1.79	0.109	0.139	0.088	0.110	0.065	0.079	0.135	0.175
Aug. 2021	-0.68	-0.51	-0.76	-0.61	-0.34	-0.04	-0.34	-0.04	-0.013	0.014	-0.014	0.007	-0.015	0.000	-0.018	0.019
Feb. 2022	1.21	1.36	1.12	1.26	1.58	1.84	1.59	1.85	0.123	0.143	0.099	0.114	0.072	0.082	0.153	0.181
Aug. 2022	-0.64	-0.49	-0.73	-0.60	-0.26	-0.01	-0.26	-0.01	-0.002	0.017	-0.005	0.009	-0.008	0.002	-0.004	0.022
Feb. 2023	1.21	1.37	1.12	1.26	1.62	1.86	1.62	1.86	0.131	0.145	0.106	0.115	0.077	0.083	0.164	0.183
Aug. 2023	-0.60	-0.49	-0.70	-0.60	-0.19	0.00	-0.19	0.00	0.005	0.018	0.001	0.010	-0.004	0.002	0.005	0.024
Feb. 204	1.25	1.37	1.16	1.27	1.68	1.86	1.69	1.87	0.136	0.146	0.109	0.115	0.080	0.083	0.170	0.184
Aug. 2024	-0.57	-0.50	-0.67	-0.61	-0.14	-0.01	-0.14	-0.02	0.010	0.019	0.004	0.010	-0.001	0.003	0.011	0.024
Feb. 2025	1.28	1.34	1.19	1.23	1.73	1.83	1.73	1.84	0.140	0.146	0.112	0.116	0.082	0.084	0.175	0.185

Table 6.13: Bridge Displacements for Shrinkage Models (L = 400 ft and Straight Bridges)

Date	Displacement (in.)															
	Longitudinal								Lateral							
	Pile Head				Deck				Pile Head				Deck			
	Interior		Exterior		Interior		Exterior		Interior		Exterior		Interior		Exterior	
	CEB-FIP 90	ACI 209R	CEB-FIP 90	ACI 209R	CEB-FIP 90	ACI 209R	CEB-FIP 90	ACI 209R	CEB-FIP 90	ACI 209R	CEB-FIP 90	ACI 209R	CEB-FIP 90	ACI 209R	CEB-FIP 90	ACI 209R
May 2020	-0.14	-0.14	-0.14	-0.14	0.02	0.02	0.02	0.02	0.005	0.005	0.005	0.005	0.005	0.005	0.005	0.005
Aug. 2020	-0.84	-0.64	-0.84	-0.64	-0.56	-0.17	-0.56	-0.17	-0.010	0.000	-0.006	-0.005	0.000	-0.008	-0.017	0.002
Feb. 2021	1.09	1.28	1.09	1.28	1.44	1.79	1.44	1.79	0.041	0.050	0.020	0.021	-0.004	-0.012	0.066	0.084
Aug. 2021	-0.73	-0.56	-0.73	-0.56	-0.34	-0.04	-0.34	-0.04	-0.005	0.003	-0.005	-0.004	-0.004	-0.010	-0.006	0.009
Feb. 2022	1.17	1.31	1.17	1.31	1.59	1.85	1.59	1.85	0.045	0.052	0.021	0.022	-0.007	-0.013	0.074	0.087
Aug. 2022	-0.69	-0.57	-0.69	-0.57	-0.26	-0.04	-0.26	-0.04	-0.002	0.004	-0.005	-0.004	-0.006	-0.011	-0.001	0.010
Feb. 2023	1.17	1.27	1.17	1.27	1.62	1.82	1.62	1.82	0.047	0.052	0.021	0.022	-0.009	-0.013	0.078	0.087
Aug. 2023	-0.65	-0.56	-0.65	-0.56	-0.19	-0.02	-0.19	-0.02	0.000	0.004	-0.004	-0.004	-0.007	-0.011	0.002	0.011
Feb. 204	1.21	1.29	1.21	1.29	1.68	1.84	1.69	1.84	0.049	0.052	0.022	0.022	-0.010	-0.013	0.080	0.088
Aug. 2024	-0.63	-0.55	-0.63	-0.55	-0.15	-0.01	-0.15	-0.01	0.001	0.004	-0.004	-0.004	-0.008	-0.011	0.005	0.011
Feb. 2025	1.24	1.30	1.24	1.30	1.73	1.85	1.73	1.85	0.050	0.052	0.022	0.022	-0.010	-0.013	0.082	0.088

6.7.3 Soil Type

The performance of IABs can be evaluated by the soil–pile interactions since pile deflections accommodate their movement. Therefore, we added four additional soil types to the default layered soil adapted from the Big Springs bridge site in order to cover an acceptable range of soil consistency. These soil types are dense sand, loose sand, very stiff clay and very soft clay. According to Figure 6.66, for a 400–ft long bridge, the longitudinal displacement of the interior pile head increases by 46% when the radius of curvature increases from 600 to 1000 ft. By further increasing the radius of curvature, however, this displacement remains nearly constant. It also shows that bridges with different soil types surrounding their piles exhibit the same amount of longitudinal displacements, regardless of the soil type. For the lateral movement, on the other hand, as the bridge becomes less curved, displacements decrease constantly, which is expected because with less curve there will less eccentricity. According to Figure 6.67, for the 400–ft long bridge with the highest curvature (R = 600 ft), there is a slight difference in the lateral displacements among different soil types, but for larger radii of curvature, this difference is not noticeable. Long CMP sleeves may explain why bridge displacements seem independent of soil type. In all models, CMP sleeves and loose sand were assumed to surround the top 18 ft of piles, similar to the Big Springs bridge site. This part of the pile was therefore not modeled with soil. The deformation of piles below 18 ft seems that it is not large enough to significantly affect the bridge's behavior. Movements of interior piles and interior/exterior decks follow the similar pattern (Figure 6.68 to Figure 6.73). Unlike bridge displacements, pile head moments and stresses are not independent of soil type. When the radius of curvature changes from 600 to 1000 ft (Figure 6.74), pile head stress/moment increases greatly, but it remains nearly constant thereafter. For example, a 400–ft long bridge with a radius of curvature of 600 ft in dense sand would have a maximum pile head stress of 5 ksi while a bridge of the identical length and soil condition with a radius of curvature of 1,000 ft would have a maximum pile head stress of 12 ksi. According to Figure 6.75, for a 400–ft long bridge with a radius of curvature of 600 ft, very soft clay, loose sand, very stiff clay and dense sand soil conditions causes higher pile head bending moments, in order. In contrast, curved bridges with larger radii of curvature (radius of curvature ≥ 1,000 ft) behave differently. First of all, the order of maximum pile head moments is reversed. Specifically, the highest moments are observed in bridges with dense sand, very stiff clay, loose sand and very soft clay soil conditions which is a more expected trend since dense and stiff clay cause higher reaction than loose sand and soft clay, resulting in higher bending moment. Unlike the bridge with 600–ft radius of curvature, bending moments caused by different soil types are noticeable here. In addition, bending moment and stress remain almost constant for bridges with radii of curvature greater than 1,000 ft (Figure 6.74 and Figure 6.75). For instance, when the soil condition of a 400–ft long bridge with a radius of curvature larger than 600 ft, changes from very soft clay to dense sand, the maximum pile head moment increases by 50%. When the radius of curvature increases from 1,800 ft to infinity (a straight bridge), the maximum bending moment of the pile head drops slightly (Figure 6.75). Finally, the top and bottom flanges on girders do not appear to be greatly affected by soil type at the girder–abutment Connection. Modeling bridges with different soil types results in slight differences of girder flange stresses, but they are not significant (Figure 6.76 and 6.77). The maximum stresses and bending moments values are observed at locations below where the CMP sleeves end. The CMP sleeves does help reduce the influence of IAB longitudinal and lateral movements independent to the surrounding soil types.

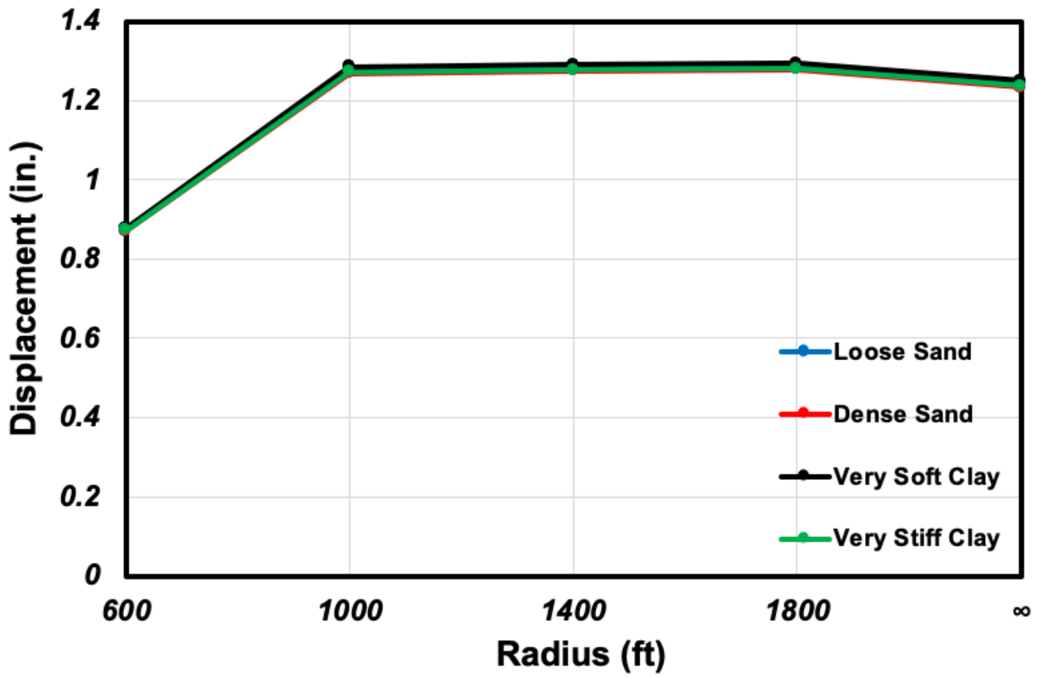

Figure 6.66: Interior Pile Head Longitudinal Displacement for Different Soil Types (L = 400 ft)

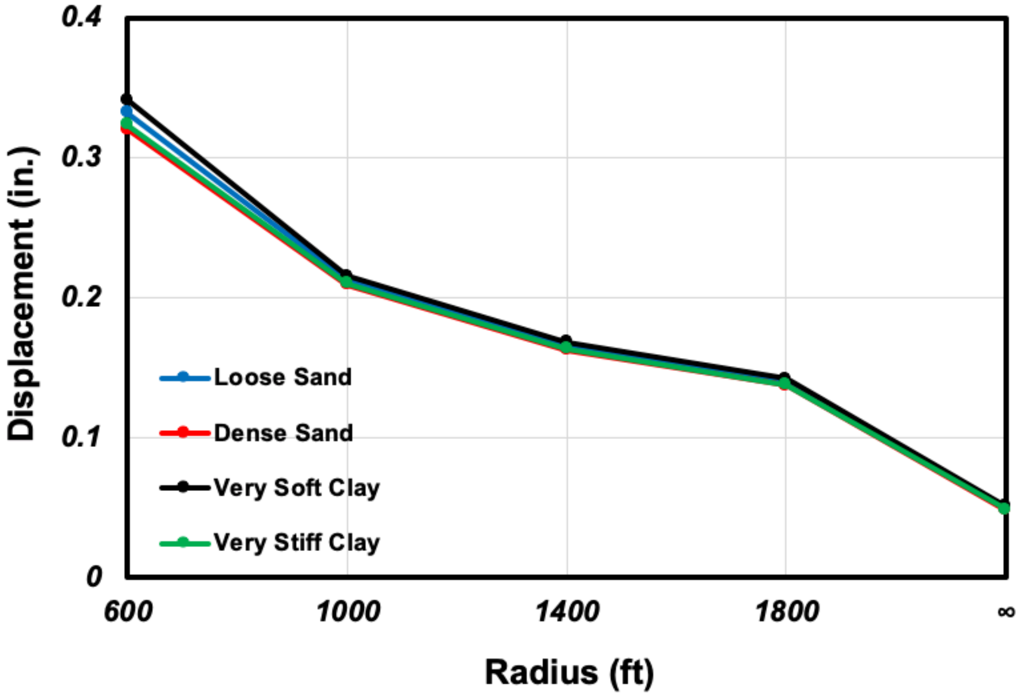

Figure 6.67: Interior Pile Head Lateral Displacement for Different Soil Types (L = 400 ft)

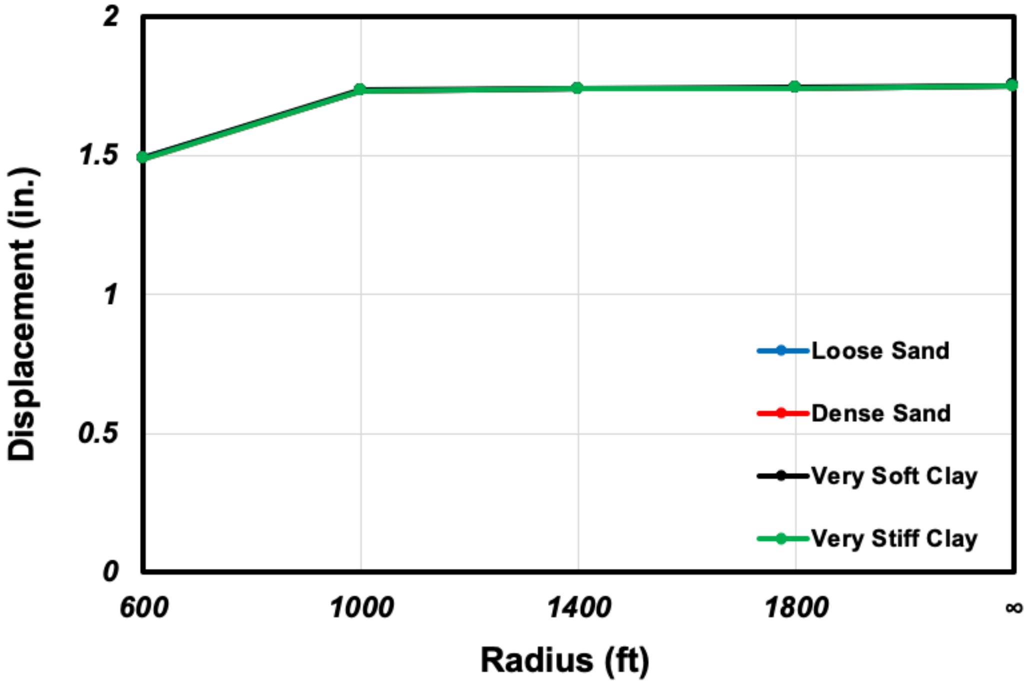

Figure 6.68: Interior Deck Longitudinal Displacement for Different Soil Types (L = 400 ft)

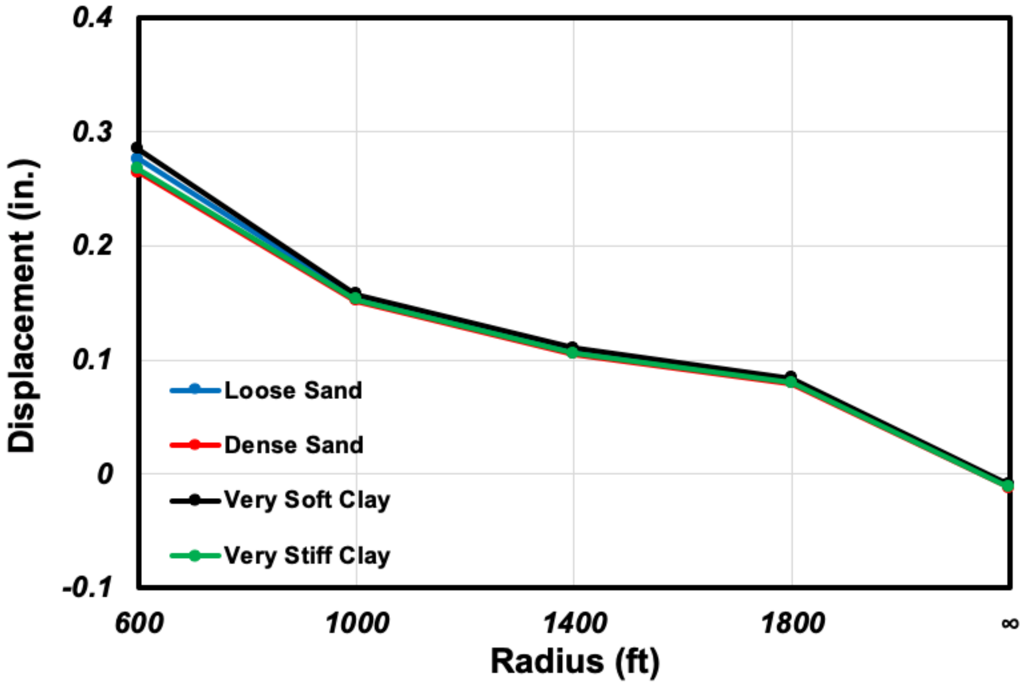

Figure 6.69: Interior Deck Lateral Displacement for Different Soil Types (L = 400 ft)

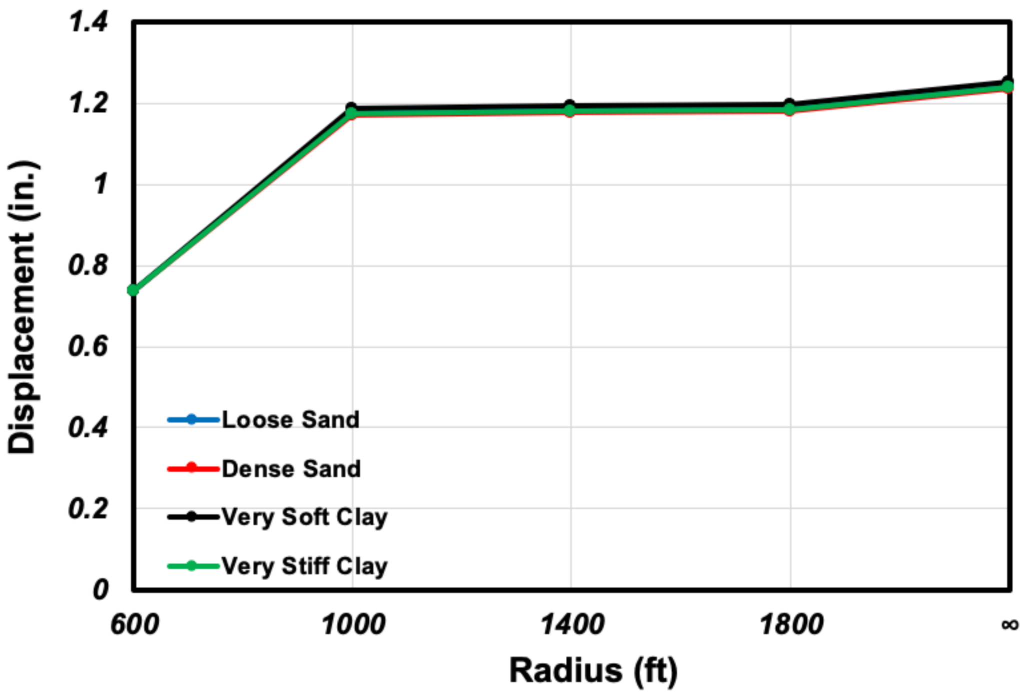

Figure 6.70: Exterior Pile Head Longitudinal Displacement for Different Soil Types (L = 400 ft)

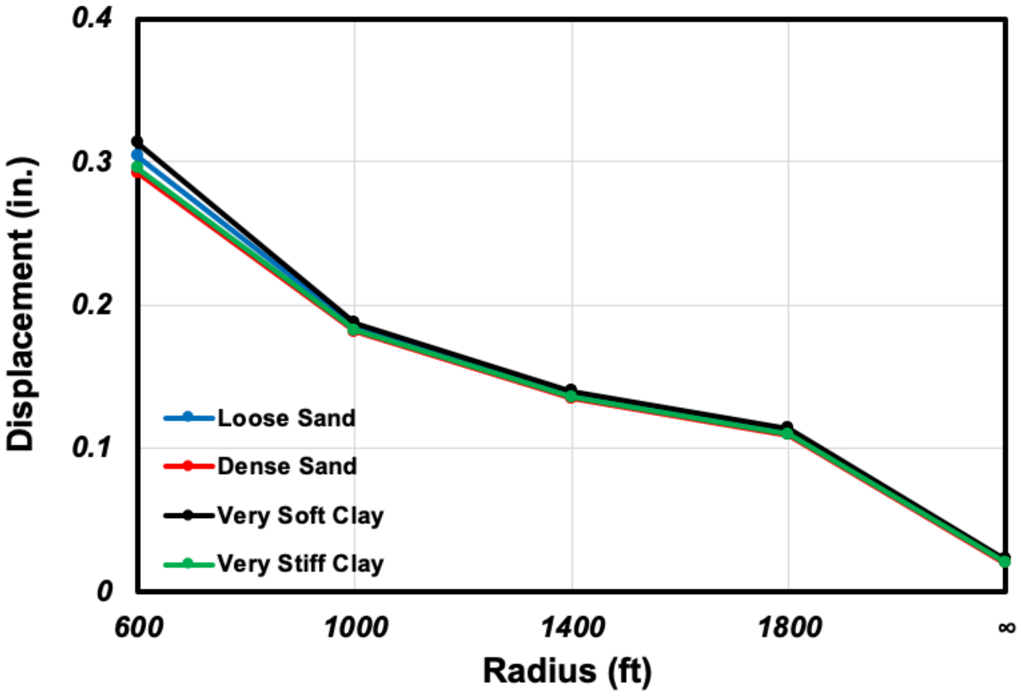

Figure 6.71: Exterior Pile Head Lateral Displacement for Different Soil Types (L = 400 ft)

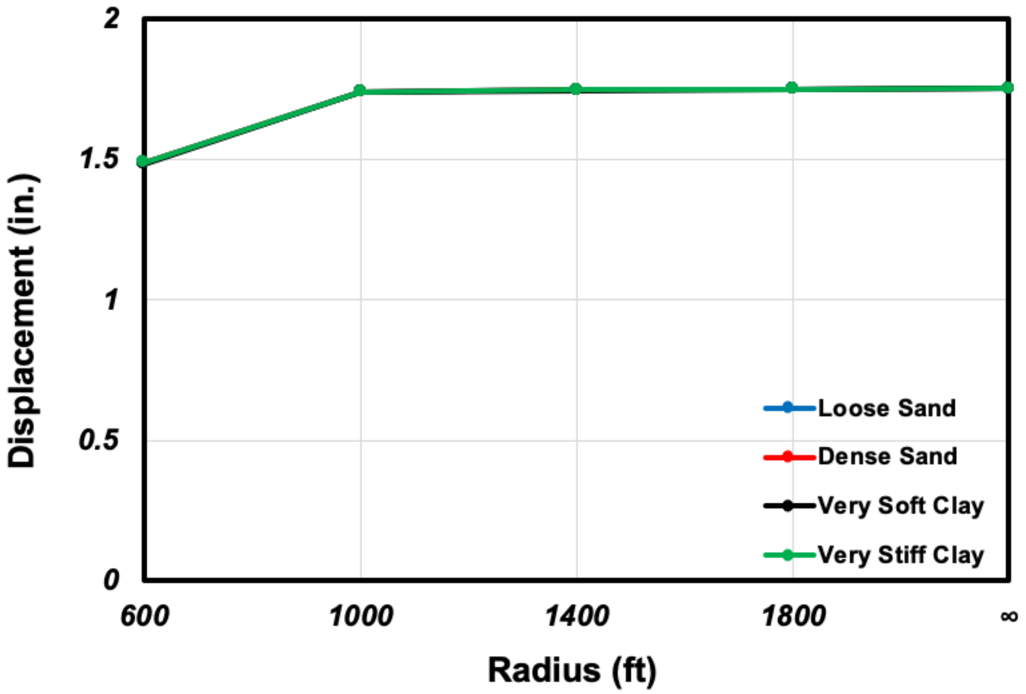

Figure 6.72: Exterior Deck Longitudinal Displacement for Different Soil Types (L = 400 ft)

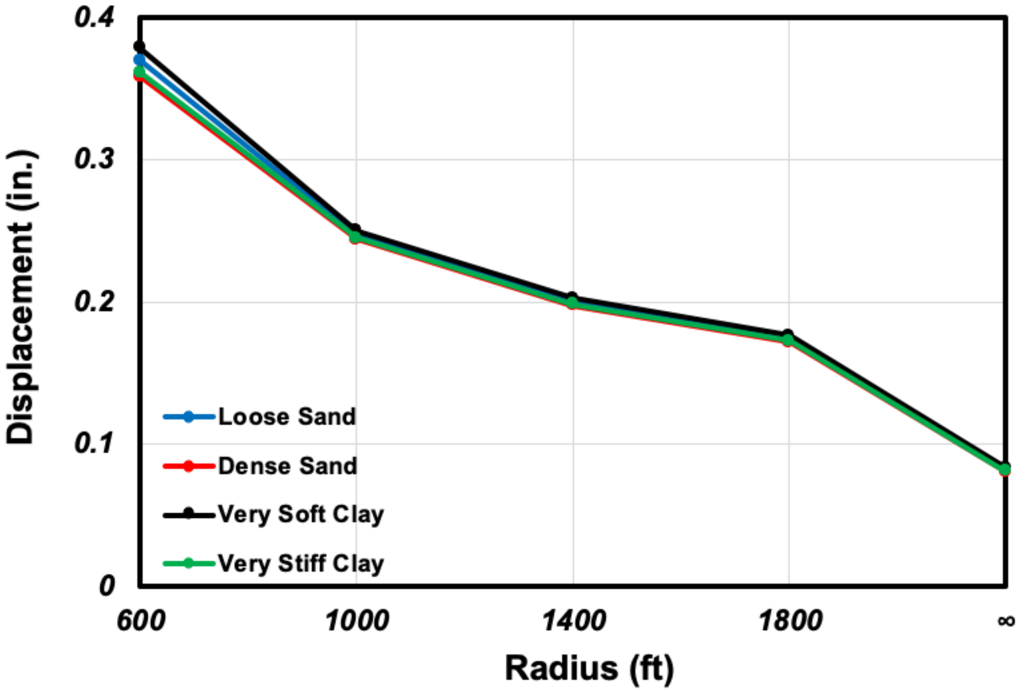

Figure 6.73: Exterior Deck Lateral Displacement for Different Soil Types (L = 400 ft)

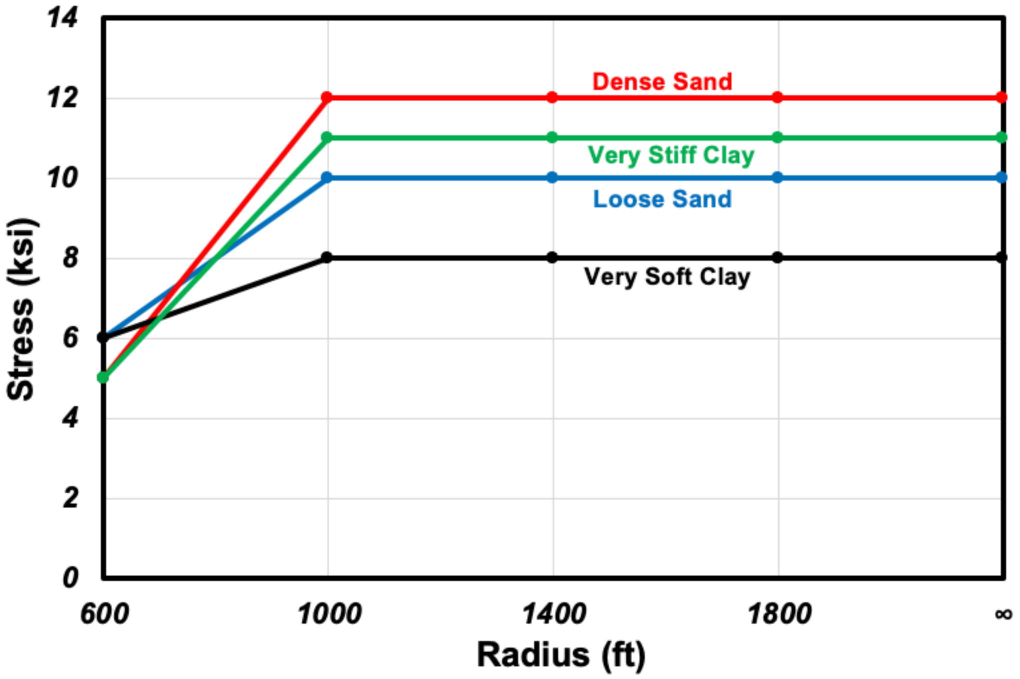

Figure 6.74: Pile Max. von Mises Stress at the Pile–Abutment Connection for Different Soil Types (L = 400 ft)

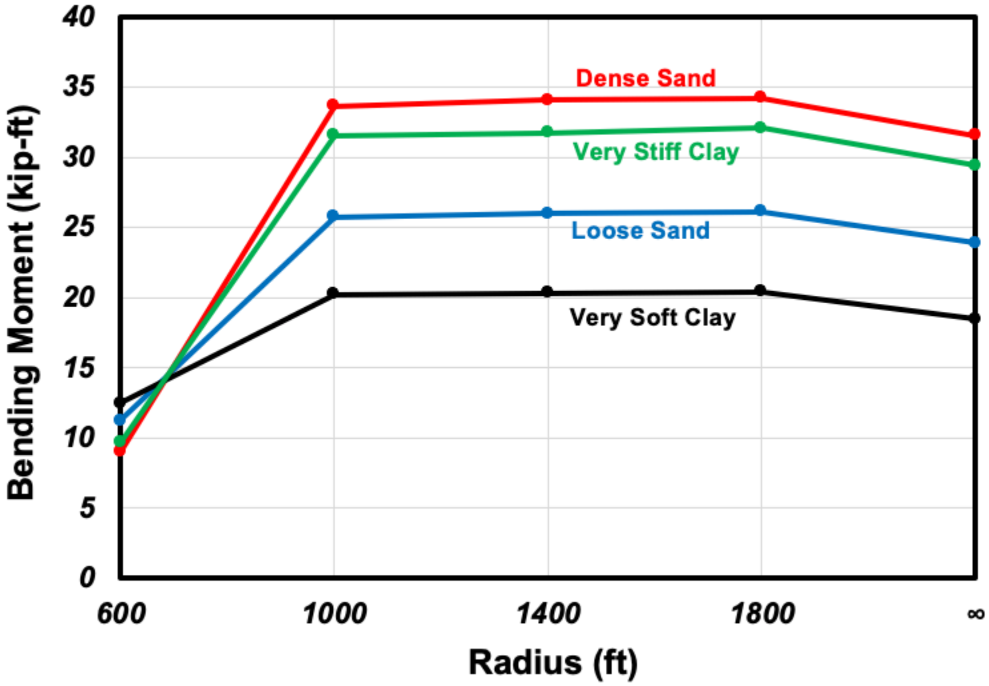

Figure 6.75: Pile Max. Bending Moment at the Pile–Abutment Connection for Different Soil Types (L = 400 ft)

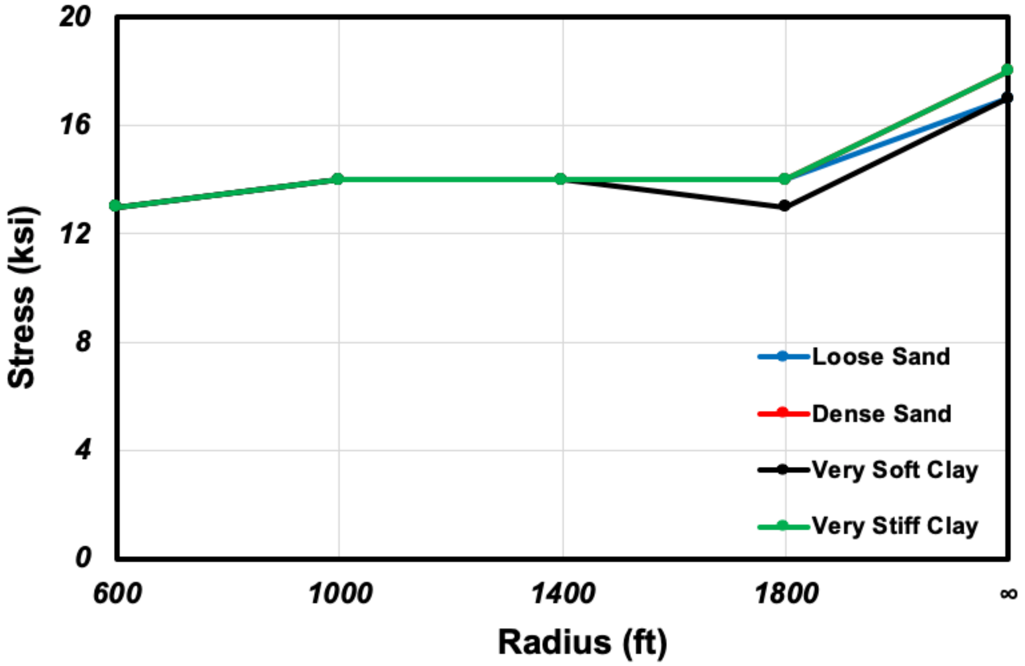

Figure 6.76: Girder Bottom Flange Maximum von Mises Stress at the Girder–Abutment Connection for Different Soil Types (L = 400 ft)

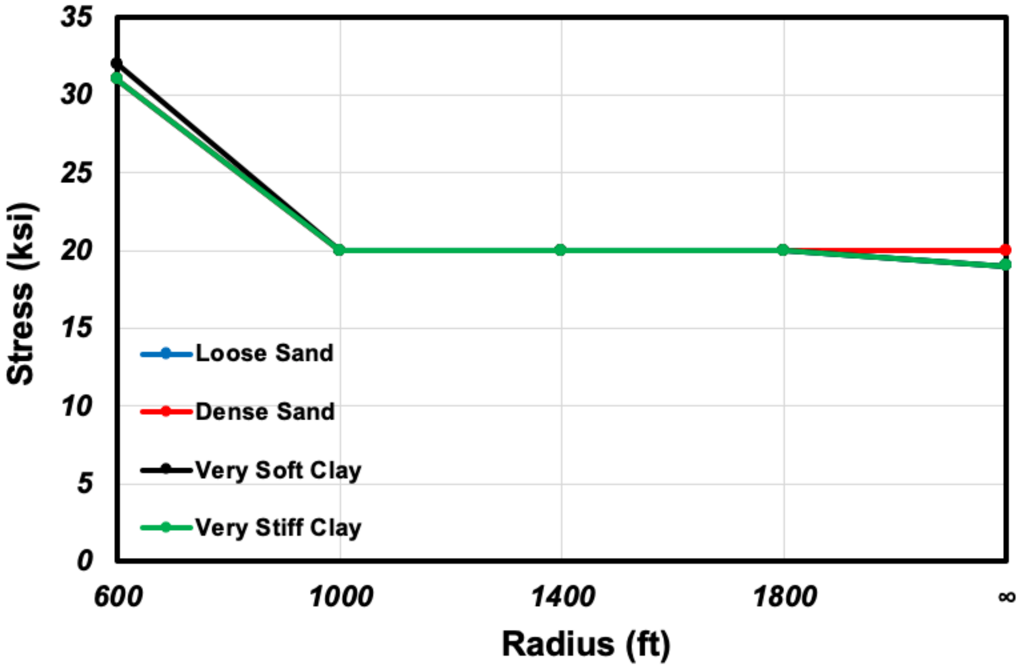

Figure 6.77: Girder Top Flange Maximum von Mises Stress at the Girder–Abutment Connection for Different Soil Types (L = 400 ft)

6.7.4 Bearing

Intermediate bridge bearings play an important role in determining the overall performance of the integral abutment bridge. Aside from the default bearing configuration which consists of both rollers and guided rollers (longitudinal rollers), the research team also considered three additional configurations including all rollers, all guided rollers, and all fixed (pinned). As shown in Figure 6.78, all bridges with different bearing configurations experience the same amount of longitudinal Interior pile head movement. It is evident from Figure 6.79 that mixed, guided roller, and fixed bearing configurations show very similar trends, with mixed configuration showing the largest lateral displacements while fixed and guided roller configurations are very close. In contrast, the configuration with all rollers behave differently specifically for the most curved bridge (R = 600 ft). As the radius increases over 1,000 ft, the general trend follow other boundary conditions. In contrast to other configurations where lateral displacements range from 0.31 to 0.35 in., the bridge with all rollers configuration moves only 0.09 in. laterally with the radius of 600 ft. Movements of the exterior pile head and the interior and exterior deck follow this pattern (Figure 6.80 to Figure 6.85). Figures 6.86 and 6.87 show that for all bearing configurations, the bending moment and stress at the pile head are quite close. Figures 6.88 and 6.89 demonstrate that girder flanges experience comparable stress levels regardless of the type of bearings.

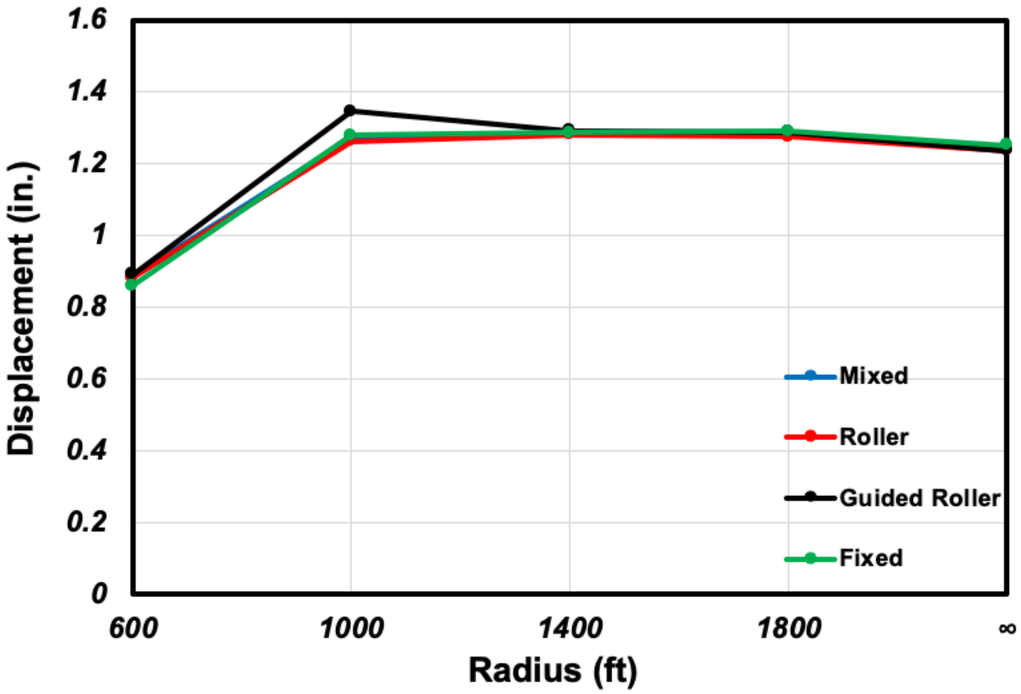

Figure 6.78: Interior Pile Head Longitudinal Displacement for Different Bearing Configurations (L = 400 ft)

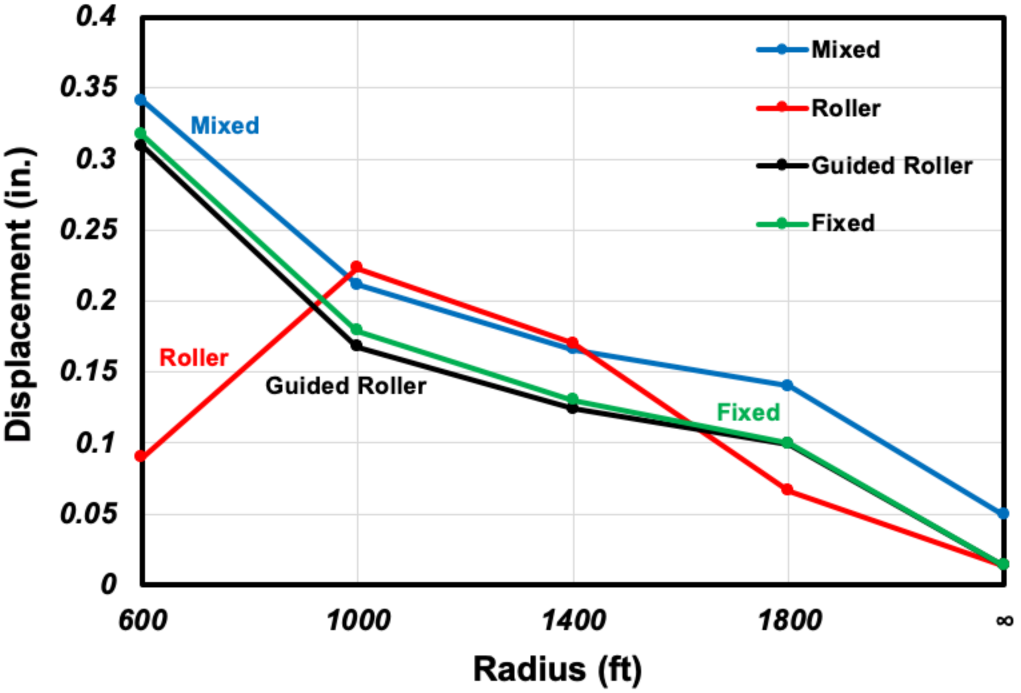

Figure 6.79: Interior Pile Head Lateral Displacement for Different Bearing Configurations (L = 400 ft)

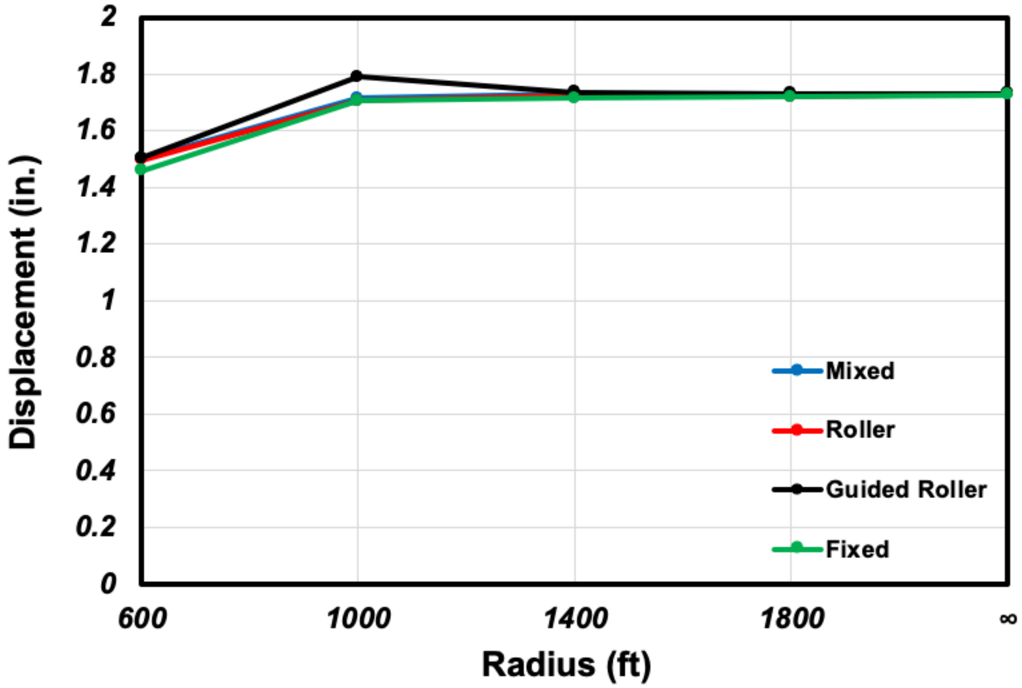

Figure 6.80: Interior Deck Longitudinal Displacement for Different Bearing Configurations (L = 400 ft)

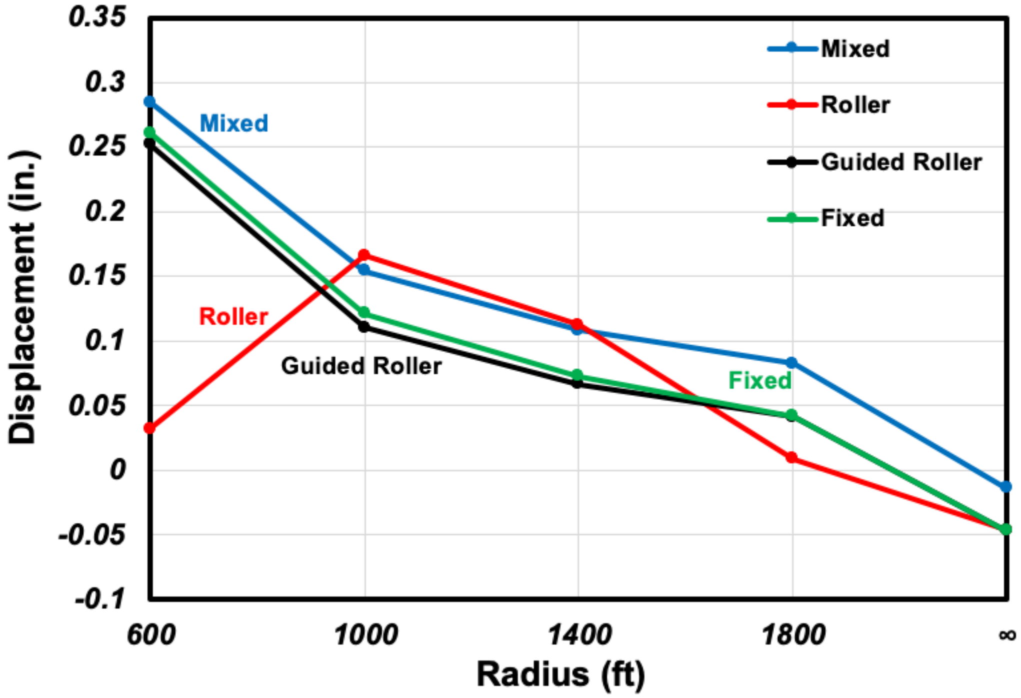

Figure 6.81: Interior Deck Lateral Displacement for Different Bearing Configurations (L = 400 ft)

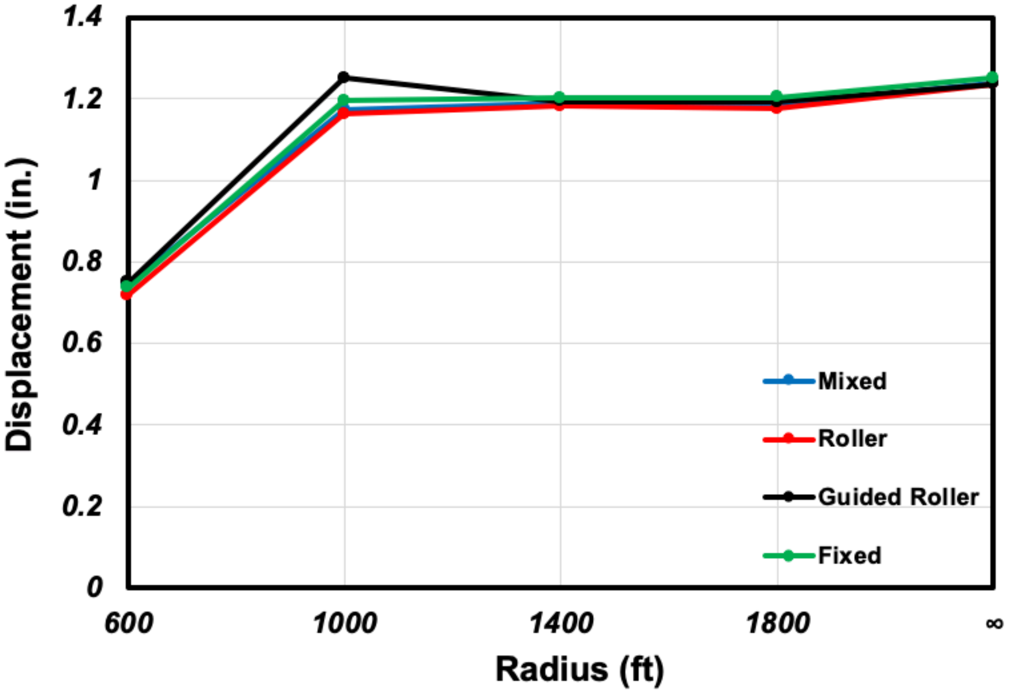

Figure 6.82: Exterior Pile Head Longitudinal Displacement for Different Bearing Configurations (L = 400 ft)

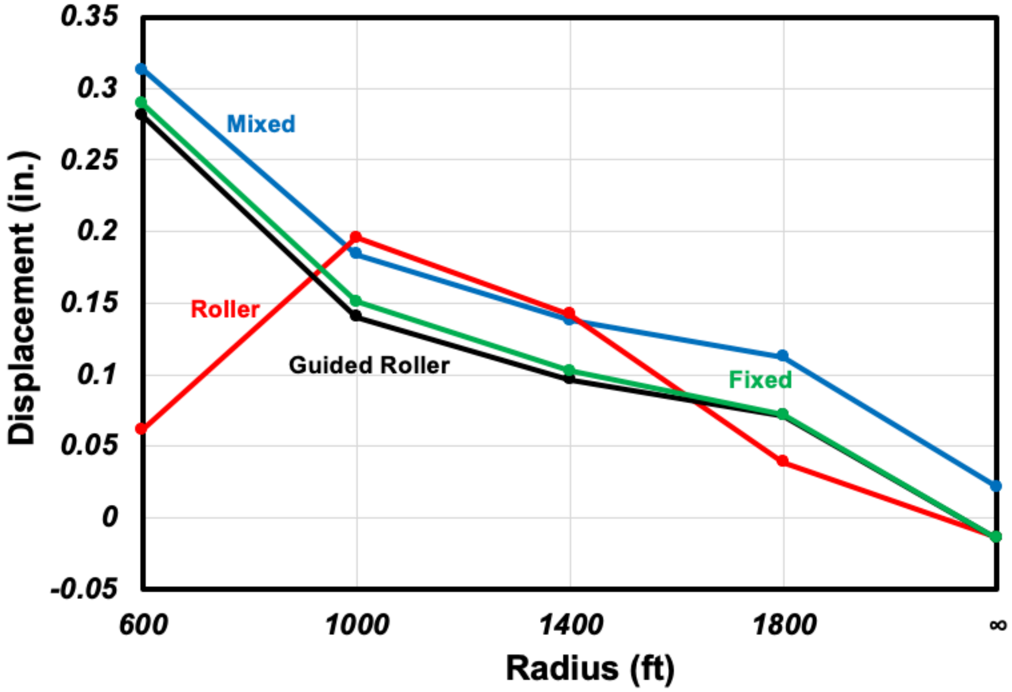

Figure 6.83: Exterior Pile Head Lateral Displacement for Different Bearing Configurations (L = 400 ft)

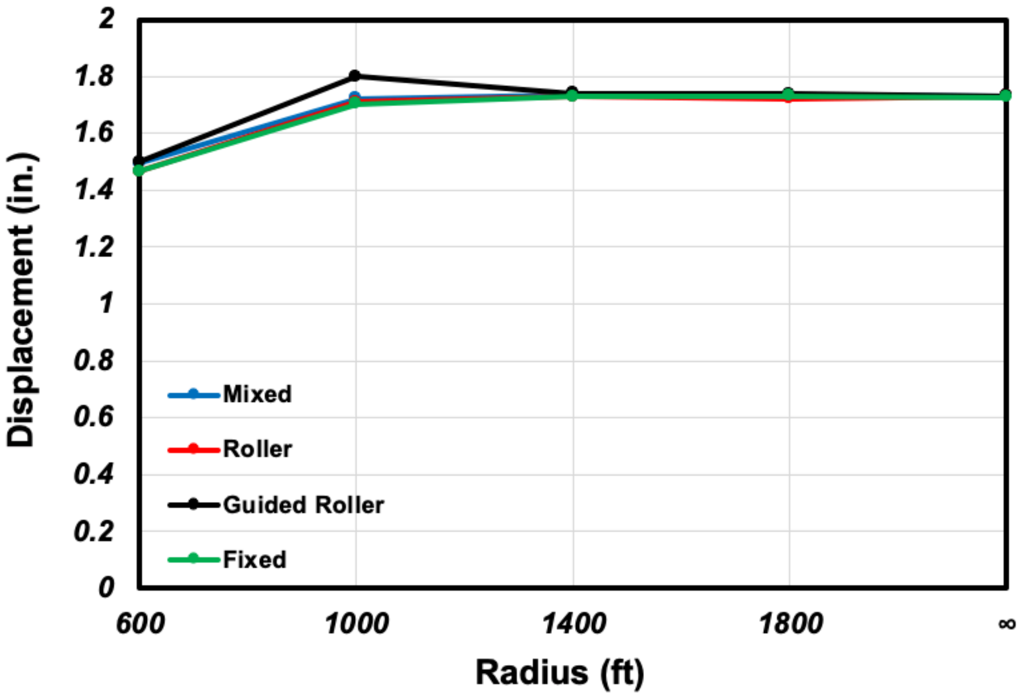

Figure 6.84: Exterior Deck Longitudinal Displacement for Different Bearing Configurations (L = 400 ft)

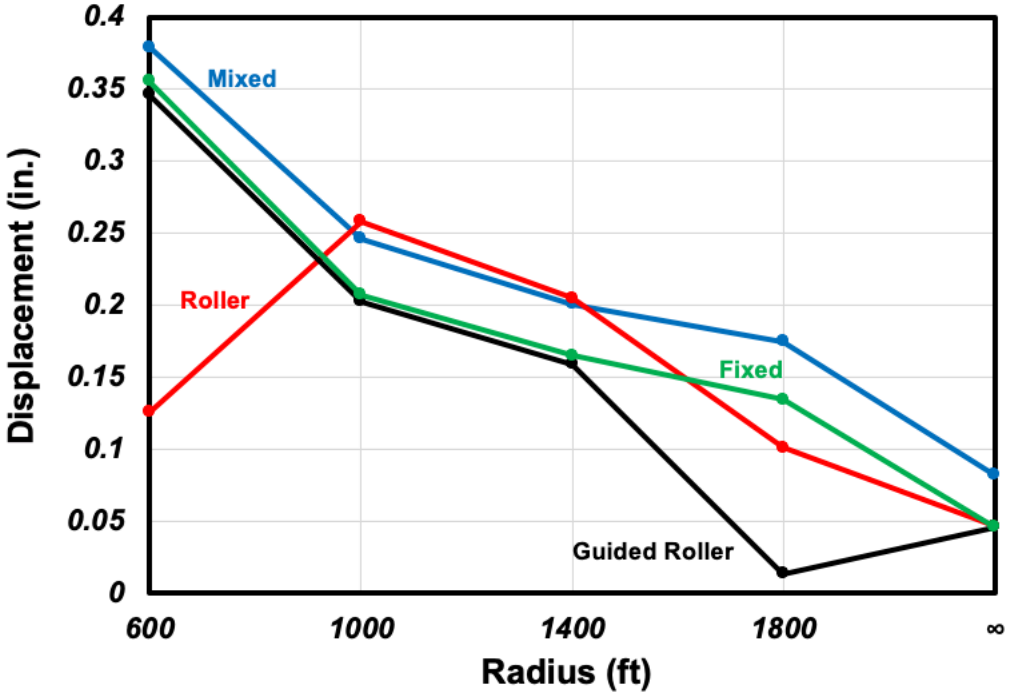

Figure 6.85: Exterior Deck Lateral Displacement for Different Bearing Configurations (L = 400 ft)

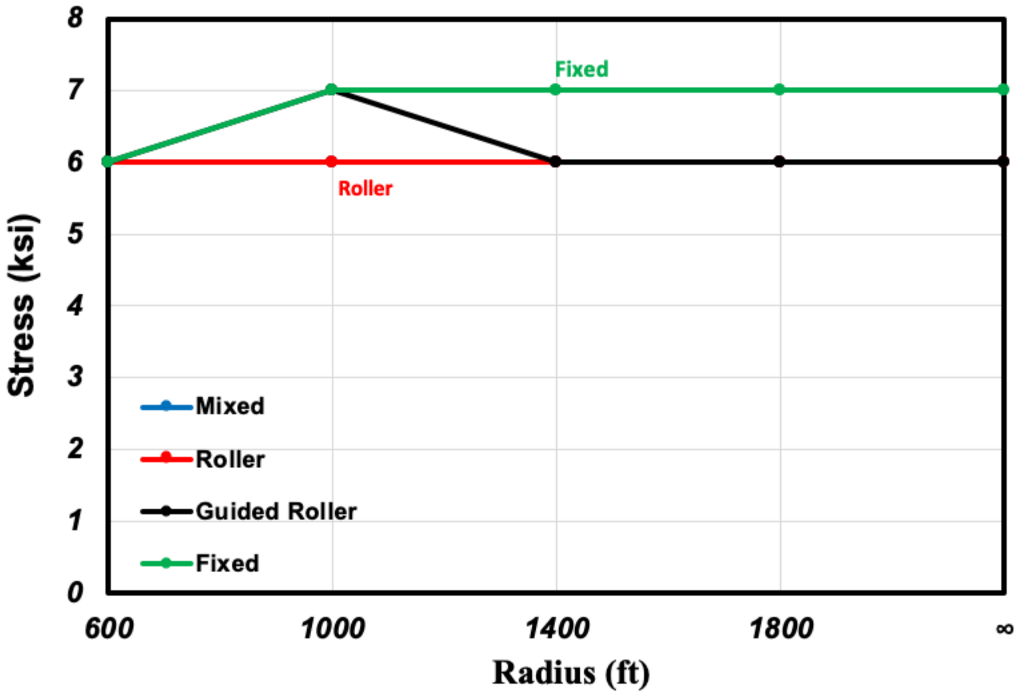

Figure 6.86: Pile Max. von Mises Stress at the Pile–Abutment Connection for Different Bearing Configurations (L = 400 ft)

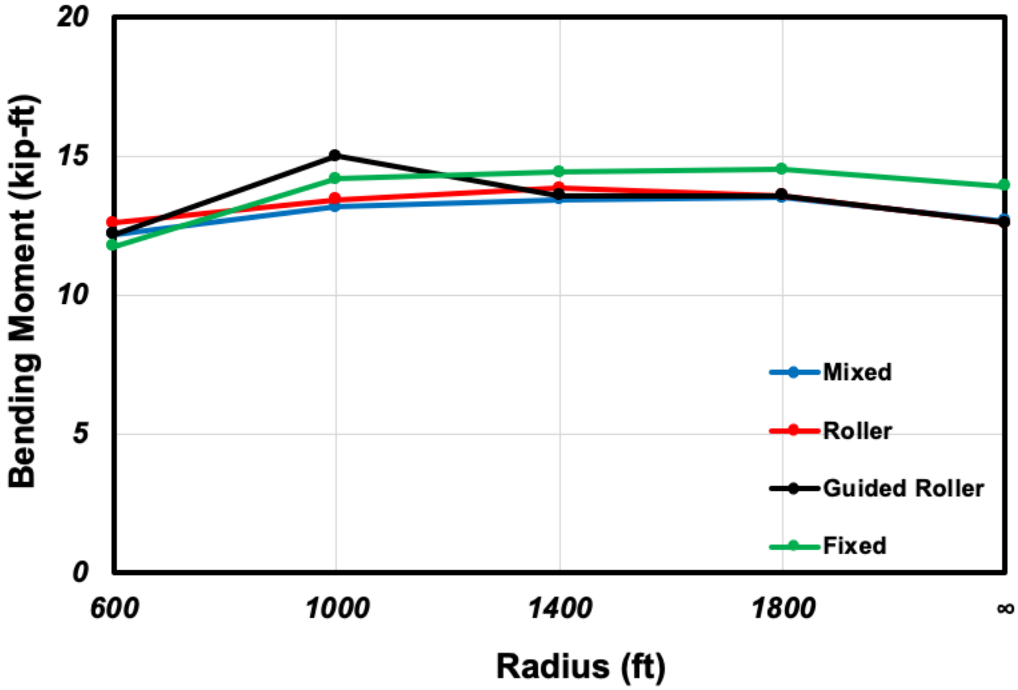

Figure 6.87: Pile Max. Moment at the Pile–Abutment Connection for Different Bearing Configurations (L = 400 ft)

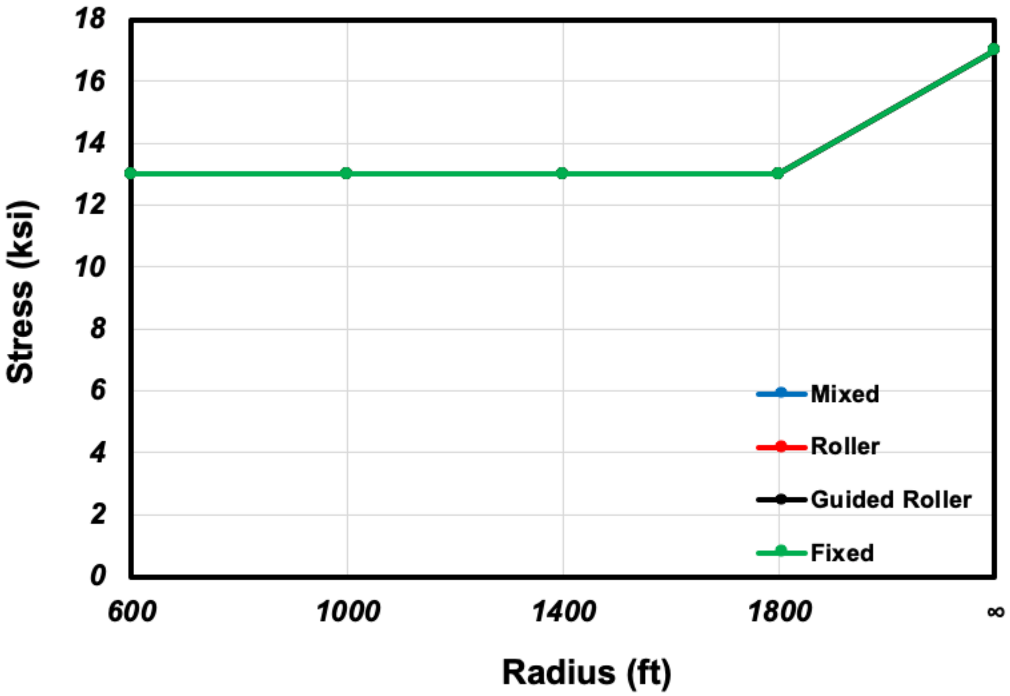

Figure 6.88 Girder Bottom Flange Max. von Mises Stress at the Girder–Abutment Connection for Different Bearing Configurations (L = 400 ft)

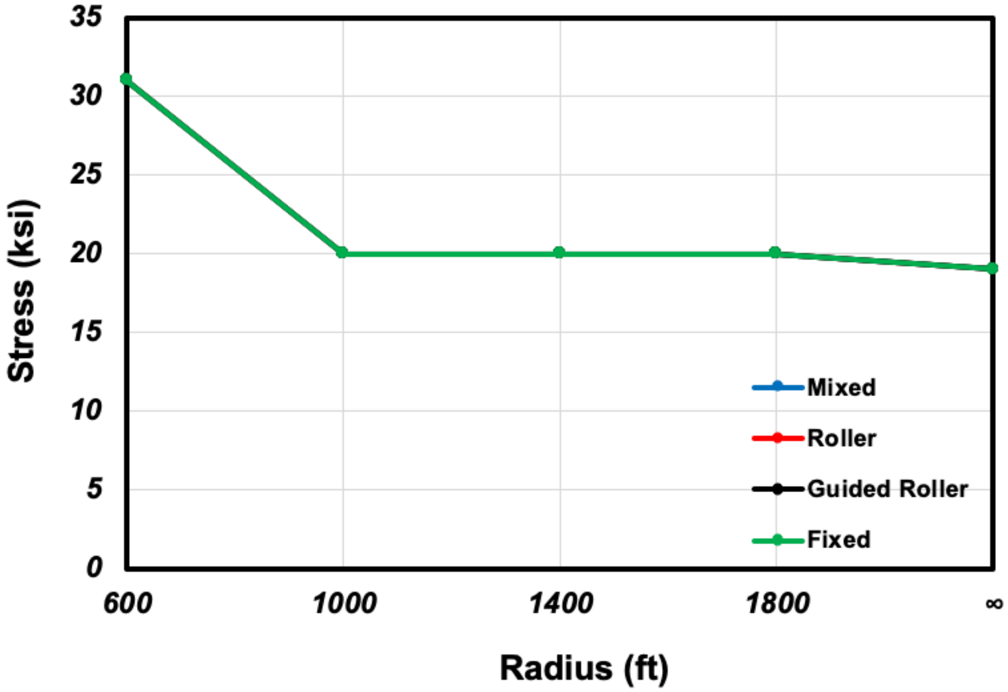

Figure 6.89 Girder Top Flange Max. von Mises Stress at the Girder–Abutment Connection for Different Bearing Configurations (L = 400 ft)

To better understand why the 400–foot long bridge with a 600–ft radius of curvature (degree of curvature = 38.2°) and all Rollers bearing configurations behave differently than other bearing types, we also showed the results for the 200–ft long bridge. Figure 6.90 shows a zigzag pattern in the longitudinal displacement of the Interior pile head with respect to the radius of curvature. Therefore, the longitudinal displacements of pile heads and radii of curvature of a 200–ft long bridge with two equal spans do not correlate linearly. Also shown in this figure is that the Roller bearings behave differently than the other three bearing types. This becomes evident for smaller radii of curvature. For example, in a bridge with a 200 ft radius of curvature, the longitudinal displacements of pile heads for fixed, mixed, and guided roller configurations are approximately equal (0.21 in.), but 0.55 in. for a bridge with roller bearings. Considering the lateral movement of interior pile heads, not only are the values different between all rollers configuration others, but their directions also differ. These differences are shown in Figure 6.91. Movements of the exterior pile head and interior/exterior deck follow the same pattern as for Interior piles. At the pile head where it connects to the abutment, Figures 6.98 and 6.99 show the stresses and bending moment, respectively.

Bridges with all roller bearing configurations experience smaller moments and stresses for radii up to 1,000 ft. These differences are 85%, 28% and 78% for radii of curvature of 200, 600 and 1,000 ft, respectively. There is no significant difference between a bridge with roller bearings and a bridge with other types of bearings for radii larger than 1,000 ft. According to Figures 6.100 and 6.101, the bottom and top flange stresses of the girder at the girder–abutment connection are not affected by different bearing types. This trend is similar to the 400–ft long bridge.

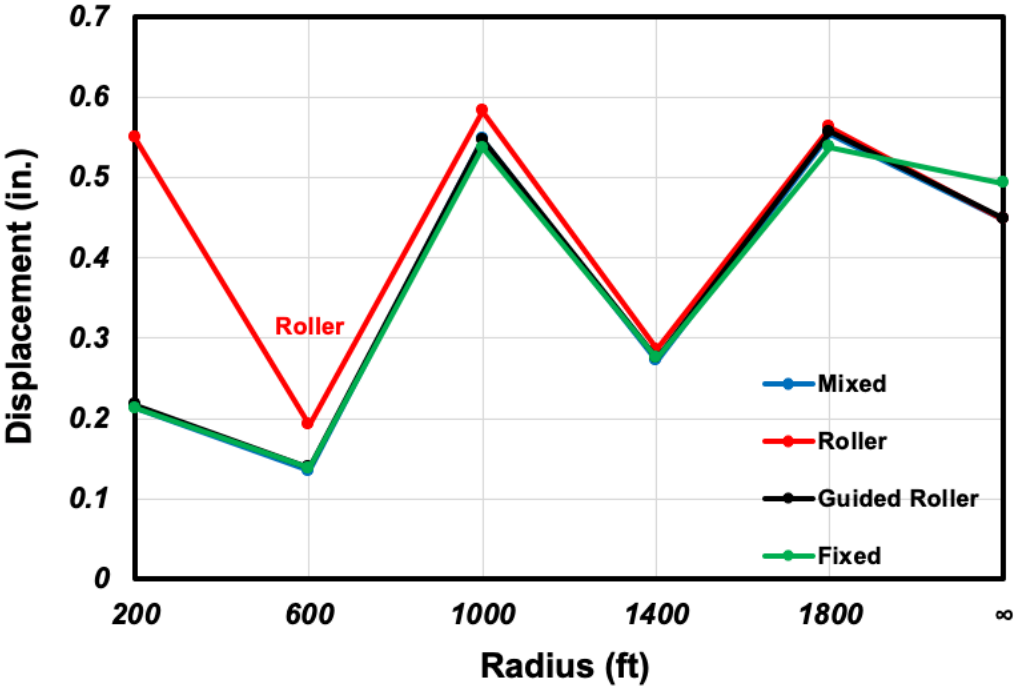

Figure 6.90: Interior Pile Head Longitudinal Displacement for Different Bearing Configurations (L = 200 ft)

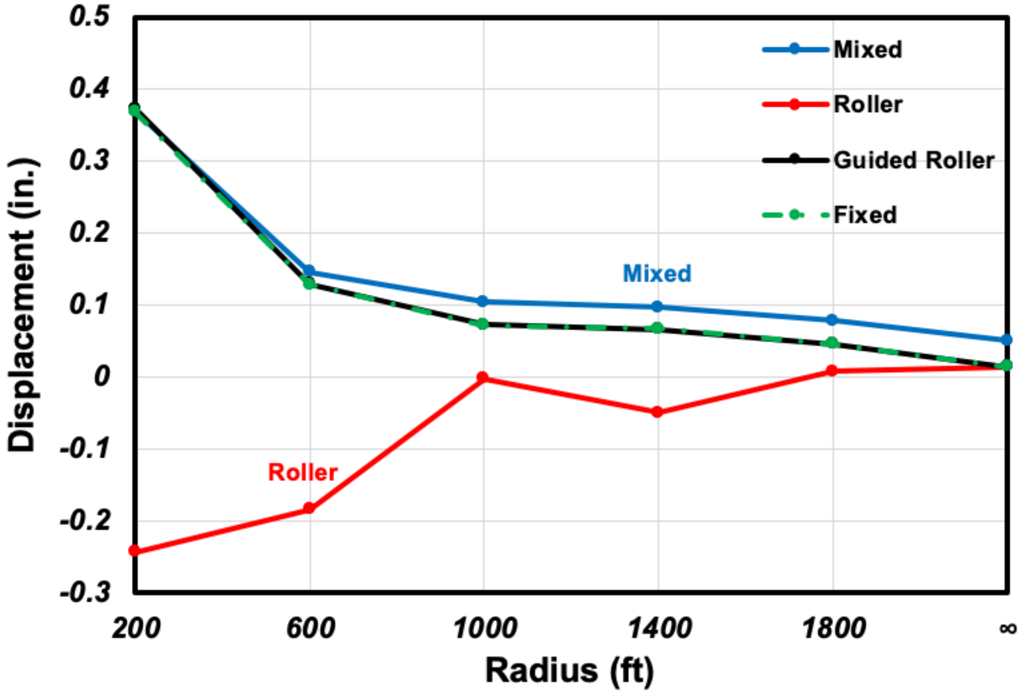

Figure 6.91: Interior Pile Head Lateral Displacement for Different Bearing Configurations (L = 200 ft)

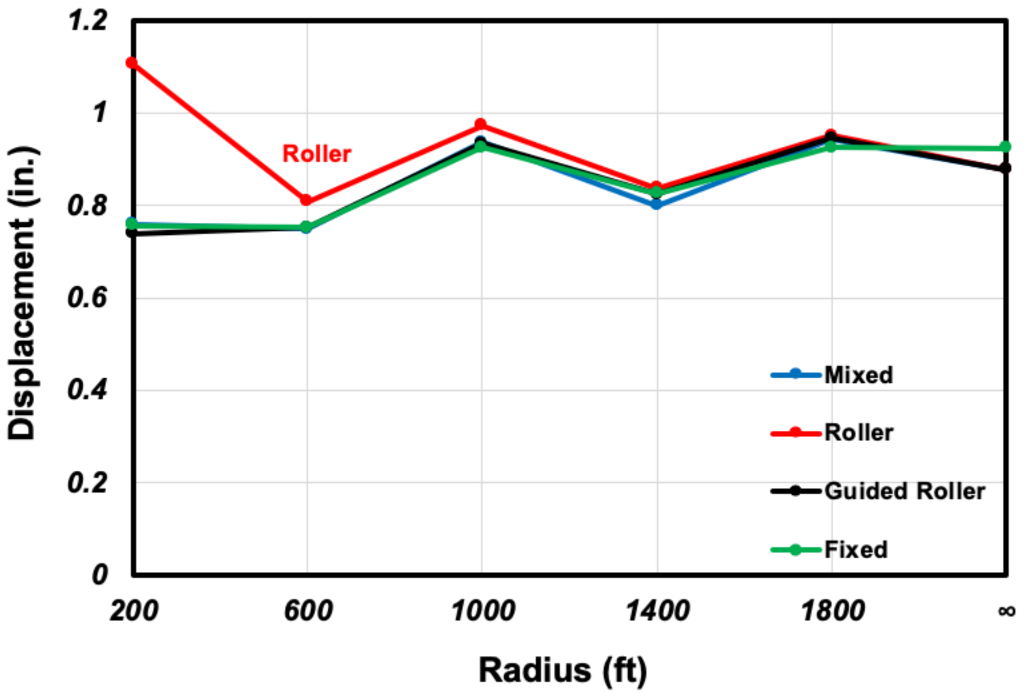

Figure 6.92: Interior Deck Longitudinal Displacement for Different Bearing Configurations (L = 200 ft)

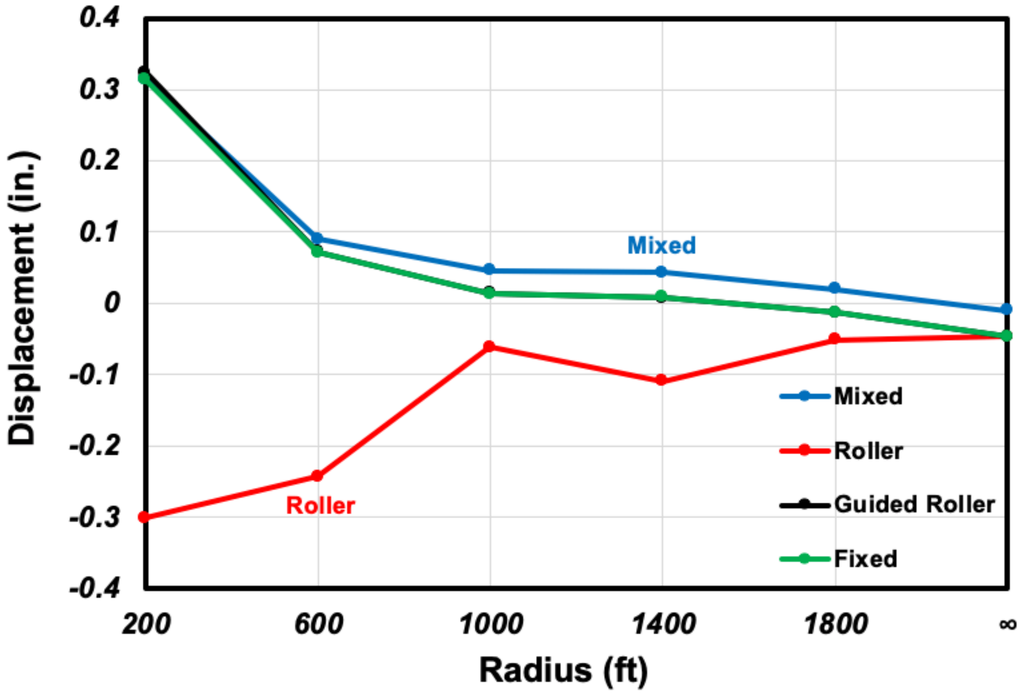

Figure 6.93: Interior Deck Lateral Displacement for Different Bearing Configurations (L = 200 ft)

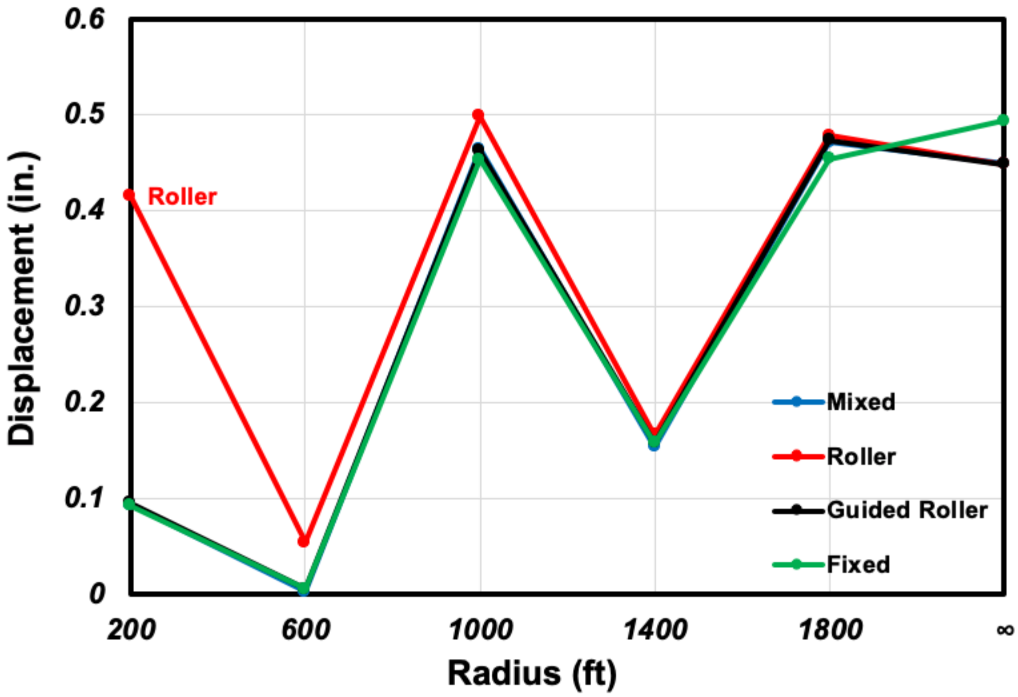

Figure 6.94: Exterior Pile Head Longitudinal Displacement for Different Bearing Configurations (L = 200 ft)

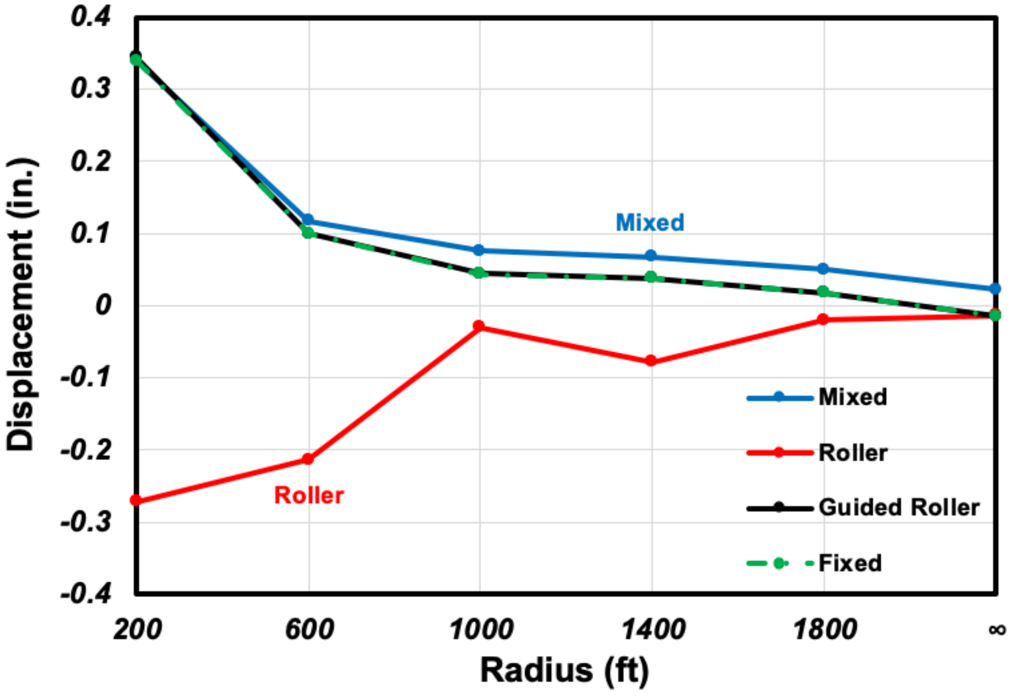

Figure 6.95: Exterior Pile Head Lateral Displacement for Different Bearing Configurations (L = 200 ft)

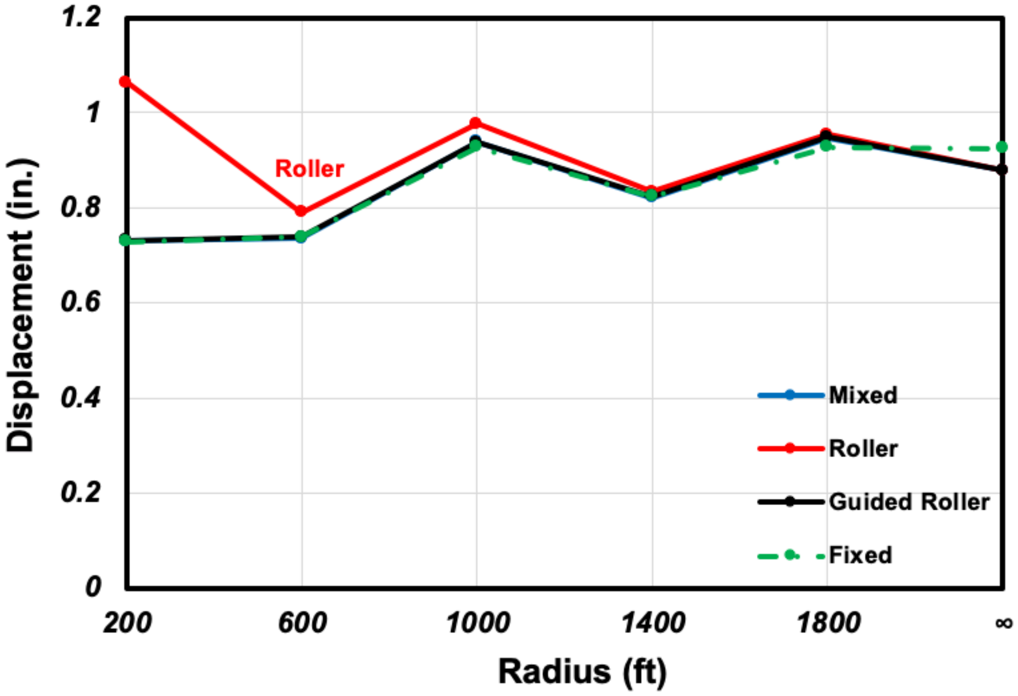

Figure 6.96: Exterior Deck Longitudinal Displacement for Different Bearing Configurations (L = 200 ft)

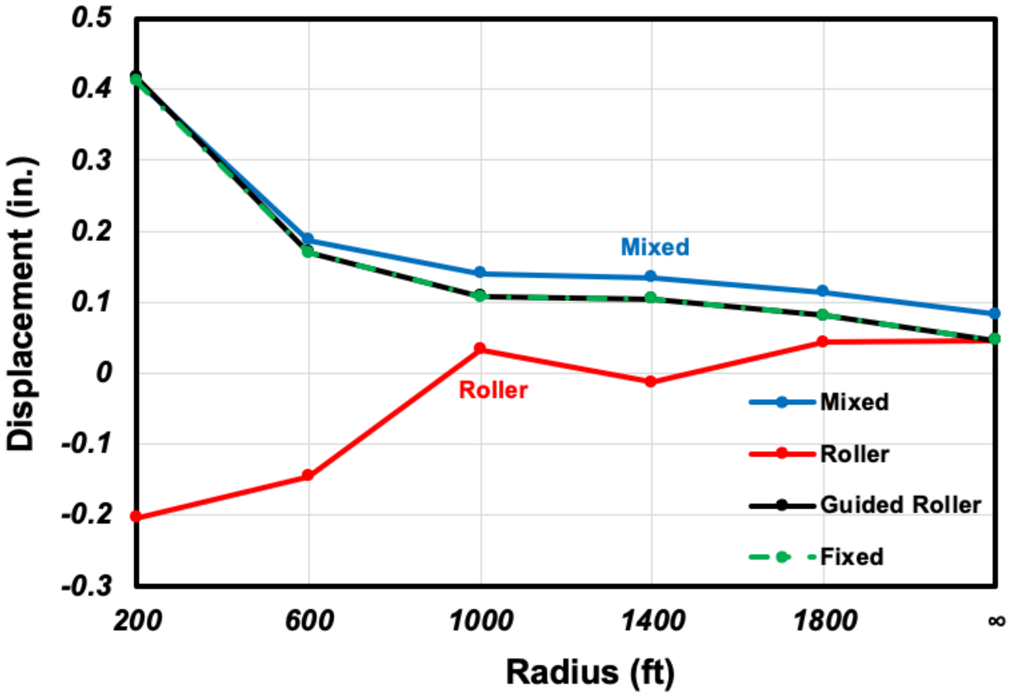

Figure 6.97: Exterior Deck Lateral Displacement for Different Bearing Configurations (L = 200 ft)

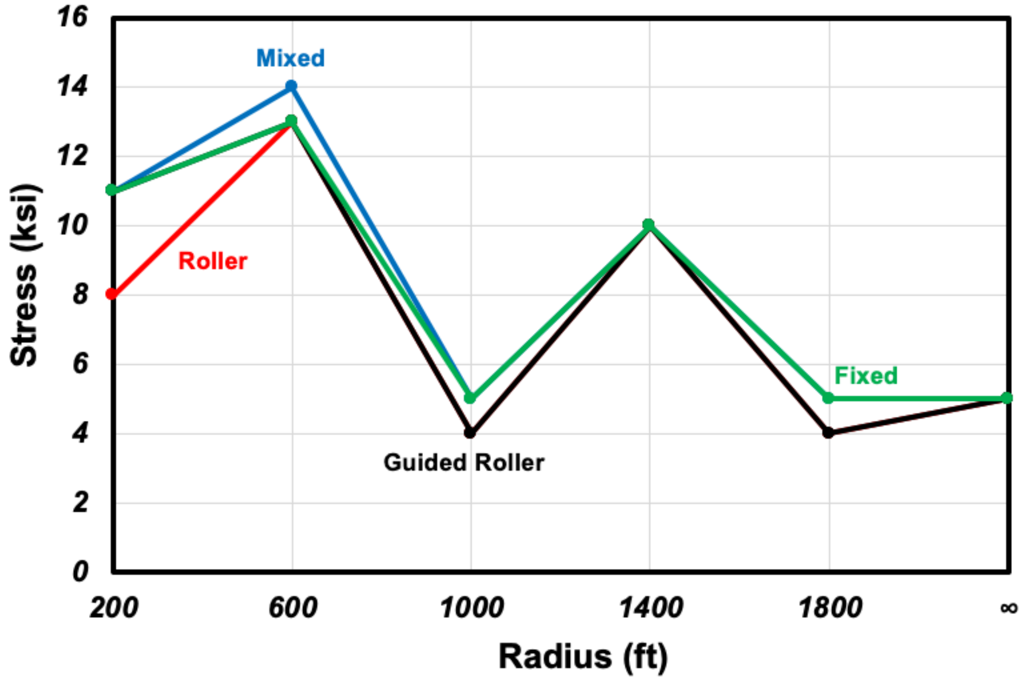

Figure 6.98: Pile Max. von Mises Stress at the Pile–Abutment Connection for Different Bearing Configurations (L = 200 ft)

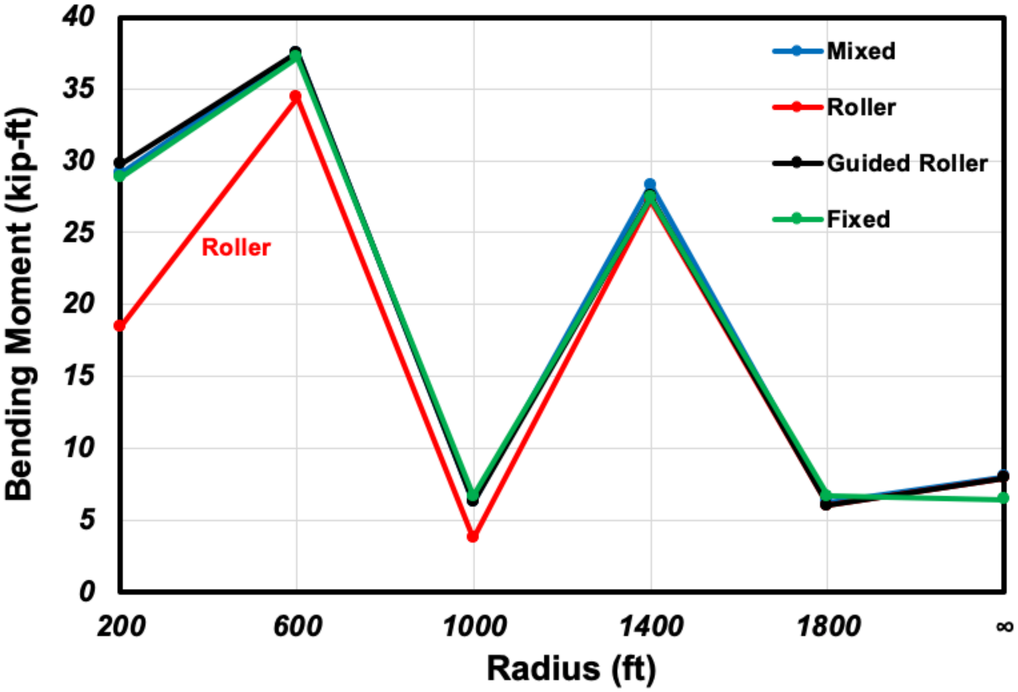

Figure 6.99: Pile Max. Moment at the Pile–Abutment Connection for Different Bearing Configurations (L = 200 ft)

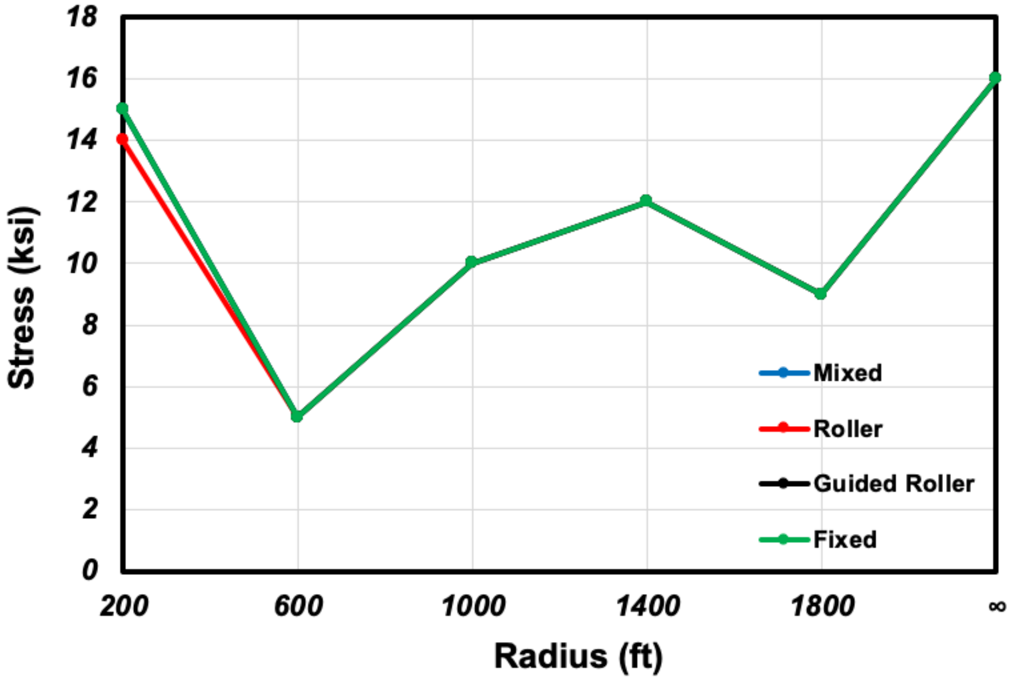

Figure 6.100: Girder Bottom Flange Max. von Mises Stress at the Girder–Abutment Connection for Different Bearing Configurations (L = 200 ft)

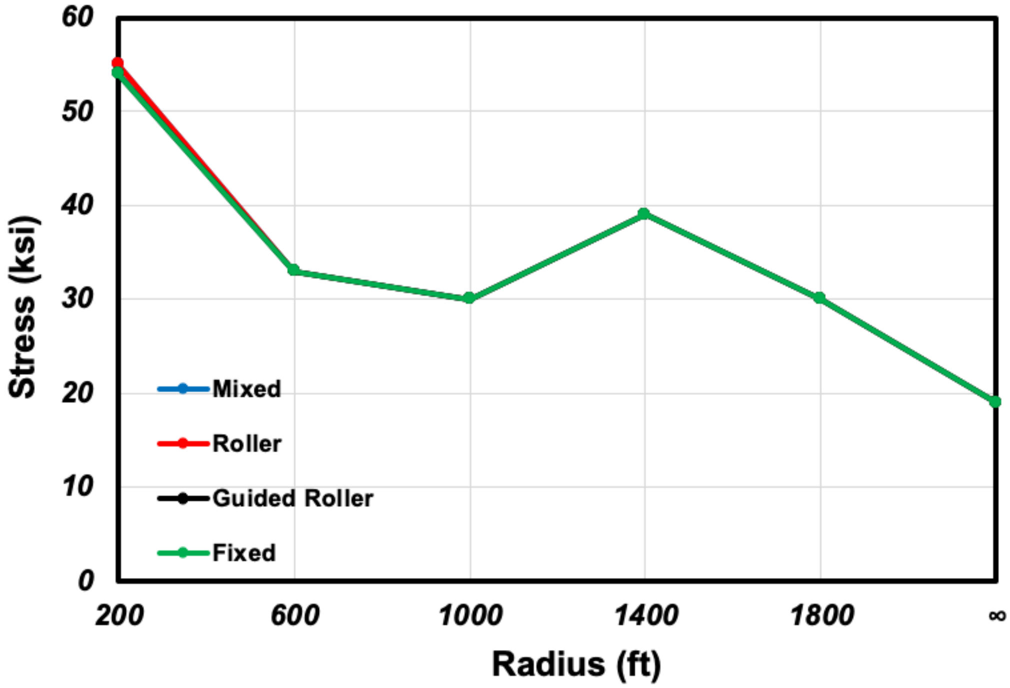

Figure 6.101: Girder Top Flange Max. von Mises Stress at the Girder–Abutment Connection for Different Bearing Configurations (L = 200 ft)

6.7.5 Pile

As reported by Paraschos (2016), steel H piles are used to support abutments in 98% of the integral abutment bridges constructed in US. According to this study, 56% of these states align the web of the pile parallel to the center line of the abutment (this will be referred to as the weak axis of the H pile), 31% install them with the web of the pile perpendicular to the centerline of the abutment (this will be referred to as the strong axis of the H pile), and the rest 13% use a combination of these two orientations. In this parametric study, it was decided to add pipe piles (which are typically used where both longitudinal and lateral displacements are expected) additional to the H piles with different orientation. A H Pile section was considered to better understand the effects of pile type and orientation. HP 12×89 which has the weak axis moment of inertia close to that of the default pipe pile section was selected. Table 6.14 shows the properties of these two sections. This HP section was placed around both strong and weak axes to evaluate the difference.

Table 6.14: Pipe Pile and H pile Section Properties

Pile Sections	**Area ($in.^2$)**	**Moment of Inertia ($in.^4$)**	
		Strong Axis	**Weak Axis**
Pipe 12×0.375	13.7	231.6	231.6
HP 12×89	25.9	693	224

Figures 6.102 through 6.113 show the results of different pile types and orientations. According to Figure 6.102, the longitudinal displacements of the interior pile head are almost identical for all pile types except for H pile in weak axis orientation with a 600 ft radius of curvature. As compared to other cases, this displacement is 15% less the other cases.

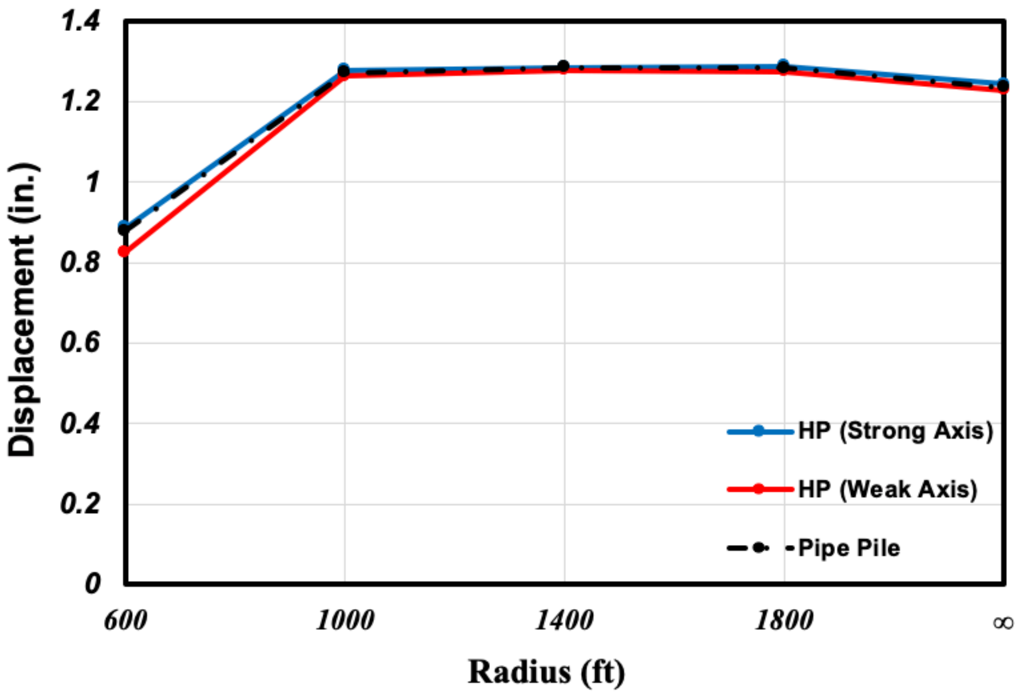

Figure 6.102: Interior Pile Head Longitudinal Displacement for Different Pile Sections (L = 400 ft)

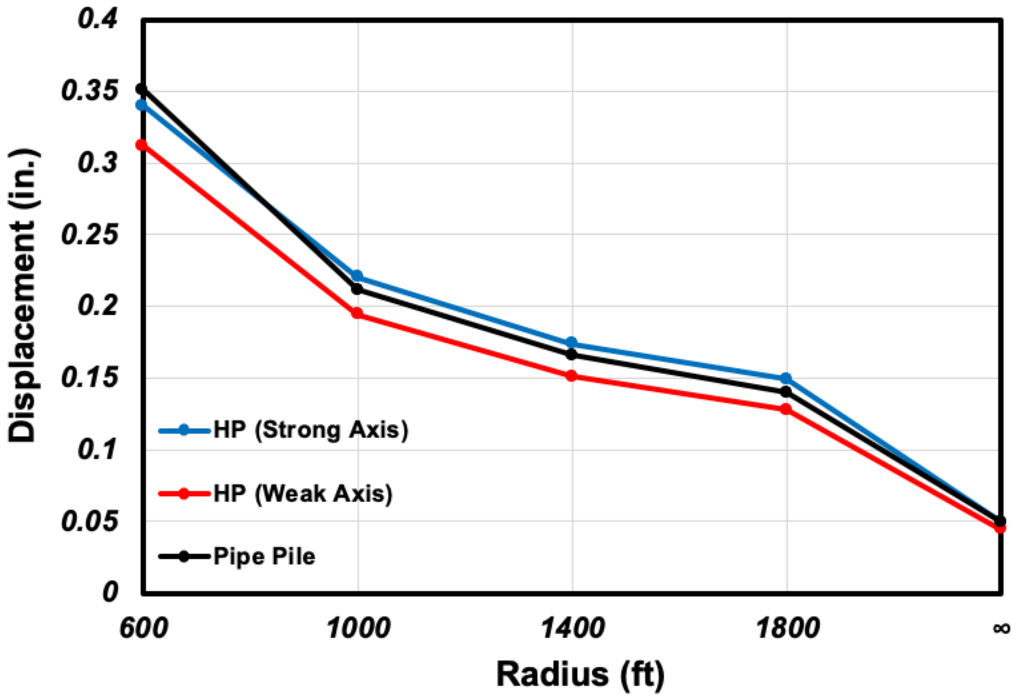

Figure 6.103: Interior Pile Head Lateral Displacement for Different Pile Sections (L = 400 ft)

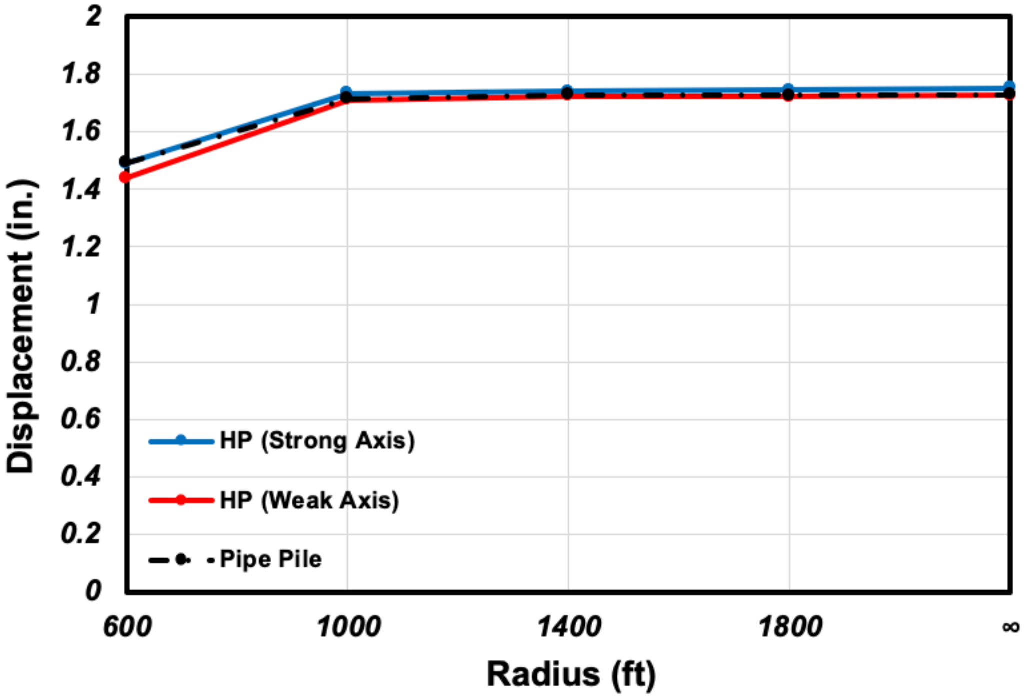

Figure 6.104: Interior Deck Longitudinal Displacement for Different Pile Sections (L = 400 ft)

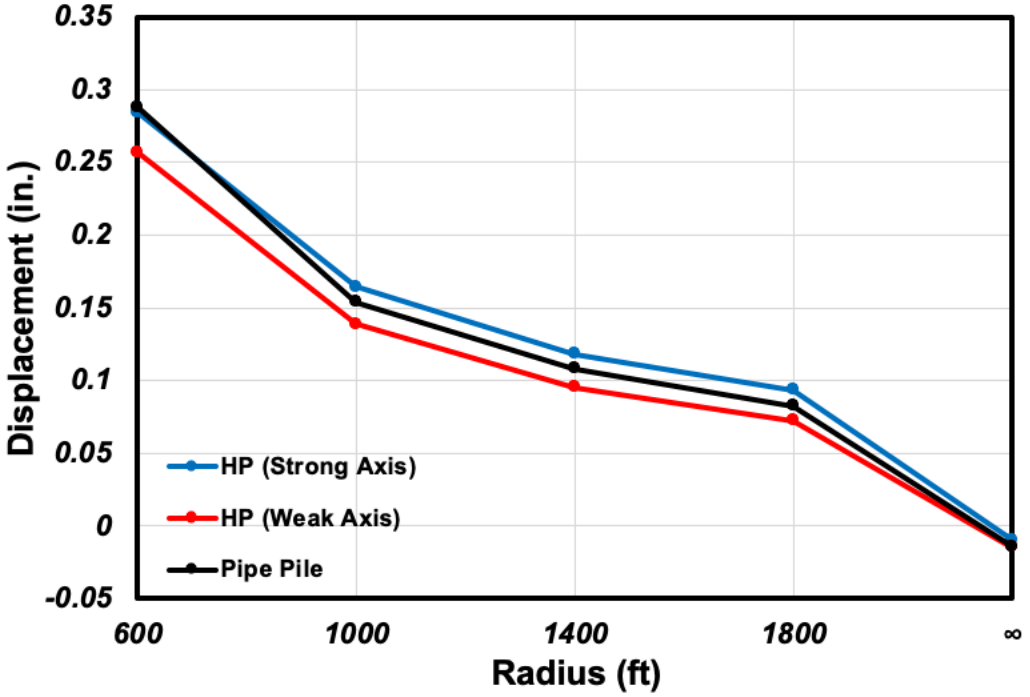

Figure 6.105: Interior Deck Lateral Displacement for Different Pile Sections (L = 400 ft)

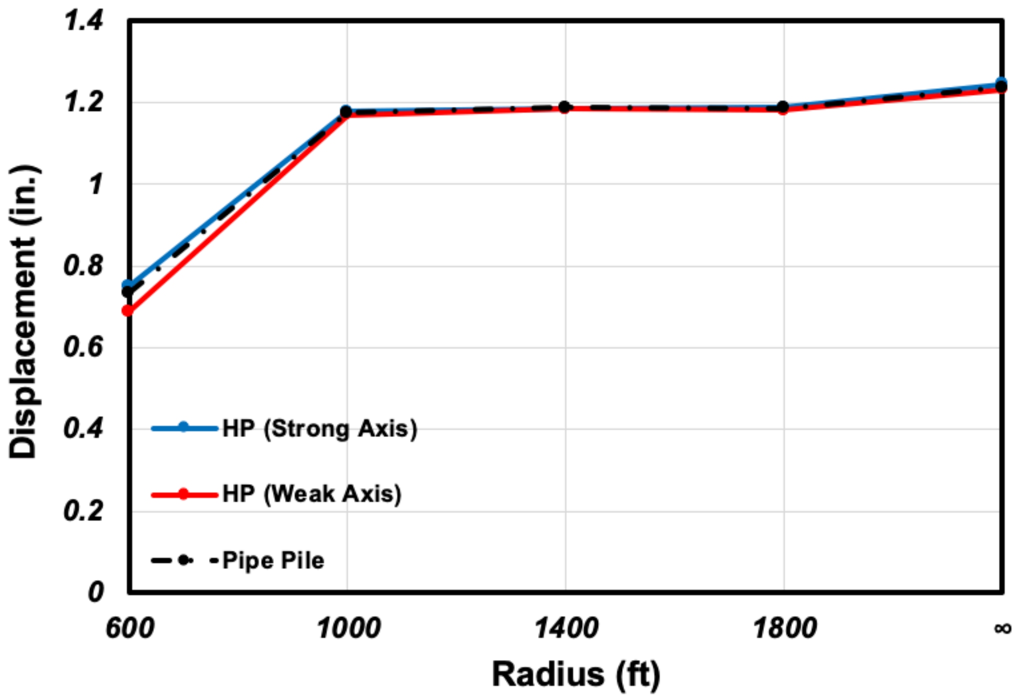

Figure 6.106: Exterior Pile Head Longitudinal Displacement for Different Pile Sections (L = 400 ft)

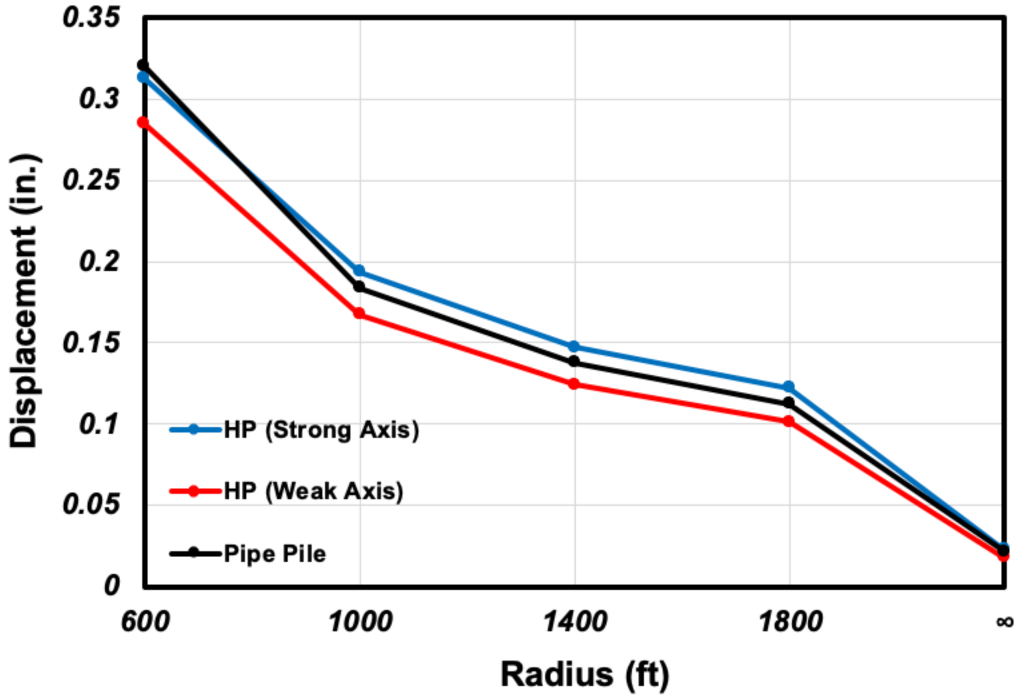

Figure 6.107: Exterior Pile Head Lateral Displacement for Different Pile Sections (L = 400 ft)

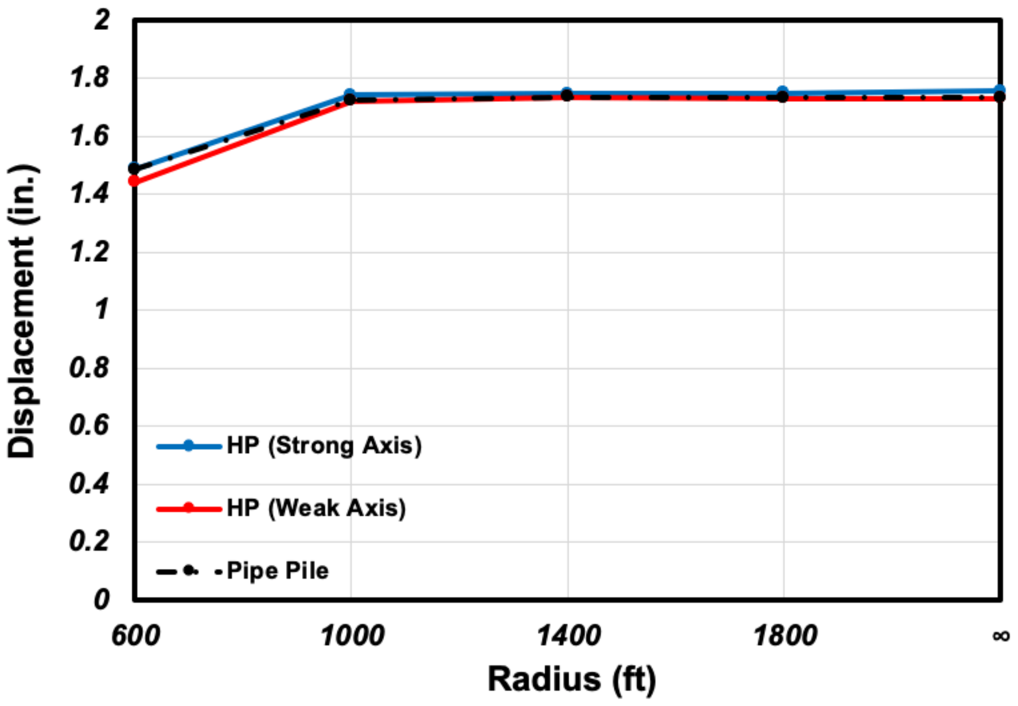

Figure 6.108: Exterior Deck Longitudinal Displacement for Different Pile Sections (L = 400 ft)

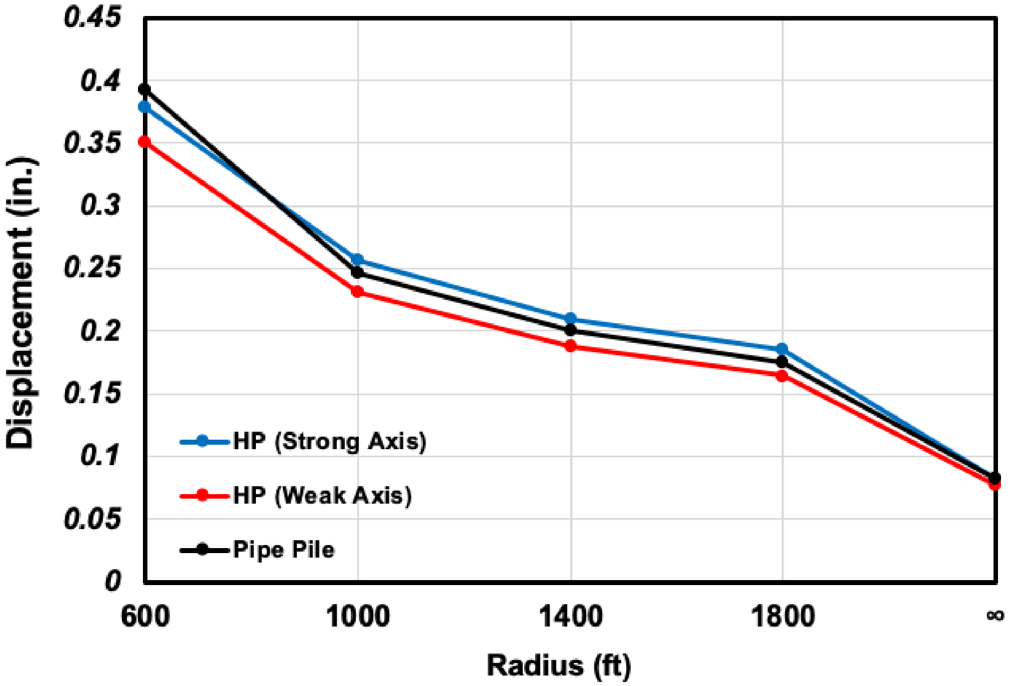

Figure 6.109: Exterior Deck Lateral Displacement for Different Pile Sections (L = 400 ft)

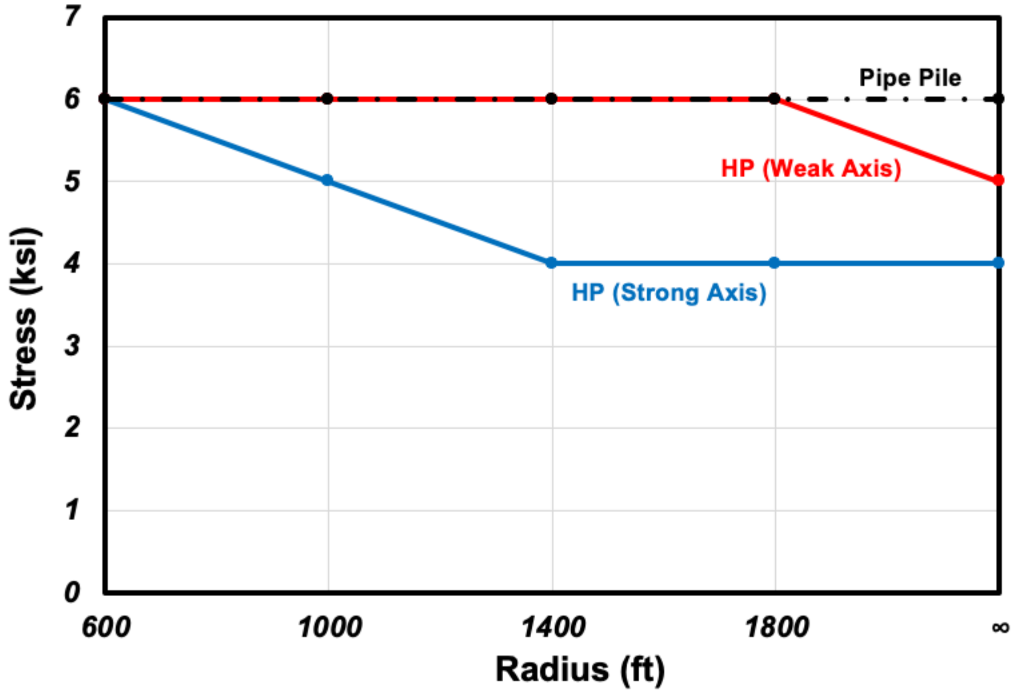

Figure 6.110: Pile Max. von Mises Stress at the Pile–Abutment Connection for Different Pile Sections (L = 400 ft)

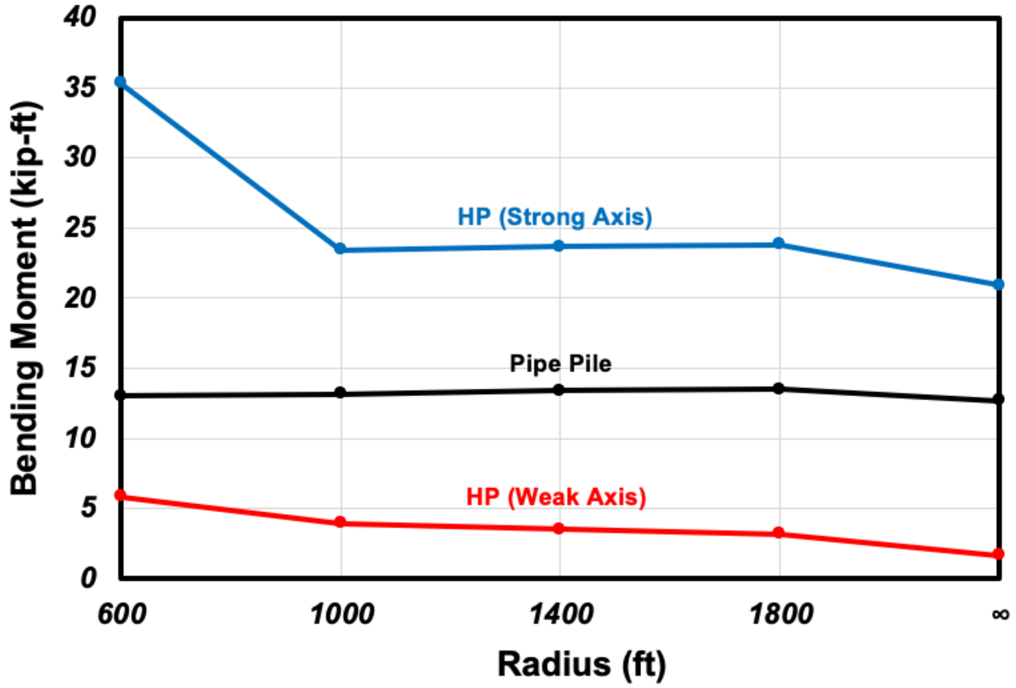

Figure 6.111: Pile Max. Moment at the Pile–Abutment Connection for Different Pile Sections (L = 400 ft)

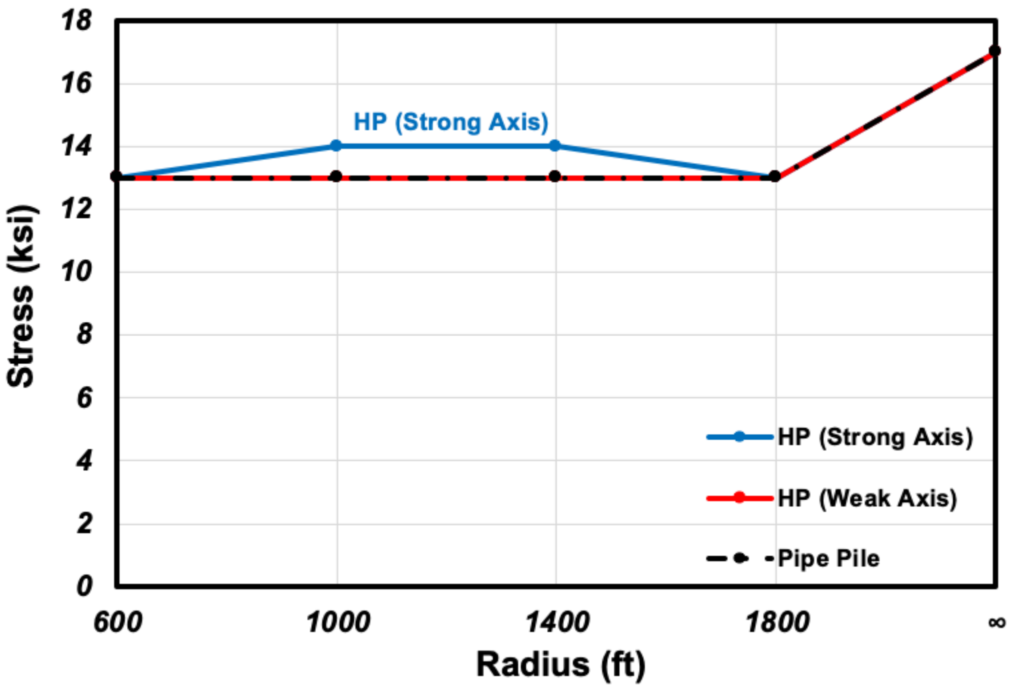

Figure 6.112: Girder Bottom Flange Max. von Mises Stress at the Girder–Abutment Connection for Different Pile Sections (L = 400 ft)

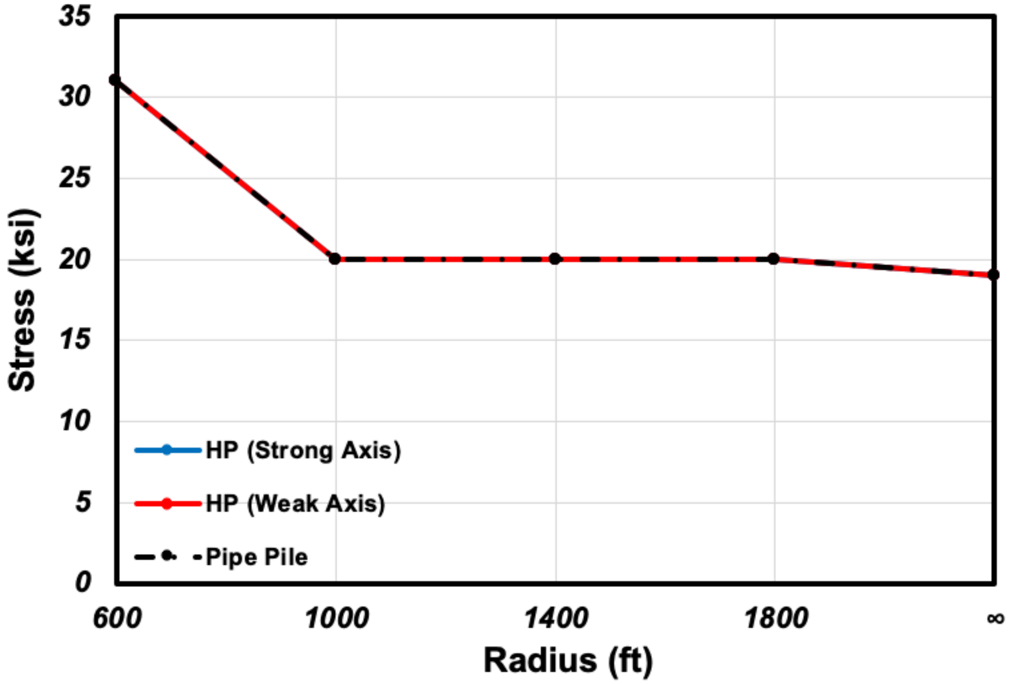

Figure 6.113: Girder Top Flange Max. von Mises Stress at the Girder–Abutment Connection for Different Pile Sections (L = 400 ft)

Figure 6.103 indicates that H pile in weak axis experience the smallest interior pile head lateral displacements while pipe pile and H pile in strong axis show nearly identical lateral movements. These three converge to a closer value as the radius of curvature increases.

Identical patterns can be observed in the movements of exterior piles, interior, and exterior decks (Figures 6.104 to 6.109). According to Figure 6.110, although there is constant von Mises stress at the pipe pile head for all radii of curvature, this stress decreases for H piles as the bridge becomes straight (as curvature decreases). Strong axis H piles experience the lowest pile head stress, except for bridges with 600–ft radius curvatures. Figure 6.111 shows the bending moments of pile heads. According to this figure, there is a difference in behavior between the three pile types. The largest pile head bending moments are experienced by strong axis H piles, followed by pipe piles, and weak axis H piles. In addition, the moments in H piles decreases as the bridge becomes less curved, whereas the moments in pipe piles remain nearly constant. The decrease in moment as the curvature decreases is more noticeable with the strong axis H pile than the weak axis H pile. Figures 6.112 and 6.113 illustrate stresses in girders at their connections to abutments. These figures indicate that all three pile types experience comparable stresses, except for a small difference in girder bottom flange stresses for bridges with 1,000 and 1,400 ft radius of curvature.

6.8 Summary

In this chapter, a parametric study was conducted for a curved full integral abutment bridge model with various parameters including length, radius of curvature, pile type, soil type, intermediate bearing configuration, and shrinkage models. The results show that the bridge total length and its longitudinal displacements behave approximately linear regardless of the bridge curvature. However, a bridge with a smaller radius of curvature exhibits larger lateral displacements. Except for the 200–ft long bridges, the maximum von Mises stress at pile–abutment connection appears to follow a linear relationship with the increase in bridge length. There is a linear increase in the maximum von Mises stress at the girder–abutment connection as the bridge gets longer. And ss the bridges become longer, the maximum stress at the top flange of girders decreases. In shrinkage model graphs, the bridge is shown to have inward (in the direction of contraction) displacements. Although the displacements of ACI 209R and CEB–FIP 90 models differ in the first couple of years after the construction completed, this study demonstrates that both models show close displacements after 5 years of the construction which is consistent with what other studies in literature reported. This is possibly because the IAB movements are govern by the combination of shrinkage of the concrete bridge deck and annual thermal cycles and the concrete shrinkage levels out after 5 years of cycles.

According to the parametric study results, the type of soil surrounding the pile has little to no influence on bridge displacements when a long CMP sleeve (18 ft) is used. Pile stresses, however, differ among various soil types, with dense sand experiencing the highest stresses, followed by very stiff clay, loose sand, and very soft clay (except for shorter bridges, where the order is reversed).

While the longitudinal movements of curved bridges are seemingly independent of the bearing type, the lateral displacements are highly affected by the types of bearings placed in the intermediate piers. Parametric study results also demonstrate that the mixed bearings exhibit the highest lateral displacements, followed by the fixed and guided rollers. For all bearing types, the lateral displacement decreases as the bridge becomes longer, except for roller bearings. Bridges with this bearing type behave differently, specifically for bridges with smaller curvatures. There is no difference in pile von Mises stresses among different bearing types. It appears that pile types and orientations do not affect longitudinal displacements while having little impact to lateral displacements.

Pile head moments and stresses changes by the type and orientation of the piles. Weak axis H piles, pipe piles, and strong axis H piles experience largest bending moments at the pile–abutment connections. However, the stress associated with these bending moments (ranging between 5 to 35 ft-kips) are less than 10 ksi.

7. SUMMARY AND CONCLUSION

7.1 Summary

A curved full integral abutment bridge in Big Springs, Nebraska was selected for field instrumentation. As indicated in the literature review, there are not many studies that investigated the behavior of curved full integral abutment bridges. Many states department of transportation, has constantly supported the efforts through several decades, and most recently included long-term field monitoring efforts into several research projects to continue the studies on the complex behavior of such bridge system. The reason for continuous support is due to the fact that although the behavior may be complex and not fully understood, there are many benefits of eliminating the joints in a bridge and creating the system to be jointless. The curved full integral abutment bridge in Big Springs, Nebraska has been monitored for a full annual cycle between 2021 and 2022. Not all sensors survived or were able to contribute to the monitoring scheme. However, useful data (backfill pressure, pile top displacement, tilt, and moisture contents) are still being recorded and this data can be used for fine tuning the finite element model that was developed in this study.

7.2 Conclusions

The finite element model was analyzed under temperature and shrinkage loads to make comparisons with the field measurements. Our comparisons were based on pressure cells, tilt meters, and inclinometer measurements. The overall magnitudes of the backfill pressure is comparable between the model and the field measurements. However, the trend was in a different pattern for their annual cycles due to the fact that field data indicates a build-up pressure for the annual cycle. The comparisons made for the inclinometer deflections were used to compare the displacement profile of the pile. Although, the inclinometer casing was not directly attached to the pile, it was in close proximity to be justified for pile measurement comparisons. The displacement at the bottom of the abutment, which is the top of the pile had comparable amounts of movements in both the numerical simulation and the field measurements. The tilts that were measured on the abutments had 20 to 25% difference between the model and the field measurements. However, the annual trend due to temperature change were very similar in pattern. A parametric study was conducted for a curved full integral abutment bridge model with various parameters including length, radius of curvature, pile type, soil type, bearing, and shrinkage models. Based on the parametric study, following conclusions are provided.

7.2.1 Length and Curvature

- The results show that bridge total length and its longitudinal displacements behave approximately linear regardless of the bridge curvature.
- However, bridges with higher degrees of curvature (with a smaller radius of curvature) exhibits larger lateral displacements. For every increase in radius of curvature, the bridge lateral displacement increases. And, this increase is more noticeable for shorter bridges.
- Except for the 200–ft long bridges, the maximum stress at pile–abutment connection appears to follow a linear relationship with the bridge length. There is a linear increase in the maximum stress at the girder–abutment connection as the bridge gets

longer. As the bridges become longer, the maximum stress at the top flange of girders decreases.

- Girder bottom flange stress at the girder–abutment connection point linearly increases with bridge length, regardless of bridge curvature, except for the 200–ft long bridge. For all bridge lengths, straight bridges experience the largest bottom flange stresses compared to curved bridges.
- Shorter bridges experience higher stresses in their girder top flanges at the point of connection between the girder and abutment. Increasing bridge length decreases these stresses, and for bridges exceeding 600 ft, there is no difference in stress among different curvature radii.

7.2.2 Shrinkage Model

- Regarding the shrinkage models, the bridge is shown to have inward (in the direction of contraction) displacements. Although the displacements of ACI 209R and CEB–FIP 90 models differ in the first couple of years after construction is completed.
- There is a noticeable difference between the two models in the first couple of years as a result of higher initial rate of shrinkage for the ACI 209R model. However, over time, bridge models behave more similarly. Both models show comparable displacements for less curved bridges (radius of curvature > 600 ft) after 5 years of the construction which is consistent with what other studies in literature reported. This is possibly because the IAB movements are govern by the combination of

shrinkage of the concrete bridge deck and annual thermal cycles and the concrete shrinkage levels out after 5 years of cycles.

- However, for the 400–ft long bridge with 600–ft radius of curvature, longitudinal movements of the bridge differ between the two shrinkage models, even after 5 years. Yet, both shrinkage models produce nearly identical lateral movements after 5 years.

7.2.3 Soil Type

- According to the parametric study results, the type of soil surrounding the pile has little to no influence on bridge displacements when a long CMP sleeve (18 ft) is used. Pile stresses, however, differ among various soil types, with Dense Sand experiencing the highest stresses, followed by Very Stiff Clay, Loose Sand, and Very Soft Clay (except for shorter bridges, where the order is reversed).

- Bridges with different soil types surrounding their piles exhibit the comparable amount of longitudinal and lateral displacements, regardless of the soil type. Long CMP sleeves surrounding the top 18 ft of each pile may explain why bridge displacements seem independent of soil type.

- Unlike bridge displacements, pile head moments and stresses are not independent of soil type. When the radius of curvature changes from 600 to 1000 ft, pile head stress/moment increases greatly, but it remains nearly constant thereafter. For a 400–ft long bridge with a radius of curvature of 600 ft, Very Soft Clay, Loose Sand, Very Stiff Clay and Dense Sand soil conditions cause the highest pile head bending moments, in order. In contrast, curved bridges with larger radii of curvature (radius of curvature ≥ 1000 ft) behave differently. First of all, the order of maximum pile head moments is reversed, meaning that the highest moments are observed in bridges with Dense Sand, Very Stiff Clay, Loose Sand and Very Soft Clay soil conditions. In addition, bending moment and stress remain nearly constant for bridges with radii of curvature larger than 600 ft.

- Top and bottom flanges stresses on girders do not appear to be greatly affected by the different soil type at the girder–abutment connection point.

7.2.4 Bearing Type

- Despite the fact that longitudinal movements of curved bridges are seemingly independent of the bearing type.
- Lateral displacements are highly affected by types of bearings placed in the intermediate piers. Parametric study results demonstrate that the mixed (combination of fixed and rollers) configuration exhibit the highest lateral displacements, followed by the fixed and guided rollers. For all bearing types, the lateral displacement decreases as the bridge becomes longer, except for roller bearings. Bridges with this bearing type behave differently, specifically for bridges with smaller radius of curvatures.
- For all bearing configurations, the bending moment and stress at the pile head are comparable. Stress on girder flanges show no differences regardless of the type of bearing.

7.2.5 Pile Type and Orientation

- It appears that pile types and orientations do not affect longitudinal displacements while having little to no impact on lateral displacements.
- Largest head bending moments are experienced by strong axis H piles, followed by pipe and weak axis H piles. In addition, the moments in H piles decreases as the bridge becomes less curved, whereas the moments in pipe piles remain nearly constant. The rate of decrease in moments for strong axis H piles is noticeable than the case for the weak axis H pile. However, the stress associated with these bending moments (ranging between 5 to 35 ft-kips) are less than 10 ksi.
- All three pile types experience similar level of stresses in their top and bottom flanges at the girder–abutment connection point.

7.2 Recommendations

Based on the Figures in Chapter 6, the following formulas were developed using a simple linear regression. It is recommended to use these formulas with caution since they cannot be generalized for all cases. The formulas are valid only if the bridge meets the following assumptions:

- It is a jointless integral abutment bridge.
- Each abutment is supported on a single row of 12–in pipe piles.
- The width of the bridge is 36 ft with four steel girders.
- Top 18 ft of each pile is enclosed in CMP sleeves.
- The ambient temperature oscillates between -10 °F and +120 °F.

- Bearing configuration is a mixture of rollers and longitudinal rollers.
- Bridge length spans between 200 ft to 1200 ft.

7.2.1 Deck Longitudinal Displacement

The following single formula can be used for deck longitudinal displacements above both the interior and exterior girders since the longitudinal displacements of these corners are only slightly different. All units are in feet but unit conversion is recommended to obtain displacements in inches.

$$Y = 2891X - 6 \tag{7-1}$$

where, X is the deck longitudinal displacement (ft), and Y is the bridge length (ft).

7.2.2 Pile Head Longitudinal Displacement

Similar to the longitudinal displacements of the deck, inner and outer pile heads move very similarly. As a result, a single formula is presented for both displacements. All units are in feet but unit conversion is recommended to obtain displacements in inches.

$$Y = 2974X + 104 \tag{7-2}$$

where, X is the pile head longitudinal displacement (ft), and Y is the bridge length (ft).

7.2.3 Pile Head Stress and Moment

Maximum pile head stress for bridges longer than or equal to 400 ft can be calculated using the following formula.

$$Y = 35X + 177 \tag{7-3}$$

where, X is the von Mises stress (ksi), and Y is the bridge length (ft).

Similarly, maximum pile head moment for bridges longer than or equal to 400 ft can be obtained using following the formula.

$$Y = 11X + 248 \tag{7-4}$$

where, X is the bending moment (kip-ft), and Y is the bridge length (ft).

7.3 Further Research

It would be beneficial to continue the long-term monitoring of the embedded sensors that are already installed at the site. Although, some sensors are not available (fiber optic cables mainly), there are still useful data which can be extracted from the pressure cells, tiltmeters, and inclinometers. However, the inclinometer measurements will require manual site visits. In order to directly extract information of the superstructure displacements, rather than indirect calculations based on inclinometer measurements and tiltmeter measurements, it would be useful to newly add conventional strain gauges or long-range displacement gauges to the instrumentation plan and remotely collect continuous data. This information was not able to be retrieved from the fiber optic sensing in this research. In addition, since the CMP sleeves isolate the influence of superstructure movements efficiently, comparisons between semi-integral abutment bridges and full-integral abutment bridges in Nebraska would be of interest based on additional monitoring efforts of semi-integral jointless bridges.

REFERENCES

AASHTO (2003), *Guide Specifications for Horizontally Curved Steel Girder Highway Bridges 2003 with Design Examples for I-Girder and Box-Girder Bridges*, American Association of State Highway and Transportation Officials, Washington, DC, 392 pp.

AASHTO (2017), *LRFD Bridge Design Specifications*, American Association of State Highway and Transportation Officials, Washington, DC, 1781 pp.

Abendroth, R.E., Greimann, L.F., Thomas, M., and Kirkpatrick, C. (1998), "Field Testing of Integral Abutments," Research Interim Report HR-399 – Iowa DOT, Iowa State University, Ames, IA, 18 pp.

Abendroth, R.E., and Greimann, L.F. (2005), "Field Testing of Integral Abutments," Research Report HR-399 – Iowa DOT, Iowa State University, Ames, IA, 819 pp.

Arsoy, S., Barker, R.M., and Duncan, J.M. (1999), "The Behavior of Integral Abutment Bridge," Research Report FHWA/VTRC 00-CR3, Virginia Transportation Research Council, Virginia Polytechnic and State University, Blacksburg, VA, 33 pp.

Barr, P.J., Halling, M.W., Huffaker, C., and Boyle, H. (2013), "Behavior and Analysis of an Integral Abutment Bridge," Research Report No. UT-13.12, Utah Department of Transportation, Brigham Young University, Provo, UT, 98 pp.

Burdette, E.G., Deatherage, J.H., and Goodpasture, D.W. (1999), "Behavior of Laterally Loaded Piles Supporting Bridge Abutments – Phase I," Research Report No. TNSPR-RES1081, Tennessee Department of Transportation, University of Tennessee, Knoxville, TN

Burdette, E.G., Deatherage, J.H., and Goodpasture, D.W. (2002), "Behavior of Concrete Integral Abutment Bridges" *Concrete International*, Vol. 24, No. 7, pp. 59-63.

Burdette, E.G., Tidwell, J.B., Ingram, E.E., Goodpasture, D.W., Howard, S.C., Wasserman, E.P., and Deatherage, J.H. (2004), "Lateral Load Tests on Prestressed Concrete Piles Supporting Integral Abutments," *PCI Journal*, Vol. 49, No. 5, pp. 70-77.

Burdette, E.G., Deatherage, J.H., and Goodpasture, D.W. (2007), "Behavior of Laterally Loaded Piles Supporting Bridge Abutments – Phase II," Research Report No. TNSPR-RES1190, Tennessee Department of Transportation, University of Tennessee, Knoxville, TN, 57 pp.

Brillouin Optical Time-Domain Reflectometer (BOTDR) Single Mode Fiber (SMF-28) information retrieved from THORLABS Inc. (https://www.thorlabs.com/)

Civjan, S., Lacroix, J., Takeuchi, A., and Higgins, K. (2021), "Curved Steel Girder Integral Abutment Bridges in Vermont, USA," BSCES Civil Engineering Practice, Vol. 29, No. 1, Boston Society of Civil Engineers Section, pp. 28-44.

Cook, A.E. (2010), "Instrumentation and Monitoring of an Integral Abutment Bridge Supported on HP-Steel Piles/Concrete Drilled Shafts," M.S. Thesis, Department of Civil, Construction, and Environmental Engineering, Iowa State University, Ames, IA, 119 pp.

Coduto, D.P. (2001), *Foundation Design: Principles and Practices*, 2nd Edition, Prentice-Hall, Inc., New Jersey.

CSI (2016), *CSI Analysis Reference Manual*, Computer and Structures, Inc., Berkeley, CA, 556 pp.

Das, B.M., and Sivakugan, N. (2019), *Principles of Foundation Engineering*, 9th Edition, Cengage Learning, Boston, MA.

Doust, S.E. (2011), "Extending Integral Concepts to Curved Bridge Systems," Ph.D. Dissertation, Department of Civil Engineering, University of Nebraska-Lincoln, Lincoln, NE, 351 pp.

Duncan, J.M., Byrne, P., Wong, K.S., and Mabry, P. (1980), "Strength, Stress-strain and Bulk Modulus Parameters for Finite Element Analyses of Stresses and Movements in Soil Masses," Report No. UCB/GT/80-01, University of California, Berkeley, CA, 80 pp.

Dunker, K.F., and Abu-Hawash, A. (2005), "Expanding the Use of Integral Abutments in Iowa," *Proceedings of the 2005 Mid-Continent Transportation Research Symposium*, Ames, IA, Aug., 13 pp.

Fennema, J.L., Laman, J.A., and Linzell, D.G. (2005), "Predicted and Measured Response of an Integral Abutment Bridge," *ASCE Journal of Bridge Engineering*, Vol. 10, No. 6, pp. 666-677.

Frosch, R. J., Chovichien, V., Durbin, K., and Fedroff, D. (2006), "Jointless and Smoother Bridges: Behavior and Design of Piles," Research Report FHWA/IN/JTRP-2004/24, INDOT/Purdue Joint Transportation Program, West Lafayette, IN., 488 pp.

Frosch, R.J., Kreger, M.E., and Talbott, A.M. (2009), "Earthquake Resistance of Integral Abutment Bridges," Research Report FHWA/IN/JTRP-2008/11, INDOT/Purdue Joint Transportation Program, West Lafayette, IN., 223 pp.

Frosch, R.J., and Lovell, M.D. (2011), "Long-Term Behavior of Integral Abutment Bridges," Research Report FHWA/IN/JTRP-2011/16, INDOT/Purdue Joint Transportation Program, West Lafayette, IN., 149 pp.

Frosch, R.J., Bobet, A., and Khasawneh, Y. (2014), "Reduction of Bridge Construction and Maintenance Costs through Coupled Geotechnical and Structural Design of Integral Abutment Bridges," Research Report FHWA/IN/JTRP-2014/06, INDOT/Purdue Joint Transportation Program, West Lafayette, IN., 167 pp.

Greimann, L.F., Abendroth, R.E., Johnson, D.E., and Ebner, P.B. (1987), "Pile Design and Tests for Integral Abutment Bridges," Research Report HR-273 – Iowa DOT, Iowa State University, Ames, IA, 302 pp.

Greimann, L.F., Phares, B.M., Deng, Y., Shryack, G., and Hoffman J. (2014), "Field Monitoring of Curved Girder Bridges with Integral Abutment Bridges," Research Report FHWA TPF-5(169) and InTrans Project 08-323, Iowa State University, Ames, IA, 252 pp.

Guo, Z. (2015), "Numerical Analysis of Passive Force on Skewed Bridge Elements," M.S. Thesis, Department of Civil and Environmental Engineering, Brigham Young University, Provo, UT, 120 pp.

Hoffman, J.J. (2013), "Analytical and Field Investigation of Horizontally Curved Girder Bridges," M.S. Thesis, Department of Civil, Construction, and Environmental Engineering, Iowa State University, Ames, IA, 73 pp.

Isenhower, W.M., Wang, S., Vasquez, L.G. (2020), *LPILE v2019 Technical Manual*, Ensoft, Inc., Austin, TX, 271 pp.

Itasca, *FLAC* (2015), *Version 8.0: Fast Lagrangian Analysis of Continua-User's Guide*, Itasca Consulting Group Inc., Minneapolis, MN, 77 pp.

Jessee, S.J. (2012), "Skeew Effects on Passive Earth Pressures based on Large-Scale Tests," M.S. Thesis, Department of Civil and Environmental Engineering, Brigham Young University, Provo, UT, 77 pp.

Kalayci, E., Civjan, S.A., and Breña, S.F. (2012), "Parametric Study on the Thermal Response of Curved Integral Abutment Bridges," *Engineering Structures*, Vol. 43, pp. 129-138.

Kaufmann, W., and Alvarez, M. (2011), "Swiss Federal Roads Office Guidelines for Integral Bridges," *Structural Engineering International*, Vol. 21, No. 2, pp. 189-194.

Kim, W.S. (2008), "Load and Resistance Factor Design for Integral Abutment Bridges," Ph.D. Dissertation, Department of Civil and Environmental Engineering, The Pennsylvania State University, University Park, PA, 254 pp.

Kim, W.S., and Laman, J.A. (2010), "Numerical Analysis Method for Long-Term Behavior of Integral Abutment Bridges," *Engineering Structures*, Vol. 32, No. 8, pp. 2247-2257.

Kim, W.S., Laman, J.A., and Linzell, D.G. (2011), "Prediction of Concrete Integral Abutment Bridge Unrecoverable Displacements," *ACI SP 284 – 11: Andy Scanlon Symposium on Serviceability and Safety of Concrete Structures: From Research to Practice*, pp. 155-174.

Kirupakaran, K. (2013), "Soil-Structure Interaction Studies for Understanding the Behavior of Integral Abutment Bridges," Ph.D. Dissertation, School of Civil Engineering and Environmental Science, The University of Oklahoma, Norman, OK, 192 pp.

Laman, J.A., and Kim, W. (2009), "Monitoring of Integral Abutment Bridges and Design Criteria Development," Research Report FHWA-PA-2009-005-PSU002, Pennsylvania Transportation Research Council, University Park, PA, 650 pp.

Lindeburg, M.R. (2014), *Civil Engineering Reference Manual for the PE Exam*, 14th Edition, Professional Publications, Inc., Belmont, CA.

Lovell, M.D. (2010), "Long-Term Behavior of Integral Abutment Bridges," Ph.D. Dissertation, School of Civil Engineering, Purdue University, West Lafayette, IN, 336 pp.

Moorty, S., and Roeder, C.W. (1992), "Temperature-Dependent Bridge Movements," *ASCE Journal of Structural Engineering*, Vol. 118, No. 43, pp. 1090-1105.

Paul, M., Laman, J.A., and Linzell, D.G. (2005), "Thermally Induced Superstructure Stresses in Prestressed Girder Integral Abutment Bridges," *Transportation Research Record: Journal of the Transportation Research Board, CD 11-S*, pp. 287-297.

Kim, S., Eun, J., Alhowaidi, Y., and Robertson, D. (2021), "Feasibility Study: Alternatives to Prevent Settlements and Bumps at Bridge Approach," Research Report for SPR-P1(20) M106, Nebraska Department of Transportation, Research Section, Lincoln, NE, 161 pp.

Kondner, R.L. (1963), "Hyperbolic stress-strain response: cohesive soils," *Journal of the Soil Mechanics and Foundations Division*, Vol. 89, No. 1, pp. 115-143.

Kulicki, J.M., Wassef, W.G., Kleinhans, D.D., Yoo, C.H., Nowak, A.S., and Grubb, M. (2006), "Development of LRFD Specifications for Horizontally Curved Steel Bridges," NCHRP Report 563, National Cooperative Highway Research Program, Transportation Research Board, Washington, DC, 73 pp.

Morcous, G., and Abo-Elkhier, M. (2021), "Design and Detailing of Cast-in-Place and Precast Concrete Approach Slabs," SPR-1(20) Report M108, NDOT, Lincoln, NE, 95 pp.

NDOT (2016), *Bridge Office Policies and Procedures (BOPP),* Nebraska Department of Transportation, https://dot.nebraska.gov/media/2912/bopp-manual.pdf

Olson, S.M., Holloway, K.P., Buenker, J.M., Long, J.H., and LaFave, J.M. (2013), "Thermal Behavior of IDOT Integral Abutment Bridges and Proposed Design Modifications," Research Report FHWA-ICT-12-022, Illinois Center for Transportation, IDOT/University of Illinois, Urbana Champaign, IL, 88 pp.

Paraschos, A. (2016), "Effects of Wingwall Configurations on the Behavior of Integral Abutment Bridges," Ph.D. Dissertation, Department of Civil and Environmental Engineering, University of Maryland, College Park, MD, 344 pp.

Russell, D.N. (2014), "The Influence of Pile Shape and Pile Sleeves on Lateral Load Resistance," M.S. Thesis, Department of Civil and Environmental Engineering, Brigham Young University, Provo, UT, 166 pp.

Shamsabadi, A. (2007), "Three-Dimensional Nonlinear Seismic Soil-Abutment-Foundation-Structure Interaction Analysis of Skewed Bridges," Ph.D. Dissertation, Department of Civil and Environmental Engineering, University of Southern California, Los Angeles, CA, 380 pp.

Schanz, T., Vermeer, P.A., and Bonnier, P.G. (1999), "The Hardening Soil Model: Formulation and Verification," *Beyond 2000 in Computational Geotechnics – 10 Years of PLAXIS*, Balkema, Rotterdam, pp. 1-16.

Sherafati, A. (2011), "Expanding the Length of Jointless Bridges by Providing Rotational Capacity over the Pile Head," Ph.D. Dissertation, Department of Civil Engineering, University of Nebraska-Lincoln, Lincoln, NE, 352 pp.

Shryack, G.L. (2012), "Field Monitoring and Evaluation of Curved Girder Bridges," M.S. Thesis, Department of Civil, Construction, and Environmental Engineering, Iowa State University, Ames, IA, 144 pp.

Smith, K.M. (2014), "Passive Force on Skewed Bridge Abutments with Reinforced Concrete Wingwalls Based on Large-Scale Tests," M.S. Thesis, Department of Civil and Environmental Engineering, Brigham Young University, Provo, UT, 186 pp.

Snow, S.K. (2019), "Numerical Analysis of Passive Force on Skewed Bridge Abutments with Reinforced Concrete Wingwalls," M.S. Thesis, Department of Civil and Environmental Engineering, Brigham Young University, Provo, UT, 109 pp.

Thanasattayawibul, N. (2006), "Curved Integral Abutment Bridges," Ph.D. Dissertation, Department of Civil and Environmental Engineering, University of Maryland, College Park, MD, 383 pp.

Vermeer, P.A. (1978), "A Double Hardening Model for Sand," *Géotechnique*, Vol. 28, No. 4, pp. 413-433.

White 2nd, H. (2007), "Integral Abutment Bridges: Comparison of Current Practice Between European Countries and The United States of America," Research Report FHWA/NY/SR-07/152, Special Report 152, New York State Department of Transportation, 21 pp.

Wolde-Tinsae, A.M. (1981), "State-of-the-Art Methods for Design of Integral Bridge Abutments," Research Report HR-227 – Iowa DOT, Iowa State University, Ames, IA, 97 p.

Zheng, Y., and Fox, P. J. (2017), "Numerical Investigation of the Geosynthetic Reinforced Soil–Integrated Bridge System under Static Loading," *Journal of Geotechnical and Geoenvironmental Engineering*, Vol. 143, No. 6, Paper: 04017008.

APPENDICES

APPENDIX A

Properties of Foundation Soil and Backfill Soil

Table A.1: Properties of Foundation Soil obtained from Borehole Logs of Abutments

Location	Depth (*m*)	Soil Type	SPT *N* value	Remarks
South Abutment	5.5*–9	Clayey Silt	2	Water table exists at 2.4 *m* from the top
	9–11	Sand	13	
	11–16.5	Sand and Gravel	16	
	16.5–21.3	Clayey Silt	25	
North Abutment	5.5*–7.3	Silty sand	28	Water table exists at 1 *m* from the top
	7.3–11	Sand	14	
	11–17	Sand and Gravel	16	
	17–19.5	Clayey Silt	25	
	19.5–21.3	Sand	26	

*The elevation starts from 5.5 m, above which the backfill soil is placed for both abutments.

Table A.2: Properties of Backfill Soil obtained from Laboratory Tests (Kim et al., 2021)

Property	Value
D_{60}	0.69
D_{30}	0.41
D_{10}	0.22
Coefficient of uniformity (C_u)	3.14
Coefficient of uniformity (C_c)	1.11
Specific gravity (G_s)	2.65
Internal friction angle (°)	30

Note: Laboratory tests were conducted based on ASTM D-422, ASTM D-854, and ASTM D-3080.

APPENDIX B

Numerical Simulation Model of the Backfill

The backfill has been modeled through spring stiffnesses in the numerical structural model used for parametric studies and details are introduced in Chapter 5. However, this backfill can be separately modeled with finite element models to study the behavior of soil behind the IAB structure. This Appendix B introduces this soil modeling process. The backfill soil can be subjected to loads that are coming from the integral abutment bridge structure which moves based on the daily and seasonal contraction and expansion cycles additional to the concrete time-dependent behavior (shrinkage).

A two-dimensional finite difference analysis using FLAC 2D (Fast Larangian Analysis of Continua) can be used to model the north abutment of the bridge. The bridge model (Figure A.1) is restrained at the bottom in both horizontal and vertical directions. Moreover, a roller is placed on both sides to confine any horizontal movements while allowing vertical deformation (excluding the abutment, which is allowed to displace in both directions). In addition, the mesh is constructed to be of diminutive size towards the top of the soil, to capture small responses in the model due to the loading conditions.

The backfill soil can be modeled using the plastic hardening (PH) model, a built-in function in FLAC. Schanz et al. (1999) developed the PH model in light of the theory of plasticity. This constitutive model is based on previous works in the literature (Konder, 1963; Vermeer 1978; Duncan, 1980).

Unlike the linearly elastic-perfectly plastic stress-strain representation in Mohr-Coulomb (MC) model, the PH model gives a nonlinear hyperbolic representation of the soils. In addition, the stiffness parameter in the later model depends on the stress level (i.e., changes with depth). These hyperbolic non-linear soil models have been successfully implemented previously to capture the backfill behavior behind the abutment by Zheng and Fox (2017). The backfill soil input parameters that can be used for the soil model are shown in Table A.3.

The roadway foundation soils (granular subbase and subgrade sand) can be simulated as an elastic-perfectly plastic material with Mohr-Coulomb failure criteria, and their properties were obtained from previous work (Kim et al., 2021). In addition, the foundation and embankment soils can be modeled as elastic-perfectly plastic material with MC- failure criteria, and their properties are shown in Table A.4.

Table A.3: Plastic Hardening Input Parameters used to Represent Backfill Soil

Property	Value	Reference
E_{50}^{ref} (MPa)	32	Nam and Thao (2011); Abu Farakh et al. 2019
E_{ur}^{ref} (MPa)	128	Duncan et al. (1980); Surarak et al. 2012
E_{odo}^{ref} (MPa)	32	Duncan et al. (1980); Surarak et al. (2012)
m	0.55	Schanz et al. (1999)
Poisson’s ratio	0.25	Hatami and Bathurst (2002)
Cohesion	0	
Soil density (kN/m^3)	17.2	NDOT
Friction angle (°)	30	NDOT
Dilatancy angle (°)	6	Hatami and Bathurst (2002)

Table A.4: Properties of the Embankment and the Foundation Soil behind the IAB

Parameter	Type of soil		
	Embankment Soil	**Foundation 1**	**Foundation 2**
Modulus of Elasticity (MPa)	33	40	50
Soil density (kN/m^3)	18	17	16
Poisson's ratio	0.25	0.2	0.25
Cohesion (kPa)	0	10	15
Friction angle (°)	28	25	35

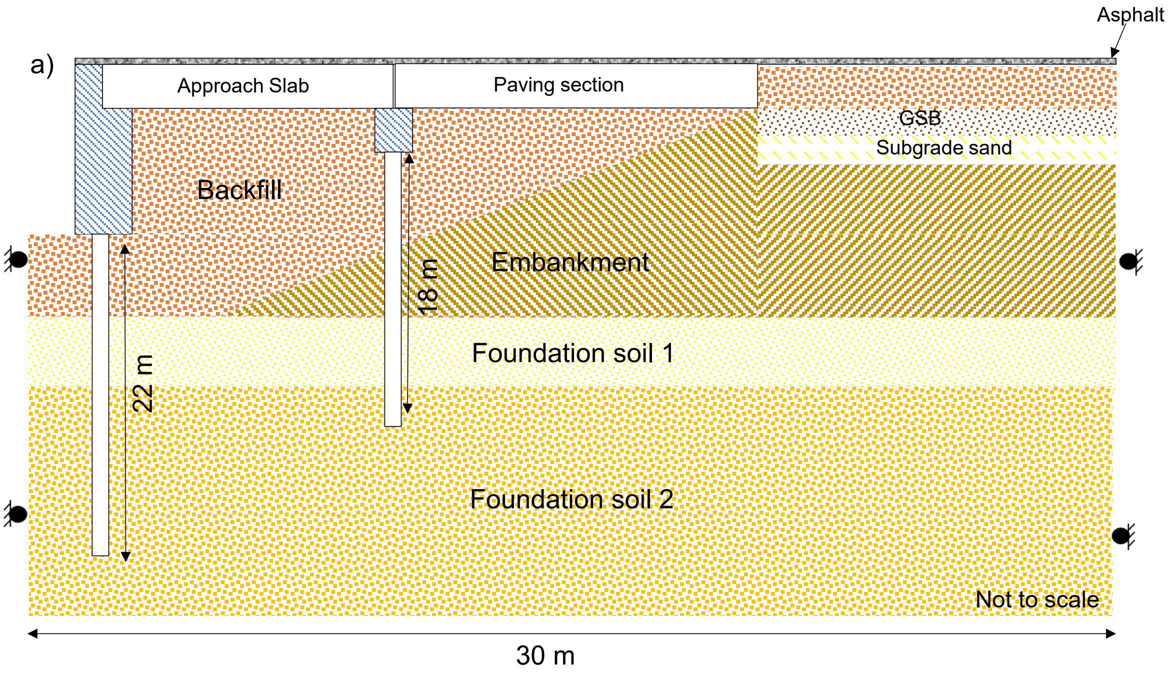

Figure A.1: Numerical Simulation Model to Investigate Thermal Loading Effect on backfill of the North Abutment

The embankment and foundation soil materials can be modeled as elastic-perfectly plastic material with MC-failure criterion, and their properties are shown in Table A.4. The abutment and grade beam piles could be modeled using the pile elements in FLAC 2D. The pile elements interact with the soil through shear and normal coupling springs. More details on obtaining the shear and normal springs constant are presented in (Kim et al., 2021; Itasca 2015). The input parameters for the pile elements used in this study are summarized in Table A.5.

Table A.5: Input Parameters for the Normal and Shear Spring Constant used in the North Abutment

Spring type	**Depth (m)**	**Stiffness MN/m/m**	**Cohesion strength kN/m**	**Friction angle (°)**
Normal	0-2	0.8	7.5	3.4
	2-10	6.3	19.88	15.4
	10-20	8.55	27.44	19.3
Shear	0-2	0.28	4.71	21
	2-10	1.43	14.13	26.25
	10-20	2.55		